Alignment and Structure in MHD Dynamos

Submitted by Daniel Miller, to the University of Exeter as a thesis for the degree of Doctor of Philosophy in Mathematics, January 2019

I certify that all material in this thesis which is not my own work has been identified and that any material that has previously been submitted and approved for the award of a degree by this or any other University has been acknowledged.

(Signature) _____

Abstract

Magnetic fields are ubiquitous within astrophysical settings. There is strong evidence to suggest that some of these magnetic fields, for example the Sun's, are maintained through a dynamo process whereby energy is exchanged between a flow and a magnetic field. Magnetohydrodynamics (MHD) is the branch of mathematics where this interaction is studied.

The initial amplification of a weak seed field is often modelled using the kinematic dynamo approximation where the flow is not influenced by the magnetic field. This approximation to the early behaviour of a nonlinear dynamo problem, where the magnetic field grows exponentially during a kinematic phase and then saturates into a nonlinear regime, has the benefit of being far less computationally intensive.

In this thesis, I examine three different topics within MHD dynamos.

First, I examine how measuring alignment of the flow and magnetic field during a kinematic dynamo can reveal changes to the magnetic field structure. This I show to be useful both within individual simulations and when comparing magnetic fields within parameter studies.

Secondly, I examine nonlinear dynamos where the flow and magnetic field are strongly aligned and have almost identical energies. I reproduce, and give an explanation for, a previously unexplained behaviour. Furthermore, I show that aligned flow and magnetic fields can exist for increasingly complex forcings and as such the aligned state is remarkably robust.

Finally, I consider a number of different nonlinear dynamos for a family of forcings with different magnetic field structures during their kinematic phase. Using Minkowski Func-

tions to quantify the structures, I show that, where the magnetic field becomes sufficiently strong, the magnetic fields become (or remain) ribbon-like in the nonlinear regime. As such, the influence that stagnation points in the flow have on the magnetic field structure is less than in the kinematic dynamo equivalent.

Acknowledgements

Throughout the PhD I have been extremely fortunate to have the help and support of a large number of people. I am immensely grateful to them all.

I am grateful to the Engineering and Physical Sciences Research Council for providing me with a studentship that made my research possible.

In addition I am immensely grateful for the help and support of my PhD supervisor Dr Joanne Mason throughout the PhD process. Her patience and insights were invaluable in my development as a researcher. I am also grateful for the help and insights of my second supervisor Professor Andrew Gilbert throughout the PhD.

Finally I would like to thank my wife Laura for her love and support during the PhD.

Contents

List of Figures

List of Tables

Chapter 1

Thesis Outline, Overview of MHD and Dynamo Theory

1.1 Outline of Thesis

This thesis is split into a number of chapters. Chapters 1 and 2 contain preliminary information which is important for the understanding of the original results within the thesis.

The remainder of this chapter contains information on the particular set of MHD equations that I solve and a summary of a number of important MHD results. This is then supplemented by appendices A and B where I prove a number of anti-dynamo theorems and show conservation of the ideal MHD quantities.

Chapter 2 then contains information on how the MHD equations are solved numerically. It includes information on the following:

- How the induction equation is simplified for a subset of flow profiles
- A general outline of how the MHD equations are solved
- Specific information on the timestepping schemes used throughout the thesis.

My results are then split into three chapters, each with a different theme. Two of these (chapters 4 and 5) are concerned with the role that alignment of the flow and magnetic

field plays within MHD. An overview of related literature as well as motivation for my work on alignment can be found in chapter 3.

Finally, in chapter 6 I examine changes in magnetic field structure once the magnetic field is strong enough to affect the evolution of the flow. Motivations for this work and an overview of existing literature can be found in the first section of the chapter.

As each of the chapters is intended to be independent all three chapters of results ends with a discussion on the findings and ideas for future research. This is instead of having a single section at the end of the thesis.

1.2 Deriving the Governing Equations

To derive the governing equations we require the Navier-Stokes equation (1.1a), Ohm's law (1.1b) and Maxwell's equations (1.1c)-(1.1f) as well as the assumption that the speed of the plasma , U, is less than the the speed of light, c.

$$\rho\frac{D\mathbf{u}}{Dt} = -\nabla p + \mu\nabla^2\mathbf{u} + \mathbf{F} \qquad (1.1a)$$

$$\mathbf{j} = \sigma(\mathbf{E} + \mathbf{u}\times\mathbf{B}) \qquad (1.1b)$$

$$\varepsilon_0\nabla\cdot\mathbf{E} = \rho_c \qquad (1.1c)$$

$$\nabla\times\mathbf{E} = -\frac{\partial\mathbf{B}}{\partial t} \qquad (1.1d)$$

$$\nabla\cdot\mathbf{B} = 0 \qquad (1.1e)$$

$$\frac{1}{\mu_0}\nabla\times\mathbf{B} = \mathbf{j} + \varepsilon_0\frac{\partial\mathbf{E}}{\partial t} \qquad (1.1f)$$

where ρ_c is the electrical charge density, ε_0 is the free space permitivity, μ_0 is the free space magnetic permeability and the speed of light is given by $c = \sqrt{\varepsilon_0\mu_0}$, $\mathbf{E}$ is the electric field, $\mathbf{B}$ is the magnetic flux density (commonly referred to as simply the "magnetic field") and σ is the electrical conductivity.

1.2.1 The Equation of Motion

The electrical conductivity of the plasma allows for two additional forces to be present within the flow and must therefore be represented in the equation of motion. The electrical charge density exerts a force $\rho_c\mathbf{E}$ and the current exerts a Lorentz force $\mathbf{j}\times\mathbf{B}$. Adding both of these forces to the Navier-Stokes equations gives (1.2)

$$\rho \frac{D\mathbf{u}}{Dt} = -\nabla p + \mu \nabla^2 \mathbf{u} + \mathbf{j} \times \mathbf{B} + \rho_c \mathbf{E} + \mathbf{F} \tag{1.2}$$

where the advective derivative is defined as $D/Dt = \partial/\partial t + (\mathbf{u} \cdot \nabla)$. Dimensional analysis along with the assumption about the speed of the fluid however shows that one of these terms is sufficiently small to be neglected. By non-dimensionalisng (1.1d) and assuming both terms make a contribution and are thus of equivalent magnitude it must be true that

$$\frac{E}{L} \sim \frac{B}{T}. \tag{1.3}$$

where E is a typical magnitude of $\mathbf{E}$, B is a typical magnitude of $\mathbf{B}$, L is a typical length and T is a typical time. Now taking this result and applying it to the ratio of the first term on the left hand side of (1.1f) and the second term on the right hand side we obtain

$$\frac{|\frac{\nabla \times \mathbf{B}}{\mu_0}|}{|\varepsilon_0 \frac{\partial \mathbf{E}}{\partial t}|} \sim \frac{\frac{B}{L\mu_0}}{\varepsilon_0 \frac{E}{T}} = \frac{\frac{ET}{L^2 \mu_0}}{\varepsilon_0 \frac{E}{T}} = \frac{c^2}{U^2}. \tag{1.4}$$

therefore $\frac{\nabla \times \mathbf{B}}{\mu_0} \gg \varepsilon_0 \frac{\partial \mathbf{E}}{\partial t}$ and we may neglect the second term on the right hand side of (1.1f) yielding

$$\mu_0 \mathbf{j} \approx \nabla \times \mathbf{B}. \tag{1.5}$$

Non-dimensionalising (1.1c) gives

$$|\rho_c| \sim \frac{\varepsilon_0 E}{L}. \tag{1.6}$$

We now have all of the dimensions that we require to compare the relative size of the two additional force terms

$$\frac{|\rho_c \mathbf{E}|}{|\mathbf{j} \times \mathbf{B}|} \sim \frac{\frac{\varepsilon_0 E^2}{L}}{\frac{B^2}{\mu_0 L}} = \frac{U^2}{c^2} \tag{1.7}$$

thus

$$\frac{|\rho_c \mathbf{E}|}{|\mathbf{j} \times \mathbf{B}|} \ll 1. \tag{1.8}$$

As the size of the term generated by the electrical charge density is much smaller than the

Lorentz force we can neglect it within the equation of motion leaving equation (1.9).

$$\rho\frac{D\mathbf{u}}{Dt} = -\nabla p + \mu\nabla^2\mathbf{u} + \mathbf{j}\times\mathbf{B} + \mathbf{F} \tag{1.9}$$

1.2.2 The Induction Equation

To get an equation to describe the evolution of the magnetic field I take the curl of (1.1b), substitute in both (1.1d) and (1.5) then use the vector identity $\nabla\times(\nabla\times\mathbf{B}) = \nabla(\nabla\cdot\mathbf{B}) - \nabla^2\mathbf{B}$ along with (1.1e), this gives

$$\frac{\partial\mathbf{B}}{\partial t} = \nabla\times(\mathbf{u}\times\mathbf{B}) + \eta\nabla^2\mathbf{B} \tag{1.10}$$

where η is called the magnetic diffusivity and is given by the equation $\eta = (\mu_0\sigma)^{-1}$. Equation (1.10), referred to as the induction equation, describes how the magnetic field evolves. The first term on the right, $\nabla\times(\mathbf{u}\times\mathbf{B})$, causes the magnetic field to grow whereas the second term, $\eta\nabla^2\mathbf{B}$, diffuses the magnetic field away.

If the field is incompressible, $\nabla\cdot\mathbf{u} = 0$, the curl term may be expressed as

$$\nabla\times(\mathbf{u}\times\mathbf{B}) = (\mathbf{B}\cdot\nabla)\mathbf{u} - (\mathbf{u}\cdot\nabla)\mathbf{B} \tag{1.11}$$

and we see that the term responsible for the growth of the magnetic field is made of two components. The first term, $(\mathbf{B}\cdot\nabla)\mathbf{u}$, causes growth through the stretching of the flow field. The second,$(\mathbf{u}\cdot\nabla)\mathbf{B}$, causes tangling of the magnetic field lines.

Removing the incompressibility restriction, non-dimensionalising by setting $\mathbf{B} = B_0\mathbf{B}$, $\mathbf{u} = \frac{L}{T}\mathbf{u}$, $t = Tt$, $\nabla = \frac{1}{L}\nabla$, $U = \frac{L}{T}$, and substituting into (1.10) yields

$$\frac{\partial\mathbf{B}}{\partial t} = \nabla\times(\mathbf{u}\times\mathbf{B}) + \frac{\eta}{LU}\nabla^2\mathbf{B} \tag{1.12}$$

$$= \nabla\times(\mathbf{u}\times\mathbf{B}) + \frac{1}{R_m}\nabla^2\mathbf{B}. \tag{1.13}$$

Where the non-dimensional number R_m is called the magnetic Reynold's number and de-

scribes the relative importance of the advective and diffusive terms in the induction equation.

$$R_m \approx \frac{Advection}{Diffusion} \tag{1.14}$$

Note that the scalings used to form (1.13) give a flow turnover time of order 1 and an electromagnetic diffusion time of order R_m [45].

The two extreme regimes of the parameter are of particular importance. In the regime $R_m \ll 1$ the second term of the right hand side dominates and the induction equation can be approximated simply as a diffusion equation

$$\frac{\partial \mathbf{B}}{\partial t} \approx \eta \nabla^2 \mathbf{B}. \tag{1.15}$$

Dimensional analysis of this by setting $t = \tau_{diffusion}$, $\nabla^2 = L^{-2}$ and $\mathbf{B} = B_0 \mathbf{B}$ thus gives an estimate for the diffusive timescale

$$\tau_{diffusion} \sim \frac{L^2}{\eta}. \tag{1.16}$$

At the other extreme, $R_m \gg 1$, the advective term dominates

$$\frac{\partial \mathbf{B}}{\partial t} \approx \nabla \times (\mathbf{u} \times \mathbf{B}) \tag{1.17}$$

this is often referred to as the “ideal limit” or the “perfectly conducting limit”. This equation allows us to obtain an estimate for the advective timescale

$$\tau_{advection} \sim \frac{L}{U}. \tag{1.18}$$

Note that it is typically true that $\tau_{diffusion} > \tau_{advection}$ thus we typically expect the advection to act on a much faster timescale than the diffusion.

1.3 Summary of Conserved Quantities

Within unforced, incompressible, three dimensional MHD with zero diffusion, there are three conserved quantities. These are derived from volume integrals relating to equations (1.9) and (1.10). In each, $\mathbf{b} = \mathbf{B}/\rho$. The first is the total kinetic and magnetic energy

$$E = \int_v \frac{\mathbf{u}^2}{2} + \frac{\mathbf{b}^2}{2} dV. \tag{1.19}$$

The second is the magnetic-helicity which describes the degree of linkage within the magnetic field [74]

$$H_m = \int_V \mathbf{A} \cdot \mathbf{b} dV \tag{1.20}$$

and where $\mathbf{b} = \nabla \times \mathbf{A}$. The third is the cross-helicity which is a measure of the angular alignment of the magnetic field and the velocity field

$$H_c = \int_V \mathbf{u} \cdot \mathbf{b} dV. \tag{1.21}$$

An outline of how these conserved quantities are derived can be found within Appendix B.

1.4 A Solar Dynamo

Dynamo action is the action of converting one form of energy to another. In this case we are interested in converting kinetic energy to magnetic energy. One way of explaining why dynamo action is necessary for the Sun is to estimate the time it would take the Sun's magnetic field to decay away without a means of generating field. Consider the diffusive time-scale (1.22)

$$\tau_{diffusion} \sim \frac{L^2}{\eta}. \tag{1.22}$$

Now if we were to naively follow the reasoning often used to justify a geophysical dynamo we could take as an example of a typical length scale the Sun's radius

$$\text{Radius of the Sun} \approx 7 \times 10^8 m \tag{1.23}$$

estimates of the magnetic diffusivity for different regions in the Sun are given on page 79 of [87] as

$$\eta \approx \begin{cases} 10^4 m^2 s^{-1} & \text{Photosphere} \\ 10^3 m^2 s^{-1} & \text{Chromosphere} \\ 1 m^2 s^{-1} & \text{Corona.} \end{cases} \tag{1.24}$$

This yields the following estimates for the diffusive time-scale within the Sun

$$\tau_{diffusion} \approx \begin{cases} O(10^5) \text{ Years} & \text{Photosphere} \\ O(10^6) \text{ Years} & \text{Chromosphere} \\ O(10^9) \text{ Years} & \text{Corona} \end{cases} \tag{1.25}$$

However the above reasoning is flawed. The problem, as explained by P.H.Roberts on pages 1 and 2 of [88] is that the Sun's magnetic field is highly turbulent. As a result the correct length scale to use is a turbulent one and is much smaller than the radius of the Sun used above. A turbulent magnetic diffusivity must also be used and the result is that the diffusive timescale is in fact of the order of a decade. Estimates of the age of the Sun put it at approximately 5×10^9 years old which is much older than this turbulent diffusive timescales. We thus require a mechanism by which magnetic fields can be generated, with a dynamo the most likely candidate.

Another indicator that the Sun's magnetic field is evolving as a consequence of dynamo action can be seen by looking at the sunspot cycle. Consider figure 1.1 which shows the yearly average sunspot numbers. What we see is that with the exception of two so called "grand minima" where sunspot numbers were uncharacteristically low (the Maunder minima between 1645 and 1715 and the Dalton minimum approximately between 1800-1820) the period of the sunspot numbers is approximately 11 years. At the end of the 11 years the Sun's magnetic field reverses its polarity and thus the 11 year cycle is one half

of a larger 22 year cycle. This thus seems to indicate that the magnetic field of the Sun has a time dependence and thus that there must be a mechanism driving its evolution.

This is supported by figure 1.2 which shows the predominant location of the sunspots upon the Sun's surface. Here we see that the sunspots are initially predominantly located at latitudes of approximately $\pm 30^{\circ}$ however over a period of approximately 11 years they migrate towards the equator and this behaviour repeats periodically. This repeated cycle is another indicator that the Sun has an underlying dynamo mechanism generating its magnetic field.

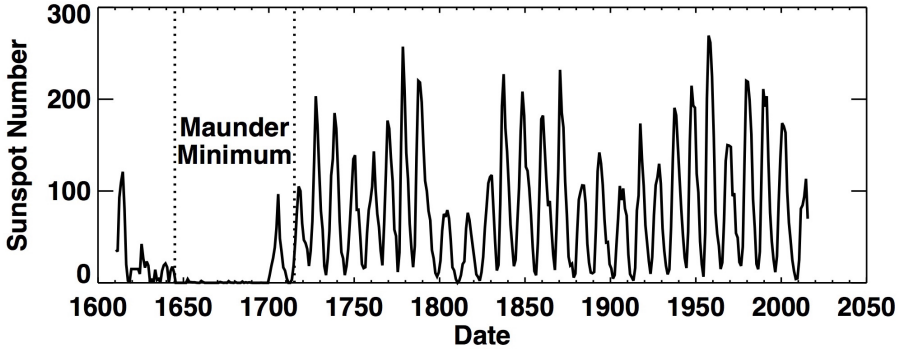

Figure 1.1: Yearly averages of sunspot numbers taken from [54].

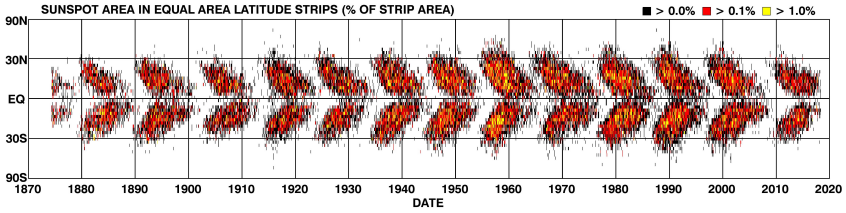

Figure 1.2: Butterfly diagram of the location of sunspots taken from [54].

We thus see that both the strength of the Sun's magnetic field and its periodic time dependence indicate that a dynamo is responsible for the evolution of the Sun's magnetic field.

During section 3 I briefly discuss the solar wind. The effective magnetic Reynolds number of the solar wind has been estimated to be $260,000 \pm 20,000$ by Weygand et al. [107]. In comparison, the magnetic Reynolds number for the photosphere is estimated to be 10^6 and 10^9 for the deep convection zone [106]

1.5 Kinematic Dynamos

Consider the case where the magnetic field is initially small. The Lorentz force in (1.9) is therefore small. This allows us to make a simplifying approximation that the Lorentz force may be neglected and that as a result the field does not act on the flow. This then allows us to prescribe a flow $\mathbf{u}$ and solve (1.10) independently of (1.9). Furthermore due to the structure of (1.10) the induction equation is linear in $\mathbf{B}$ therefore solutions are of the form

$$\mathbf{B}(x,y,z,t) = \mathbf{B}'(x,y,z)e^{\sigma t} \tag{1.26}$$

and this further simplifies the problem. The aim of kinematic dynamo theory is to find flows for which the dynamo growth rate, given by the real component of σ, is positive. The hope is that by prescribing a flow and evolving only the induction equation we can observe robust behaviour that is still important when we model the full system but may be obscured by the complexities of the dynamics. The flow can be selected using a number of different criteria. One common way of selecting the flow is to pick a flow that in some way mimics behaviour that we either observe. Another is to pick a flow that makes the numerics more simple.

1.5.1 Anti-Dynamo Theorems and Bounds on R_m

The issue of whether a certain flow can give rise to dynamo action is further complicated by the fact that there exists a number of different theorems which prove that flows of a particular form do not yield dynamo action. Below I state a number of these theorems which are then proven within Appendix A.

1. **Impossibility of Maintaining a 2.5D Magnetic Field by Dynamo Action**: A magnetic field that vanishes at infinity, is of the form $(B_x(x,y,t), B_y(x,y,t), B_z(x,y,t))$ in a cartesian geometry and is driven by an incompressible flow cannot be maintained by dynamo action.

2. **Zeldovich's Anti-Dynamo Theorem**: A planar incompressible flow of the form $\mathbf{u} = \big(u_x(x,y,z,t), u_y(x,y,z,t), 0\big)$ in a bounded volume V at whose boundaries the magnetic field vanishes cannot maintain a magnetic field.

3. **Cowling's Anti-Dynamo Theorem**: An axisymmetric magnetic field which vanishes at infinity cannot be maintained by dynamo action.

4. **Impossibility of a Dynamo Driven by a Purely Toroidal Flow**: An incompressible, purely toroidal, flow of the form $\mathbf{u} = \mathbf{u}_T = \nabla \times (\mathbf{x}\psi_T) = -\mathbf{x} \times \nabla\psi_T$, where $\mathbf{x}$ is the position vector, cannot maintain a dynamo.

As well as anti-dynamo theorems which tell us whether a particular flow can generate dynamo action (or whether a flow can sustain a magnetic field with a particular structure) there are also a number of proofs giving lower bounds on what R_m is needed for dynamo action. These are stated below and proven in appendix A

1. **The Childress Bound**: For kinematic dynamo action to be possible we require $R_m^1 > \pi$

2. **The Backus Bound**: For kinematic dynamo action to be possible we require $R_m^2 > \pi^2$

Note that in these bounds the definition of the magnetic Reynolds number is different, in particular

$$R_m^1 = \frac{u_{max} \times a}{\eta} \tag{1.27}$$

$$R_m^2 = \frac{e_{max} \times a^2}{\eta} \tag{1.28}$$

where a is the radius of a sphere and u_{max} and e_{max} are defined in (1.29) and (1.30).

$$u_{max} \leq \left(\int_V |\mathbf{u}|^2 \right)^{\frac{1}{2}} \tag{1.29}$$

$$2e_{ij} = \partial_i u_j + \partial_j u_i$$

$$e_{max} \leq \left(\int_V |\mathbf{e}_{ij}|^2 \right)^{\frac{1}{2}} \tag{1.30}$$

The origins of these quantities is detailed in appendix A.

Chapter 2

Code Development and Checks

2.1 Introduction

In this section I outline the numerical aspects of each of the sections which contain my research. As such the sections are intended to be read when they are referred to in later chapters however they have been designed to also make sense if read from start to finish.

Section 2.2 contains the numerical information, as well as theory which simplifies the numerics, for my kinematic dynamo code. In this section I show how the magnetic field of flows with no z dependence can be conveniently reduced in complexity by proving that they can only depend upon z via a complex exponential. I also show how the particular form of the incompressible flows that I use within my kinematic simulations allows for the writing of the inductive term, $\nabla \times (\mathbf{u} \times \mathbf{B})$, in the induction equation in terms of mode couplings which vastly speeds up computation. Finally I outline the process that my code goes through in solving the induction equation and then show that my code obtains results in agreement with those already published. During this section I do not explicitly write out the timestepping schemes used, both for ease of reading and to save writing them multiple times. Instead they are given in section 2.4.

In section 2.3 I outline important computational information related to my code which solves both the equation of motion and the induction equation simultaneously. I outline how the divergence free condition on both $\mathbf{u}$ and $\mathbf{B}$ is maintained by a projection method. I then

outline the general methodology of the code with timestepping schemes again omitted and found inside section 2.4. Finally I again test my code to ensure it is outputting what we expect.

In section 2.5 I outline how I use the power spectrum and autocorrelation methods to calculate the period of time series at various points within my work. Finally in section 2.6 I outline how Poincare sections are calculated. These are used later within chapter 4 to look at how adding time dependence changes the chaotic nature of trajectories.

2.2 Solving the Induction Equation

2.2.1 The z Dependence of the Magnetic Field Within 2.5D Dynamos

A 2.5D dynamo is defined to be a kinematic dynamo whose flow (2.1) has all three components but each component only depends upon two dimensions.

$$\mathbf{u} = u_x(x,y)\widehat{\mathbf{e}}_x + u_y(x,y)\widehat{\mathbf{e}}_y + u_z(x,y)\widehat{\mathbf{e}}_z \tag{2.1}$$

As such the magnetic field only depends on z via a multiplication by an exponential, a statement that I will now prove via the separation of variables method. As $\mathbf{u}$ contains no z dependence I seek solutions for $\mathbf{B}$ of the form $\mathbf{B}(x,y,z,t) = F(z)\tilde{\mathbf{B}}(x,y,t)$. Applying the divergence free condition on the magnetic field yields (2.3).

$$\partial_x B_x + \partial_y B_y + \partial_z B_z = F(z)(\partial_x \tilde{B}_x + \partial_y \tilde{B}_y) + F'(z)\tilde{B}_z = 0 \tag{2.2}$$

$$\frac{F'(z)}{F(z)} = -\frac{(\partial_x \tilde{B}_x + \partial_y \tilde{B}_y)}{\tilde{B}_z} \tag{2.3}$$

Now defining a vector $\mathbf{A}$ such that $\mathbf{A} = \mathbf{u} \times \tilde{\mathbf{B}}$ and thus $F(z)\mathbf{A} = \mathbf{u} \times \mathbf{B}$ the induction equation may be written as (2.4).

$$F(z)\frac{\partial \tilde{\mathbf{B}}}{\partial t} = \nabla \times (F(z)\mathbf{A}) + \eta \nabla^2 \mathbf{B}$$
$$= F(z)\begin{pmatrix} \partial_y A_z \\ -\partial_x A_z \\ \partial_x A_y - \partial_y A_x \end{pmatrix} + F'(z)\begin{pmatrix} -A_y \\ A_x \\ 0 \end{pmatrix} + F(z)\eta \nabla_H^2 \tilde{\mathbf{B}} + \eta F''(z)\tilde{\mathbf{B}} \qquad (2.4)$$

where $\nabla_H^2 = \partial_{xx} + \partial_{yy}$. Now using equation (2.3) to replace $F'(z)$ in equation (2.4) and dividing through by $F(z)$ yields (2.5):

$$\eta \frac{F''(z)}{F(z)}\tilde{\mathbf{B}} = \frac{\partial \tilde{\mathbf{B}}}{\partial t} + \begin{pmatrix} -\partial_y A_z \\ \partial_x A_z \\ -\partial_x A_y + \partial_y A_x \end{pmatrix} + \frac{(\partial_x \tilde{B}_x + \partial_y \tilde{B}_y)}{\tilde{B}_z}\begin{pmatrix} -A_y \\ A_x \\ 0 \end{pmatrix} - \eta \nabla_H^2 \tilde{\mathbf{B}} \qquad (2.5)$$

thus for each component of the magnetic field $\tilde{B}_x, \tilde{B}_y$ and $\tilde{B}_z$ equation (2.4) can be rearranged to equations (2.6)-(2.8).

$$\frac{F''(z)}{F(z)} = \frac{1}{\eta \tilde{B}_x}\left[\frac{\partial \tilde{B}_x}{\partial t} + \begin{pmatrix} -\partial_y A_z \\ \partial_x A_z \\ -\partial_x A_y + \partial_y A_x \end{pmatrix} + \frac{(\partial_x \tilde{B}_x + \partial_y \tilde{B}_y)}{\tilde{B}_z}\begin{pmatrix} -A_y \\ A_x \\ 0 \end{pmatrix} - \eta \nabla_H^2 \tilde{B}_x\right] \qquad (2.6)$$

$$\frac{F''(z)}{F(z)} = \frac{1}{\eta \tilde{B}_y}\left[\frac{\partial \tilde{B}_y}{\partial t} + \begin{pmatrix} -\partial_y A_z \\ \partial_x A_z \\ -\partial_x A_y + \partial_y A_x \end{pmatrix} + \frac{(\partial_x \tilde{B}_x + \partial_y \tilde{B}_y)}{\tilde{B}_z}\begin{pmatrix} -A_y \\ A_x \\ 0 \end{pmatrix} - \eta \nabla_H^2 \tilde{B}_y\right] \qquad (2.7)$$

$$\frac{F''(z)}{F(z)} = \frac{1}{\eta \tilde{B}_z}\left[\frac{\partial \tilde{B}_z}{\partial t} + \begin{pmatrix} -\partial_y A_z \\ \partial_x A_z \\ -\partial_x A_y + \partial_y A_x \end{pmatrix} + \frac{(\partial_x \tilde{B}_x + \partial_y \tilde{B}_y)}{\tilde{B}_z}\begin{pmatrix} -A_y \\ A_x \\ 0 \end{pmatrix} - \eta \nabla_H^2 \tilde{B}_z\right] \qquad (2.8)$$

each of these equations is a function of z only on the left hand side and a function of x, y, t on the right hand side. Thus it must be true that $F''(z)/F(z) = C$ where C is some constant. Now by considering the possible sign of the constant and that to be physical we

require $\mathbf{B}$ to be finite for $|z| \to \infty$ we are able to find the form of $F(z)$.

Case 1: $C < 0$, let $C = -\lambda^2$

$$F''(z) + \lambda^2 F(z) = 0 \tag{2.9}$$

$$F(z) = A_1 e^{\lambda z} + B_1 e^{-\lambda z} \tag{2.10}$$

Requiring $\mathbf{B} < \infty$ for $|z| \to \infty$ yields $A_1 = B_1 = 0$ thus this case yields no solutions.

Case 2: $C = 0$

$$F(z) = A_2 z + B_2 \tag{2.11}$$

Requiring $\mathbf{B}$ be finite for $|z| \to \infty$ yields $A_2 = 0$ however $F(z) = B_2$ is a possible solution.

Case 3: $C > 0$, let $C = k^2$

$$F''(z) - k^2 F(z) = 0 \tag{2.12}$$

$$F(z) = A_3 e^{ikz} + B_3 e^{-ikz} \tag{2.13}$$

Requiring $\mathbf{B}$ be finite for $|z| \to \infty$ places no restrictions upon A_3 and B_3 thus $F(z) = A_3 e^{ikz} + B_3 e^{-ikz}$ is a solution. The form of the magnetic field is therefore (2.14)

$$\mathbf{B}(x,y,z,t) = A\tilde{\mathbf{B}}(x,y,t)e^{ikz} + B\tilde{\mathbf{B}}(x,y,t)e^{-ikz}. \tag{2.14}$$

Requiring that this be real and relabelling $A\tilde{\mathbf{B}}(x,y,t) = \mathbf{B_1}(x,y,t)$ and $B\tilde{\mathbf{B}}(x,y,t) = \mathbf{B_2}(x,y,t)$ yields (2.15)

$$(\mathbf{B}_2^I + \mathbf{B}_1^I)\cos(kz) + (\mathbf{B}_1^R - \mathbf{B}_2^R)\sin(kz) = 0. \tag{2.15}$$

and in general (2.16a) and (2.16b) must be true.

$$\mathbf{B}_2^I = -\mathbf{B}_1^I \qquad \text{(2.16a)} \qquad\qquad \mathbf{B}_1^R = \mathbf{B}_2^R \qquad \text{(2.16b)}$$

thus $\mathbf{B}_1$ and $\mathbf{B}_2$ form a complex conjugate pair and $\mathbf{B}$ can be written as (2.17)

$$\mathbf{B}(x,y,z,t) = \sum_k \left[\mathbf{b}_k(x,y,t)e^{ikz} + \text{Complex Conjugate}\right]. \tag{2.17}$$

For individual k modes this exponential then cancels out of the induction equation due to its linearity and we can solve for $\mathbf{b}_k$. Note that the $C = 0$ case is included in (2.17) through the $k = 0$ term. Noting that the linearity of the induction equation gives a time dependence of $\exp\left(pt + i\omega t\right)$ where both p and ω are real functions of k enables us to express (2.17) in the form (2.18) where $\mathbf{b}(x,y,t) = \mathbf{b}'(x,y)\exp(pt + i\omega t)$ and $\Re$, $\Im$ denote real and imaginary parts respectively.

$$\mathbf{B}(x,y,z,t) = 2\sum_k \exp(pt)\left[\Re\{\mathbf{b}'(x,y)\}\cos(kz+\omega t) - \Im\{\mathbf{b}'(x,y)\}\sin(kz+\omega t)\right] \tag{2.18}$$

The ability to reduce the magnetic field $\mathbf{B}$ to the form (2.17) therefore means that we are able to reduce the system that we are required to solve to two spatial dimensions. The benefit of this is that computations can be performed much faster. However we must be mindful of the fact that we are solving for $\mathbf{b}$ rather than $\mathbf{B}$. To reconstruct $\mathbf{B}$ we would have to solve for all k and then use (2.18) to reconstruct the magnetic field. However if we are only interested in the behaviour and form of $\mathbf{B}$ at large time, as is often the case, then we simply have to find the value of k corresponding to the largest p as the exponential dependence of (2.18) on this real part of the growth rate would then ensure that this provides the majority of the contribution to the full $\mathbf{B}$ at large time.

To summarise the use of a 2.5D flow enables us to express the z dependence of the magnetic field as a sum of modes each dependent only on a complex exponential in the z direction and whose form I have proven. The linearity of the induction equation then enables us to solve for each of these modes independently. Furthermore the magnetic field depends only on time via a complex exponential and thus if we are only interested in the behaviour at large time then the mode whose vertical wavenumber k corresponds to the largest real part of the growth rate p is a good approximation to the field as a whole. Substituting an individual mode $\mathbf{b}(x,y,t)\exp(ikz)$ into the induction equation and cancelling exponentials yields the induction equation for a single mode (2.19) where $\nabla_H = (\partial_x, \partial_y, 0)$ and $\hat{\mathbf{z}} = (0,0,1)$.

$$\frac{\partial \mathbf{b}}{\partial t} = \nabla_H \times (\mathbf{u} \times \mathbf{b}) + ik\hat{\mathbf{z}} \times (\mathbf{u} \times \mathbf{b}) + (\nabla_H - k^2)\mathbf{b} \tag{2.19}$$

The induction equation for a single mode thus depends only upon two spatial dimensions and can be solved with vastly less computational resources.

2.2.2 Making Use of Mode Coupling Within Incompressible Kinematic Dynamos

If a flow is incompressible then the induction term may be simplified to

$$\nabla \times (\mathbf{u} \times \mathbf{B}) = (\mathbf{B} \cdot \nabla)\mathbf{u} - (\mathbf{u} \cdot \nabla)\mathbf{B}. \tag{2.20}$$

All flows that I consider within kinematic dynamo calculations are sums and products of sine and cosine functions. As such each can be expressed as a small number of Fourier modes and (2.20) can be expressed as a small number of Fourier mode couplings. This is best illustrated via an example. Consider a flow

$$\mathbf{u} = \begin{pmatrix} \sin(y) \\ \sin(x) \\ 0 \end{pmatrix}. \tag{2.21}$$

The first term on the right of (2.20) then becomes

$$(\mathbf{B} \cdot \nabla)\mathbf{u} = \begin{pmatrix} B^y \cos(y) \\ B^x \cos(x) \\ 0 \end{pmatrix}. \tag{2.22}$$

now consider only the $\widehat{\mathbf{e}}_x$ component of this. Expressing the magnetic field in terms of the sum of its Fourier nodes, rewriting the cosine term using Euler's identity and rearranging yields:

$$B^y\cos(y) = \left(\frac{e^{iy}+e^{-iy}}{2}\right)\sum_{m=-N}^{N}\sum_{n=-N}^{N}\widehat{B}^y_{m,n}e^{imx}e^{iny} \tag{2.23}$$

$$= \frac{1}{2}\sum_{m=-N}^{N}\sum_{n=-N}^{N}\widehat{B}^y_{m,n}e^{imx}(e^{in_+y}+e^{in_-y}) \tag{2.24}$$

where $n_+ = n+1$ and $n_- = n-1$. Now

$$B^y\cos(y) = \frac{1}{2}\sum_{m=-N}^{N}e^{imx}\left(\sum_{n_+=-N+1}^{N+1}\widehat{B}^y_{m,n_+-1}e^{in_+y}+\sum_{n_-=-N-1}^{N-1}\widehat{B}^y_{m,n_-+1}e^{in_-y}\right) \tag{2.25}$$

$$= \frac{1}{2}\sum_{m=-N}^{N}e^{imx}\left(\sum_{n_+=-N}^{N}\widehat{B}^y_{m,n_+-1}e^{in_+y}+\sum_{n_-=-N}^{N}\widehat{B}^y_{m,n_-+1}e^{in_-y}\right). \tag{2.26}$$

The beauty of this is that as the N and $-N$ terms of the original sum are fixed at 0 I have simply changed the limits of the sum above back to between $-N$ and N and then renamed n^+ and n^- as n (I could have relabelled them as any dummy variable name I wished). This allows me to collate the two sums once more:

$$B^y\cos(y) = \frac{1}{2}\sum_{m=-N}^{N}e^{imx}\left(\sum_{n=-N}^{N}\widehat{B}^y_{m,n-1}e^{iny}+\sum_{n=-N}^{N}\widehat{B}^y_{m,n+1}e^{iny}\right) \tag{2.27}$$

$$= \frac{1}{2}\sum_{m=-N}^{N}\sum_{n=-N}^{N}e^{imx}e^{iny}(\widehat{B}^y_{m,n-1}+\widehat{B}^y_{m,n+1}) \tag{2.28}$$

The same can be done for the other components of $(\mathbf{B}\cdot\nabla)\mathbf{u}$ as well as $(\mathbf{u}\cdot\nabla)\mathbf{B}$. This ability to express gradients as sums is a useful method of speeding up kinematic calculations. This method also readily adapts to products of sine and cosine functions as these simply correspond to a mode being coupled to more nearby modes. This provides very little problems as an arbitrary number of coupled nodes can be modelled simply by "cushioning" the mesh sufficiently. For example for 64 Fourier nodes where the nth node couples only to the nodes in the range n-2 : n+2 we can simply define our mesh to be $-34 \leq m,n \leq 34$.

2.2.3 General Methodology of Induction Equation Solver

1. First a divergence free initial magnetic field is specified. This is generally a random seed field generated from a random normal distribution with a specified amplitude.

2. Specify the flow $\mathbf{u}$. If the flow is time dependent this will have to be done at each timestep.

3. Take the Fourier transform of both using Python's FFT algorithm.

4. Use one of the timestepping schemes from section 2.4 to timestep the induction equation. The z component of the magnetic field is found using the divergence free condition to ensure that the magnetic field remains divergence free. Products are calculated in real space.

5. At set time intervals calculate (2.29) using numerical integration.

$$ME = \frac{1}{V}\int_V \frac{\mathbf{B}^2}{2} dV \tag{2.29}$$

   where the integral is over $x \in (0, 2\pi)$ and $y \in (0, 2\pi)$. For 2.5D flows the integral is over one wavelength $2\pi/k_z$ in the z direction or if the flow is fully 3D then the integral is again over $0 - 2\pi$.

6. As successful kinematic dynamos grow exponentially I now find the growth rate of the exponential growth. I find $Q = \ln(ME)/2$. Then use a linear least squares fit method to calculate the gradient of Q, this is the growth rate. The R^2 value for the least squares fit is also calculated to check that the relationship between Q and time is indeed linear.

7. Calculate the difference between the growth rate at this time and the previous time it was calculated. If this difference is less than a given tolerance then the run ends. Alternative end conditions can be specified if I want the run to be of a particular length of if I want to examine particular quantities.

2.2.4 Code Test Using the Work of Otani

To test that the code is working correctly I produce results for the Otani flow and compare them to those already published. For the majority of the flows that I will consider, there already exists a body of literature with results making use of that particular flow. Thus, for each flow that I consider, I first check that my code reproduces a number of published results before reproducing new results and some of these are shown in their respective sections. In addition to this, I also checked that the code reproduced the published growth rates of Otani within [78] and in [29] for the same flow.

The tests were performed using the numerical method outlined in section 2.4.1. I perform a parameter scan of the vertical wavenumber k_z for the "Otani flow", also referred too as the "MW+" flow in [29]. The Otani flow is given in [78] as (2.30).

$$\mathbf{u_1} = \begin{pmatrix} 2\sin^2(t)\sin(y) \\ 2\cos^2(t)\sin(x) \\ \sin^2(t)\cos(y) + \cos^2(t)\cos(x) \end{pmatrix} \tag{2.30}$$

I took identical initial conditions and number of nodes as the authors and was able to replicate results within [78]. Furthermore I took the same flow and plotted asymptotic growth rate against vertical wavenumber k_z, the result is shown within figure 2.1 alongside the published result from [29]. I find my code produces results in good agreement with figure 2.1 on page 34 of [29]

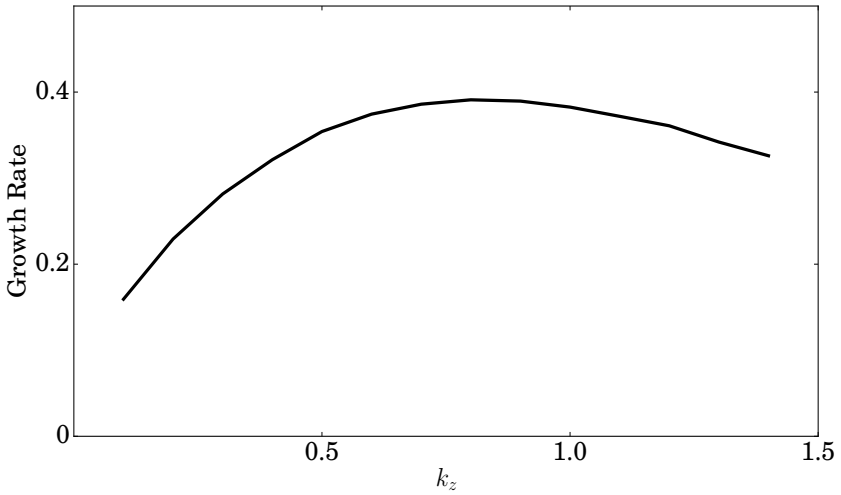

(a) Plot of growth rate vs k_z for the Otani flow.

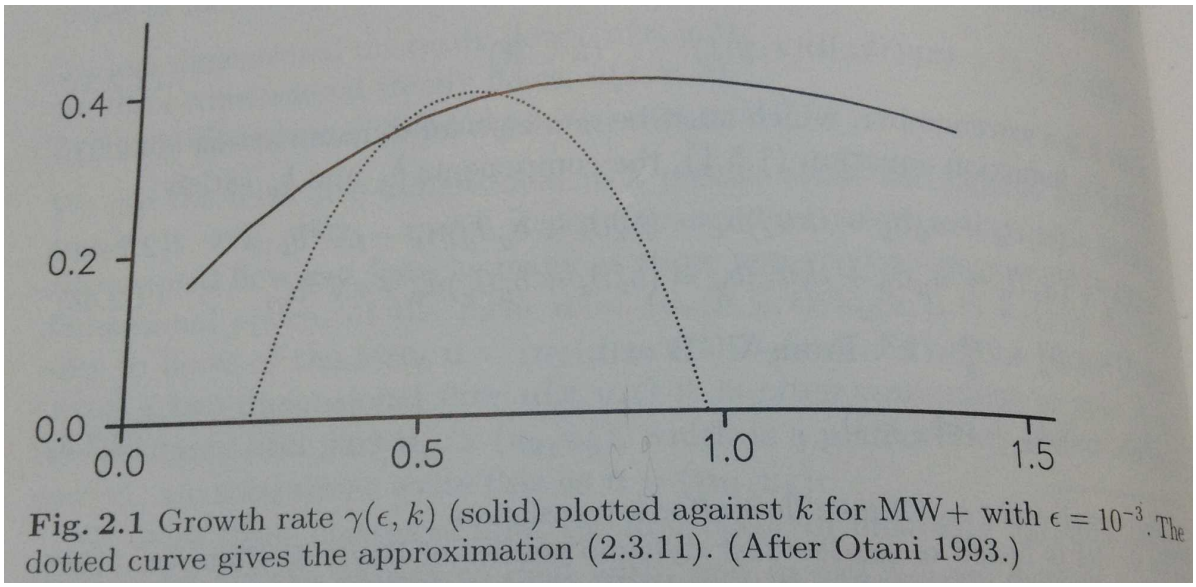

(b) Figure 2.1 from [29].

Figure 2.1: Plot of growth rate vs k_z within my simulation (a) and the published result within [29] (b) (solid curve). The curves are in good agreement.

2.3 Simultaneous Solving of the Equation of Motion and the Induction Equation

2.3.1 Maintaining the Divergence-Free Condition on the Flow and Magnetic Field

When solving 2.5D kinematic dynamos the z component of the magnetic field can be specified so as to ensure $\nabla \cdot \mathbf{B} = 0$. However this isn't the case once the problem becomes fully

three dimensional due to the impossibility of dividing by the $k_z = 0$ mode. Thus we need an alternate way to maintain the divergence free condition when evolving the flow field as well as the magnetic field as we will be only interested in three dimensional examples. As such another method must be used to ensure the flow remains incompressible and the magnetic field solenoidal. The method that I choose to use is the pressure projection method. Consider the equation of motion (2.31)

$$\begin{aligned}\frac{\partial \mathbf{u}}{\partial t} &= (\mathbf{B}\cdot\nabla)\mathbf{B} - (\mathbf{u}\cdot\nabla)\mathbf{u} - \nabla P + \nu\nabla^2\mathbf{u} + \mathbf{F} \\ &= NLU(\mathbf{u},\mathbf{B}) - \nabla P + \nu\nabla^2\mathbf{u} + \mathbf{F}. \end{aligned} \tag{2.31}$$

Taking the divergence of (2.31) and assuming fluid incompressibility ($\mathbf{F}$ is also incompressible) yields (2.32)

$$\begin{aligned}\nabla^2 P &= \nabla\cdot\Big(NLU(\mathbf{u},\mathbf{B}) + \mathbf{F}\Big) \\ &= \nabla\cdot\Big(NLU(\mathbf{u},\mathbf{B})\Big). \end{aligned} \tag{2.32}$$

Thus the i^{th} component of ∇P within Fourier space is given by

$$k_i P = -\frac{k_i k_j}{k_l k_l}\widehat{NLU}_j. \tag{2.33}$$

Substituting this into equation (2.31) and defining the quantity Q_{ij} as in (2.34) yields (2.35)

$$Q_{ij} = \delta_{ij} - \frac{k_i k_j}{k_l k_l} \tag{2.34}$$

$$\frac{\partial \widehat{u}_i}{\partial t} = Q_{ij}\widehat{NLU}_j - \nu\mathbf{k}^2\widehat{u}_i + \widehat{F}_i \tag{2.35}$$

which is the same as

$$Q_{ij}\left(\frac{\partial \widehat{u}_j}{\partial t} - \widehat{NLU}_j + \nu k_j k_l \widehat{u}_l - \widehat{F}_j\right) = 0 \tag{2.36}$$

due to incompressibility of $\mathbf{u}$ and $\mathbf{F}$. To maintain incompressibility the code therefore solves (2.31) with the pressure term omitted and then applies Q_{ij} to $\widehat{\mathbf{u}}$. The code also follows the common convention of ensuring $\mathbf{B}$ is divergence free by also applying Q_{ij} to the magnetic field $\widehat{\mathbf{B}}$.

2.3.2 General Methodology of Coupled Equation Solver

1. First a divergence free initial magnetic field is specified. This is generally a random seed field generated from a random normal distribution with a specified amplitude.

2. Specify the forcing $\mathbf{F}$

3. Specify the initial flow $\mathbf{u}$. This is generally related to the forcing (typically $\mathbf{F}/\nu$).

4. Take the Fourier transform of $\mathbf{u}, \mathbf{B}$ and $\mathbf{F}$ using Python's FFT algorithm.

5. Use one of the timestepping schemes from section 2.4 to timestep both equations. Projections are taken at each timestep to ensure each field stays divergence free. Products are calculated in real space.

6. At set time intervals calculate (2.37a) and (2.37a) using numerical integration.

$$ME = \frac{1}{8\pi^3}\int_V \frac{\mathbf{B}^2}{2} dV \qquad \text{(2.37a)} \qquad\qquad KE = \frac{1}{8\pi^3}\int_V \frac{\mathbf{u}^2}{2} dV \qquad \text{(2.37b)}$$

   where the integral is $x, y, z \in (0, 2\pi)$ for x, y and z.

7. A number of different stop criteria are used. For the aligned dynamos of section 5 the condition enforces saturation of both energies to a set tolerance as well as saturation of an alignment measure and time larger than a set value. For the ABC dynamos of section 6 energy saturation and minimum time is used.

2.3.3 Code Tests

I begin by checking the code against results for the incompressible Navier-Stokes equations (2.38) with Q being the operator Q_{ij} as in equation (2.34).

$$\frac{\partial \mathbf{u}}{\partial t} = Q\big(-(\mathbf{u}\cdot\nabla)\mathbf{u} + \nu\nabla^2\mathbf{u} + \mathbf{F}\big). \qquad (2.38)$$

To test whether the code correctly obtains solutions to (2.38) I define a forcing (2.39)

$$\mathbf{F} = (\mathbf{u}^\star \cdot \nabla)\mathbf{u}^\star - \nu\nabla^2\mathbf{u}^\star \tag{2.39}$$

where $\mathbf{u}^\star$ is a chosen velocity. Thus if I choose any $\mathbf{u}$ initially and then the forcing $\mathbf{F}$ via equation (2.39) and solve equation (2.38) we would expect $\mathbf{u} \to \mathbf{u}^\star$ as long as the diffusivity is sufficiently small such that no instabilities occur. To test this I use

$$\mathbf{u}^\star = \Big(\cos(z)\sin(y), \cos(x)\sin(z), \cos(y)\sin(x)\Big) \tag{2.40}$$

and $\nu = 1$ and begin my runs with a weak seed flow of $O(10^{-5})$. The $z = 0$ contours of $|\mathbf{u}|^2$ and $|\mathbf{u}^\star|^2$ are shown in figure 2.2 and show that both appear identical. As a more precise measure of their similarity within figure 2.3a I show the energies against time in the flow and the expected solution and in figure 2.3b I show the $\max_{\mathbf{x},\mathbf{y},\mathbf{z}} \Big\{ |(\mathbf{u} - \mathbf{u}^\star)|^2 \Big\}$. What we see is that by a time of about $t = 6$ the maximum difference over the entirety of the domain is $O(10^{-12})$ and this remains at this value. A number of other profiles for $\mathbf{u}^\star$ were tested, all yielded similar agreement.

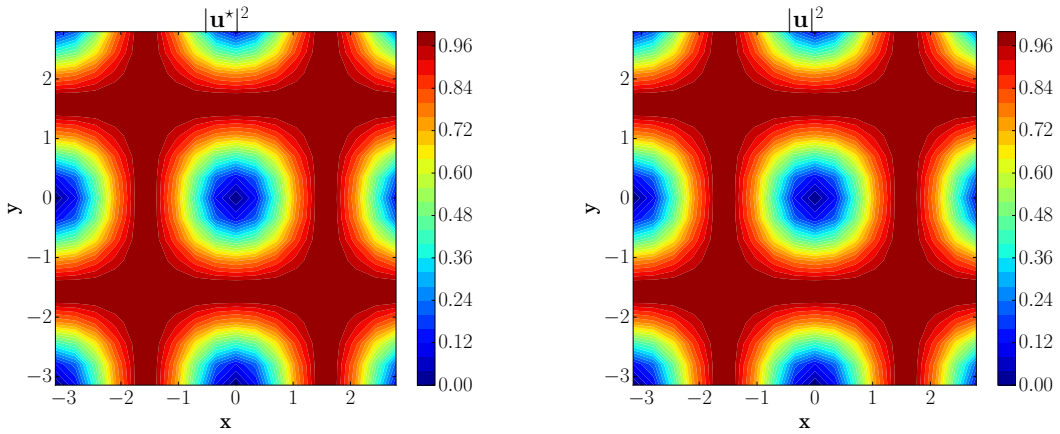

(a) $|\mathbf{u}^\star|^2\Big|_{z=0}$ (b) Final flow structure of $|\mathbf{u}|^2\Big|_{z=0}$

Figure 2.2: Contour plots of the flow and its expected solution.

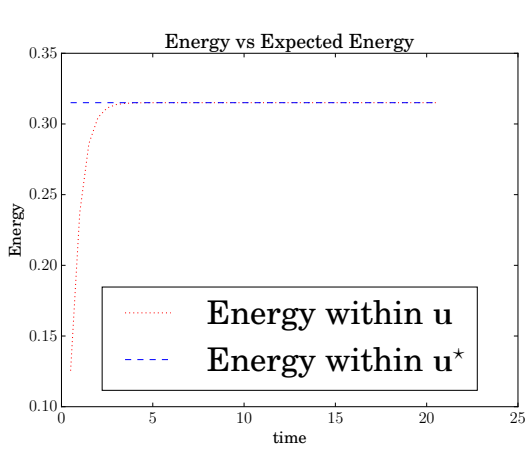

(a) Plot of Energy against time

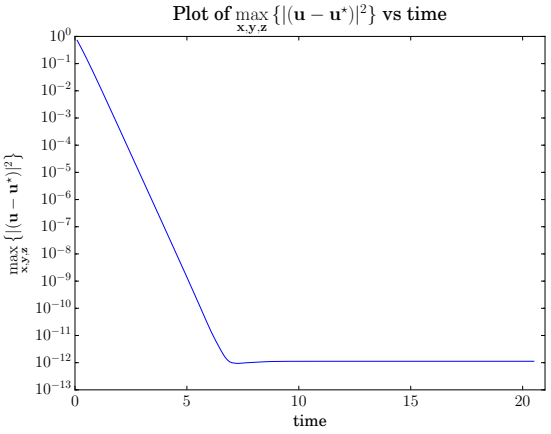

(b) Plot of $\max_{\mathbf{x},\mathbf{y},\mathbf{z}} \left\{ |(\mathbf{u}-\mathbf{u}^\star)|^2 \right\}$ against time

Figure 2.3

I also check the code against published results which include a magnetic field. The forcing is the ABC forcing which is defined as

$$\mathbf{F}_{ABC} = \nu \begin{pmatrix} A\sin(z) + C\cos(y) \\ B\sin(x) + A\cos(z) \\ C\sin(y) + B\cos(x) \end{pmatrix} \tag{2.41}$$

Figures 2.4a and 2.4b show energies for the $ABC = 1:1:1$ flow with $R_m = R_e = 12$. Good agreement for the final values is found with figure 3 within [37] which is shown in figure 2.5.

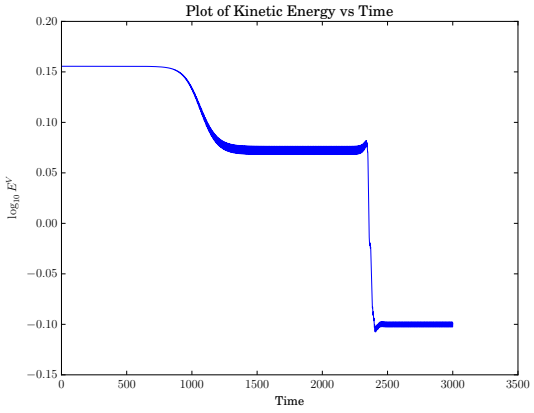

(a) Kinetic Energy

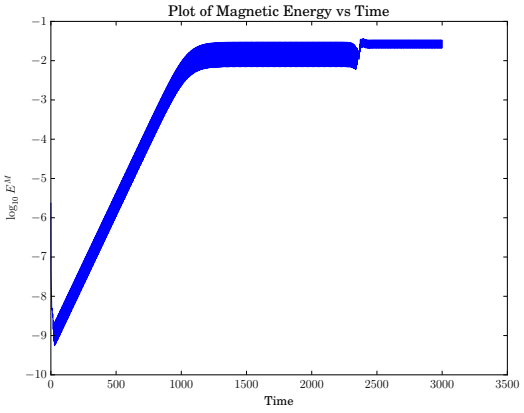

(b) Magnetic Energy

Figure 2.4: Kinetic and magnetic energies for $\mathbf{F}_{ABC}$ with $A:B:C = 1:1:1$, a random initial magnetic field, $\nu\mathbf{u}_0 = \mathbf{F}_{ABC}$ and $\nu = \eta = 1/12$. When comparing to the results of Galanti et al shown in figure 2.5 good agreement is seen. In particular the transitions between different regimes are accurately found.

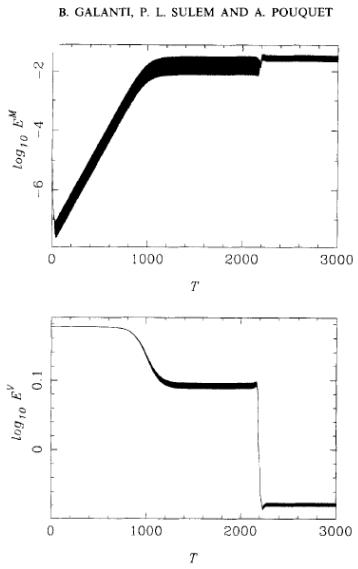

Figure 2.5: Figure 3 from [37] to compare against the results in figure 2.4.

From these tests I therefore conclude that the code is indeed working correctly as it reproduces a large number of published results.

2.4 Timestepping Schemes

In this section I outline how the induction equation and equation of motion are discretised and timestepped. As a reminder the induction equation is given by (2.43) and the equation of motion for the fluid by (2.45) where the pressure term has been omitted due to the fact that I only use it to ensure incompressibility (see section 2.3.1)

$$\frac{\partial \mathbf{B}}{\partial t} = \nabla \times (\mathbf{u} \times \mathbf{B}) + \eta \nabla^2 \mathbf{B} \tag{2.42}$$

$$= \mathbf{NLB}(\mathbf{u}, \mathbf{B}) + \eta \nabla^2 \mathbf{B} \tag{2.43}$$

$$\frac{\partial \mathbf{u}}{\partial t} = (\mathbf{B} \cdot \nabla)\mathbf{B} - (\mathbf{u} \cdot \nabla)\mathbf{u} + \nu \nabla^2 \mathbf{u} + \mathbf{F} \tag{2.44}$$

$$= \mathbf{NLU}(\mathbf{u}, \mathbf{B}) + \nu \nabla^2 \mathbf{u} + \mathbf{F}. \tag{2.45}$$

These can then be expressed in Fourier space as (2.46) and (2.47) for the $\mathbf{k} = (k_x, k_y, k_z)$ Fourier mode and where summations have been omitted for brevity.

$$\frac{\partial \widehat{\mathbf{B}}_\mathbf{k}}{\partial t} = \widehat{\mathbf{NLB}}_\mathbf{k} - \eta \mathbf{k}^2 \widehat{\mathbf{B}}_\mathbf{k} \tag{2.46}$$

$$\frac{\partial \widehat{\mathbf{u}}_\mathbf{k}}{\partial t} = \widehat{\mathbf{NLU}}_\mathbf{k} - \nu \mathbf{k}^2 \widehat{\mathbf{u}}_\mathbf{k} + \widehat{\mathbf{F}}_\mathbf{k} \tag{2.47}$$

2.4.1 Adams-Bashforth: Crank-Nicholson Scheme

I begin by showing the scheme for the induction equation then show the result for the equation of motion also. A Crank-Nicholson scheme is used for diffusion and is given by (2.48) with the superscript i denoting the ith timestep.

$$\frac{\widehat{\mathbf{B}}_\mathbf{k}^{(i+1)} - \widehat{\mathbf{B}}_\mathbf{k}^{(i)}}{\Delta t} = -\eta \mathbf{k}^2 \frac{\widehat{\mathbf{B}}_\mathbf{k}^{i+1} + \widehat{\mathbf{B}}_\mathbf{k}^{i}}{2}. \tag{2.48}$$

The induction component of the equation is timestepped using the second order Adams-Bashforth method. This is shown in equation (2.49)

$$\frac{\widehat{\mathbf{B}}_\mathbf{k}^{(i+1)} - \widehat{\mathbf{B}}_\mathbf{k}^{(i)}}{\Delta t} = \frac{3\widehat{\mathbf{NLB}}_\mathbf{k}^{i} - \widehat{\mathbf{NLB}}_\mathbf{k}^{i-1}}{2}. \tag{2.49}$$

Due to the fact that the Adams-Bashforth scheme requires knowledge of the $i-1$ term the first step requires the use of an Euler scheme (2.50) for the induction term.

$$\widehat{\mathbf{B}}_\mathbf{k}^{(i+1)} = \widehat{\mathbf{B}}_\mathbf{k}^{(i)} + \Delta t \widehat{\mathbf{NLB}}_\mathbf{k}^{(i)} \tag{2.50}$$

The evolution at timestep $i = 1$ from $i = 0$ thus uses an Euler: Crank-Nicholson hybrid (2.51).

$$\widehat{\mathbf{B}}_\mathbf{k}^{(i+1)} = \frac{2 - \eta \mathbf{k}^2 \Delta t}{2 + \Delta t \eta \mathbf{k}^2} \widehat{\mathbf{B}}_\mathbf{k}^{(i)} + \frac{2\Delta t}{2 + \Delta t \eta \mathbf{k}^2} \widehat{\mathbf{NLB}}_\mathbf{k}^{(i)} \tag{2.51}$$

All subsequent timesteps are then computed using a Adams-Bashforth: Crank-Nicholson hybrid shown in equation (2.52)

$$\widehat{\mathbf{B}}_\mathbf{k}^{(i+1)} = \frac{2 - \eta \mathbf{k}^2 \Delta t}{2 + \Delta t \eta \mathbf{k}^2} \widehat{\mathbf{B}}_\mathbf{k}^{(i)} + \frac{\Delta t}{2 + \Delta t \eta \mathbf{k}^2} \left[3\widehat{\mathbf{NLB}}_\mathbf{k}^{(i)} - \widehat{\mathbf{NLB}}_\mathbf{k}^{(i-1)} \right]. \tag{2.52}$$

Similarly for the equation of motion we define $\widehat{\mathbf{NLUF}}_\mathbf{k} = \widehat{\mathbf{NLU}}_\mathbf{k} + \widehat{\mathbf{F}}_\mathbf{k}$ and the timestepping

scheme is then (2.53)

$$\widehat{\mathbf{u}}_{\mathbf{k}}^{(i+1)} = \frac{2-\nu\mathbf{k}^2\Delta t}{2+\Delta t\nu\mathbf{k}^2}\widehat{\mathbf{u}}_{\mathbf{k}}^{(i)} + \frac{\Delta t}{2+\Delta t\nu\mathbf{k}^2}\left[3\widehat{\mathbf{NLUF}}_{\mathbf{k}}^{(i)} - \widehat{\mathbf{NLUF}}_{\mathbf{k}}^{(i-1)}\right]. \tag{2.53}$$

2.4.2 Adams-Bashforth: Crank-Nicholson Predictor and Adams-Moulton: Crank-Nicholson Scheme Corrector

The benefit of the explicit nature of the numerical method in section 2.4.1 is that no knowledge of the next time step is required to compute it. Explicit methods however have the downside that a larger timestep is required than when working with implicit methods. This can lead to codes being incredibly time consuming to run.

Predictor-corrector methods overcome the obstacles of implicit methods by using an explicit method to calculate a first approximation to the solution. This solution is then substituted into an implicit method as our "knowledge of the next timestep" and a "corrected" solution is obtained. This has the downside that we have to do twice as many calculations than we would have had we just used an explicit method. However what it allows us to do is to use a much larger timestep. Thus for different spatial resolutions careful consideration must be taken whether it is quicker to run at a smaller timestep or whether computational time can be gained by adding a corrector scheme and using a larger timestep.

A predictor of an Adams-Bashforth scheme is used (see section 2.4.1). This is then corrected by an Adams-Moulton: Crank-Nicholson scheme. The Adams-Moulton scheme is given by (2.54).

$$\frac{\widehat{\mathbf{B}}_{\mathbf{k}}^{(i+1)} - \widehat{\mathbf{B}}_{\mathbf{k}}^{(i)}}{\Delta t} = \frac{5\widehat{\mathbf{NLB}}_{\mathbf{k}}^{i+1} + 8\widehat{\mathbf{NLB}}_{\mathbf{k}}^{i} - \widehat{\mathbf{NLB}}_{\mathbf{k}}^{i-1}}{12} \tag{2.54}$$

At the ith timestep a "predictor" value for each of the components of $\widehat{\mathbf{B}}_{\mathbf{k}}$, is thus calculated using the Adams-Bashforth:Crank Nicholson hybrid scheme (2.55). This is then used to make an estimate of $\widehat{\mathbf{NLB}}_{\mathbf{k}}^{i+1}$, denoted $\widehat{\mathbf{NLB}}_{\mathbf{k}}^{i+1/2}$, which is then used to "correct" and produce $\widehat{\mathbf{B}}_{\mathbf{k}}^{i+1}$ from (2.56).

$$\widehat{\mathbf{B}}_{\mathbf{k}}^{(i+1/2)} = \frac{2-\eta\mathbf{k}^2\Delta t}{2+\Delta t\eta\mathbf{k}^2}\widehat{\mathbf{B}}_{\mathbf{k}}^{(i)} + \frac{\Delta t}{2+\Delta t\eta\mathbf{k}^2}\left[3\widehat{\mathbf{NLB}}_{\mathbf{k}}^{(i)} - \widehat{\mathbf{NLB}}_{\mathbf{k}}^{(i-1)}\right] \tag{2.55}$$

$$\widehat{\mathbf{B}}_{\mathbf{k}}^{(i+1)} = \frac{2-\eta\mathbf{k}^2\Delta t}{2+\Delta t\eta\mathbf{k}^2}\widehat{\mathbf{B}}_{\mathbf{k}}^{(i)} + \frac{\Delta t}{6(2+\Delta t\eta\mathbf{k}^2)}\left[5\widehat{\mathbf{NLB}}_{\mathbf{k}}^{(i+1/2)} + 8\widehat{\mathbf{NLB}}_{\mathbf{k}}^{(i)} - \widehat{\mathbf{NLB}}_{\mathbf{k}}^{(i-1)}\right]. \tag{2.56}$$

The equivalent equations for the fluid equation of motion are given by (2.57) and (2.58) and where again $\widehat{\mathbf{NLUF}}_{\mathbf{k}} = \widehat{\mathbf{NLU}}_{\mathbf{k}} + \widehat{\mathbf{F}}_{\mathbf{k}}$. Note that The predictor for both $\widehat{\mathbf{NLB}}_{\mathbf{k}}$ and $\widehat{\mathbf{NLUF}}_{\mathbf{k}}$ must be calculated before the corrector as the equations are coupled.

$$\widehat{\mathbf{u}}_{\mathbf{k}}^{(i+1/2)} = \frac{2-\nu\mathbf{k}^2\Delta t}{2+\Delta t\nu\mathbf{k}^2}\widehat{\mathbf{u}}_{\mathbf{k}}^{(i)} + \frac{\Delta t}{2+\Delta t\nu\mathbf{k}^2}\left[3\widehat{\mathbf{NLUF}}_{\mathbf{k}}^{(i)} - \widehat{\mathbf{NLUF}}_{\mathbf{k}}^{(i-1)}\right] \tag{2.57}$$

$$\widehat{\mathbf{u}}_{\mathbf{k}}^{(i+1)} = \frac{2-\nu\mathbf{k}^2\Delta t}{2+\Delta t\nu\mathbf{k}^2}\widehat{\mathbf{u}}_{\mathbf{k}}^{(i)} + \frac{\Delta t}{6(2+\Delta t\nu\mathbf{k}^2)}\left[5\widehat{\mathbf{NLUF}}_{\mathbf{k}}^{(i+1/2)} + 8\widehat{\mathbf{NLUF}}_{\mathbf{k}}^{(i)} - \widehat{\mathbf{NLUF}}_{\mathbf{k}}^{(i-1)}\right] \tag{2.58}$$

2.4.3 Adams-Bashforth Predictor and Adams-Moulton Corrector Each Treating Diffusion Exactly

Rather than using a Crank-Nicholson method to timestep the diffusive terms we can also timestep the diffusion exactly using an exponential method. Multiplying (2.46) and (2.47) by $\exp(\eta\mathbf{k}^2 t)$ and $\exp(\nu\mathbf{k}^2 t)$ respectively yields (2.59) and (2.60) where $\widehat{\mathbf{NLUF}}_{\mathbf{k}} = \widehat{\mathbf{NLU}}_{\mathbf{k}} + \widehat{\mathbf{F}}_{\mathbf{k}}$.

$$\frac{\partial}{\partial t}\left(\widehat{\mathbf{B}}_{\mathbf{k}}\exp(\eta\mathbf{k}^2 t)\right) = \widehat{\mathbf{NLB}}_{\mathbf{k}}\exp(\eta\mathbf{k}^2 t) \tag{2.59}$$

$$\frac{\partial}{\partial t}\left(\widehat{\mathbf{u}}_{\mathbf{k}}\exp(\eta\mathbf{k}^2 t)\right) = \widehat{\mathbf{NLUF}}_{\mathbf{k}}\exp(\eta\mathbf{k}^2 t) \tag{2.60}$$

Discretizing (2.59) and (2.60) for timestepping, noting that $i = n\Delta t$ and dividing through by the exponential yields (2.61) and (2.62) for the magnetic field and (2.63) and (2.64) for the flow. In each $E_{\mathbf{k}}^{\eta} = \exp(-\eta\mathbf{k}^2\Delta t)$ and $E_{\mathbf{k}}^{\nu} = \exp(-\nu\mathbf{k}^2\Delta t)$

$$\widehat{\mathbf{B}}_{\mathbf{k}}^{(i+1/2)} = \widehat{\mathbf{B}}_{\mathbf{k}}^{(i)} E_{\mathbf{k}}^{\eta} + \frac{\Delta t}{2}\left[3E_{\mathbf{k}}^{\eta}\widehat{\mathbf{NLB}}_{\mathbf{k}}^{(i)} - (E_{\mathbf{k}}^{\eta})^2\widehat{\mathbf{NLB}}_{\mathbf{k}}^{(i-1)}\right] \tag{2.61}$$

$$\widehat{\mathbf{B}}_{\mathbf{k}}^{(i+1)} = \widehat{\mathbf{B}}_{\mathbf{k}}^{(i)} E_{\mathbf{k}}^{\eta} + \frac{\Delta t}{12}\left[5\widehat{\mathbf{NLB}}_{\mathbf{k}}^{(i+1/2)} + 8E_{\mathbf{k}}^{\eta}\widehat{\mathbf{NLB}}_{\mathbf{k}}^{(i)} - (E_{\mathbf{k}}^{\eta})^2\widehat{\mathbf{NLB}}_{\mathbf{k}}^{(i-1)}\right] \tag{2.62}$$

$$\widehat{\mathbf{u}}_{\mathbf{k}}^{(i+1/2)} = \widehat{\mathbf{u}}_{\mathbf{k}}^{(i)} E_{\mathbf{k}}^{\nu} + \frac{\Delta t}{2}\left[3E_{\mathbf{k}}^{\nu}\widehat{\mathbf{NLUF}}_{\mathbf{k}}^{(i)} - (E_{\mathbf{k}}^{\nu})^2\widehat{\mathbf{NLUF}}_{\mathbf{k}}^{(i-1)}\right] \tag{2.63}$$

$$\widehat{\mathbf{u}}_{\mathbf{k}}^{(i+1)} = \widehat{\mathbf{u}}_{\mathbf{k}}^{(i)} E_{\mathbf{k}}^{\nu} + \frac{\Delta t}{12}\left[5\widehat{\mathbf{NLUF}}_{\mathbf{k}}^{(i+1/2)} + 8E_{\mathbf{k}}^{\nu}\widehat{\mathbf{NLUF}}_{\mathbf{k}}^{(i)} - (E_{\mathbf{k}}^{\nu})^2\widehat{\mathbf{NLUF}}_{\mathbf{k}}^{(i-1)}\right]. \tag{2.64}$$

2.5 Calculating Periodicity

To calculate the periodicity of a time series, $A(t)$, I use two methods, both of which make use of the Fourier transform. The first is the power spectrum. The power spectrum is found by the following method.

1. Subtract the mean: $A \to A - \overline{A}$
2. Calculate the Fourier transform using the Fast Fourier transform within Python $A_f = FFT\{A\}$
3. Calculate the power P using the relationship $P = |A_f|^2$.

The periods present within the time series are then found by calculating the reciprocal of the frequency of the peaks. Note that due to the properties of the Fourier transform the power spectrum will be symmetric about the origin. The second method is the autocorrelation function. Beginning at P from above we calculate the autocorrelation function by calculating the inverse Fourier transform and keeping only the real component $ACF = Real\{IFFT\{A_{f2}\}\}$. The period is then calculated by calculating the distance between peaks.

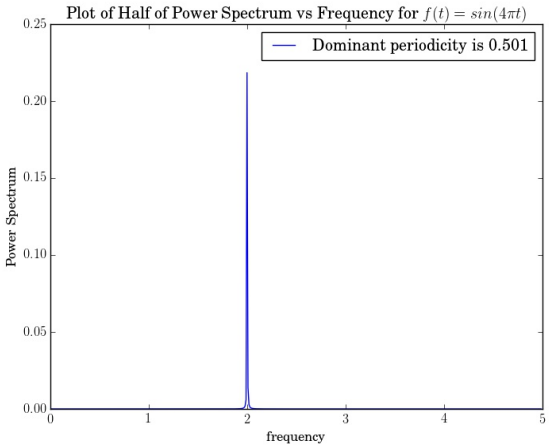

(a) Plot of the power spectrum

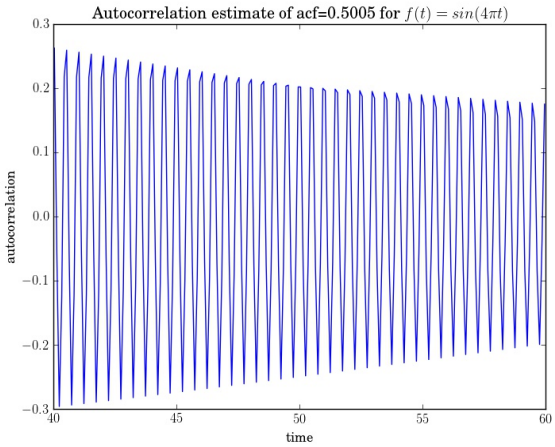

(b) Plot of the autocorrelation function

Figure 2.6: Power and autocorrelation for $f(t) = \sin(4\pi t)$.

The plots of both of these quantities for a time series $f(t) = sin(4\pi t)$ are shown in figures 2.6a and 2.6b. As you can see there is a clear peak at where we expect the period to be in the power spectrum plot using that $Period = 2\pi/4\pi = 0.5$. A simple code to measure the distance between peaks then calculates the exact same value from the autocorrelation function. One benefit of the power spectrum in this toy example is clearly visible as we have to perform less steps to obtain the period. Another benefit of the power spectrum method is that if there are two periodicities present then this will show in the power spectrum. Below I have shown $f(t) = sin(6\pi t) + sin(4\pi t)$

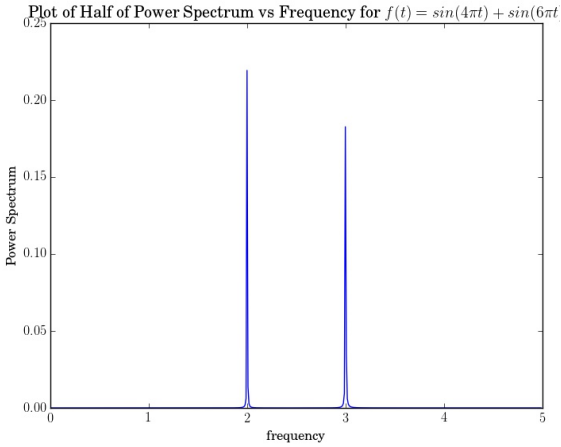

(a) Plot of the power spectrum for sum of sinusoids

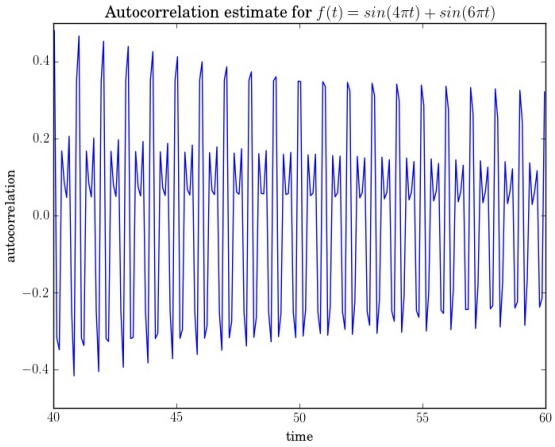

(b) Plot of the autocorrelation function

Figure 2.7: Power and autocorrelation for $f(t) = sin(6\pi t) + sin(4\pi t)$.

here we see why plotting both is of benefit. The power spectrum in figure 2.7a shows us the two periods present within the time series via the two peaks whereas the autocorrelation

function in figure 2.7b shows the larger periodicity of the time series as a whole although we have to be careful with how we extract this information.

2.6 Poincare Sections

A Poincare section is a method of measuring the amount of chaos within a flow. Defining the initial position of a fluid particle as $\mathbf{a}$ within a Lagrangian framework allows for the expression of a particle position at time t in terms of its initial position

$$\mathbf{x} = \mathbf{x}(\mathbf{a}, t). \tag{2.65}$$

The velocity is found by taking the material derivative of the position:

$$\frac{D\mathbf{x}}{Dt} = \mathbf{u} \tag{2.66}$$

however within a Lagrangian framework the material derivative is simply the partial derivative with respect to time

$$\frac{D\mathbf{x}(\mathbf{a}, t)}{Dt} = \frac{\partial \mathbf{x}(\mathbf{a}, t)}{\partial t} \tag{2.67}$$

$$= \mathbf{u}(\mathbf{a}, t). \tag{2.68}$$

Thus by specifying an initial position we may track the trajectory of a particle. A Poincare section is then a surface of dimensions $S-1$ where the system (2.68) is of dimension S. Particles are given random initial conditions lying on the surface and their positions are tracked and recorded at set intervals.

For some initial positions trajectories stay close to their initial position and trace out closed curves upon the surface. These closed curves then define integrable regions within the geometry and thus regions where there is a lack of chaos. On the other hand some trajectories starting from other initial positions move chaotically. Regions where particles move chaotically correspond to chaotic regions within the flow and the corresponding regions

of the surface have the appearance of a featureless mass of particle positions. It is the chaotic regions and their stretching properties that are desirable as the stretching of magnetic field lines that they induce has been shown to be pivotal in achieving magnetic field growth via dynamo action.

To find Poincare sections at $z = 0$ the methodology within [27] is followed and (2.68) is integrated in time for 100 random initial positions with $x \in (0, 2\pi)$,$y \in (0, 2\pi)$ and $z = 0$. To perform the timestep the following 4th order Runga-Kutta scheme is used which is suitable for solving systems of the form $\dot{\mathbf{y}} = \mathbf{f}(t_n, \mathbf{y}_n)$ where the dot denotes a time derivative.

$$\mathbf{k}_1 = \mathbf{f}(t_n, \mathbf{y}_n) \tag{2.69}$$

$$\mathbf{k}_2 = \mathbf{f}\left((t_n + \frac{h}{2}, \mathbf{y}_n + \frac{\mathbf{k}_1}{2} \right) \tag{2.70}$$

$$\mathbf{k}_3 = \mathbf{f}\left((t_n + \frac{h}{2}, \mathbf{y}_n + \frac{\mathbf{k}_1}{2} \right) \tag{2.71}$$

$$\mathbf{k}_4 = \mathbf{f}\left((t_n + h, \mathbf{y}_n + \mathbf{k}_3 \right) \tag{2.72}$$

$$\mathbf{y}_{n+1} = \mathbf{y}_n + \frac{h}{6}(\mathbf{k}_1 + 2\mathbf{k}_2 + 2\mathbf{k}_3 + \mathbf{k}_4) + O(h^5) \tag{2.73}$$

A timestep of $h = 2\pi/100$ is used and the time is ran until 5000π. At time increments of 2π (x, y) coordinates of the position of the particle modulo 2π are then plotted. One thing to note is that there is no set prescription for the number of initial positions to use and the length of time to run the trajectories for. Thus the values of $h = 2\pi/100$ and a maximum time of 5000π were chosen after trying a variety of different values. I found that a larger number of initial positions results in more chance of one being inside the integrable region and thus results in more closed curves being plotted. The result is that the integrable region has a more detailed structure. Of course this is highly dependent upon the set of initial positions that are randomly generated but is a good general rule.

Chapter 3

Motivations for Studying Alignment

3.1 Introduction to Alignment Motivations

Within this section, I motivate the study of alignment between the velocity and magnetic fields in kinematic and nonlinear (both flow and magnetic field evolved) dynamo theory by providing an overview of where it has previously been studied.

I begin in section 3.2 by showing a simple model of how a flow can act to align the two fields. Alignment within MHD has historically been studied most often within an MHD turbulence framework and this is what I review in section 3.3 where I overview alignment as a relaxation process, scale dependent alignment and observations of alignment within MHD turbulence. Whilst the majority of results within these sections will not be applicable to the alignment that I will study, the results are important as they highlight how crucial alignment is within MHD turbulence. Alignment's importance within MHD turbulence is a major motivating factor in the study of alignment within this thesis. Finally, in section 3.4, I provide an overview of previous results on alignment within nonlinear dynamo theory. In the process of doing so, I highlight a number of open questions that will be addressed within this thesis.

The focus within the chapters which consider alignment (4 and 5), is on alignment between $\mathbf{u}$ and $\mathbf{B}$ rather than cross-helicity as a topological quantity. However, quantities relating to the cross-helicity provide a useful way of measuring the alignment between the two fields

and as such cross-helicity will be measured throughout the chapters of the thesis in order to aid our understanding of the alignment.

3.2 Simple Example of Alignment: Shear Flow in a Guiding Field

One of the greatest hints that alignment between flow and magnetic field is important is that the integral quantity (3.1) is one of the three conserved quantities in three dimensional ideal MHD.

$$H_c = \int_V \mathbf{u} \cdot \mathbf{B} dV. \tag{3.1}$$

This can be re-expressed in terms of the angle of alignment θ between $\mathbf{u}$ and $\mathbf{B}$

$$H_c = \int_V |\mathbf{u}||\mathbf{B}| \cos(\theta) dV. \tag{3.2}$$

Removing the dependence of this on the magnitude of $\mathbf{u}$ and $\mathbf{B}$ enables the focus to be only on the alignment. Thus I define the related, normalised, quantity

$$H_1 = \frac{1}{V} \int_V \frac{|\mathbf{u} \cdot \mathbf{B}|}{|\mathbf{u}||\mathbf{B}|} dV \tag{3.3}$$

$$= \frac{1}{V} \int_V |\cos(\theta)| dV \tag{3.4}$$

which can be thought of as the volume average of the cosine of the angle between the magnetic and velocity fields.

For a simple example of how the cross-helicity might evolve, consider an initial magnetic field in the $\hat{z}$ direction, $\mathbf{B} = B_0 \hat{\mathbf{z}}$, with the flow profile corresponding to linear shearing

$$\mathbf{u} = \alpha z \hat{\mathbf{x}} \tag{3.5}$$

where α is a constant. Substituting (3.5) into the induction equation with $\eta = 0$ yields the

following set of equations

$$\frac{\partial B_x}{\partial t} = \alpha B_z - \alpha z \frac{\partial B_x}{\partial x} \tag{3.6}$$
$$\frac{\partial B_y}{\partial t} = -\alpha z \frac{\partial B_y}{\partial x} \tag{3.7}$$
$$\frac{\partial B_z}{\partial t} = -\alpha z \frac{\partial B_z}{\partial x}. \tag{3.8}$$

Now initially $\mathbf{B} = B_0\hat{\mathbf{z}}$ thus these equations become

$$\frac{\partial B_x}{\partial t} = \alpha B_0 \tag{3.9}$$
$$\frac{\partial B_y}{\partial t} = 0 \tag{3.10}$$
$$\frac{\partial B_z}{\partial t} = 0. \tag{3.11}$$

Integrating and using that at $t = 0$, $\mathbf{B} = (0,0,B_0)$ we obtain that

$$\mathbf{B} = \begin{pmatrix} \alpha B_0 t \\ 0 \\ B_0 \end{pmatrix} \tag{3.12}$$

and so

$$\mathbf{u} \cdot \mathbf{B} = \alpha^2 B_0 z t \tag{3.13}$$

thus

$$\frac{|\mathbf{u} \cdot \mathbf{B}|}{|\mathbf{u}||\mathbf{B}|} = \frac{|\alpha^2 B_0 z t|}{|\alpha z|\sqrt{\alpha^2 B_0^2 t^2 + B_0^2}} \tag{3.14}$$
$$\lim_{t\to\infty} \frac{|\mathbf{u} \cdot \mathbf{B}|}{|\mathbf{u}||\mathbf{B}|} \approx \frac{|\alpha^2 B_0 z t|}{|\alpha z||\alpha B_0 t|} \tag{3.15}$$
$$= 1 \tag{3.16}$$

and so the volume averaged integral of this (H_1) tends to 1 as $t \to \infty$ also.

The initial direction of $\mathbf{B}$ and its direction in the asymptotic limit are shown in figure 3.1. For large time (3.12) is approximately in the $\hat{\mathbf{x}}$ direction and is thus parallel with the velocity (3.5). Thus the action of a shear flow on a guiding magnetic field causes the magnetic field and velocity profile to become more and more aligned and correspondingly the value of $|H_1|$ becomes approximately 1. Thus we see that a value of $H_1 = \pm 1$ corresponds to completely aligned/anti-aligned velocity and magnetic fields. Initially of course

$$\mathbf{u} \cdot \mathbf{B}\Big|_{t=0} = 0 \tag{3.17}$$

and so

$$|H_1|\Big|_{t=0} = 0 \tag{3.18}$$

and so of course perpendicular magnetic field and velocity profiles correspond to $H_1 = 0$.

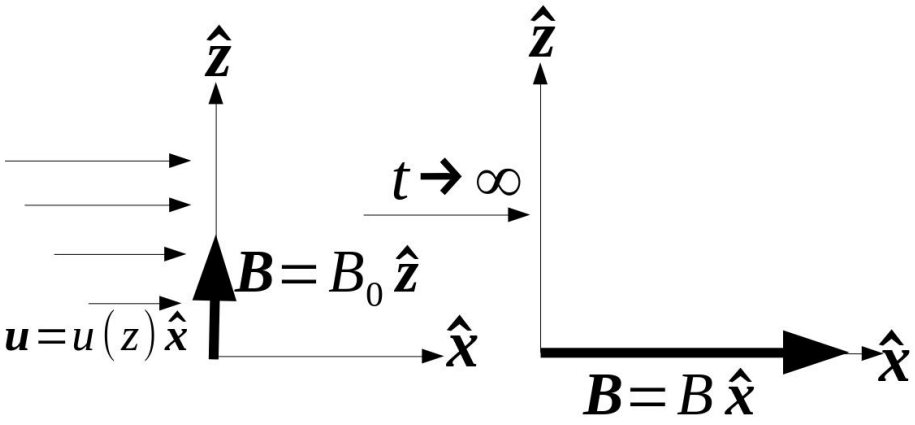

Figure 3.1: Effect of a shear flow on a guiding field.

3.3 Alignment within Turbulence

In this section, I consider alignment between the fluctuating magnetic and velocity fields within MHD turbulence. I consider three different sub-fields of MHD turbulence: relaxed, field guided and solar wind data. In each of these, I show that alignment has been extensively studied and plays a number of key roles. The fact that alignment has been so

frequently shown to be important within MHD turbulence, points to its importance within the field of MHD as a whole and is a major motivator for the study of alignment within other MHD regimes in this thesis.

3.3.1 Alignment as a Relaxation Process within MHD Turbulence

Alignment between the velocity and magnetic fields plays a key role within relaxed MHD turbulence. Within relaxed MHD turbulence, the aim, starting from a given initial condition, is to solve equations (3.19) and (3.20) for the fluctuating velocity and magnetic fields.

$$\frac{\partial \mathbf{u}}{\partial t} = (\mathbf{b}\cdot\nabla)\mathbf{b} - (\mathbf{u}\cdot\nabla)\mathbf{u} + \nu\nabla^2\mathbf{u} - \nabla P \tag{3.19}$$

$$\frac{\partial \mathbf{b}}{\partial t} = (\mathbf{b}\cdot\nabla)\mathbf{u} - (\mathbf{u}\cdot\nabla)\mathbf{b} + \eta\nabla^2\mathbf{b} \tag{3.20}$$

Note that the pressure, P, includes the magnetic pressure. Thus, $P = p + \mathbf{B}^2/2$. The absence of a forcing term within (3.19) gives "relaxed MHD turbulence" its name and importantly means that there is no source term for either the total energy (3.23)

$$E_B = \frac{1}{2} < \mathbf{b}^2 > \quad (3.21) \qquad E_v = \frac{1}{2} < \mathbf{u}^2 > \quad (3.22) \qquad E = E_B + E_v \quad (3.23)$$

or the other two quadratic invariants of the MHD equations, which in 2D are H_c and A.

$$H_c = \frac{1}{2} < \mathbf{u}\cdot\mathbf{b} > (3.24) \qquad \mathbf{b} = \nabla \times \mathbf{a} \quad (3.25) \qquad A = < \mathbf{a}^2 > \quad (3.26)$$

and in 3D are the energy, H_c and H_m.

$$H_m = \frac{1}{2} < \mathbf{a}\cdot\mathbf{b} > \tag{3.27}$$

In all of these quantities, $<>$ is an average, usually spatial. The aim within relaxed MHD turbulence is to examine the evolution of the energies and quadratic invariants and their spectra within Fourier space in an effort to gain an understanding of how these quantities move between the large and small scales. Two key processes govern this evolution,

selective decay (SD) and dynamic alignment (DA).

In SD the relationship of E with A within 2D and E with H_m within 3D is key. SD posits that if E decays to as small a value as possible under the constraint that either A or H_m is kept fixed then a "relaxed" state would be reached where both H_c and E_v are both zero. Furthermore, E_B would become confined to the largest wavelength allowed by the boundary conditions. Further information about this process may be found within, for example, [65] and the review article [86].

The second key process, and the one that is of particular interest to us, is that of DA. This relaxation process is characterised by an increase in the correlation between the fluctuating velocity and magnetic fields and thus an increase within their alignment. One consequence of increased alignment can be seen from considering the equality (3.28)

$$\frac{(\mathbf{u}\times\mathbf{b})^2}{|\mathbf{u}|^2|\mathbf{b}|^2}+\frac{(\mathbf{u}\cdot\mathbf{b})^2}{|\mathbf{u}|^2|\mathbf{b}|^2}=1 \tag{3.28}$$

where we see that an increase within $\mathbf{u}\cdot\mathbf{b}$ must result in a weakening of $\mathbf{u}\times\mathbf{b}$. As it is this term that governs the nonlinear interactions within the induction equation, it is thus expected that a stronger $\mathbf{u}\cdot\mathbf{b}$ will result in a weakening of the nonlinear interactions and it is this that is one of the primary motivations behind the study of alignment in relaxed MHD turbulence.

For the rest of this section, I will summarise some of the key results within the field. Two review articles of relaxation and constraints within MHD turbulence with a broader scope and more depth than is required here are [70] and [86] respectively.

Within the solar wind, as detailed later within section 3.3.3, there is a strong correlation between the velocity and magnetic fields. One of the first papers to attribute this to relaxation processes was [33] by Dobrowolny, Mangeney and Veltri. In this paper, the concept that an initially correlated magnetic and velocity field (non-zero initial H_c) could relax to a more correlated state (higher H_c) is put forward as an explanation for the large amount of correlation present within the solar wind. The authors use dimensional analysis to show that MHD turbulence with an initial amount of H_c can relax to a state where a high degree

of alignment is present. Support for this idea was provided by Grappin et al. [53] where theoretical techniques and numerical simulations are used to show that MHD turbulence with initially non-zero H_c will relax to a state with larger H_c. They find that energy is transferred to the small scales faster than H_c and thus dissipates at a faster rate. Within [53] the initial value of the correlation coefficient ρ

$$\rho = \frac{< \mathbf{u} \cdot \mathbf{b} >}{\sqrt{< \mathbf{u}^2 >< \mathbf{b}^2 >}} \tag{3.29}$$

is 0.1 and grows to a maximum of 0.9 and so nonlinear interactions are still present. The issue of what happens as $\rho \to 1$ is addressed in the follow up paper [52] by Grappin et al. Grappin et al show that the weakening of nonlinear interactions caused by DA as $\rho \to 1$ results in a change to the energy spectra from the $-3/2$ power law which they found in their previous paper. The paper thus shows that high correlation between the two fields can alter the distribution of energy at a wavenumber k.

In [67], Matthaeus et al. consider 2D relaxed MHD turbulence via the use of numerical simulations. They use four different initial conditions to examine the evolution of correlations between the fluctuating fields and the energy spectra. They find that if initially $H_c > 0$, then the correlation between the two fields increases over time. They also find that the presence of alignment cannot prevent the transfer of energy to small scales but can at best slow it down. This is further seen by Pouquet, Meneguzzi and Frisch [85] albeit for a different set-up. They also find evidence within both 2D and 3D, as did Grappin et al in [53] and [52], that where dynamic alignment occurs correlations become opposite in sign in the large and the small scales. The paper thus provides further support for the existence of DA as a relaxation process.

The papers so far have shown that when an initially non-zero H_c is present DA acts to increase the correlation between the fluctuating magnetic and velocity fields via a slower cascade to small scales of H_c than E. What these papers did not examine, however, is the interplay between DA and SD. This was the topic of the papers [105],[102] and [103] which seek solutions to the question: If DA wants to relax the system to a state with high correlation and $E_v \approx O(E_B)$ but SD aims to make E_v as small as possible and condensate

E_B into the largest wavelengths allowed by the boundary conditions, how does the system evolve?

The first attempt to address this question was made by Ting, Matthaeus and Montgomery within [105]. In this paper, Ting et al. perform a large number of 2D simulations with varying amounts of E/A and $\frac{1}{2}E/H_c$ in their initial conditions. They then examine the evolution of E/A and $\frac{1}{2}E/H_c$ as the simulation progresses. By plotting E/A on the vertical axis and $E/2H_c$ on the horizontal axis they show that, for all initial conditions, the system is attracted to states on the curves

$$\frac{E}{A} = 2\left(\frac{E}{2H_c}\right)^2\left[1 \pm \sqrt{1-\left(\frac{E}{2H_c}\right)^2}\right] \tag{3.30}$$

after a significantly large time. They also show that these curves may be found analytically by a variational method whereby E is extremized subject to fixed A and H_c.

Further investigation of the interplay between SD and DA is performed in three dimensions by Stribling and Matthaeus [102]. The authors investigate the spectral distribution of H_c/E and H_m/E for ideal ($\nu = \eta = 0$) relaxed MHD turbulence. They find that H_c accumulates at the larger scales and they find a weak inverse cascade of H_c when an inverse cascade of H_m occurs. This is significant as it was previously shown in [53] and others that where DA is the only relaxation process H_c cascades to smaller scales, albeit at a slower rate than the energy. The presence of magnetic-helicity, H_m, has therefore been shown to alter the direction of the cascade of H_c.

Support for a change in cascade direction is provided by Stribling and Matthaeus [103]. This paper builds upon the work done within [105] by performing a parameter study of 3D relaxed MHD turbulence for the 3D ideal invariants E, H_c and H_m to examine the competition between DA and SD. By use of a similar variational method to minimize E subject to constant H_m and H_c as that within [105], the authors find a minimum energy curve within the $|H_m|/E$, $2|H_c|/E$ parameter space. They use a large number of initial conditions for E_v/E_B, H_m/E and $2H_c/E$. For those with $E_v \ll E_B$ or $E_B \ll E_v$ they find that neither SD or DA is the dominant process as H_m and H_c remain unchanged. Instead

it is posited that it is E_v/E_B tending towards its equilibrium value that is the dominant process for these initial conditions. They find that where $H_m \gg H_c$ initially SD dominates and where initially $H_c \gg H_m$ DA dominates. No inverse cascades were found for the DA dominated regimes but inverse cascade of both H_m and E_B were found where SD was dominant. Where significant amounts of H_m and H_c are present in the initial condition, SD and DA are found to both play a role and H_c and H_m undergo an inverse cascade with E_B and E_v accumulating at large scales, $H_m/E_B \approx 1$ and significant correlation present. The direction of cascade of the alignment measure H_c is therefore found to be dependent upon whether or not H_m is present. This therefore supports the previous result, [102], by the same authors.

Patches of strong local alignment have also been found within relaxed MHD. Matthaeus et al. [69] and Servidio, Matthaeus and Dmitruk [95] found that a rapid relaxation process can cause patches of strong alignment to occur. The patches of strong alignment between $\mathbf{u}$ and $\mathbf{b}$ as well as $\nabla \times \mathbf{b}$ and $\mathbf{b}$ lead to regions of weak nonlinearity which inhibit the energy cascade and lead to intermittency (see [71] for a review of intermittency). Evidence for the presence of this process within the solar wind was then reported by Servidio et al. [96]. In [96], by using data from the multi spacecraft *Cluster*, the authors show that patches of local alignment occur within the solar wind. Furthermore, they found that this local correlation can be present even when $H_c = 0$ due to a symmetry of aligned and anti-aligned regions present. Relaxed MHD turbulence therefore appears to have multiple processes by which the magnetic and fluid fields become aligned with the alignment able to occur both globally and locally.

In conclusion, alignment between the fluctuating magnetic and velocity fields has been shown to play an important role within relaxed MHD turbulence. Where no H_m is present, this alignment is found to be the dominant process in relaxed MHD due to a slower cascade of H_c to small scales than that of the energy. The picture becomes more complex with H_m present with H_c now cascading to large scales rather than small. Evidence for patches of strong local alignment playing a role in the development of intermittency has also been found and linked to observations of intermittency within the solar wind. The literature thus

shows that alignment plays a crucial role in the evolution and structure of the fluctuating magnetic field.

3.3.2 Scale Dependent Dynamic Alignment within MHD Turbulence with a Large Scale Field

In this section, I consider MHD turbulence with a guiding field and outline how scale dependent dynamic alignment (SDDA) has been shown to play an important role.

As the discussion in this section is predominantly centred around the work of Boldyrev and his collaborators I will use his notation conventions. These are outlined by Boldyrev within [16]. The evolution of the fluctuating velocity and magnetic fields is expressed in terms of evolution eequations for the Elsässer variables $\mathbf{z} = \mathbf{v} - \mathbf{b}$ and $\mathbf{w} = \mathbf{v} + \mathbf{b}$, where V_A is the Alfvén velocity, $\mathbf{V}_A = \mathbf{B}_0/\sqrt{4\pi\rho}$, $\mathbf{B}_0$ is a constant guiding field, ρ is the fluid density, $P = p/\rho + \mathbf{b^2}/2$ is the total pressure, $\mathbf{v}$ is the fluctuating velocity field and $\mathbf{b}$ is the fluctuating magnetic field, normalised by $\sqrt{4\pi\rho}$. The factor of 4π in the normalisation is due to the authors use of SI units.

$$\frac{\partial \mathbf{z}}{\partial t} + \big(\mathbf{V}_A \cdot \nabla\big)\mathbf{z} + \big(\mathbf{w} \cdot \nabla\big)\mathbf{z} = -\nabla P \tag{3.31}$$

$$\frac{\partial \mathbf{w}}{\partial t} - \big(\mathbf{V}_A \cdot \nabla\big)\mathbf{w} + \big(\mathbf{z} \cdot \nabla\big)\mathbf{w} = -\nabla P \tag{3.32}$$

The focus is understanding how the presence of a large scale mean magnetic field alters the energy spectra. Traditionally, two theoretical models of the interactions between Alfvén wave packets (eddies) have been proposed: one for isotropic turbulence and one for anisotropic.

Theory for isotropic turbulence (where eddies are the same size in the field parallel and perpendicular directions) was outlined in the papers by Iroshnikov and Kraichnan in [56] and [59] respectively. These papers show that the energy spectra should have a power law of $-3/2$.

$$E_{IK}(k) \propto k^{-\frac{3}{2}} \tag{3.33}$$

Goldreich and Sridhar [50] instead considered the anisotropic case where eddies are elongated along the guide magnetic field. In this case, the energy in the direction perpendicular to the guide field is instead found to have a $-5/3$ power law.

$$E_{GS}(k_\perp) \propto k_\perp^{-\frac{5}{3}} \tag{3.34}$$

The problem, however, is that numerical simulations [61] and [77] with a strong guide field and clear anisotropy present produces an E_{IK} spectrum and not the predicted E_{GS} spectrum and so the theory and simulations are in disagreement.

To explain this disagreement, the idea of SDDA was proposed by Boldyrev. Boldyrev [16] showed that having the fluctuating fields become more aligned at small scales, resulting in weakening of the nonlinear interactions, could reproduce the G-S energy spectrum for weak guiding fields but would produce the I-K energy spectrum for strong guiding fields; a result that is in good agreement with numerical results. In [17], Boldyrev builds on [16] by examining only the case of a strong guiding field. He proposes that due to a constant energy flux perfect alignment cannot be reached. This then allows Boldyrev to propose that within the inertial range the fluctuating magnetic and velocity fields become aligned with angle θ_λ at scale λ

$$\theta_\lambda \propto \lambda^{\frac{1}{4}}. \tag{3.35}$$

This then produces the I-K spectrum in the direction perpendicular to the guiding magnetic field $\mathbf{B}_0$. This quantity, (3.35), is measurable and thus allows for the theory of SDDA to be tested against simulations.

Mason et al in [62] then build on [17] by performing numerical simulations. They obtain results supporting SDDA within the inertial range and find the angle to be in agreement with (3.35), resulting in a field perpendicular I-K energy spectrum (3.36).

$$E_{\perp} \propto k_{\perp}^{-\frac{3}{2}} \tag{3.36}$$

This was followed up with results of more simulations in Mason et al [63], again finding (3.36) to be the perpendicular energy spectrum.

Boldyrev et al in [18] then showed that relation (3.36) is consistent with structure functions obtained by extending isotropic results by Politano and Pouquet (see references within the paper). SDDA has thus been shown to be theoretically sound and consistent with numerical simulations.

MHD turbulence is said to be balanced if

$$\int_V \mathbf{u} \cdot \mathbf{b} dV = 0 \tag{3.37}$$

and corresponds to a balance between Alfvén wave packets propagating and counter propagating along the magnetic field lines of the large scale field. If however (3.37) does not hold, then the MHD turbulence is said to be imbalanced. The solar wind is a natural example of where MHD turbulence is imbalanced and as such much can be learned about the effects of an imbalance by studying solar wind data.

Within [79], Perez and Boldyrev show that SDDA is consistent with both balanced and imbalanced turbulence. They find that the regions of balanced and imbalanced turbulence both show the scaling (3.36) of the perpendicular energy spectrum. This thus suggests that a region of balanced turbulence can be understood as a superposition of regions of imbalanced turbulence, all of which exhibit an energy scaling (3.36). Motivated by solar wind data, Podesta and Bhattacharjee [82] then extended the results within [79] by taking into account the proportion of the domain made up of positively and negatively aligned fluctuations.

Perez and Boldyrev [80] examined numerical simulations of steady state incompressible MHD turbulence, that is both balanced and imbalanced, in an attempt to understand the conflicting results of [79], [82], [13], [60] and [26] where there was disagreement on

whether or not energy spectra were the result of SDDA. They study the energy spectra $E^{\pm}$

$$E^{\pm} = \frac{1}{4}\int_V (\mathbf{u} \pm \mathbf{b})^2 dV \tag{3.38}$$

and in balanced turbulence find $k^{-\frac{3}{2}}$ for both $E^{\pm}$. In the case of imbalanced MHD turbulence Perez and Boldyrev find that $E^{\pm}$ have the same scaling

$$E^{\pm}[k_{\perp}] \propto k_{\perp}^{-\frac{3}{2}} \tag{3.39}$$

but an amplitude that depends on the amount of cross-helicity. These results support the findings of [79] and [82] and the authors note consistency with results of Beresenyak and Lazarian [13] in that both positive and negative energy spectra scale with the same exponent. However, a difference in exponents occurs between the results of Perez and those of Beresenyak and Lazarian. This has been suggested to be the result of a lack of resolution within [13]. The results in [80] are however inconsistent with those of Chandran within [26] who find $E^{\pm}[k_{\perp}]$ to be different depending on the amount of imbalance within the turbulence. However, the majority of the literature suggests that the energy spectra found do indeed result from SDDA.

Perez et al [81] performed further high resolution numerical simulations to measure the energy spectra for both balanced and imbalanced MHD turbulence. They take the kinematic and magnetic diffusivities to be equal and so the Reynolds numbers are also. In the balanced case, their results provide further evidence of SDDA with a $-3/2$ energy spectrum power law present. In the imbalanced case, they find that $E^{-} \propto k^{-\frac{3}{2}}$ for all of their Reynolds numbers. E^{+} does not show this result for moderate Reynolds number. However, they postulate that it will become proportional to it for sufficiently large Reynolds number. They also show results in support of [64] where Mason et al. showed that the alignment scaling extends into the dissipation region for a given Reynolds number as long as there is sufficient resolution.

In conclusion, scale dependent dynamic alignment (SDDA) between the fluctuating velocity and fluctuating magnetic field has been shown both analytically and numerically to

be the probable reason as to why numerical simulations show a $-3/2$ exponent for the perpendicular energy spectrum. Over the decade since Boldyrev first outlined this theory, increasingly high resolution numerical simulations have shown good agreement with this theory and a number of the conflicting results have been addressed. Alignment between the fluctuating velocity and magnetic fields thus plays a key role in field guided turbulence via the scale dependent dynamic alignment mechanism.

3.3.3 Observations of Alignment within MHD Turbulence

In addition to more theoretical studies, alignment of the fluctuating flow and magnetic fields has also been studied by looking at data taken from solar wind experiments. In this section, I briefly overview literature which measures the alignment present within the solar wind. All $\mathbf{u}$ and $\mathbf{b}$ in this section refer to the fluctuating components of the field.

Alfvén waves have the property that the velocity field and magnetic field perturbations are parallel to each other and normal to the propagation of the wave itself. For a full discussion of Alfvén waves see [87].

One of the earliest papers to examine alignment in the solar wind data is [12] by Belcher and Davis. The authors use Mariner 5 data from 1967 to look at Alfvén waves in the interplanetary medium. Belcher and Davis found that Alfvén waves moving away from the Sun dominate the microscale, less than 0.01 Astronomical units (AU), half of the time.

[33] built on this by showing that the dominance of the Alfvénic fluctuations propagating away from the Sun is due to the properties of the turbulence, in particular that there is no net cross-helicity. Matthaeus and Goldstein in [66] used Voyager data of the solar wind to examine more thoroughly the three rugged invariants of MHD which they define to be

$$H_c = \frac{1}{2}\int_V \mathbf{u}\cdot\mathbf{b}dV \qquad \text{(3.40a)} \qquad H_m = \int_V \mathbf{a}\cdot\mathbf{b}dV \qquad \text{(3.40b)}$$

$$E = \frac{1}{2}\int_V \frac{\mathbf{u}^2+\mathbf{b}^2}{2}dV \qquad \text{(3.40c)}$$

they found a difference in the results depending upon the distance from the Sun with the fluctuating fields closer to the Sun showing evidence of being Alfvénic but this disappearing

at a larger distance from the Sun. They find evidence that close to the Sun the Alfvénic fluctuations move away from the Sun. Roberts et al. in [90] used Helios and Voyager data to show that Alfvénic fluctuations travelling away from the Sun are dominant. They found that the Alfvénic fluctuations become less dominant by 1AU which is a result supported by [66].

Bavassano and Bruno in [11] also looked at properties of solar wind fluctuations in Helios 1 and 2 data over a period of low solar activity for distances 0.3-1AU. They find strong correlations between the fluctuating velocity and magnetic fields for correlation timescales of 1-12 hours. However, for timescales between 12hours and 3 days, the dominance of these "Alfvénic" fluctuations is much less and is dominated by features due to magnetic and thermal pressure. These results support those in [90] in that they find strong Alfvénic fluctuations close to the Sun and that Alfvénic correlations decrease at a larger distance from the Sun.

Roberts et al. in [91] used a 2D MHD spectral code to show that observed properties of the Alfvénicity of the magnetic and velocity fluctuations can be explained by shear driven turbulence. Goldstein et al in [51] backed up results in [90] and [11] by looking at data from Ulysses at high latitudes and comparing them to the results obtained by Helios in the ecliptic plane. These results support previous results showing that large scale shear reduces the Alfvénicity of fluctuations more rapidly than without shear. They show that at high latitudes the turbulence remains more Alfvénic at larger distances due to the reduced shear.

Matthaeus et al in [68] took a more analytical approach, giving a possible theory as to how shear overcomes the natural tendency to become more Alfvénic as radial distance increases. Boldyrev's power law scaling of turbulence (see section 3.3.2) has also been tested against solar wind data. Podesta et al in [83] used data from the WIND spacecraft and showed that, at scales with reliable data, half of the windows of data sampled had results in agreement with Boldyrev's theory. The results within the other data windows were also explained by the presence of high speed solar winds.

In summary, measuring alignment and in particular measuring whether the fluctuating magnetic and velocity fields are “Alfvénic”, is a key component of analysing MHD data from the interplanetary medium and the solar wind. In particular, the presence of Alfvénic correlations is frequently used to suggest the presence of Alfvén waves in the solar wind. As such, one of the key results found using alignment is that the magnetic and velocity fluctuations are highly aligned close to the Sun.

3.4 Alignment within Nonlinear Dynamos

Alignment has been looked at in a number of papers looking at the fully dynamical problem. In this section, I will outline some of the key results. The study of alignment has primarily focussed on Alfvénic dynamos (sometimes referred to as $u \sim B$ dynamos). In these dynamos, it appears that following the exponential growth of the magnetic field (in the kinematic phase) saturation of the kinetic and magnetic energies occurs when the magnetic and velocity fields become almost parallel. Forcings, which yield a dynamo that saturates in this fashion, are of particular interest because they give magnetic and kinetic energies which saturate at approximately the same value, known as equipartition. Steiner and Ferriz-Mas within [101] gave an approximation for the solar magnetic energy by assuming flux is generated by an interface dynamo near the base of the convection zone to be $10^{32}J$. The available kinetic energy over the solar cycle is also estimated within [101] to be $10^{33}J$. Equipartition dynamos are thus of interest due to their ability to generate magnetic and kinetic energies that are of the same magnitude and thus of potential astrophysical relevance.

The PhD thesis of Archontis [8] is widely regarded as being the first study of an Alfvénic dynamo. This was followed up by the paper by Dorch and Archontis [36]. In [36], Dorch and Archontis looked at the fully compressible three dimensional MHD equations in a periodic domain. They use an initial velocity profile

$$\mathbf{u}_0 = \begin{pmatrix} \sin(z) \\ \sin(x) \\ \sin(y) \end{pmatrix} \tag{3.41}$$

with a weak divergence free magnetic field and a forcing

$$\mathbf{f} = \frac{-k(t)}{R_e}\nabla^2\mathbf{u}_0 \tag{3.42}$$

within the equation of motion

$$\frac{D\mathbf{u}}{Dt} = -\nabla P + \nu\nabla^2\mathbf{u} + \mathbf{J}\times\mathbf{B} + \mathbf{f} \tag{3.43}$$

where the forcing has a time dependence determined in such a way as to keep the kinetic energy at the same level over time. R_e is the fluid Reynolds number. Keeping the kinetic energy constant has the benefit that R_e does not change over time. The authors then vary R_e and R_m by variation of the diffusivities, η and ν, and examine the results.

The results that they found can broadly be split into two categories, $R_m \geq R_e$ and $R_e \gg R_m$. For $R_m = 100$ and $R_e = 2$ using a uniform seed field and $R_m = 100$ and $R_e = 50$ using a random seed field they found that the magnetic and kinetic energy reached a steady state near equipartition and that just before saturation of the magnetic energy, $\mathbf{u}$ and $\mathbf{B}$ become approximately parallel. This was also found to be the case for $R_m = R_e = 200$. Thus their results for $R_m \geq R_e$ show saturation of the magnetic and kinetic energies occurs at approximately the same value and that $\mathbf{u}$ and $\mathbf{B}$ become approximately parallel.

For $R_e \gg R_m$ they found that the magnetic energy saturated at a steady state much lower than the value achieved for the kinetic energy. For example, for $R_m = 100$ and $Re = 400$ the kinetic energy is shown to saturate at a value much higher than the magnetic energy with no real alignment of $\mathbf{u}$ and $\mathbf{B}$.

What [36] shows, therefore, is that there appears to be a subset of the results for this forcing within which alignment appears to be associated with a dynamo that saturates at equipartition.

Following on from [36], Cameron ad Galloway wrote two papers [22] and [23] where they examined Alfvénic dynamos. Instead of using a fully compressible code with variable forcing, they instead opted to use an incompressible code where the forcing is constant and of the form

$$\mathbf{F}_A = \nu \begin{pmatrix} \sin(z) \\ \sin(x) \\ \sin(y) \end{pmatrix} \tag{3.44}$$

where ν is the kinematic viscosity of the flow and (3.44) is sometimes named the Archontis forcing, a name that I will adhere to herein.

Cameron and Galloway found that when using the initial condition $\mathbf{u}_0 = \mathbf{B}_0 = \mathbf{F}_A/\nu$ with the magnetic diffusivity and kinematic viscosity equal, corresponding to equal R_m and R_e, an Alfvénic dynamo is achieved with the steady state solution achieved for $\mathbf{u}$ and $\mathbf{B}$ being nearby, but crucially not equal to, $\mathbf{F}_A/(2\nu)$. The kinetic and magnetic energies are also found to be equal, in line with the results obtained within [36].

One of the most interesting things that they found was that if they started with an initial random seed field for $\mathbf{B}$, rather than the initial condition stated above, then an apparent steady state solution was achieved once the dynamical regime began. In this state, the kinetic and magnetic energies are not in equipartition and the magnetic and velocity fields are not aligned. However, after the code was ran for a longer period of time the kinetic and magnetic energies both experienced a second exponential growth phase and proceeded to reach a steady state where the magnitude of the two quantities is both much larger than before and at equipartition. Figure 3.2 shows this with a measure of alignment, normalised to be between 0 and 1, plotted also

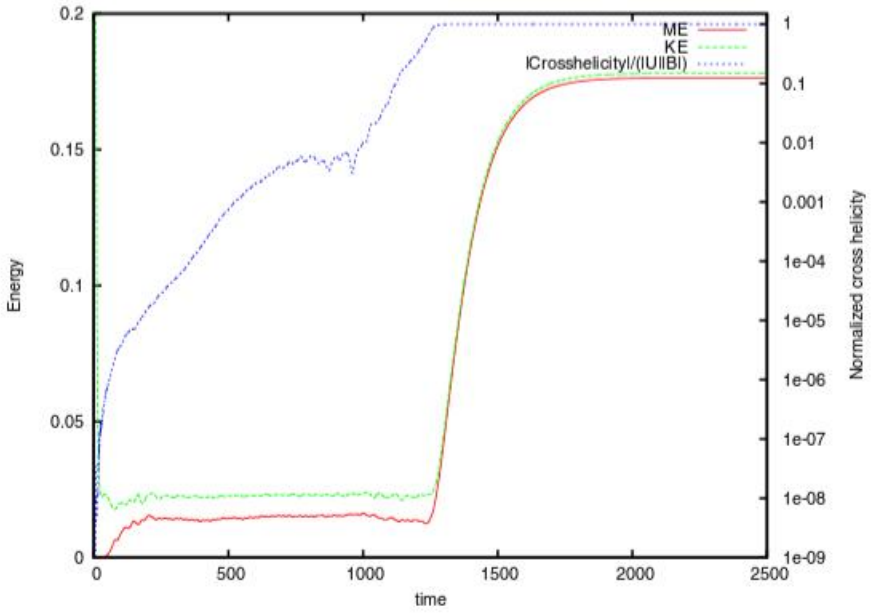

Figure 3.2: Figure 19 from [22] showing how saturation occurs at alignment.

What we can see is that although $\mathbf{u}$ and $\mathbf{B}$ appear to have saturated they are still evolving and becoming more aligned. It is only after they have become almost perfectly aligned that the second exponential growth phase occurs. This indicates that alignment is key for saturation at a steady state with an equipartition of magnetic and kinetic energy for the Archontis forcing.

[22] also shows that given a steady state solution, $(\mathbf{u}_0, \mathbf{B}_0, \eta_0)$ to the induction equation

$$\frac{\partial \mathbf{B}}{\partial t} = \nabla \times (\mathbf{u} \times \mathbf{B}) + \eta \nabla^2 \mathbf{B} \tag{3.45}$$

where $\mathbf{u}_0$ and $\mathbf{B}_0$ are parallel $(\beta \mathbf{B}_0 + \varepsilon \mathbf{u}_0, \alpha \mathbf{B}_0, \varepsilon \eta_0)$ is also a solution. Thus by specifying the forcing in the equation of motion for the fluid

$$\frac{\partial \mathbf{u}}{\partial t} + (\mathbf{u} \cdot \nabla)\mathbf{u} = \nu \nabla^2 \mathbf{u} + \frac{\mathbf{J}}{\rho} \times \mathbf{B} + \mathbf{F} - \nabla \left(\frac{P}{\rho} \right) \tag{3.46}$$

in such a way that $(\beta \mathbf{B}_0 + \varepsilon \mathbf{u}_0, \alpha \mathbf{B}_0, \varepsilon \eta_0)$ is also a solution to this we can in fact generate a solution with an arbitrary ratio of total magnetic and kinetic energies. It is thus possible to generate a steady state solution for $\nu = \varepsilon \nu_0, \eta = \varepsilon \eta_0$ if a steady state solution can be found for $\nu = \nu_0, \eta = \eta_0$.

[22] was followed by a second paper by the same authors [23]. In this second paper, they consider a more general forcing

$$\mathbf{F}_\gamma = \nu \begin{pmatrix} A\sin(z) + C\gamma\cos(y) \\ B\sin(x) + A\gamma\cos(z) \\ C\sin(y) + B\gamma\cos(x) \end{pmatrix} \tag{3.47}$$

in an attempt to find a broader variety of forcings which yield an Alfvénic dynamo. They find that for $\gamma = 0.125$, $\eta = \nu = 0.01$ and $A : B : C = 0.5 : 1 : 1$ a steady state solution is achieved where again $\mathbf{u}$ and $\mathbf{B}$ are close to equipartition and approximately parallel. For $\eta = \nu = 0.0025$ something extremely interesting occurs, this is shown in figure 3.3.

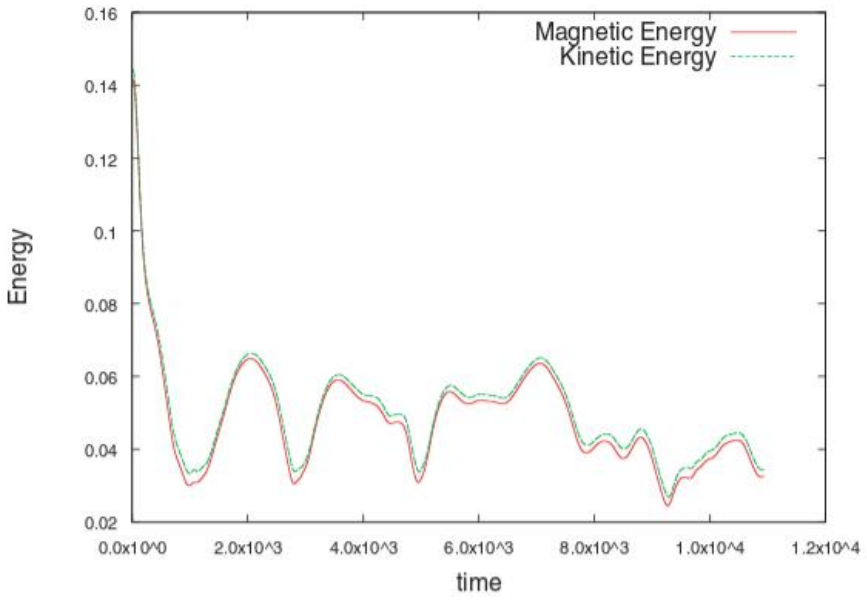

Figure 4. Time development of the magnetic and kinetic energies for the case $\gamma = 0.125$, $A : B : C = 0.5 : 1 : 1$, $\nu = \eta = 1/400$.

Figure 3.3: Figure 4 of [23] showing a non steady state Alfvénic dynamo.

What figure 3.3 shows is that although a steady state solution has not been achieved the kinetic and magnetic energies stay approximately equal over time. $\mathbf{u}$ and $\mathbf{B}$ are also found to be approximately parallel. Thus, although the final solution is not steady state and appears to vary in an irregular manner, an Alfvénic dynamo with equipartition has been obtained.

This is an intriguing result as it shows that forcings that generate Alfvénic dynamos do

not necessarily result in steady state solutions. This broadening of the types of solution obtained, makes the study of Alfvénic dynamos even more intriguing.

Cameron and Galloway go further by using the forcing prescription technique from [22] to generate a steady state solution for $\eta = \nu = 0.0025$ from the steady state solution obtained for $\eta = \nu = 0.01$. They find a steady solution for $\eta = \nu = 0.0025$ nearby the one obtained for $\eta = \nu = 0.01$. Their subsequent analysis shows that it is the heteroclinic orbits nearby stagnation points which are altered by the change in η and ν and thus the difference in energies.

What these two papers showed together is that a number of different forcings over a variety of ν and η result in an Alfvénic dynamo where the kinetic and magnetic energies are approximately equal. These papers support the initial findings in [36] that Alfvénic dynamos are interesting due to their astrophysical relevance by expanding the forcings that can generate them.

The 2007 paper [7] by Archontis, Dorch and Nordlund attempted to build on the results in [22] and [23] by performing longer runs once a steady state has been achieved and examining the results. The compressible/ incompressible codes used in [36], [22] and [23] up to this point showed results broadly in agreement with each other. [7] appeared to show that the steady state solution achieved for the Alfvénic dynamo does not remain steady state over time and in fact becomes turbulent over time. An example of this is shown in figure 3.4.

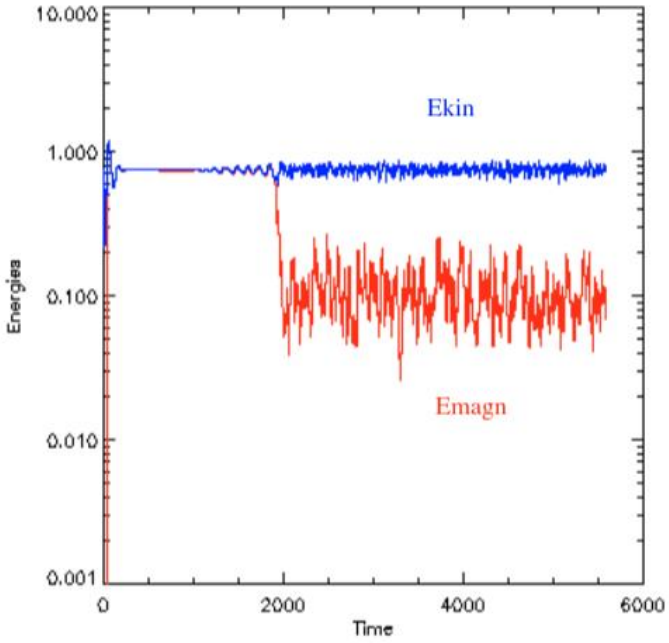

Fig. 2. Temporal evolution of the kinetic and magnetic energies for the experiment with Rm = Re = 100.

Figure 3.4: Figure 2 from [7] showing the forcings ability to knock the dynamo off of its steady state.

The results within the paper are interesting. However, Galloway in [39] later describes how it is the forcing used that is knocking the solution off of its steady state and confirm this by using a forcing of this form in his incompressible code.

Further work was done using the Archontis forcing by Alexakis within [2] where the limit of infinite magnetic Prandtl number, $P_m = \nu/\eta$, was considered. In [2], Alexakis showed that making this assumption and increasing R_m results in a magnetic field structure where the magnetic field is concentrated within ribbons which do not occupy a large proportion of the domain. Furthermore, magnetic instabilities are described for $R_m > 80$ after which the magnetic energy evolves somewhat chaotically with power laws reminiscent of turbulence.

Gilbert, Ponty and Zheligovsky within [48] build upon the, mostly numerical, work done so far by approaching Alfvénic dynamos in a more theoretical manner. The authors non-dimensionalise and define a Grashof number $G = \varepsilon^{-1}$

$$\varepsilon = \frac{FL^3}{\nu^2} \tag{3.48}$$

where F and L are typical force and length scales respectively. They show that diffusive terms of order $\varepsilon^{\frac{1}{2}}$ become important in the region surrounding stagnation points as well as a number of other rigorous analytical results.

The paper [40] by Galloway, in 2012, summarises previous work done on the ABC flows. Furthermore, it derives an equation (3.49) for the evolution of cross-helicity in the case of an incompressible flow

$$\frac{d}{dt}\int_V \mathbf{u}\cdot\mathbf{B}dV = \int_V \mathbf{F}\cdot\mathbf{B}dV + \nu\int_V \mathbf{B}\cdot\nabla^2\mathbf{u}dV + \eta\int_V \mathbf{u}\cdot\nabla^2\mathbf{B}dV \tag{3.49}$$

Now, as $\mathbf{F}$ in the papers [22] and [23] is multiplied by the fluid Reynolds number, we can see that the evolution of the cross-helicity is on a diffusive timescale and is therefore slow. As the Alfvénic dynamos have been shown to rely critically on $\mathbf{u}$, $\mathbf{B}$ evolving to an aligned state it therefore appears that the Alfvénic dynamo generated by the Archontis forcing must be slow. This is unfortunate, as astrophysical dynamos typically evolve on fast timescales and so a forcing not dependent on η or ν would be preferable.

Galloway, in [40], mentions that by looking at the evolution equations for the integral of cross-helicity and total energy and assuming $\mathbf{u}$, $\mathbf{B}$ are of the form

$$\alpha\begin{pmatrix}\sin(z)\\ \sin(x)\\ \sin(y)\end{pmatrix} \tag{3.50}$$

(as they were found to approximately be in [22]) where α is a constant and taking the Archontis forcing we can gain some insight into the constants multiplying $\mathbf{u}$ and $\mathbf{B}$. It is mentioned that this will be carried out in a later paper however to my knowledge this has not been published. I set

$$\mathbf{u} = \alpha_1\begin{pmatrix}\sin(z)\\ \sin(x)\\ \sin(y)\end{pmatrix} \tag{3.51}$$

$$\mathbf{B} = \alpha_2 \begin{pmatrix} \sin(z) \\ \sin(x) \\ \sin(y) \end{pmatrix} \tag{3.52}$$

$$\mathbf{F} = \nu \begin{pmatrix} \sin(z) \\ \sin(x) \\ \sin(y) \end{pmatrix} \tag{3.53}$$

and note that

$$\frac{1}{V}\int_0^{2\pi}\int_0^{2\pi}\int_0^{2\pi} \sin(x)^2 + \sin(y)^2 + \sin(z)^2 dV = \frac{3}{2} \tag{3.54}$$

the evolution equations for total energy is

$$\frac{d}{dt}\int_V \frac{\mathbf{u}^2 + \mathbf{B}^2}{2} dV = \int_V \mathbf{F}\cdot\mathbf{u} dV + \eta\int_V \mathbf{B}\cdot\nabla^2\mathbf{B} dV + \nu\int_V \mathbf{u}\cdot\nabla^2\mathbf{u} dV \tag{3.55}$$

thus substituting equations (3.51)-(3.53) into (3.49) and (3.55) and assuming that $\alpha_1, \alpha_2 \neq 0$ we obtain

$$\nu(\alpha_1 - \alpha_1^2) - \eta\alpha_2^2 = 0 \tag{3.56}$$

$$\nu(1 - \alpha_1) - \eta\alpha_1 = 0 \tag{3.57}$$

(3.57) immediately yields α_1 and substituting this into (3.56) yields α_2 provided $\eta \neq 0$.

$$\alpha_1 = \frac{\nu}{\nu + \eta} \tag{3.58}$$

$$\alpha_2 = \pm\alpha_1 \tag{3.59}$$

Thus, assuming we have reached a steady state solution and that $\mathbf{u}$ and $\mathbf{B}$ are parallel, we see that they are also equal in magnitude. In fact, if $\nu = \eta$ we obtain $\alpha_1 = \pm\alpha_2 = 0.5$ which is the approximate solution found in [22]

What these papers have shown is that Alfvénic dynamos are good candidates to produce equipartition values of the magnetic and kinetic energies. These dynamos saturate by an alignment of the magnetic field and velocity field and this in itself makes alignment an interesting topic to study. More information is needed to gain a better understanding of how alignment causes saturation, as well as whether a forcing can be obtained that would allow equation (3.49) to evolve on a fast time scale but the results so far certainly indicate that the role that alignment plays in dynamos is worthy of further study.

3.5 Summary of Alignment Motivations

In summary, alignment of the magnetic field and the velocity field has been studied within a broad variety of areas within MHD. Aligned velocity and magnetic fluctuations has been shown to be a natural state for unforced MHD with non-zero initial cross-helicity. Furthermore, alignment that depends upon scale, has been used to explain observed energy spectra within field guided turbulence. Within solar wind data, it has been shown that close to the Sun the fluctuating fields are aligned and moving away from the Sun in a so called "Alfvénic" state. Finally, within nonlinear dynamo theory, alignment of the full fields has been shown to play a crucial role in the workings of an equipartition dynamo.

The examination of the above literature highlights a number of different areas upon which further study would be of use. The first is the absence of any study of alignment within kinematic dynamo theory. The fact that only the magnetic field evolves within kinematic dynamo theory, requires that the only alignment that can occur is the magnetic field becoming aligned with a prescribed velocity field whose form remains unchanged. A primary aim of kinematic dynamo theory is to identify prescribed flows for which exponential growth of a seed magnetic field occurs. It is therefore interesting to examine whether there is any link between alignment and growth rate. Due to kinematic dynamo theory being less computationally intensive than other fields, it also provides an opportunity to study basic alignment mechanisms and relationships between alignment and other quantities. These can then help to provide insight into the mechanisms at work within, for example, nonlinear dynamo theory

Section 3.4 has also provided an intriguing avenue for future research. In particular the apparent role that alignment is playing within the saturation of the nonlinear dynamo within figure 3.2. Due to the astrophysical relevance of a dynamo, which saturates at equipartition, it would be beneficial to broaden the class of dynamos which achieve a final state where the flow and magnetic field are aligned and of equal energy with the aim of obtaining a better understanding of the key properties which yield equipartition dynamos. Furthermore, whether or not the two statistically steady states within figure 3.2 occur for physical reasons and whether multiple statistically steady states would be expected in general nonlinear dynamos is still an open question and one which I will address in Chapter 5.

Chapter 4

Alignment Within Kinematic Dynamo Theory

4.1 Introduction

In this chapter I examine the alignment between $\mathbf{u}$ and $\mathbf{B}$ within kinematic dynamo theory. To do this I run kinematic dynamo simulations where (4.1) is solved for the magnetic field given a flow $\mathbf{u}$

$$\frac{\partial \mathbf{B}}{\partial t} + (\mathbf{u}\cdot\nabla)\mathbf{B} = (\mathbf{B}\cdot\nabla)\mathbf{u} + \eta\nabla^2\mathbf{B}. \tag{4.1}$$

The main aims of the chapter are as follows:

- **To study alignment in 2.5 kinematic dynamos.**

  I consider two 2.5D flows $\mathbf{u}(x,y)$ in sections 4.2 and 4.3. The main aim of this work is to identify whether examining time series of the alignment measures H_1 and H_2

  $$H_1 = \frac{1}{V}\int_V \frac{|\mathbf{u}\cdot\mathbf{B}|}{|\mathbf{u}||\mathbf{B}|}dV \qquad\qquad H_2 = \frac{\int_V |\mathbf{u}\cdot\mathbf{B}|dV}{\sqrt{\int_V \mathbf{u}^2 dV \int_V \mathbf{B}^2 dV}}$$

  at each vertical wavenumber can be a useful method of identifying changes to the magnetic field structure. Some of this work was included in the conference proceeding [73].

- **To study alignment in 3D kinematic dynamos**

I consider a fully 3D flow $\mathbf{u}(x,y,z)$. The aim of this section of work is to investigate how the information on the evolution of the magnetic field structure gained from examining H_1 and H_2 can be used to understand how the magnetic field's 3D structure changes. This work is motivated by the inherent difficulty in examining 3D magnetic field structures and understanding the way in which the magnetic field's structure evolves.

- **To examine the relationship between alignment and fluid helicity in kinematic dynamos.**

  Finally I examine whether there is any relationship between the fluid helicity H_f

$$H_f = \int_V \mathbf{u} \cdot (\nabla \times \mathbf{u}) dV$$

  and alignment for a family of flows of varying H_f. This is motivated by the relationship between H_f and an alpha effect [75] as well as the result [55] of a more helical kinematic dynamo generating a larger growth rate. The aim is to determine if any relationship between alignment and both fluid helicity and growth rate exists for a particular family of flows where H_f is varied in a controlled manner.

4.2 The Roberts flow

4.2.1 Introduction

In this section I examine the relationship between the Roberts flow and alignment within kinematic dynamo theory. Taking the dot product of (4.1) with $\mathbf{B}$ and volume averaging over the periodic domain we obtain an equation for the evolution of the magnetic energy (4.3).

$$\frac{d}{dt}\int_V \frac{\mathbf{B}^2}{2} dV = \int_V \mathbf{J} \cdot (\mathbf{u} \times \mathbf{B}) dV - \eta \int_V \mathbf{J}^2 dV \tag{4.3}$$

$$J_B = J_I - J_\eta \tag{4.4}$$

where $\mathbf{J} = \nabla \times \mathbf{B}$. Growth of magnetic energy is therefore achieved by J_I overcoming the diffusive current term J_η. If $\mathbf{u}$ and $\mathbf{B}$ were perfectly aligned then J_I would vanish and no dynamo would be achieved. This suggests that alignment between the flow and magnetic fields may be an important factor in producing a kinematic dynamo. Furthermore if the current $\mathbf{J}$ and $\mathbf{u} \times \mathbf{B}$ were to be perpendicular we would again obtain no growth in magnetic energy. Alignment between these two pairs of quantities therefore plays a crucial role in the workings of the dynamo.

As shown in Chapter 3, alignment between the flow and magnetic fields has previously been studied in a variety of different MHD contexts however it has not previously been studied within kinematic dynamo theory. In the kinematic regime the lack of feedback onto the flow makes the question a case of whether the magnetic field aligns with $\mathbf{u}$ rather than both becoming aligned with one another. I focus on how H_1 and H_2 can be used to compare the dynamos at different k_z and as the dynamo evolves for a particular k_z.

I begin by defining the Roberts flow and mathematically outlining the amplification process. Following a short section on methodology I then examine alignment between $\mathbf{u}$ and $\mathbf{B}$ in sections 4.2.4, 4.2.5 and 4.2.6. In section 4.2.7 I then examine alignment between $\mathbf{J}$ and $\mathbf{u} \times \mathbf{B}$ and the relationship between this alignment and dynamo action.

4.2.2 The Flow Geometry and Dynamo Mechanism

In this section I introduce the Roberts flow and the processes of stretching and flux expulsion that govern how the dynamo amplifies magnetic fields. The Roberts flow has the form

$$\mathbf{u} = A \begin{pmatrix} \cos(y) \\ \sin(x) \\ \cos(x) + \sin(y) \end{pmatrix} \tag{4.5}$$

where A is a constant. Alternatively, it may be expressed in terms of the stream function $\psi = A(\cos(x) + \sin(y))$

$$\mathbf{u} = A\left[\frac{\partial \psi}{\partial y}, -\frac{\partial \psi}{\partial x}, \psi\right]. \tag{4.6}$$

As the flow is 2.5D the resulting magnetic field from a kinematic dynamo will have a z dependence of the form $\mathbf{B}(x,y,z,t) = \mathbf{B}'(x,y,t)\exp(ik_z z)$ where k_z is the vertical wavenumber.

To give the same kinetic energy as the flows within [55], which I will be examining later within section 4.5, I set $A = \sqrt{1.5}$ hence $\mathbf{u} = \sqrt{1.5}\big[\cos(y), \sin(x), \cos(x) + \sin(y)\big]$. The flow geometry consists of circular closed streamlines surrounding center type stagnation points separated by a network of separatrices whose intersections are hyperbolic stagnation points. This is shown below.

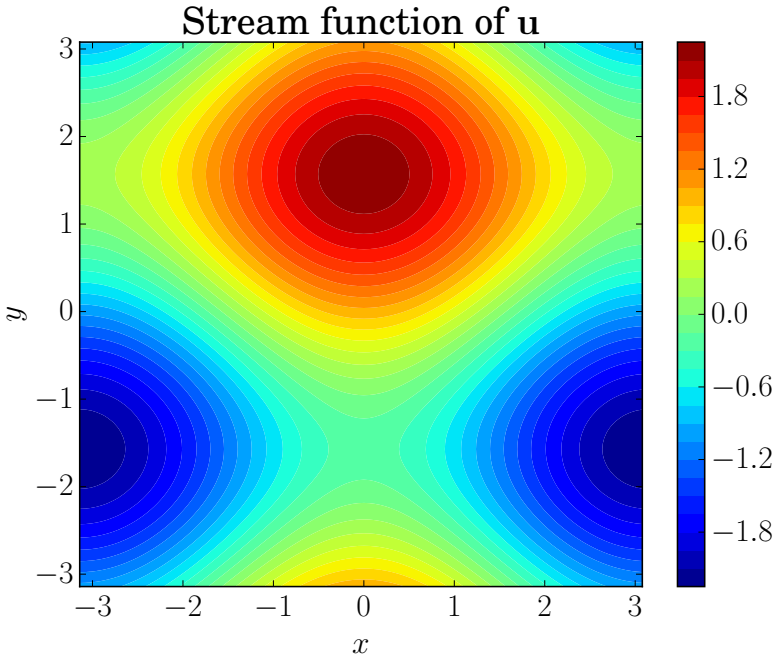

Figure 4.1: Stream function of the Roberts flow.

To show how the flow's hyperbolic stagnation points exponentially stretch the magnetic field I transform the flow with $A = 1$ to its form within [29] by the translation $y \to y + 3\pi/2$

$$\mathbf{u} = \begin{pmatrix} \sin(y) \\ \sin(x) \\ \cos(x) - \cos(y) \end{pmatrix} \tag{4.7}$$

The new stream function is therefore $\psi = \cos(x) - \cos(y)$. Insight into how the flow be-

haves can be found via a rotation of the basis. Following the analysis within [29] I make the transformation of variables (4.8a) and (4.8b).

$$x \to \frac{x' - y'}{\sqrt{2}} \qquad (4.8a) \qquad\qquad y \to \frac{x' + y'}{\sqrt{2}} \qquad (4.8b)$$

so that our new (primed) coordinate system is simply a $\pi/4$ clockwise rotation of the old one. Now setting x and y per equations (4.8a) and (4.8b) gives a stream function

$$\psi = 2\sin\left(\frac{x'}{\sqrt{2}}\right)\sin\left(\frac{y'}{\sqrt{2}}\right) \qquad (4.9)$$

meaning that the separatrices now lie on the horizontal and vertical lines $x' = \sqrt{2}n\pi$, $y' = \sqrt{2}n\pi$.

The unit vectors in the new, primed, coordinate system are (4.10a) and (4.10b)

$$\hat{\mathbf{x}}' = \frac{\hat{\mathbf{x}}}{\sqrt{2}} + \frac{\hat{\mathbf{y}}}{\sqrt{2}} \qquad (4.10a) \qquad\qquad \hat{\mathbf{y}}' = \frac{\hat{\mathbf{y}}}{\sqrt{2}} - \frac{\hat{\mathbf{x}}}{\sqrt{2}} \qquad (4.10b)$$

thus

$$\hat{\mathbf{x}} = \frac{\hat{\mathbf{x}}'}{\sqrt{2}} - \frac{\hat{\mathbf{y}}'}{\sqrt{2}} \qquad (4.11a) \qquad\qquad \hat{\mathbf{y}} = \frac{\hat{\mathbf{x}}'}{\sqrt{2}} + \frac{\hat{\mathbf{y}}}{\sqrt{2}'} \qquad (4.11b)$$

and I can now express the flow in terms of the new basis unit vectors

$$u_x\hat{\mathbf{x}} + u_y\hat{\mathbf{y}} = \sqrt{2}\sin\left(\frac{x'}{\sqrt{2}}\right)\cos\left(\frac{y'}{\sqrt{2}}\right)\hat{\mathbf{x}}' - \sqrt{2}\sin\left(\frac{y'}{\sqrt{2}}\right)\cos\left(\frac{x'}{\sqrt{2}}\right)\hat{\mathbf{y}}' \qquad (4.12)$$

$$= u_{x'}\hat{\mathbf{x}}' + u_{y'}\hat{\mathbf{y}}'. \qquad (4.13)$$

Near the stagnation point $(x', y') = (0,0)$ $x'/\sqrt{2}, y'/\sqrt{2} << 1$ and the approximation $\sin(a) \approx a$ is valid. Hence

$$\psi \approx 2\frac{x'}{\sqrt{2}}\frac{y'}{\sqrt{2}} \qquad (4.14)$$

and from (4.12)

$$u_{x'} \approx x' \qquad (4.15a) \qquad\qquad u_{y'} \approx -y' \qquad (4.15b)$$

If we now switch to a Lagrangian framework and express $u_{x'}$, $u_{y'}$ in terms of the positions in time $x'(t), y'(t)$ of the fluid elements (equations (4.16a) and (4.16b)) then we see that the solution is exponential (equations (4.16c) and (4.16d))

$$\frac{\partial x'}{\partial t} = x' \qquad (4.16a) \qquad\qquad \frac{\partial y'}{\partial t} = -y' \qquad (4.16b)$$

$$x' = A\exp(t) \qquad (4.16c) \qquad\qquad y' = B\exp(-t) \qquad (4.16d)$$

thus close to the hyperbolic stagnation points the fluid elements experience exponential stretching in the x' direction and contraction in the y'.

How the magnetic field arrives close to hyperbolic stagnation points from within the regions of closed streamlines is by a process known as flux expulsion. Consider a planar magnetic field $\mathbf{B}$ which can be expressed in terms of a magnetic potential A by (4.17)

$$\mathbf{B} = \nabla \times (A\hat{\mathbf{z}}) \tag{4.17}$$

Substituting this into the induction equation uncurling and setting the gauge equal to zero gives

$$\frac{\partial A}{\partial t} + (\mathbf{u} \cdot \nabla)A - \eta \nabla^2 A = 0 \tag{4.18}$$

by non-dimensionalising using an advective timescale we can introduce the magnetic Reynolds number R_m

$$\frac{\partial A}{\partial t} + (\mathbf{u} \cdot \nabla)A - R_m^{-1} \nabla^2 A = 0 \tag{4.19}$$

We can express the flow nearby the center type stagnation point within polar coordinates (r, θ) as (4.20)

$$\mathbf{u} = r\Omega(r)\hat{\boldsymbol{\theta}} \tag{4.20}$$

and thus our equation for the magnetic potential is

$$\frac{\partial A}{\partial t} + \Omega \frac{\partial A}{\partial \theta} - R_m^{-1} \nabla^2 A = 0. \tag{4.21}$$

Following [29] I assume the magnetic potential to be of the form

$$A = f_m(r,t) \exp(im\theta) \exp(-im\Omega t). \tag{4.22}$$

Substituting this into (4.21) and simplifying gives an evolution equation for f_m

$$\frac{\partial f_m}{\partial t}\exp(im\theta)\exp(-im\Omega t) - im\Omega A + im\Omega A = R_m^{-1}\nabla^2 A$$

$$\frac{\partial f_m}{\partial t} = -R_m^{-1}\left(m^2 f_m\left(\frac{d\Omega}{dr}\right)^2 t^2 + im\left[f_m\frac{d^2\Omega}{dr^2} + \frac{f_m}{r}\frac{d\Omega}{dr} + 2\frac{d\Omega}{dr}\frac{df_m}{dr}\right] - \frac{\partial^2 f_m}{\partial r^2} + m^2 f_m\right) \tag{4.23}$$

which for large R_m and large t can be approximated as

$$\frac{\partial f_m}{\partial t} = -R_m^{-1}m^2 f_m\left(\frac{d\Omega}{dr}\right)^2 t^2 \tag{4.24}$$

thus the dominant behaviour of the magnetic field is diffusive in nature with the diffusive timescale being

$$O\left(R_m^{\frac{1}{3}}\right) \tag{4.25}$$

and it is this diffusion of the magnetic field out of the center regions that is known as flux expulsion. For the majority of eigenmodes the magnetic field then becomes concentrated in thin sheets close and parallel to separatrix surfaces with the thickness of the sheets scaling as $1/\sqrt{Rm}$ (see page 118 of [29]).

The above picture of flux being expelled from the center regions and forming into thin sheets close to the separatrices of the flow where it becomes stretched is the behaviour of the dominant eigenmode (eigenmode with the largest growth rate) for the majority of vertical wavenumbers k_z. As I will show however there are a small number of k_z for which the magnetic field evolves differently. In [100] Soward builds upon the work done by Gilbert in [46] and Ruzmaikin in [92] on dynamo modes confined to cylindrical surfaces by showing analytically that provided certain criterion are met the Roberts flow can support growing dynamo modes which are confined to cylindrical surfaces which he labels “resonant surfaces”. These modes have the property that they evolve on an intermediate timescale which is slower than the advective timescale of the fast dynamo modes but faster than the diffusive timescale. By decoupling the velocity into

$$\mathbf{u} = \mathbf{U} + \tilde{\mathbf{u}} \tag{4.26}$$

where $\mathbf{U}$ is the primary velocity and $\tilde{\mathbf{u}}$ is a secondary velocity which is small in the region of magnetic field generation Soward shows that these resonant surfaces have the property that $\tilde{\mathbf{u}}$ and its gradients are minimised upon the resonant surfaces. It is this property that allows the "intermediate dynamo modes" to grow upon the cylindrical surfaces as it is $\tilde{\mathbf{u}}$ that is responsible for shortening the length scales of the magnetic field, a process which is essential for flux expulsion. Within the Roberts flow simulations that I will later show the values of k_z that do not produce sheets form structures consistent with these "intermediate dynamo modes". Thus, depending on the vertical wavenumber k_z (and R_m), the eigenmode of the magnetic field with the largest growth rate is either sheet-like close to the separatrices of the flow or an intermediate dynamo mode confined to one of these resonant surface within the center regions of the flow.

The Roberts flow is a slow dynamo as it was shown by Soward in [99] that as $R_m \to \infty$ the maximum dynamo growth rate, p_{max}, behaves as

$$p_{max} \approx \frac{\ln(\ln(R_m))}{\ln(R_m)}. \tag{4.27}$$

Thus $p_{max} \to 0$ as $R_m \to \infty$. Below in figure 4.2 I show how the growth rate varies with vertical wavenumber for a number of different values of R_m. We can see that even for a relatively small increase in the value of R_m the value of the growth rate is already decreasing. We also see that the vertical wavenumber with the largest growth rate is increasing as R_m increases. This phenomenon is derived by Soward in [99] for the Roberts flow.

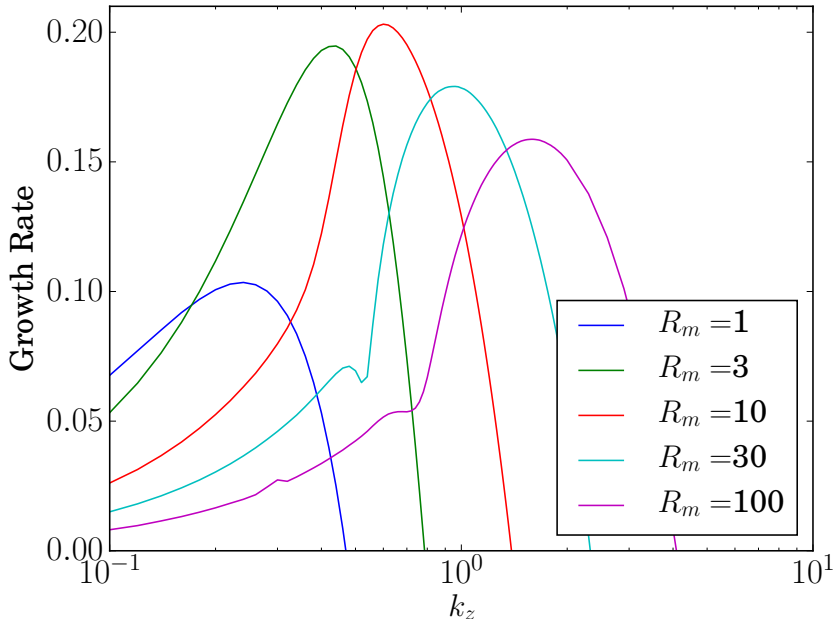

Figure 4.2: Growth rate of the Roberts dynamo for a variety of R_m. We see that the peak decreases in strength (for $R_m \geq 10$) as R_m increases and migrates to higher k_z for larger R_m.

4.2.3 Methodology

I consider the Roberts flow

$$\mathbf{u} = \sqrt{1.5}(\cos(y), \sin(x), \cos(x) + \sin(y)) \tag{4.28}$$

which is a $2.5D$ flow which is independent of both z and time t. As such solutions are of the form (4.29)

$$\mathbf{B}(x,y,z,t) = \mathbf{b}(x,y)e^{pt+ik_z z} + c.c \tag{4.29}$$

where p is a (possibly complex) growth rate, k_z is a real wavenumber which we refer to as the "vertical wavenumber" and $c.c$ means complex conjugate. Two values of R_m are considered. I will primarily be focussed upon $R_m = 100$ however a number of results will also be shown for $R_m = 1000$. Figure 4.3 shows a plot of growth rate vs k_z for $R_m = 100$ at spatial resolutions of 100^3 and 200^3 respectively to show that the growth rate is well converged at a resolution of 100^3. The growth rate has a clear peak at $k_z \approx 1.8$ as well as a kink at $k_z \approx 0.8$ believed to be due to a degenerate eigenvalue [89].

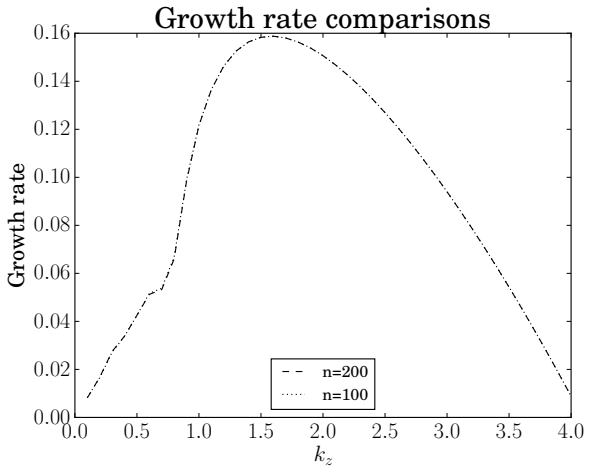

Figure 4.3: Growth rate vs k_z.

Numerical simulations are performed initially with 100 points in each spatial dimension using a pseudo-spectral method. Timestepping is performed via a second order Adams-Bashforth method (see section 2.4.1) and diffusion is treated exactly with a timestep of 0.001. To obtain a higher resolution of 200 points the 100 solution is then used as an initial condition in a code with a Adams-Bashforth Adams-Moulton predictor corrector scheme (see section 2.4.2) with diffusion treated via a Crank-Nicholson method. Furthermore in the second method computation of the nonlinear terms is simplified by making use of mode couplings. This second method is used to speed up computation with the speed up being obtained both due to the reduced timestep needed for the predictor-corrector scheme and the simplification of the nonlinear term. The growth rates of both methods were found to be in agreement and are shown in figure 4.3. Further checks of the $n = 200$ runs are shown in figure 4.4 where I show the percentage difference between the two sides of the energy equation (4.3) as well as the Taylor Microscale divided by the spatial resolution, (4.30)

$$l_b = \sqrt{\frac{\int_V |\mathbf{B}|^2 dV}{\int_V |\nabla \times \mathbf{B}|^2 dV}} \tag{4.30}$$

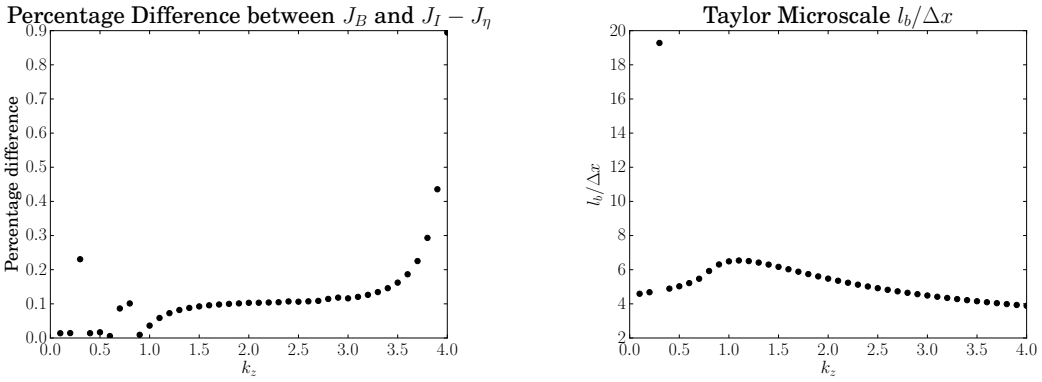

(a) Percentage difference between the two sides of the energy equation (4.3) for $n = 200$. All values are less than 1% so we conclude the simulation is well resolved.

(b) Taylor Microscale divided by the spatial resolution for $n = 200$ runs. The Taylor Microscale is a number of times larger than the spatial resolution and so the number of grid points is sufficient.

Figure 4.4: Resolution checks for runs.

both indicate the resolution is sufficient. The z component of the magnetic field is not computed but is instead found using the divergence free condition on the magnetic field. Our domain is taken to be 2π periodic in both x and y.

For consistency I will use θ to denote the angle between $\mathbf{u}$ and $\mathbf{B}$ and ϕ to denote the angle between $\mathbf{J}$ and $\mathbf{u} \times \mathbf{B}$.

4.2.4 Alignment of the Flow and Magnetic Field for $R_m = 100$

In this section I examine how alignment between the flow and velocity field can be used to give insights into the average properties of the magnetic field. I consider two measures of alignment. These are shown in equation (4.31a) and equation (4.31b) respectively. H_1 gives the volume average of $|\cos(\theta)|$ where θ is the angle between the two fields. H_1 therefore tells us the average alignment of the two fields irrespective of their magnitudes and takes a value between 0 and 1. One problem found with this measure however was that it frequently required extremely high resolution to resolve. H_2 in comparison gives us the volume average of $|\mathbf{u}||\mathbf{B}||\cos(\theta)|$ divided by the square root of the energies. The benefit of this is that it implicitly weights each alignment by the magnitude of the field at that point and so alignment between weak field makes less of a contribution than that of the stronger field. The weakness of this however is that it is not immediately obvious what value this should take for a particular value of θ and so H_2 is harder to interpret.

$$H_1 = \frac{1}{V}\int_V \frac{|\mathbf{u}\cdot\mathbf{B}|}{|\mathbf{u}||\mathbf{B}|}dV \qquad (4.31a) \qquad H_2 = \frac{\int_V |\mathbf{u}\cdot\mathbf{B}|dV}{\sqrt{\int_V \mathbf{u}^2 dV \int_V \mathbf{B}^2 dV}} \qquad (4.31b)$$

I take $R_m = 100$. In figure 4.5 I show plots of H_1 and H_2 along with the growth rate over a range of k_z. The first thing to note is the point $k_z = 0.3$ which has a distinctly different value than the others. The reason for this can be seen by looking at the structure of the magnetic field. In figure 4.6 we show the z component of the magnetic field at $z = 0$ and normalised by the magnetic energy. $k_z = 0.7$ and $k_z = 4$ are shown as typical examples of the structure for $k_z \neq 0.3$. We see that the magnetic field for $k_z = 0.3$ has a drastically different structure with the field being confined to large Ponomarenko style modes upon resonant surfaces [100], this was previously shown to be possible within [100] and seen by Courvousier [31].

The distribution of energy between the three magnetic field components is also different with 85% of the energy being in B_z for the Ponomarenko modes whereas 99% of the energy is within the B_x and B_y component (equally split) for the other k_z where the magnetic field is confined to magnetic layers of thickness $O\left(\eta^{\frac{1}{2}}\right)$ along the separatrices of the Roberts flow ([29], p.118). H_1 and H_2 thus each identify the fact that the dominant mode has a dramatically different magnetic field structure at $k_z = 0.3$, something that examination of the growth rate alone would not show.

Finally, the decrease in H_1 from 0.9 to 0.8 (see right axis of figure 4.5a) is due to the magnetic field becoming more confined into magnetic layers along the separatrices of the flow. This can be seen by comparing $k_z = 0.7$ and $k_z = 4.0$ in figure 4.6.

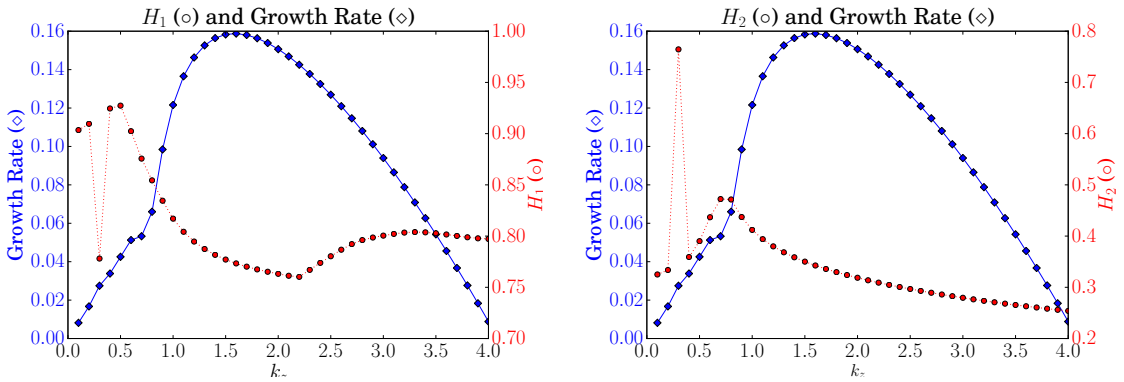

(a) H_1 (b) H_2

Figure 4.5: H_1 and H_2 for $R_m = 100$.

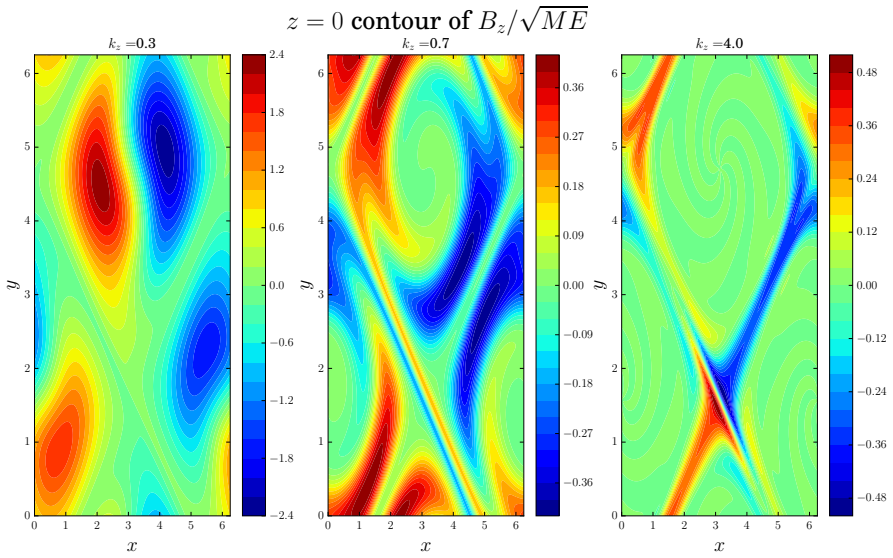

Figure 4.6: $R_m = 100$. $z = 0$ contour of $\mathbf{B}_z/\sqrt{2ME}$.

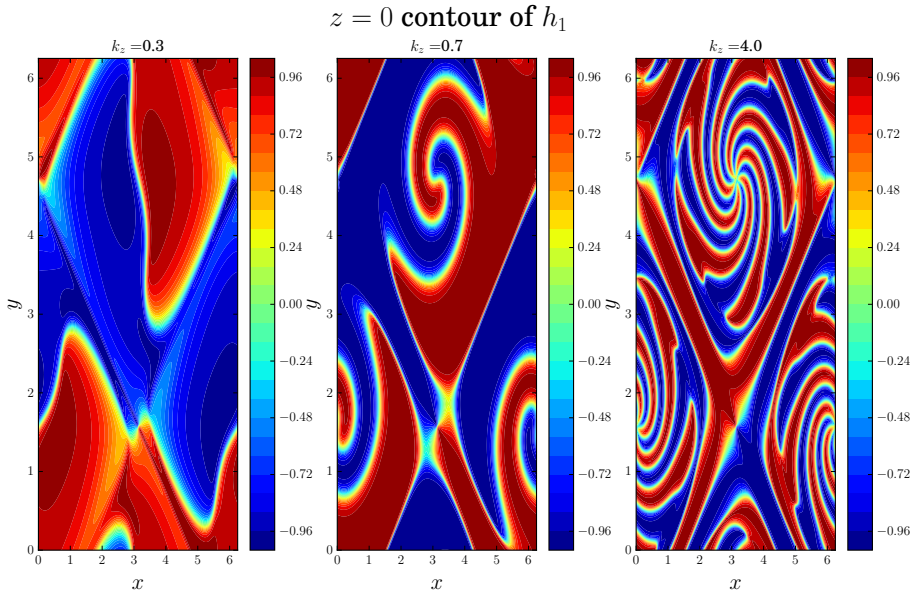

Figure 4.7: $z = 0$ contour of h_1.

$$h_1 = \frac{\mathbf{u} \cdot \mathbf{B}}{|\mathbf{u}||\mathbf{B}|} \tag{4.32}$$

In figure 4.7 I show contour plots of the quantity h_1. This quantity is the unsigned integrand of H_1. As such it gives $\cos(\theta)$, where θ is the angle between $\mathbf{u}$ and $\mathbf{B}$. In all cases we see that the domain is split into roughly equal amounts of positive and negative alignment. I also note that the alignment values are close to maximal rather than spread over all possible values. The spiral like shapes in the center regions of 0.7 and 4.0 can be attributed to

the flux expulsion mechanism, see for example my description within section 4.2.2 or the heuristic description of the behaviour of the Roberts flow within [29].

In figure 4.8 I show histograms of θ. A red background shows theta for which the fields are more aligned than perpendicular with a green background showing the opposite. The subtitles show the proportion, A, of the total grid points whose values correspond to aligned field and the proportion ME_A/ME of the total magnetic energy that is contained within the aligned regions. We see a large proportion of the domain is made up of aligned field at small k_z. This proportion then decreases to a value in the range $60-70\%$ for higher k_z. As the proportion of aligned field decreases we see that more than 96% of the energy continues to be contained within the aligned regions, showing just how important the aligned regions of field are to the growth of the dynamo.

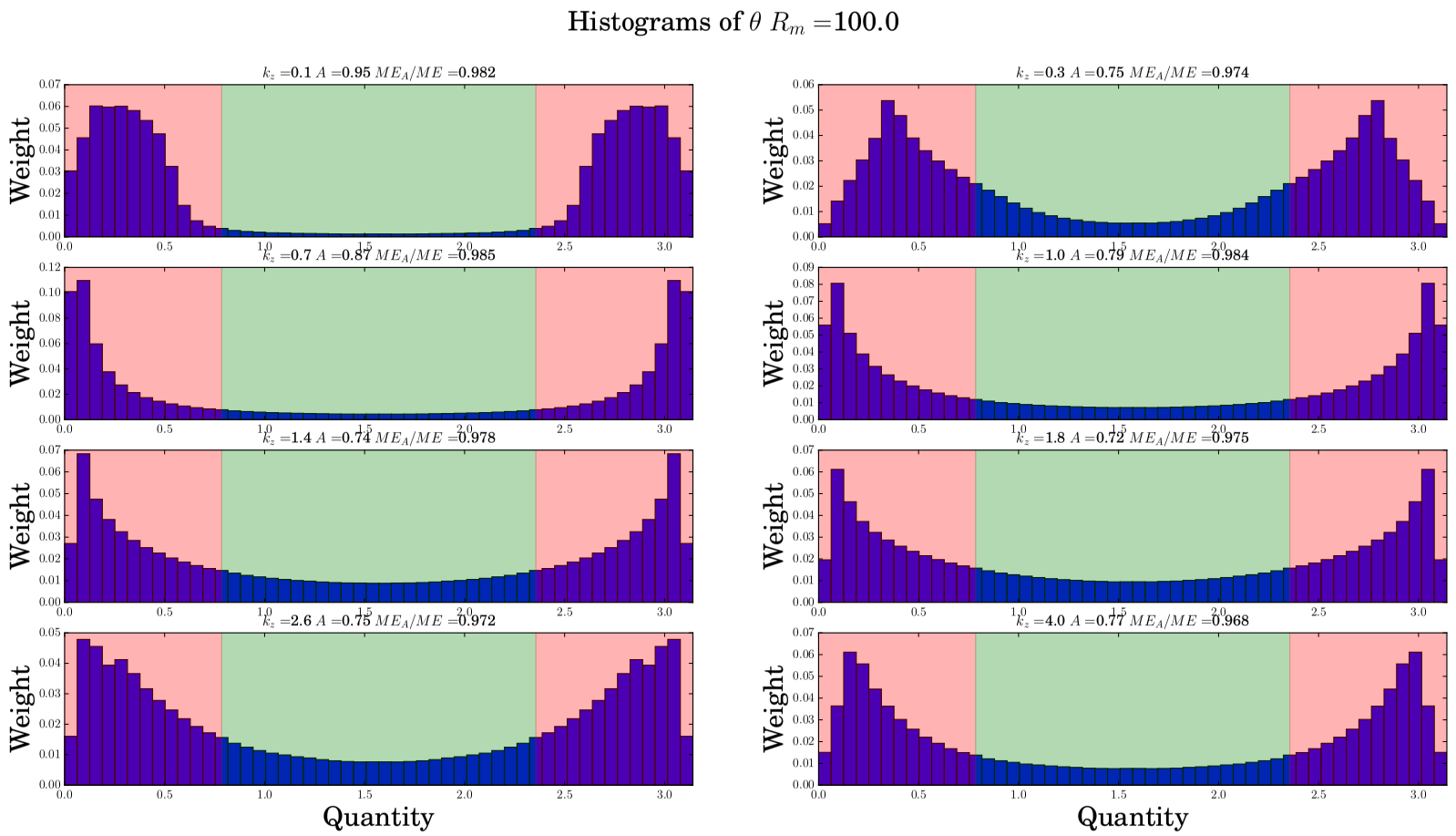

Figure 4.8: Histogram of θ for $R_m = 100$. Red background indicates θ for which the fields are more aligned than perpendicular and green is the opposite. We see that most of the field has an angle corresponding to being more aligned than perpendicular.

In conclusion I have found that both measures of alignment considered within this section are useful in distinguishing changes to the dominant eigenmode's magnetic field structure as k_z is varied.

4.2.5 Alignment of the Flow and Magnetic Field for $R_m = 1000$

In this section I extend the previous section's results by considering alignment within the Roberts dynamo for $R_m = 1000$. I examine whether there may be some dependence of the value of H_1 and H_2

$$H_1 = \frac{1}{V}\int_V \frac{|\mathbf{u}\cdot\mathbf{B}|}{|\mathbf{u}||\mathbf{B}|}dV \qquad (4.33a) \qquad H_2 = \frac{\int_V |\mathbf{u}\cdot\mathbf{B}|dV}{\sqrt{\int_V \mathbf{u}^2 dV \int_V \mathbf{B}^2 dV}} \qquad (4.33b)$$

on the structure of the magnetic field's dominating eigenmode. The aim is to see if H_1 and H_2 continue to be an indicator of changes to modal structure at higher R_m.

The code that I use makes use of the predictor-corrector numerical scheme detailed within section 2.4.2. I use a large number of points in each spatial direction with a suitable timestep. For each of the modes selected the runs were either initialised using a random seed field attached to each Fourier mode at that k_z or in a second manner which I describe now. For the second initial condition I begin $k_z = 0.1$ using a random seed field and then after a fixed time which is so long as to ensure both H_1 and the growth rate have saturated I end the run. Once the run is finished the final magnetic field is rescaled and this is then used to initialise the next k_z. The reason for doing this is to attempt to stay on the same branch of solutions as we vary k_z. Furthermore doing this highlights the fact that the growth rate can appear converged far before the magnetic field has finished evolving in dynamo simulations. The method is also extremely useful in speeding up the code as once the eigenmode structure becomes that of a separatrix all subsequent k_z initialised with a weak seed separatrix structure converge rapidly to the same structure and thus quickly reach their final states.

Figure 4.9 shows a parameter scan of k_z for $R_m = 1000$ began with a random seed field at $k_z = 0.1$ but subsequently following this branch in the manner described above. What we see is that the values of H_1 and H_2 do not vary a great deal as k_z is changed. In both cases however $k_z = 0.3$ experiences a large jump in value and clearly stands out as being

different. If we examine the growth rate closely we see that the $k_z = 0.3$ value also appears to be slightly out of place with its surrounding values, however this is not so obvious as the dramatic change in H_1 and H_2.

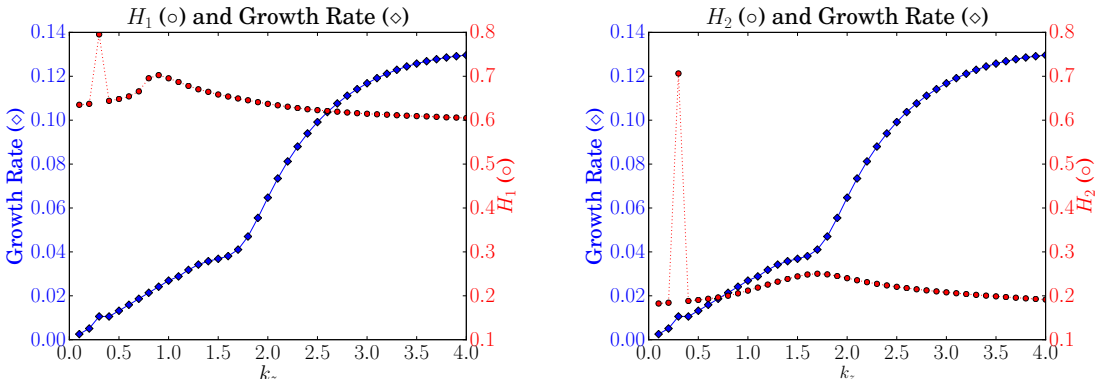

(a) H_1 (b) H_2

Figure 4.9: H_1 and H_2 for $R_m = 100$.

Time series of H_1 can also provide useful information on how the structure of the magnetic field is evolving. In figure 4.10 I show the results of a run for $k_z = 0.6$ which was began with a seed magnetic field. We see that the magnetic field begins with a Ponomarenko mode structure and through a flux expulsion mechanism settles to its final structure which is separatrix like. During the evolution the magnetic field gets pulled into the regions next to the null lines of the flow where it experiences exponential stretching and the energy becomes predominantly contained within the x and y components of the magnetic field. Whereas the growth rate saturates quickly H_1 shows how the magnetic field structure does not settle until a much later time. This figure also shows that large Ponomarenko modes appear to consistently have a value at approximately 0.8 and separatrix modes have a value of about 0.6-0.65. This information enables us to predict the structure of the field from a time series of H_1 alone without having to plot a large number of contours. It is also interesting to note that H_1 exhibits oscillations when it is not in the separatrix structure. This will be explored within section 4.2.6.

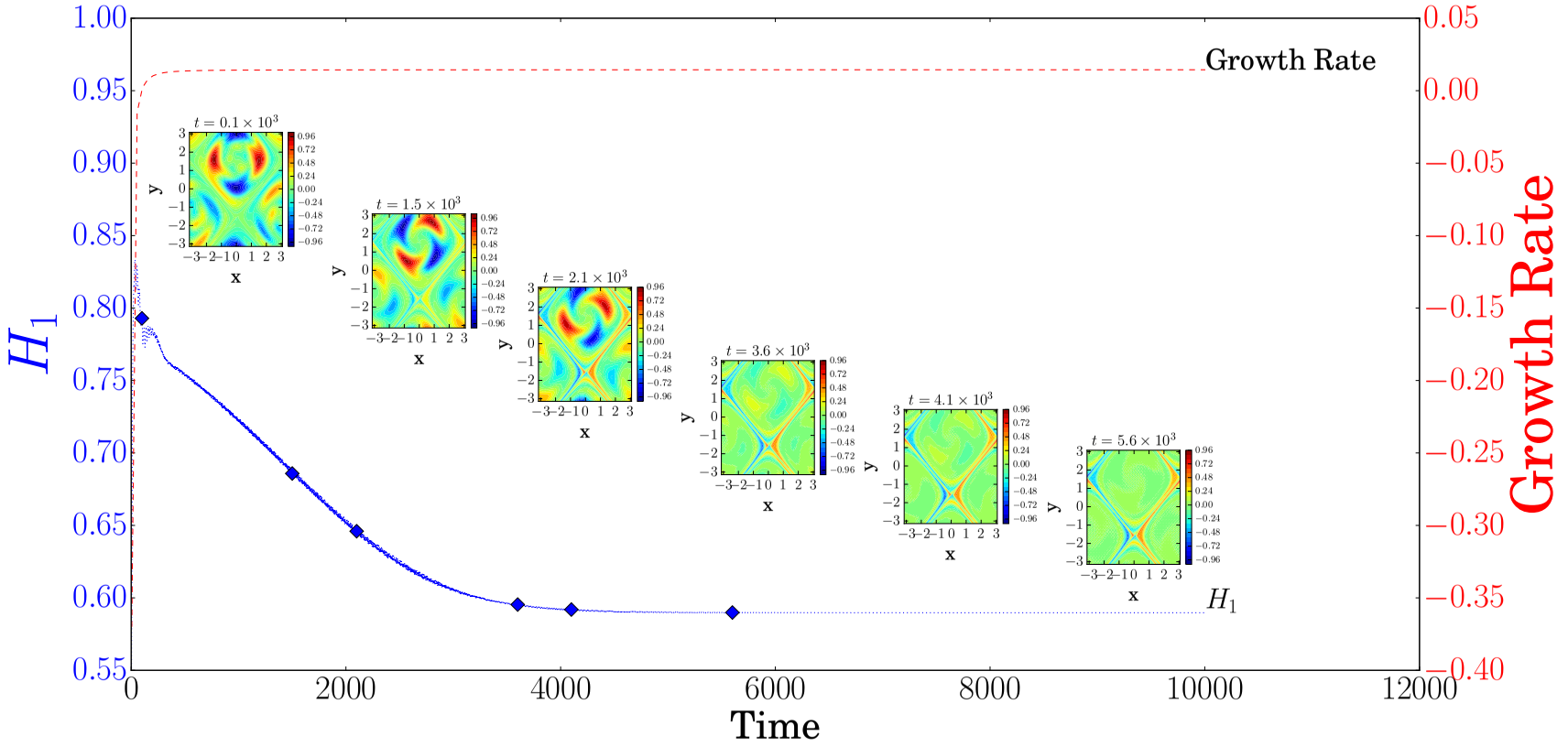

Figure 4.10: Time series of H_1 for $R_m = 100$ and $k_z = 0.6$. The growth rate settles quickly, which hides the fact that the magnetic field structure has not finished evolving. In comparison, H_1 continuing to evolve shows that the magnetic field structure is still changing. This highlights a particularly useful feature of examining alignment within kinematic dynamo simulations.

4.2.6 Periodicity within the Roberts Flow for $R_m = 1000$

In this section I examine the periodicity of H_1 seen within section 4.2.5. The values of k_z are split into two broad categories; ones where H_1 oscillates and ones where it does not. Looking at the B_z component of the magnetic field for a variety of k_z it is apparent that the two different types of magnetic field structures within section 4.2.5 dictate whether or not oscillations occur. I find that the large scale Ponomarenko modes, present only when k_z is in a small region of values close to 0.3, correspond to oscillations whereas dominant modes with a separatrix structure, present for all over values of k_z, do not.

Figure 4.11 shows the final structure of B_z as well as the evolution of H_1 for $k_z = 0.3$. The magnetic field is confined to the large Ponomarenko style modes which rotate with a well defined period. H_1 also oscillates with a clear period both as it's decreasing (on average) and when its mean saturates. The period of the oscillations does however appear to change during the evolution which is shown within figures 4.11c and 4.11d and confirmed using power spectra in figures 4.12a and 4.12b where we see that once H_1 becomes statistically steady its period halves from 12.5 to 6.25. An analysis of the periodicity of B_z by tracking the position of the largest value within the domain yields a period of 12.5 throughout. The period of H_1 therefore appears to be partially explained by oscillations in the magnetic field however it halves upon settling to its final oscillating state.

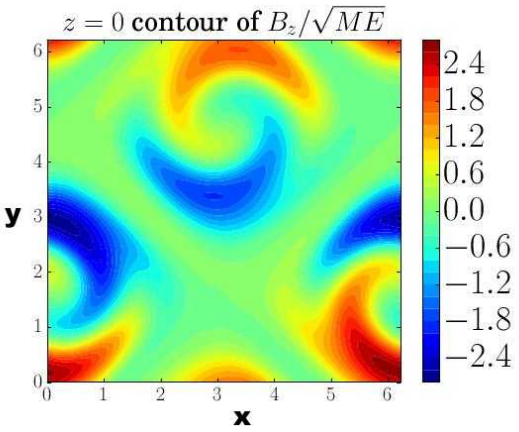

(a) $B_z/\sqrt{ME}$ at $z = 0$ and $t = 6000$

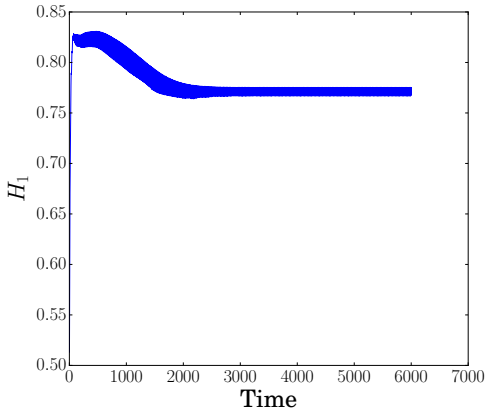

(b) Full evolution of H_1

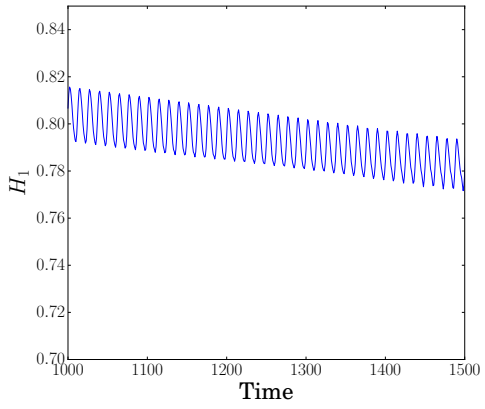

(c) Snapshot of the time series of H_1 taken as H_1 is decreasing. We see it oscillates with a well defined period.

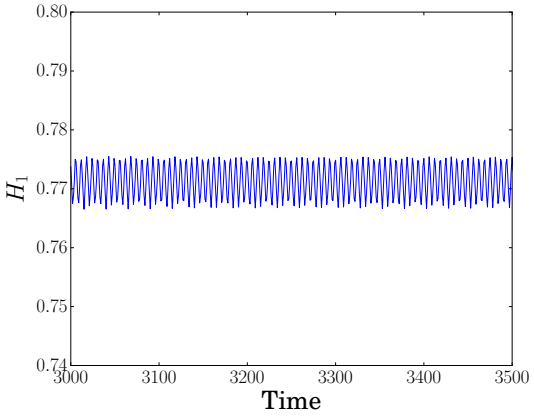

(d) Snapshot of the time series of H_1 taken during the statistically steady state of H_1. We see it oscillates with a well defined period.

Figure 4.11: Plot of the z component of the magnetic field as well as a time series of H_1 for $k_z = 0.3$ and $R_m = 1000$.

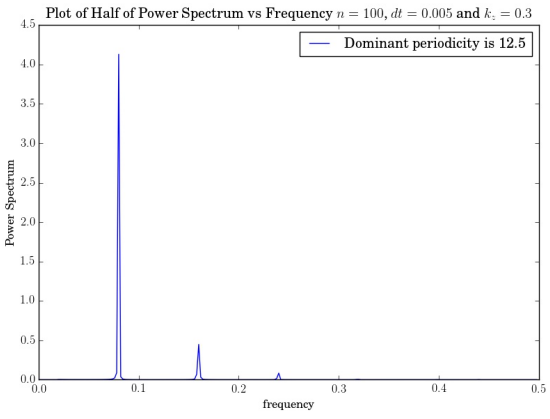

(a)

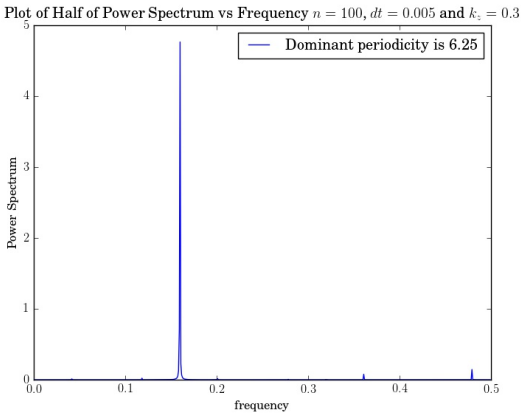

(b)

Figure 4.12: Plot of the power spectrum of H_1 for $k_z = 0.3$ and $R_m = 1000$ at a time before it has finished evolving (a) and at large time (b). We see that once H_1 finishes evolving its period halves.

Figure 4.13 illustrates how the large scale modes rotate around within the regions of closed streamlines for the case of $k_z = 0.3$. Whilst the halving of the period of H_1 is not easily explained its initial agreement with that of B_z is suggestive that it is the movement of the magnetic field causing the oscillations rather than some numerical effect and thus that it is linked to the rotation of the large scale modes.

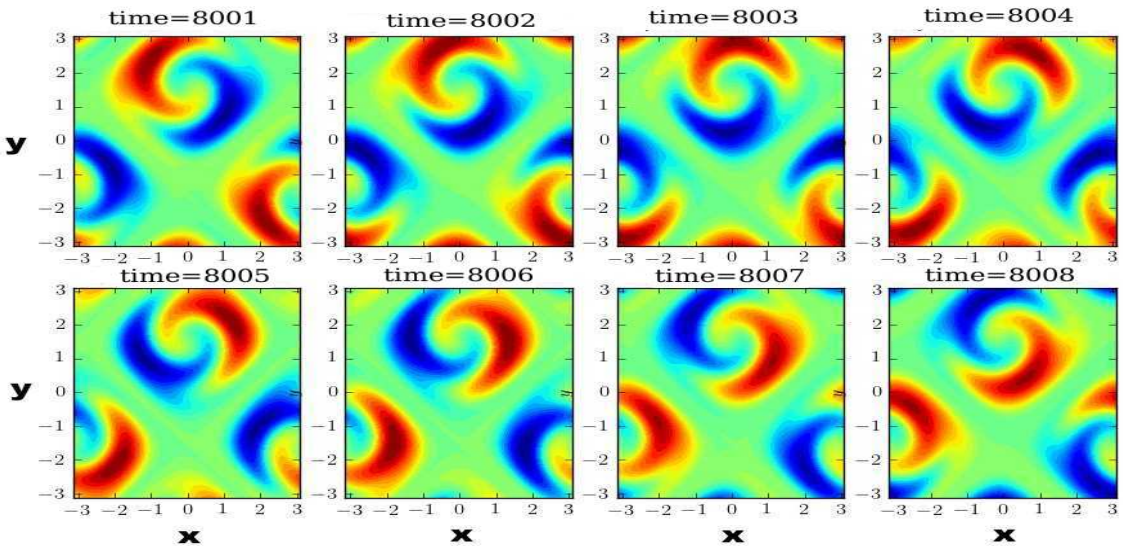

Figure 4.13: Plot of $z = 0$ contours of B_z with $k_z = 0.3$, $dt = 0.005$, $n = 100$ and $R_m = 1000$ at times $t \in (8000, 8008)$.

For values of k_z reasonably close to 0.3 (such as $k_z = 0.2$) we see some oscillations but an eventual convergence to a separatrix structure as the oscillations become negligible in amplitude once the field converges onto the separatrix. These oscillations are found to have the same period as the magnetic field. The behaviour of the magnetic field concentrating onto separatrices is explained by flux expulsion. As such the transient oscillations observed in $k_z = 0.2$ and $k_z = 0.4$ are due to $\Omega(r)$ within equation (4.22). We would expect the oscillations within H_1 to decay in amplitude as less flux is contained within the regions of closed streamlines over time and this is found to be the case.

For $k_z = 0.3$ it is clear that the magnetic field's behaviour is not that of flux expulsion as the magnetic field remains in the center regions. As such a mode crossing has occurred with the new dominant mode having a non-zero imaginary time dependence. Soward showed [100] that provided certain conditions are met it is possible for the magnetic field to be contained upon resonant surfaces. One property of these surfaces is that flux expulsion

is minimised and this seems to be what we observe. In her PhD thesis [31] Courvoisier also examined the Roberts flow using an eigensolver code. She found that for $k_z = 0.3$ at $R_m = 100$ a mode crossing occurred with the dominant mode becoming oscillatory in nature for $R_m > 100$. As such my results are in agreement with those of Courvoisier.

These results suggests that the $k_z = 0.3$ mode is indeed one of Soward's "intermediate dynamo modes". H_1 becoming statistically steady appears to correspond to the point at which the magnetic field becomes concentrated upon the resonant surfaces and settles into the oscillating structure of the intermediate dynamo mode. Before this, flux expulsion acts upon the magnetic field. It thus appears that the period of H_1 is altered once convergence onto the resonant surface is achieved. Whilst the halving in the periodicity is not easily explained it is clear that the period in H_1 is being generated by the oscillations of the dominant eigenmode of the magnetic field and is thus due to physical factors rather than numerical ones.

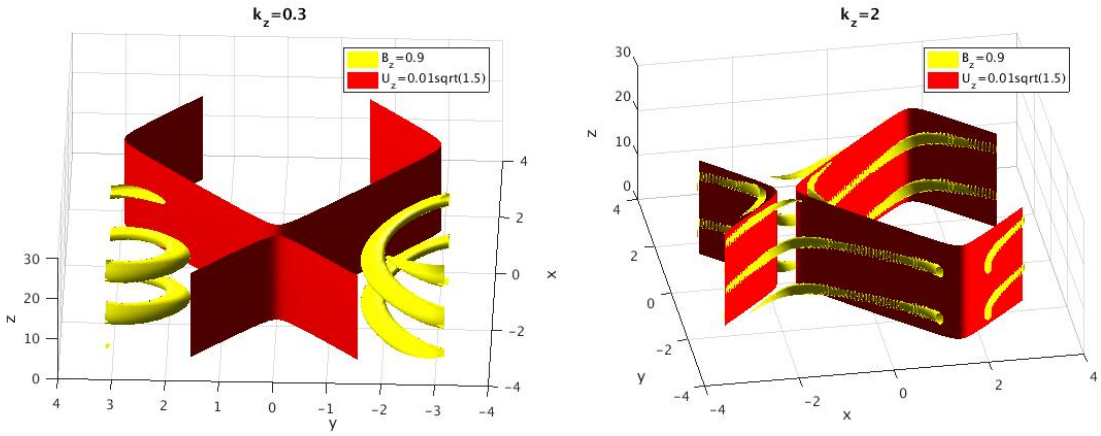

(a) Isosurface of B_z (yellow) and isosurface of u_z close to $u_z = 0$ (red) for $k_z = 0.3$. All isosurface quantities are normalised by dividing by the maximum value in the domain.

(b) Isosurface of normalised B_z (yellow) and isosurface of u_z close to $u_z = 0$ (red) for $k_z = 2$. All isosurface quantities are normalised by dividing by the maximum value in the domain.

Figure 4.14: Isosurfaces of the Roberts flow.

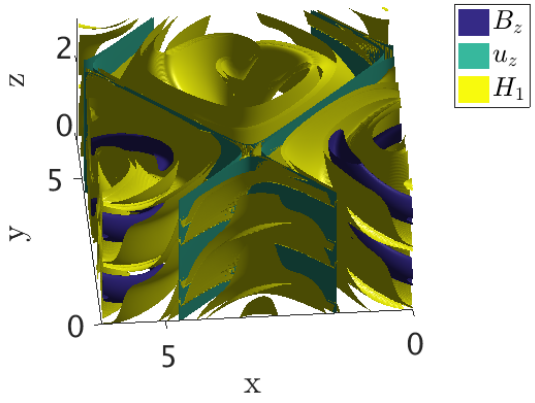

(a) 90% isosurface of B_z, 1% isosurface of u_z and 90% isosurface of H_1 for $k_z = 0.3$

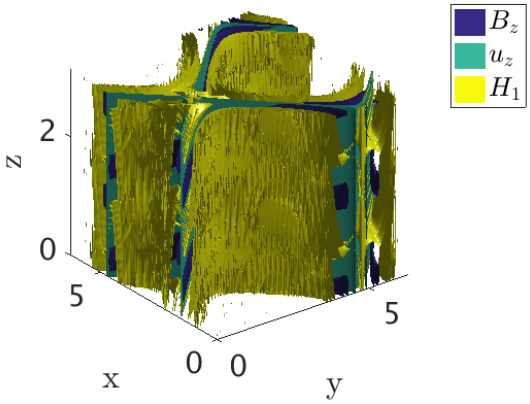

(b) 90% isosurface of B_z, 1% isosurface of u_z and 90% isosurface of H_1 for $k_z = 2$

Figure 4.15: The quantities in figure 4.14 as well as an isosurface of H_1 at a value of 0.9.

The high value of H_1 for $k_z = 0.3$, relative to the other k_z, can be understood by examining isosurfaces of the quantity. Figures 4.14 and 4.15 show isosurfaces for $k_z = 0.3$ and $k_z = 2$ at large time, with $k_z = 2$ chosen simply as an example of a separatrix structure. Figure 4.14 shows the isosurface of normalised B_z at a value of 0.9 and an isosurface of u_z at a value of $0.01\sqrt{1.5}$. For $k_z = 0.3$, B_z is confined to helical streamsurfaces whereas, for $k_z = 2$, B_z forms a separatrix structure aligned with $u_z = 0.01\sqrt{1.5}$, chosen to be close to the value $u_z = 0$. Figure 4.15 shows these two quantities, as well as the isosurface $H_1 = 0.9$. Where $k_z = 2$ the quantity H_1 is only large in the region nearby the regions in the domain where $u_z = 0$. On the other hand, for $k_z = 0.3$, H_1 is space filling and so would yield a higher volume average.

To conclude, I have shown that periodic behaviour within H_1 for $R_m = 1000$ is related to the periodicity within the magnetic field. I have shown that oscillations become negligible in amplitude at large time for k_z corresponding to separatrix modes with the period of oscillation matching that seen for the magnetic field and being explained by flux expulsion. Furthermore I have shown that the period for $k_z = 0.3$ halves at large time where previously it had matched the period of the magnetic field and appears to be one of the intermediate dynamo modes previously examined by Soward [99]. For all k_z the periodicity within the magnetic field is understood in terms of two processes, flux expulsion and the theory of resonant surfaces.

4.2.7 Alignment of J and $\mathbf{u} \times \mathbf{B}$

Consider the evolution equation for magnetic energy, (4.34), found by taking the dot product of the induction equation with $\mathbf{B}$ and integrating over a periodic geometry.

$$\frac{d}{dt}\int_V \frac{\mathbf{B}^2}{2} dV = \int_V \mathbf{J} \cdot (\mathbf{u} \times \mathbf{B}) dV - \eta \int_V \mathbf{J}^2 dV \tag{4.34}$$

$$= J_I - J_\eta \tag{4.35}$$

As the integral in the diffusive term is positive definite, growth of magnetic energy must occur due to a dominance of the first term on the left hand side over that of the second term. Furthermore, we can rewrite the first term in terms of the angle between the two quantities, ϕ

$$\int_V \mathbf{J} \cdot (\mathbf{u} \times \mathbf{B}) dV = \int_V |\mathbf{J}||\mathbf{u} \times \mathbf{B}| \cos(\phi) dV. \tag{4.36}$$

The value of J_I is therefore controlled both by the angle ϕ between the two quantities $\mathbf{J}$ and $\mathbf{u} \times \mathbf{B}$ and their magnitude.

In this section I examine the importance of ϕ within the kinematic dynamo. A number of questions are of interest. First does the volume average of the angle relate to the growth rate of the dynamo? Second, what is the relationship between $|\mathbf{J}||\mathbf{u} \times \mathbf{B}|$ and $\cos(\phi)$ within the domain? In general are they both large in the same regions or do they act against one another within significant portions of the domain and so reduce J_I? Finally; when we consider J_η also, how much do the regions of strong J_I contribute to the overall growth of the dynamo?

In this section I address each of these questions in turn. To do this I use the $R_m = 100$ simulations previously explored in section 4.2.4.

To see whether or not a volume measure of the angle ϕ relates to the growth rate I calculate a quantity analogous to H_1 and shown in equation (4.37). The result is shown within figure 4.16 with growth rate also shown. Whilst the minima of H_ϕ is close to the maxima of

the growth rate overall there does not appear to be a strong relationship between the two quantities at all. For certain the results show no evidence to suggest an increased H_ϕ results in an increased growth rate or vice versa.

$$H_\phi = \frac{1}{V}\int_V \frac{\mathbf{J}\cdot(\mathbf{u}\times\mathbf{B})}{|\mathbf{J}||\mathbf{u}\times\mathbf{B}|}dV = \frac{1}{V}\int_V \cos(\phi)dV \tag{4.37}$$

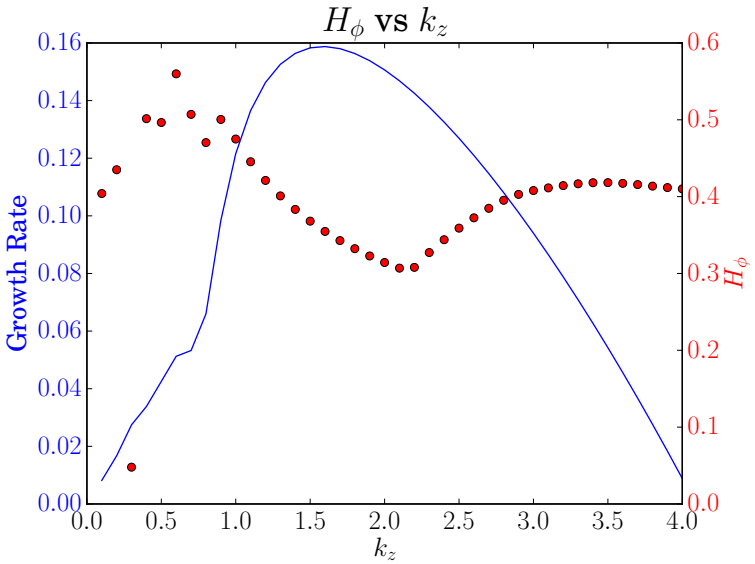

Figure 4.16: $R_m = 100$. We can see that larger growth rates do not produce more alignment on average.

It is interesting, however, that H_ϕ is positive for all k_z. However, as the growth rate is positive for all k_z also it is not unsurprising, as energy growth requires significant $\mathbf{J}\cdot(\mathbf{u}\times\mathbf{B})$. Histograms of ϕ are shown in figure 4.17. We see that predominantly the distribution is concentrated at $\pi/2$. From (4.36) we therefore see that unless these regions where $\phi \approx \pi/2$ have a large $|\mathbf{J}||\mathbf{u}\times\mathbf{B}|$ then they contribute very little to the dynamo and the majority of the work is being done in a small proportion of the domain.

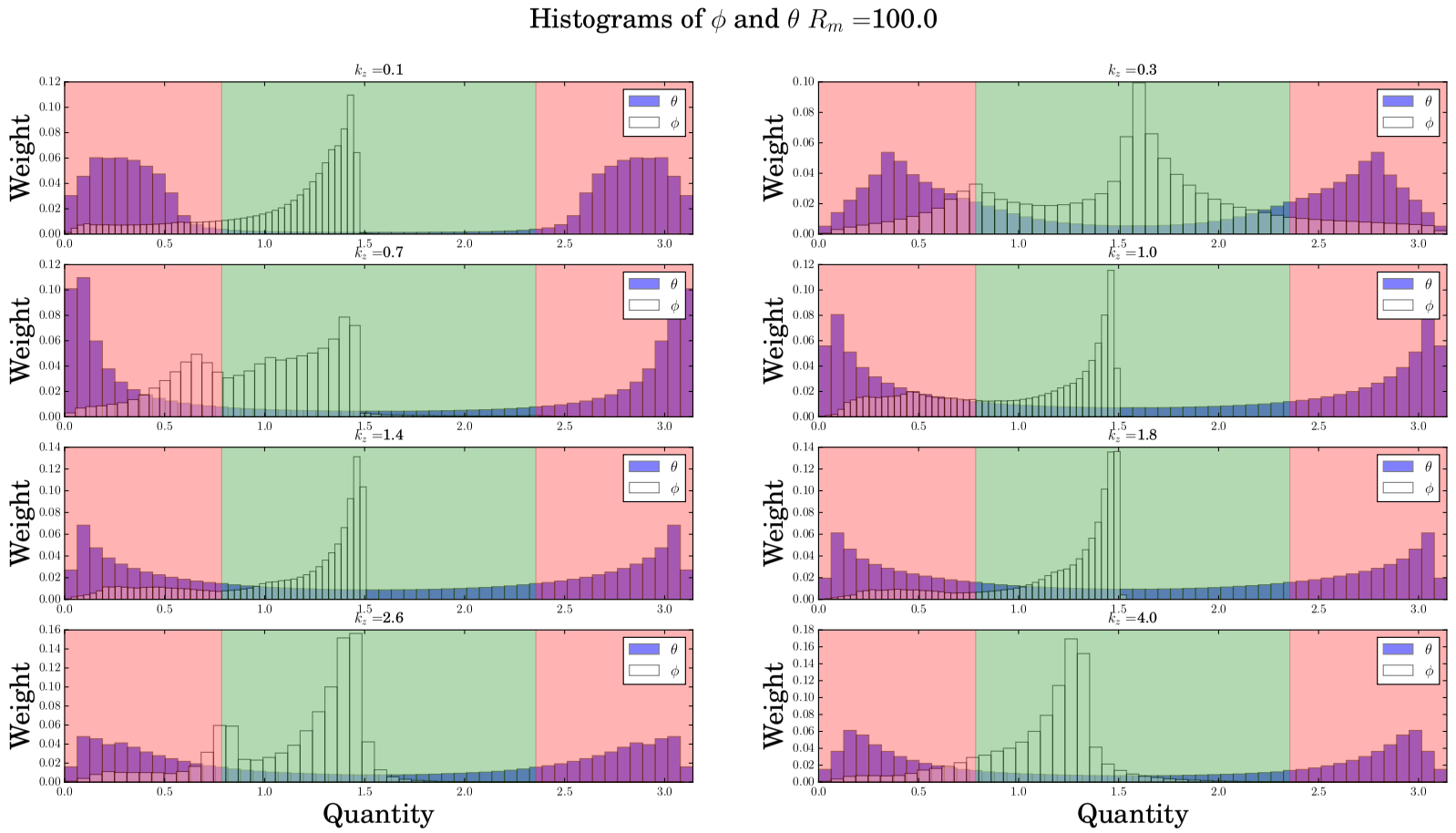

Figure 4.17: Histograms of θ and ϕ for $R_m = 100$. Red background indicates θ for which the fields are more aligned than perpendicular and green is the opposite. The histogram of ϕ has a strong peak near $\pi/2$ at each k_z with next to no alignment close to maximal alignment or anti-alignment.

Interpretation of the angle ϕ therefore also requires knowledge of the strength of $|\mathbf{J}||\mathbf{u}\times\mathbf{B}|$. I now examine the relationship between the magnitude $|\mathbf{J}||\mathbf{u}\times\mathbf{B}|$ and the angle ϕ. To do this I examine the distribution of ϕ with increasingly strong $|\mathbf{J}||\mathbf{u}\times\mathbf{B}|$ with the aim of understanding whether the regions of strongest $|\mathbf{J}||\mathbf{u}\times\mathbf{B}|$ have a preference for either aligned or perpendicular ϕ. The fraction of the field examined is defined to be the fraction (4.38) that is greater than the fraction of the maximum field strength q. The conditional probabilities for aligned (P_1), perpendicular (P_2) and neither (P_3) can then be calculated and are shown in equations (4.39)-(4.41).

$$F = \frac{|\mathbf{J}||\mathbf{u}\times\mathbf{B}|}{\max_{x,y,z}\left\{|\mathbf{J}||\mathbf{u}\times\mathbf{B}|\right\}} > q \tag{4.38}$$

$$P_1 = P(\phi < c|F > q) + P(|\phi - \pi| < c|F > q) \tag{4.39}$$

$$P_2 = P(|\phi - \pi/2| < c|F > q) \tag{4.40}$$

$$P_3 = 1 - P_1 - P_2 \tag{4.41}$$

There are 3 different parameters that need to be considered. These are the vertical wavenumber k_z, the strength of the field considered, q, and the distance we consider to be close to aligned and perpendicular, parametrised by c.

Plots of histograms at various q (figures 4.22-4.25) show peaks at 0.2 and 1.3 for a variety of k_z and q. As such $c = 0.3$ is a logical choice so that evolution of these peaks is accounted for within P_1 and P_2. $k_z = 0.3$ is omitted from all results as its different modal structure confuses the interpretation however I will comment on it at the end.

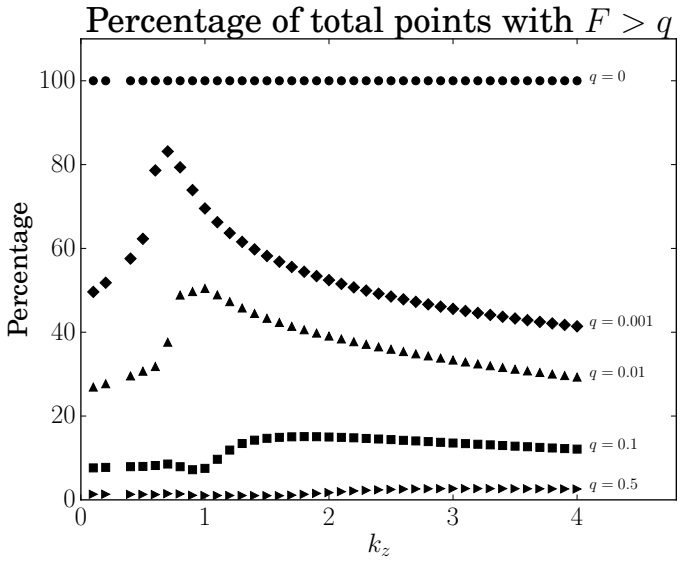

Figure 4.18: Percentage of total points with $F > q$ for varying q. We see that the majority of points have a very small q.

To understand better how (4.38) relates to k_z, in figure 4.18 I plot the percentage of field with $F > q$ for a variety of q against k_z. Furthermore, in figure 4.19 I plot histograms of (4.38) for a variety of k_z. Both show that the vast majority of points have weak values compared to the maximum value of (4.38). Matching this to the histograms in figure 4.17 shows that the vast majority of the domain has ϕ close to $\pi/2$ and $|\mathbf{J}||\mathbf{u} \times \mathbf{B}|$ weak. Although it is not necessary that this occurs at the same points there must be significant overlap.

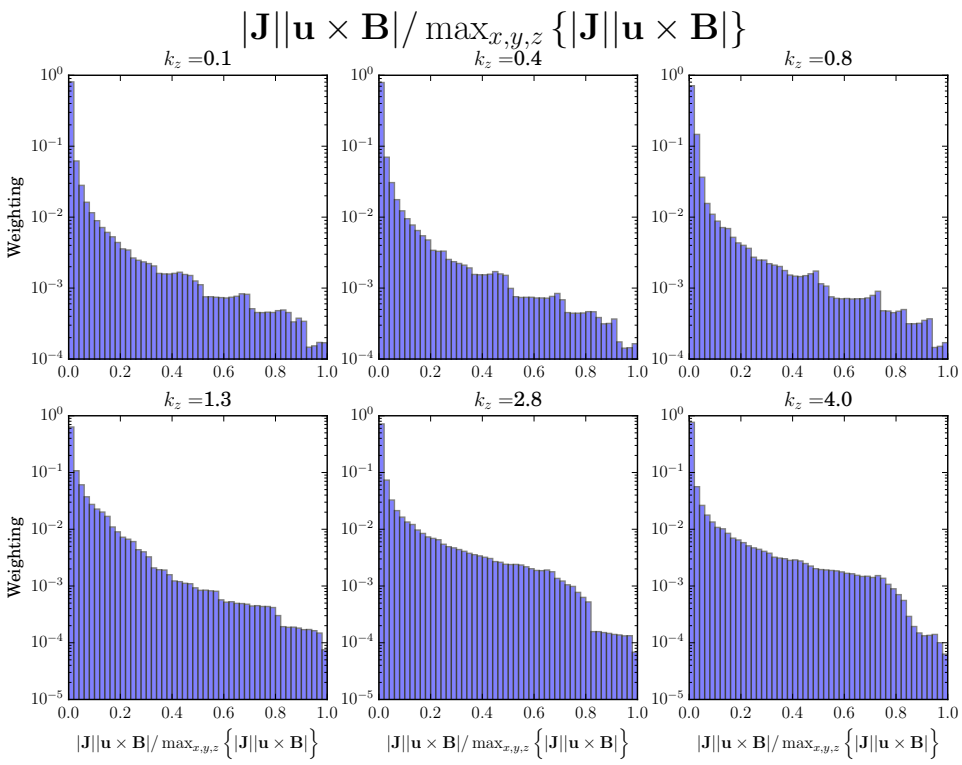

Figure 4.19: Histograms of $|\mathbf{J}||\mathbf{u}\times\mathbf{B}|/\max_{x,y,z}\left\{|\mathbf{J}||\mathbf{u}\times\mathbf{B}|\right\}$ for a variety of k_z. The vertical axis is on a logarithmic scale. We see that the majority of points have a weak value.

In figure 4.20 I show the growth rate vs k_z as well as P_1, P_2 and P_3 for a variety of q. A number of broad conclusions about the relationship between the strength of the field and the three conditional probabilities may be drawn. The first is that as we concentrate on increasingly strong field the conditional probability of aligned field increases and the conditional probability of perpendicular field decreases. This therefore shows that the perpendicular fields are concentrated in the weak values of $|\mathbf{J}||\mathbf{u}\times\mathbf{B}|$ as we previously thought. This is further illustrated in figure 4.21 which shows the aligned and perpendicular conditional probabilities plotted for a number of individual k_z against q. We see that the perpendicular fields drop to zero at low q and that the aligned fields become dominant as we concentrate on the strongest field. This is seen for all k_z. The results therefore show that regions of strong F have aligned (small) values of ϕ and that weak F correspond to perpendicular (close to $\pi/2$) values of ϕ.

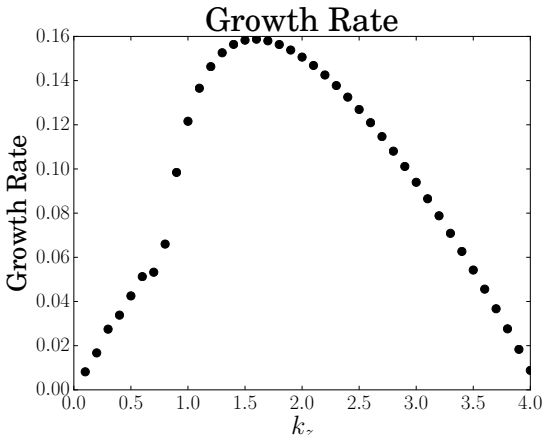

(a) Growth rate vs k_z

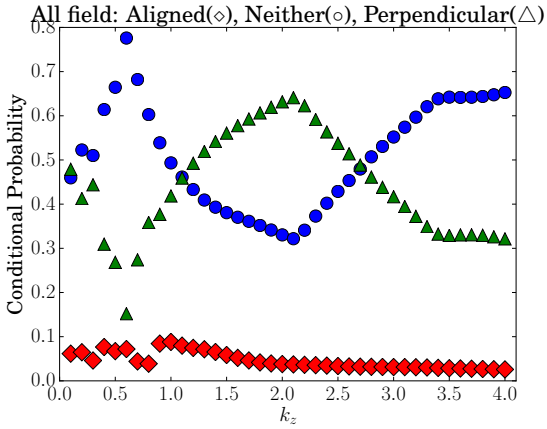

(b) $q = 0$

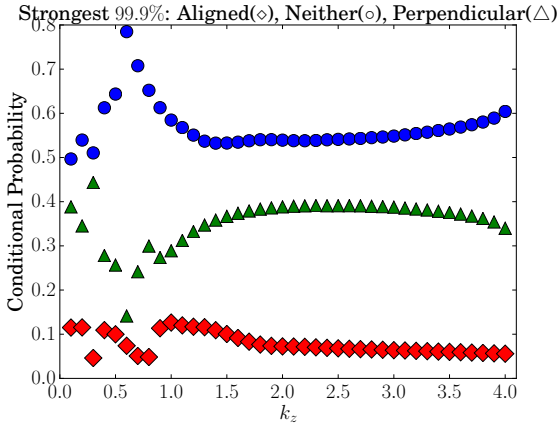

(c) $q = 0.001$

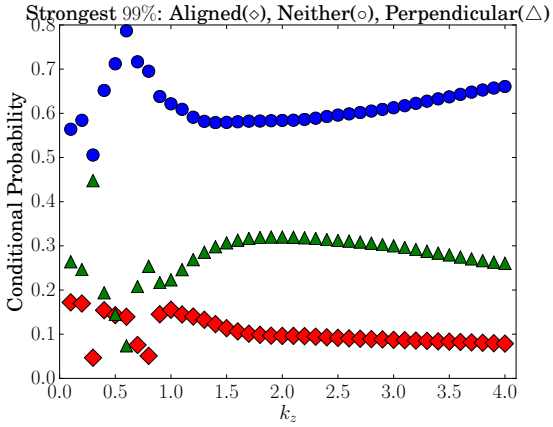

(d) $q = 0.01$

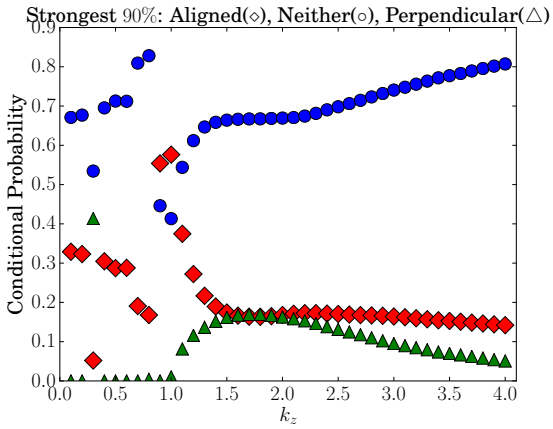

(e) $q = 0.1$

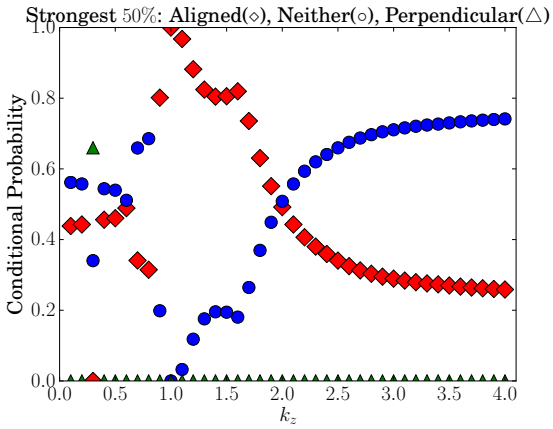

(f) $q = 0.5$

Figure 4.20: $c = 0.3$ conditional probabilities as well as growth rate.

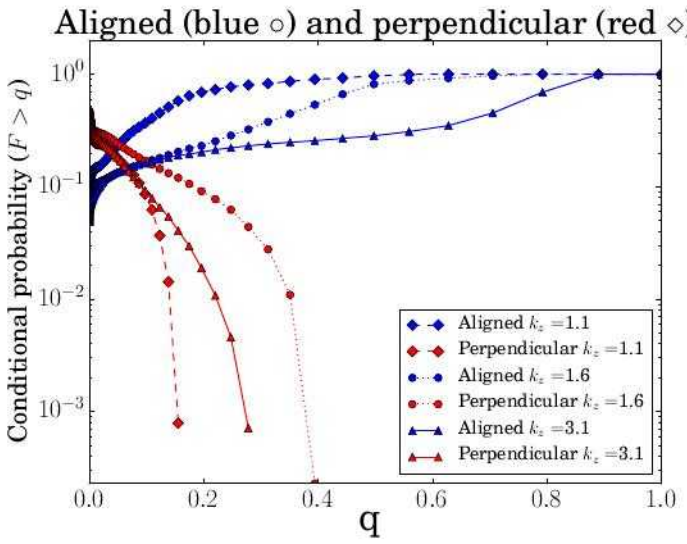

Figure 4.21: Conditional probability of aligned field and conditional probability of perpendicular field for 3 representative values of k_z. We see that as q is increased the fields become increasingly aligned with no perpendicular field.

In figures 4.22-4.25 I show histograms of the distribution of values of F. A large peak is seen in each at high ϕ and migrates to lower ϕ as we increase q. When it migrates out of the range we considered to be perpendicular ($c = 0.3$) is when we see a sharp drop in the conditional probability of the field being perpendicular in figure 4.21. As q increases we see a second peak appearing at lower ϕ. Thus as we concentrate on increasingly strong field the proportion of fields which are aligned increases. The magnitude of these two peaks varies with k_z. In particular there appears to be 3 regimes. The first is before the kink in the growth rate. Here the field has a much wider spread of ϕ with significant amounts of weighting. In the second regime, which covers the peak of the growth rate being reached and then decreasing again, there is a strong spike close to $\phi = \pi/2$ for weak field and then a spike for ϕ small for the larger values of q with the strongest field ($q > 0.5$) only having aligned fields. Finally, for large k_z where we have weak growth rates again, all but the strongest field have a peak close to $\pi/2$ but this peak migrates to lower ϕ as q increases.

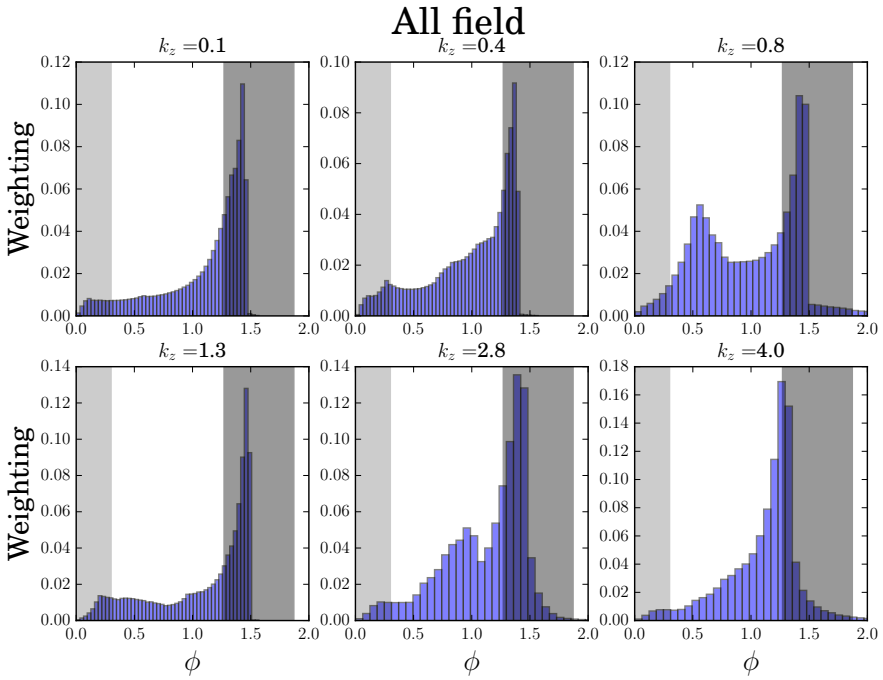

Figure 4.22: $q = 0$. Light grey background indicates aligned region, dark grey is perpendicular. For $k_z < 0.8$ there is one dominant peak but some significant spread of ϕ also. For $0.8 < \phi < 2.5$ there is one dominant peak and for $\phi > 2.5$ some spread is again seen as well as the dominant peak. The results show that the majority of points have $\mathbf{J}$ and $\mathbf{u} \times \mathbf{B}$ close to perpendicular.

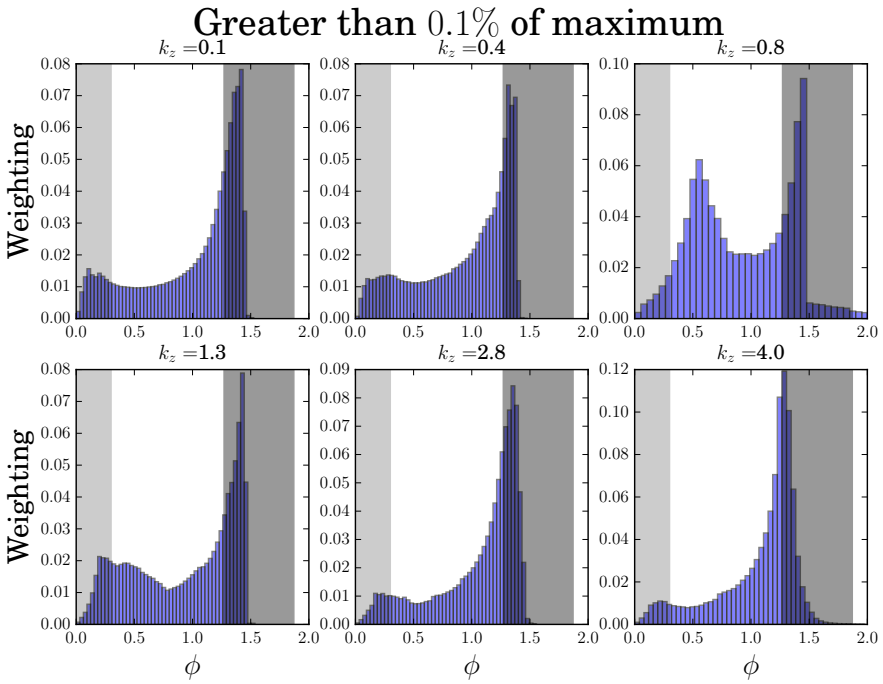

Figure 4.23: $q = 0.001$. Light grey background indicates aligned region, dark grey is perpendicular. For $k_z < 0.8$ there is one dominant peak but some significant spread of ϕ also. For $0.8 < \phi < 1.9$ there is one dominant peak and a second smaller peak at low ϕ and for $\phi > 1.9$ there is again one dominant peak near $\pi/2$. The results show that the majority of points have $\mathbf{J}$ and $\mathbf{u} \times \mathbf{B}$ close to perpendicular.

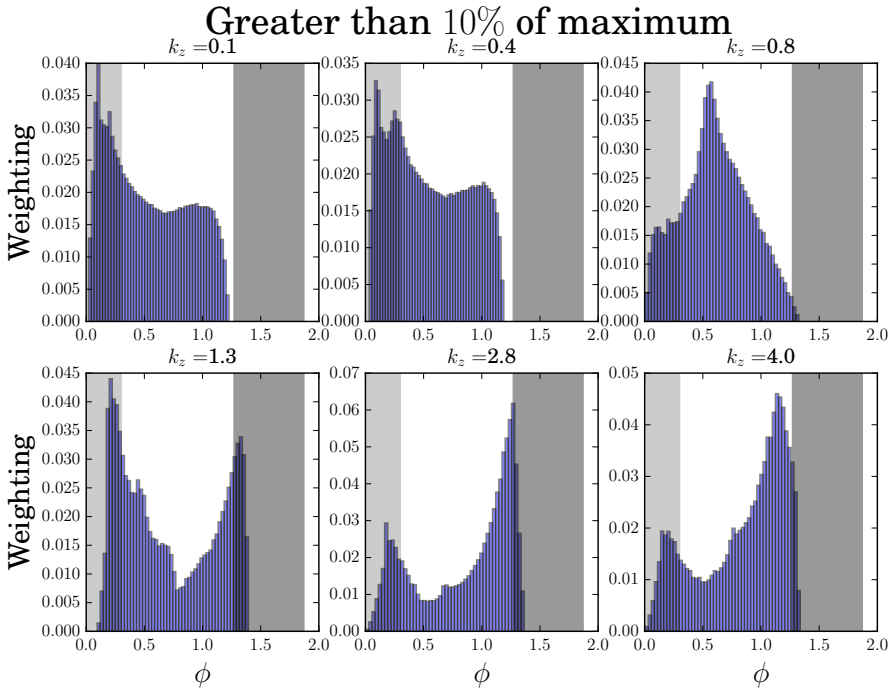

Figure 4.24: $q = 0.1$. Light grey background indicates aligned region, dark grey is perpendicular. For $k_z < 0.8$ there is a significant number of points across all values of ϕ except the values closest to $\pi/2$. For $k_z > 1.8$ there is a peak at low ϕ and one at higher ϕ with the one at higher ϕ becoming dominant at high k_z. Note that this peak has moved to lower k_z then for $q = 0.001$.

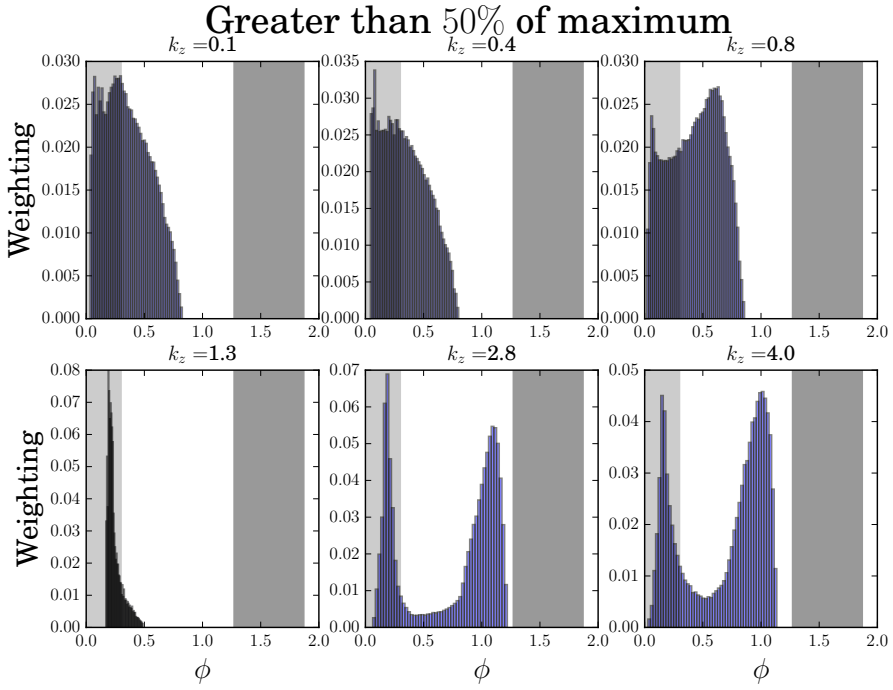

Figure 4.25: $q = 0.5$. Light grey background indicates aligned region, dark grey is perpendicular. For $k_z < 0.8$ ϕ is well distributed amongst $\phi < 0.8$. For $0.8 < \phi < 1.9$ there is one dominant peak at low ϕ and for $k_z > 1.9$ a second peak again emerges at higher k_z although this is much lower than seen for lower q.

By examining increasingly strong $|\mathbf{J}||\mathbf{u}\times\mathbf{B}|$ relative to its maximal value in the domain I have thus shown that for $k_z \neq 0.3$ the strongest values of $|\mathbf{J}||\mathbf{u}\times\mathbf{B}|$ have an increased proportion of ϕ which are close to zero. Regions where $|\mathbf{J}||\mathbf{u}\times\mathbf{B}|$ is strong and ϕ is close to zero have a large $\mathbf{J}\cdot(\mathbf{u}\times\mathbf{B})$. Equation (4.34) for the magnetic energy evolution thus shows that this means that the integrand of the first term on the left hand side will be large in regions of aligned $\mathbf{J}$ and $\mathbf{u}\times\mathbf{B}$. However this does not necessarily translate to growth of the dynamo in these regions as we still have to consider the current squared term J_η.

To examine the contribution of these regions to growth of the dynamo I plot contours of ϕ in figure 4.26; contours of the integrand of the right side of (4.34) divided by its infinity norm in figure 4.27 and contours of the infinity norm of $\mathbf{B}^2$ in figure 4.28. We see that the regions where ϕ is close to zero match well with the regions where the energy integrand is close to its maximal value. One possible reason for this can be seen in figure 4.28 where we see that these regions are the regions where the magnetic field is strongest. Regions of aligned $\mathbf{J}$ and $\mathbf{u}\times\mathbf{B}$ thus provide a large contribution to the growth of the dynamo and are thus of vital importance.

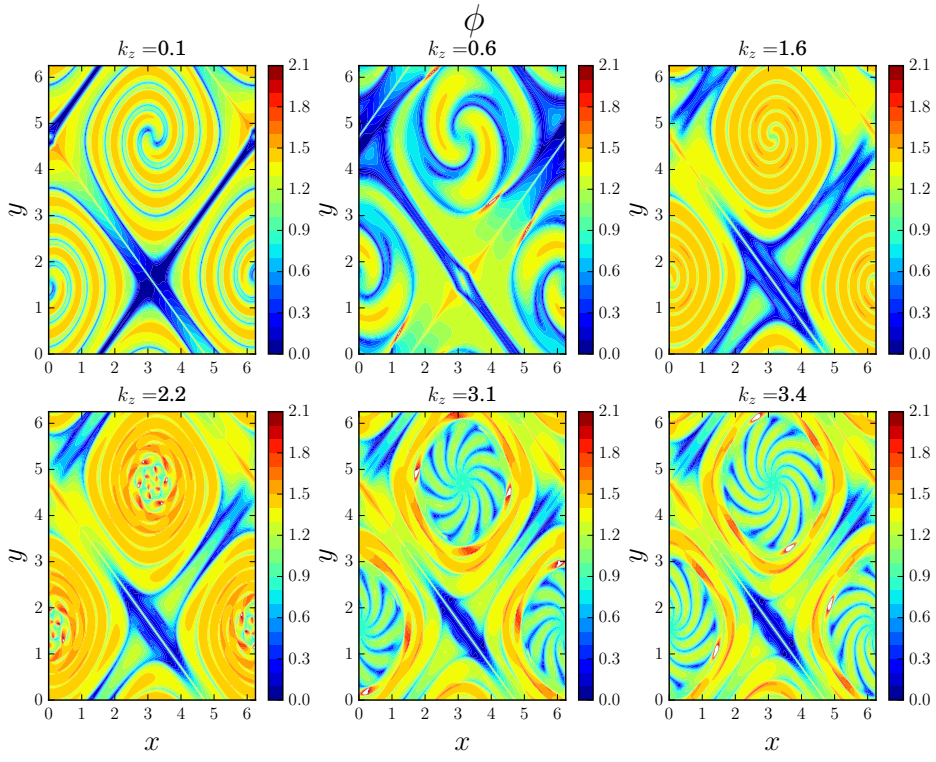

Figure 4.26: $z = 0$ contours of ϕ for a variety of k_z.

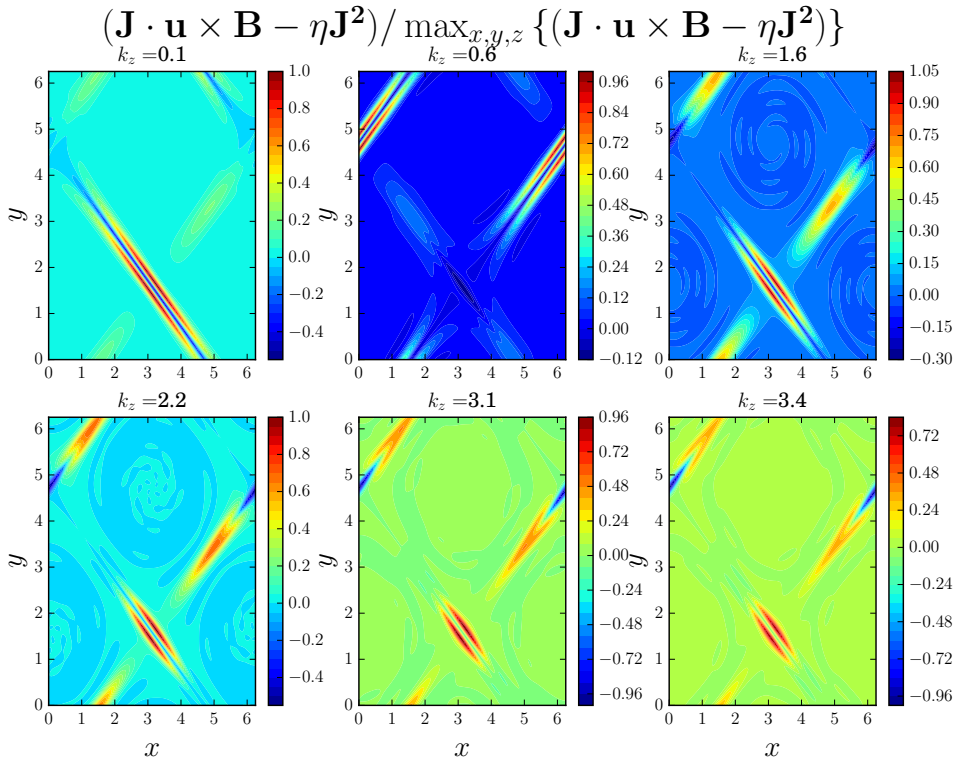

Figure 4.27: $z = 0$ contours of $(\mathbf{J}\cdot\mathbf{u}\times\mathbf{B}-\eta\mathbf{J}^2)/\max_{x,y,z}\left\{(\mathbf{J}\cdot\mathbf{u}\times\mathbf{B}-\eta\mathbf{J}^2)\right\}$ for a variety of k_z.

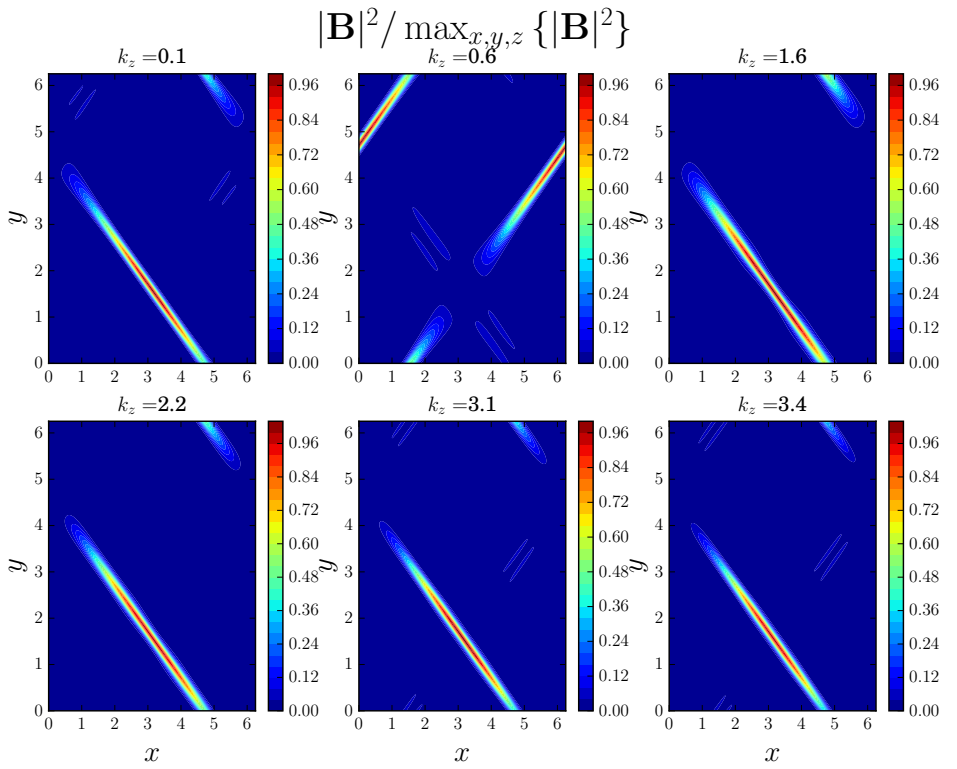

Figure 4.28: $z = 0$ contours of $\mathbf{B}^2$ for a variety of k_z.

Finally I make some notes on $k_z = 0.3$. As the magnetic field structure is different for this

mode it was omitted from the above analysis so as to not confuse interpretation. In figure 4.29 I show the conditional probabilities of aligned and perpendicular fields against q for a number of k_z. We see that for $k_z = 0.3$ the probability of aligned goes to zero as we focus on the strongest values of F and the values of perpendicular go to one. This is the opposite behaviour to that seen for all other k_z.

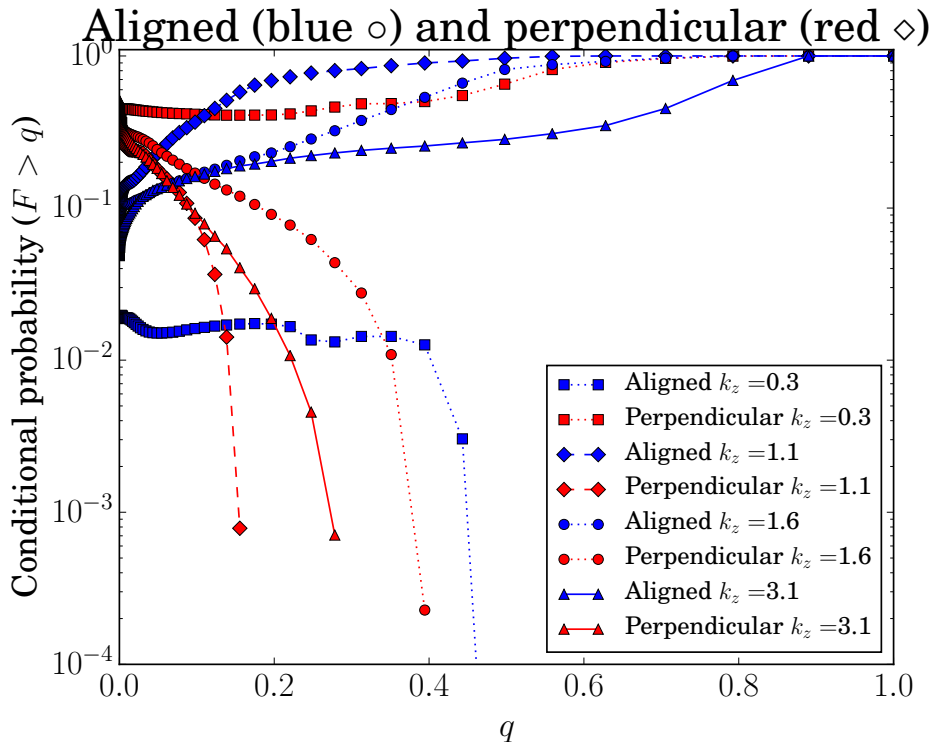

Figure 4.29: Conditional probability of aligned and perpendicular field for increasingly strong F. $k_z = 0.3$ curves have square points and behave differently to the other values.

In figure 4.30 I show $z = 0$ contour plots of F (a), ϕ (b), $(\mathbf{J}\cdot(\mathbf{u}\times\mathbf{B}) - \eta\mathbf{J}^2)/\max_{x,y,z}\left\{\mathbf{J}\cdot(\mathbf{u}\times\mathbf{B}) - \eta\mathbf{J}^2\right\}$ (c). We again see that the behaviour for $k_z = 0.3$ is different to that seen for all other k_z. Instead of regions of aligned ϕ ($\phi \approx 0$) combining with regions of strong $|\mathbf{J}||\mathbf{u}\times\mathbf{B}|$ to give the regions of strong energy growth instead it is the regions of $\phi \approx 0$ combining with mild values of $|\mathbf{J}||\mathbf{u}\times\mathbf{B}|$ to give the regions of strong energy growth. Regions of strong F therefore correspond to regions of perpendicular $\mathbf{J}$ and $\mathbf{u}\times\mathbf{B}$ and thus these regions do not provide large contributions to the energy growth.

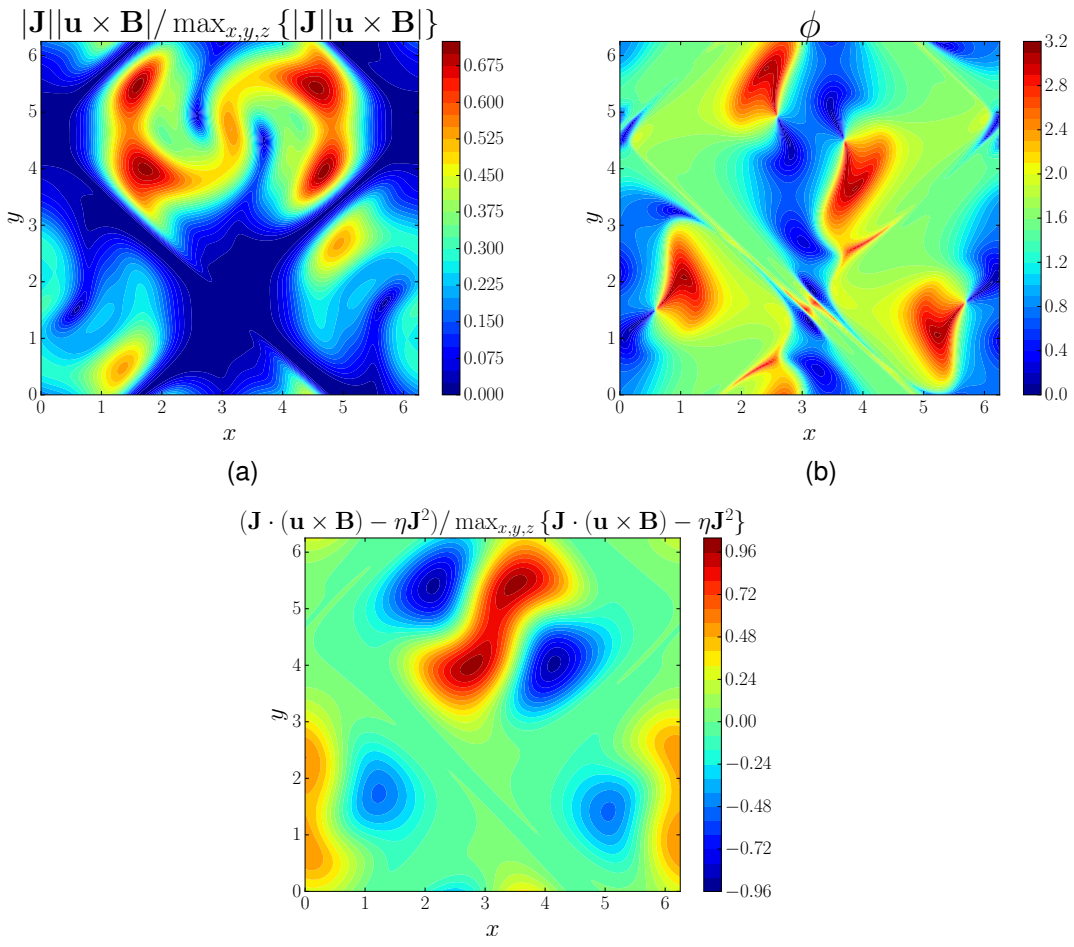

Figure 4.30: F (a), ϕ (b), $(\mathbf{J}\cdot(\mathbf{u}\times\mathbf{B})-\eta\mathbf{J}^2)/\max_{x,y,z}\left\{\mathbf{J}\cdot(\mathbf{u}\times\mathbf{B})-\eta\mathbf{J}^2\right\}$ (c). The regions of strong F are not in the regions corresponding to aligned ϕ as was the case for all other k_z but are instead in regions of perpendicular ϕ. As such, the regions of strong $\mathbf{J}\cdot(\mathbf{u}\times\mathbf{B})$ come from the product of intermediate values of $|\mathbf{J}||\mathbf{u}\times\mathbf{B}|$ with strongly aligned and anti-aligned values of $\cos(\phi)$. This can be seen by comparing the strongly red region of figure (c) to the same region in the other two plots.

To summarise: In this section I have examined the alignment of $\mathbf{J}$ and $\mathbf{u}\times\mathbf{B}$ for the Roberts flow with $R_m = 100$ at a variety of vertical wavenumbers. I have shown that there is no relationship between the volume averaged $\cos(\phi)$ and the growth rate. Furthermore I have shown that across the entire domain and all strengths of $|\mathbf{J}||\mathbf{u}\times\mathbf{B}|$ ϕ is preferentially perpendicular. However in the regions where $|\mathbf{J}||\mathbf{u}\times\mathbf{B}|$ is strongest this relationship breaks down and in fact a large proportion of ϕ are close to zero. I then showed that these regions with strong $|\mathbf{J}||\mathbf{u}\times\mathbf{B}|$ and small ϕ are vital to the workings of the dynamo due to their contributions to J_I within the induction equation.

4.2.8 Summary of Results for the Roberts Flow

In this section I have examined numerical simulations of kinematic dynamo action for the Roberts flow for both $R_m = 100$ and $R_m = 1000$. I have shown that for both R_m the alignment measures H_1 and H_2 clearly show when changes to the magnetic fields dominant eigenmode occur. I therefore showed that both are useful as a diagnostic tool for highlighting structural changes to the magnetic field within kinematic dynamo simulations. I have also shown that oscillations which appear in H_1 during $R_m = 1000$ runs for $k_z \approx 0.3$ are due to movement of the magnetic field upon resonant surfaces.

Furthermore, I have shown that the amount of alignment between $\mathbf{J} = \nabla \times \mathbf{B}$ and $\mathbf{u} \times \mathbf{B}$ is dependent upon the strength of $|\mathbf{J}||\mathbf{u} \times \mathbf{B}|$. I have shown that regions of strong $|\mathbf{J}||\mathbf{u} \times \mathbf{B}|$ and $\phi \approx 0$ match well for $k_z \neq 0.3$. The behaviour of $k_z = 0.3$ is different due to the magnetic field not being confined to channels but instead existing on resonant surfaces in the center regions of the flow. Alignment between $\mathbf{J}$ and $\mathbf{u} \times \mathbf{B}$ is therefore crucial to the workings of the dynamo as it is the regions of the domain where these two quantities are aligned where the positive contributions to the change in magnetic energy occur.

In subsequent sections I will focus upon the alignment between $\mathbf{u}$ and $\mathbf{B}$ and the relationship between this and the magnetic field structure as I believe this to be the most interesting result. To do this I will consider a number of different kinematic dynamos increasingly different from the Roberts flow to see whether alignment between flow and field continues to indicate changes to the magnetic field.

4.3 Alignment within the Cat's Eye Flow

4.3.1 Introduction and Flow Geometry

In section 4.2 I showed how alignment can be a useful tool in identifying changes to the structure of the dominant eigenmode in kinematic dynamo simulations of the Roberts flow. I now test whether this is also true for a second kinematic dynamo closely related to the Roberts dynamo. The flow has a form (4.42) and a structure as seen in figure 4.31 and is

referred to as the Cat's Eye Flow.

$$\mathbf{u} = \sqrt{\frac{3}{5}} \begin{pmatrix} 2\sin(y) \\ \sin(x) \\ \cos(x) - 2\cos(y) \end{pmatrix} \tag{4.42}$$

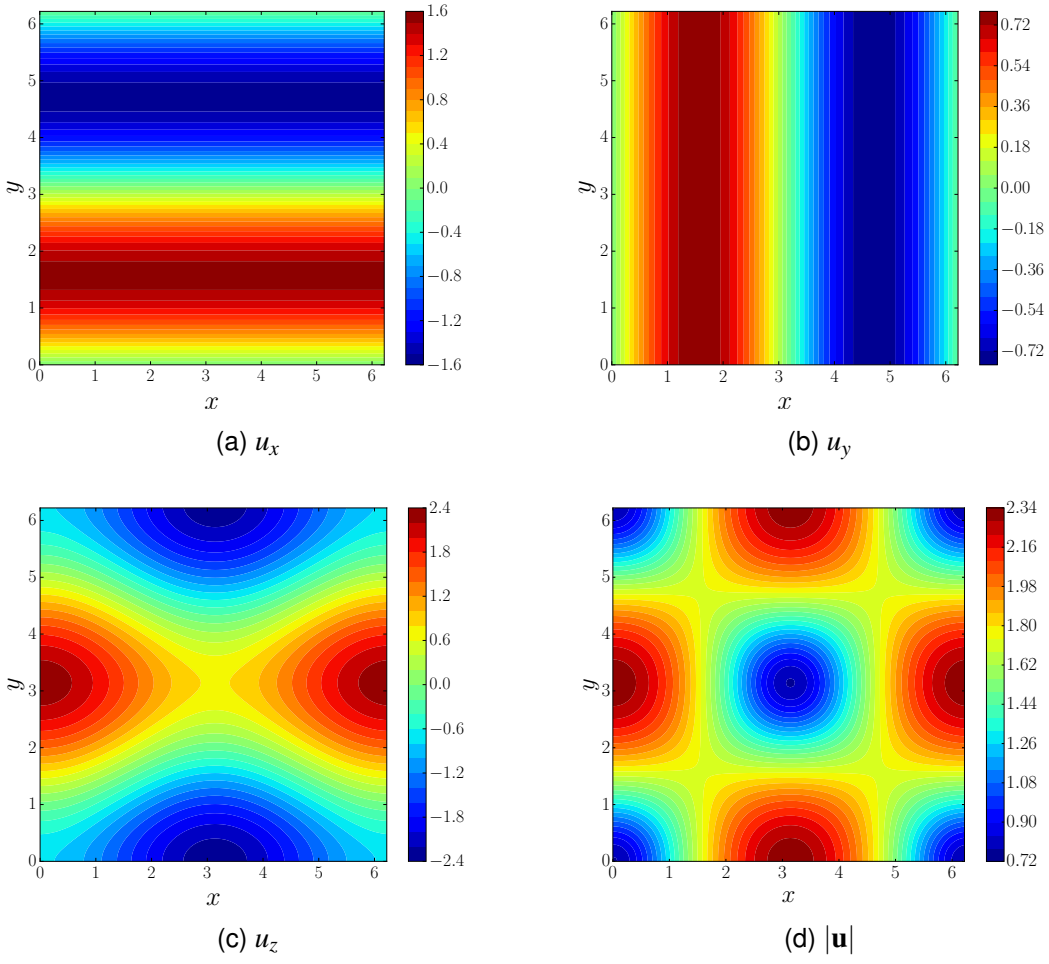

(a) u_x (b) u_y

(c) u_z (d) $|\mathbf{u}|$

Figure 4.31: All 3 components of the flow as well as $|\mathbf{u}| = \sqrt{u_x^2 + u_y^2 + u_z^2}$.

The flow has previously been examined by Childress and Gilbert [29] and by Courvoisier et al. [30]. The flow has the useful property of having a variety of different magnetic field structures as the vertical wavenumber is varied. This allows us to examine the relationship between magnetic field structures and changes to alignment for more magnetic field structures than was possible for the Roberts flow.

In figure 4.32 I show figure 9 from [30]. This figure shows the four different structures of the magnetic field's dominant eigenmode observed by Courvoisier et al within [30]. For

$k_z = 3.8$ and $k_z = 0.001$ the dominant eigenmode has a long thin structure that lies in the channels between the regions of strong flow. This structure is sometimes referred to as separatrix-like. For $k_z = 1.0$ and $k_z = 0.3$ the magnetic field is concentrated in large Ponomarenko modes of different sizes that lie within the regions of strong flow. We therefore have a number of different structures we can examine.

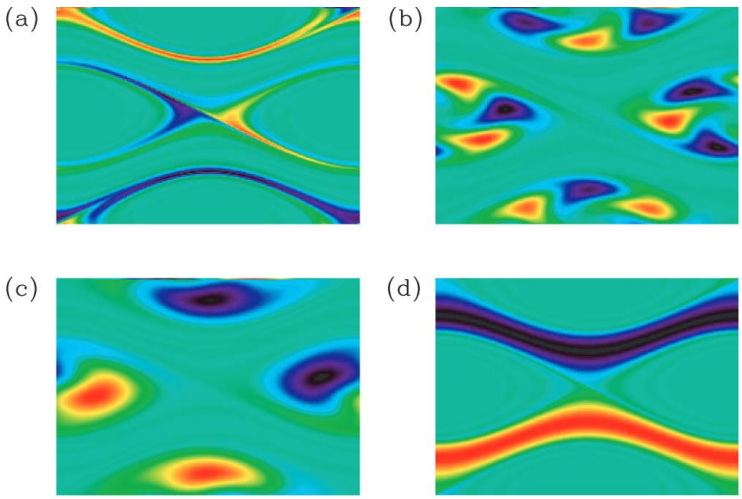

Figure 9. Magnetic field structure for $R = 1000$ and (a) $k = 3.8$ (cat's eye mode), (b) $k = 1.0$ (Ponomarenko mode, $m = 3$), (c) $k = 0.3$ (Ponomarenko mode, $m = 1$), and (d) $k = 0.001$ (α-effect mode). In each case B_z is plotted in the (x, y)-plane with positive field yellow/red and negative field blue/black.

Figure 4.32: Figure 9 from [30]. The plot shows the z component of the magnetic field for $k_z = [3.8, 1.0, 0.3, 0.001]$. In each case the magnetic field structure is different.

As with the previous section I use H_1 and H_2 to measure the alignment within the dynamo.

$$H_1 = \frac{1}{V}\int_V \frac{|\mathbf{u}\cdot\mathbf{B}|}{|\mathbf{u}||\mathbf{B}|}dV \qquad (4.43a) \qquad H_2 = \frac{\int_V |\mathbf{u}\cdot\mathbf{B}|dV}{\sqrt{\int_V \mathbf{u}^2 dV \int_V \mathbf{B}^2 dV}} \qquad (4.43b)$$

These quantities are measured for the various modal structures as k_z is varied to examine whether the changing structure can be seen from the measures of alignment alone. To examine the changes with k_z I run simulations for $k_z \in (0.001, 8)$ with $k_z = 0.001$ standalone to show the different mode structure at extremely low k_z. The $k_z \in (0.2, 2)$ are then in increments of 0.1 and $k_z \in (2, 8)$ are in increments of 0.4. The simulations are run with $R_m = 1000$ to be in agreement with the authors of [30] and a spatial resolution of 128^2. A second order Adams-Bashforth: Adams-Moulton method with diffusion being treated using a Crank-Nicholson method is used for timestepping, see section 2.4.2.

4.3.2 Results

In figures 4.33a and 4.33b I show plots of H_1 and H_2 vs k_z. For H_1 we immediately see that there appears to be a split: before $k_z < 1.9$ the values are about 0.80, except 0.2 which is 0.73 and 0.001 which is of a similar value to the higher k_z. For $k_z \geq 1.9$ H_1 decreases from 0.67 to 0.60 where it appears to asymptote. The distinction is again seen with H_2 however 0.2 and 0.8 appear to be outliers.

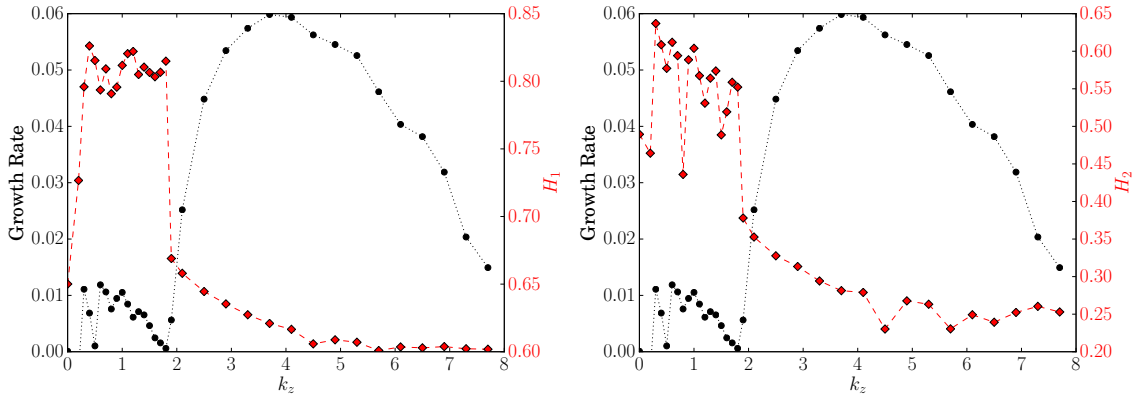

(a) Plot of H_1 vs k_z

(b) Plot of H_2 vs k_z.

Figure 4.33

To understand the difference between the regimes seen in H_1 in figure 4.34 I plot $|\mathbf{B}|/\sqrt{ME}$ for a variety of k_z. We see that at $k_z = 1.9$ the magnetic field transitions from having a Ponomarenko mode structure that exists in the regions of strong flow seen in figure 4.31 to separatrix structures existing in the channels between the strong regions. As the structure transitions from Ponomarenko modes to separatrix modes the Ponomarenko modes get smaller in size and more numerous.

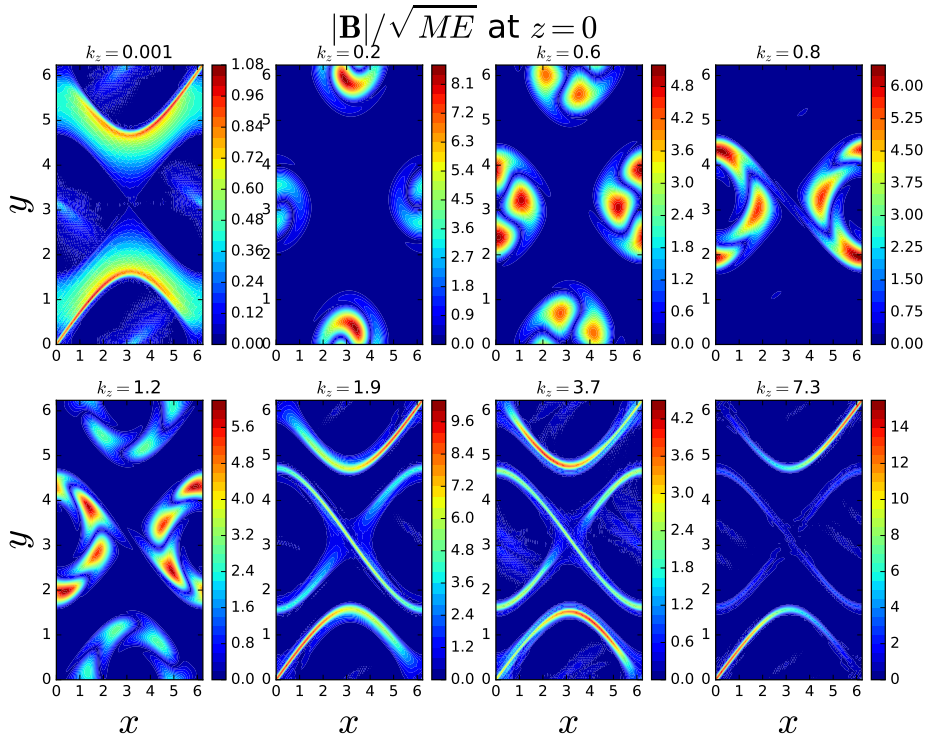

Figure 4.34: $|\mathbf{B}|/\sqrt{ME}$ for $k_z \in (0.001, 7.3)$. We see a variety of different mode structures as k_z is varied. At $k_z = 1.8$ the structure of the mode changes from large scale Ponomarenko modes to separatrix modes.

Comparing figure 4.34 to figures 4.33a and 4.33b we see that H_1 and H_2 both yield information on the structure. The jump between the two regimes for H_1 shows that the type of structure is different between the two regimes and thus identifies the values which give Ponomarenko modes and those which give separatrix modes. On the other hand H_2 shows a decrease before the jump and thus also shows that the Ponomarenko modes are becoming more separatrix like as we approach the critical k_z where the structure change occurs.

Examining the $k_z = 0.2$ subplot within figure 4.34 explains why H_1 is weaker for $k_z = 0.2$ in figure 4.33a. We see that the modes are smaller and only present at high strength in two regions rather than four. As well as this we see that the growth rate is negative and so dynamo action does not occur, as a result we do not expect the the magnetic field structure to evolve in the same manner. For $k_z = 0.8$ we also see that the modes at $(x = \pi, y = 0)$ and $(x = \pi, y = 2\pi)$ are missing. This removal appears to skew the results of H_2 even though the modal structure of the modes still present has not changed. For $k_z = 0.001$ we see the α effect mode previously seen within [30]. This mode exists in the

channels between the regions of strong flow and is separatrix like. As such its values being consistent with those of the Cat's Eye modes at higher k_z further supports the conclusion that alignment measures are a useful tool for identifying the difference between structures.

To summarise: the aim of examining the Cat's Eye flow was to test whether or not the measures of alignment continue to be a useful diagnostic tool in identifying changes to modal structure as k_z is varied for a flow other than the Roberts flow. I have shown that both H_1 and H_2 clearly indicate where changes to modal structure occur as k_z is varied, supporting the results I have previously shown for the Roberts flow. The result shows that the measures clearly distinguish between the large modes in the centre regions of the flow and elongated structures within the channels between the centre regions of the flow. As such the measures are useful to quickly identify large changes in modal structure however they are not precise enough to distinguish between similar structures and so can only be reliably used to distinguish completely different structures rather than, for example, a gradual elongation of a particular structure.

4.4 Alignment within a Three Dimensional Steady Flow

4.4.1 Introduction

So far I have considered flow profiles which are independent of z. This then leaves the vertical wavenumber k_z as a free parameter to be assigned. Within this section I instead consider a fully three dimensional flow profile. The magnetic field generated therefore does not only depend upon the z direction via an exponential but is instead itself also fully three dimensional.

I examine the Kolmogorov flow (see [29] and [45]) given in equation (4.44). This is chosen due to its fast computational speed relative to the more commonly examined 111 ABC flow. As the results so far have shown that the main benefit of examining H_1 (4.45a) and H_2 (4.45b) is in identifying changes to the magnetic field structure as k_z is varied, a problem that does not exist for 3D flows, the aim is to identify whether the usefulness of alignment is restricted only to $2.5D$ kinematic dynamos.

$$\mathbf{u} = \begin{pmatrix} \sin(z) \\ \sin(x) \\ \sin(y) \end{pmatrix} \tag{4.44}$$

$$H_1 = \frac{1}{V}\int_V \frac{|\mathbf{u}\cdot\mathbf{B}|}{|\mathbf{u}||\mathbf{B}|}dV \qquad (4.45a) \qquad H_2 = \frac{\int_V |\mathbf{u}\cdot\mathbf{B}|dV}{\sqrt{\int_V \mathbf{u}^2 dV \int_V \mathbf{B}^2 dV}} \qquad (4.45b)$$

4.4.2 Flow Geometry and Numerics

The flow has 8 stagnation points in the fundamental domain $x, y, z \in (-\pi, \pi)$ where $-\pi$ and π are the same due to the periodic boundary conditions. Calculating the Jacobian, J, of the flow

$$J_{ij} = \frac{\partial u_i}{\partial x_j}$$

at each of the eight stagnation points and then calculating the eigenvalues and eigenvectors reveals that they are split into two broad categories. The first group, with similar properties to the α type stagnation points of the 1:1:1 ABC flow of Dorch in [35] and also identified by Galloway and O'Brian in [44] for the Kolmogorov flow, have one positive eigenvalue (the unstable eigendirection) and two negative ones (stable eigendirections). These are at $(0,0,0)$, $(0,-\pi,-\pi)$, $(-\pi,0,-\pi)$ and $(-\pi,-\pi,0)$ respectively where $-\pi$ is the same point as π due to periodicity. These stagnation points thus have one eigendirection where streamlines diverge and a plane perpendicular to this eigendirection where streamlines converge. The other four stagnation points, $(0,0,-\pi)$, $(0,-\pi,0)$, $(-\pi,0,0)$ and $(-\pi,-\pi,-\pi)$, behave in a similar manner to the β type stagnation points of [35] in that they have two unstable eigendirections and one stable eigendirection. I will refer to these two groups of eigenvalues as α and β type stagnation points respectively. The unstable eigendirection of the α type stagnation points are connected to the stable eigendirection of the β type stagnation points by heteroclinic trajectories.

The Kolmogorov flow has been investigated briefly by Galloway and Proctor in [45] and again by Galloway and O'Brian in [44]. Line C within figure 4.35, taken from [45], shows the growth rate of the Kolmogorov flow versus R_m. This curve is suggestive that the flow is

a fast dynamo although the growth rate has yet to asymptote. In [44] the authors show that the flux accumulates at α type stagnation points in two cigars, each of opposite polarity. This will be examined further using my numerical results in this section.

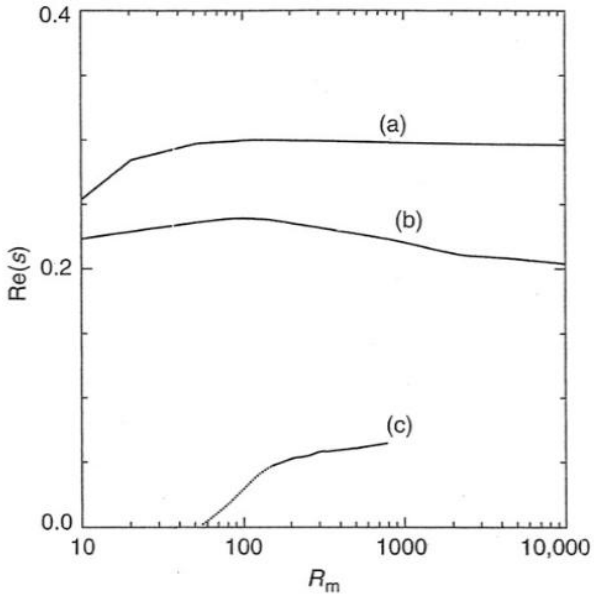

Figure 4.35: Figure 2 of [45] showing growth rates for three kinematic dynamos. Curve (c) is for the Kolmogorov flow.

The code used for this section uses the Adams-Bashforth: Crank Nicholson scheme detailed within section 2.4.1. Rather than taking advantage of Fourier mode couplings the code instead calculates $\mathbf{u} \times \mathbf{B}$ in real space, computes a fast Fourier transform, and then computes $\nabla \times (\mathbf{u} \times \mathbf{B})$ within Fourier space at each timestep and is thus a pseudo-spectral method rather than the fully spectral method used to examine the Roberts and Cat's eye flows. The code is initially run with a spatial resolution of 64^3 and the final field is then used as an initial condition for a run using 128 points in each direction which is ran for an additional 100 time units (20000 timesteps). As a check, curve (c) from 4.35 was replicated at 64^3 using my code with the results being in good agreement. All runs are performed with $R_m = 100$.

4.4.3 Results

To examine the relationship between alignment and magnetic field structure I begin by examining the time series of the two quantities H_1 and H_2. Figure 4.36 shows the growth rate (black curve, left axis) and the two alignment quantities (right axis) for the $n = 128$

run. At this scale the alignment quantities look uninteresting as they appear to saturate to a steady state. However upon zooming into each of the curves we see that each has a time dependent periodicity.

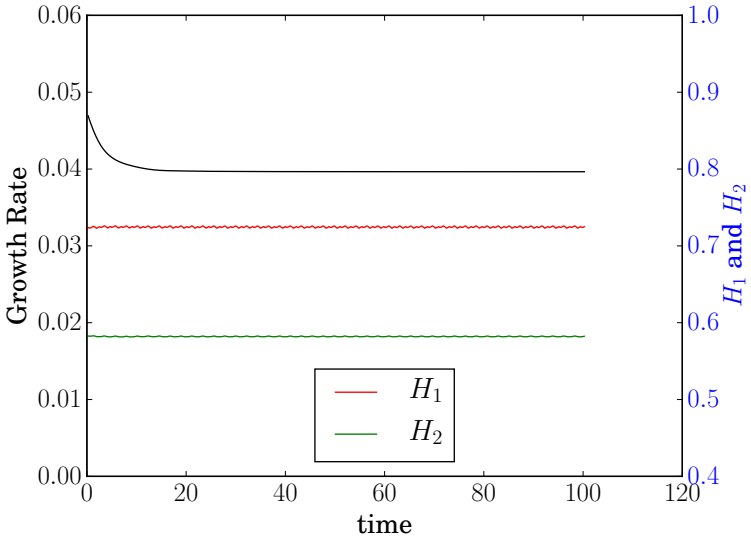

Figure 4.36: Growth rate (black curve, left axis) and the two alignment quantities (right axis) for the $n = 128$ run. The growth rate has saturated and H_1 and H_2 at this scale appear steady however each has small oscillations.

Figure 4.37 shows each of the alignment quantities but for a smaller range on the vertical axis. Both have a small oscillation which has a well defined periodicity. I now examine how this periodic behaviour relates to the magnetic field structure.

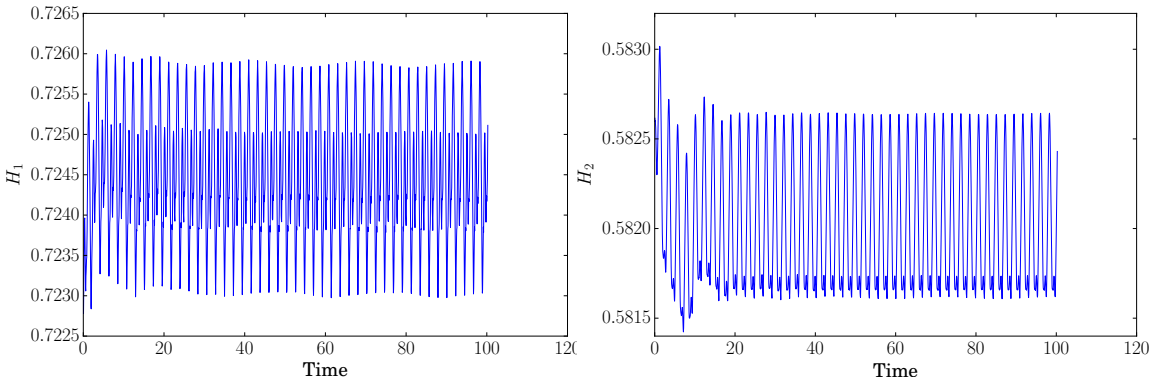

(a) Plot of H_1 vs time, a strong periodic behaviour is observed.

(b) Plot of H_2 vs time. A strong periodic behaviour is observed.

Figure 4.37: H_1 and H_2 for the entirety of the 128^3 run. A strong periodic behaviour is observed.

To examine the 3D structure I look at isosurfaces of the magnetic field during an oscillation. In figure 4.38 I show the time interval $t \in (20, 24)$ where I examine snapshots of the

magnetic field. For H_1 I find that the large maxima and minima correspond to changing magnetic field structure but the remaining 3 peaks were not seen to correspond to any clear structure changes. As such the small changes in amplitude for H_1 are more complicated than can be explained by the magnetic field morphology alone. I find however that evolution toward and away from maxima of H_2 match well with changes to the magnetic field which I will now outline.

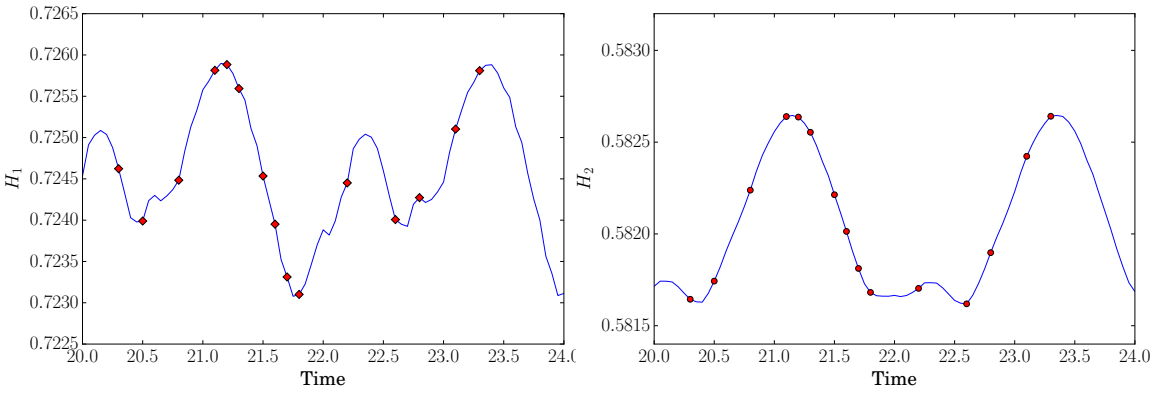

(a) Plot of H_1 vs time for $t \in (20, 24)$.

(b) Plot of H_2 vs time for $t \in (20, 24)$.

Figure 4.38: A snapshot of the time series seen in figure 4.37. Red points indicate the points which I later plot isosurfaces of the magnetic field.

In figures 4.39-4.42 I show 65% isosurfaces of $|\mathbf{B}|$ (purple cigars) and 10% isosurfaces of $|\mathbf{u}|$. Both are normalised by dividing by the largest value in the domain so that an $X\%$ isosurface has the clear interpretation of being the regions of the domain containing the field stronger than $X\%$ of the maximum field strength. The 4 separate figures correspond to the 4 different stages of the magnetic field evolution.

In figure 4.39 I show the first stage between $t = 20.3$ and $t = 21.1$. This corresponds to going from the base of the maxima of H_2 to the maxima itself. The isosurfaces show that as the maxima of H_2 is approached one cigar gets shorter and thinner.

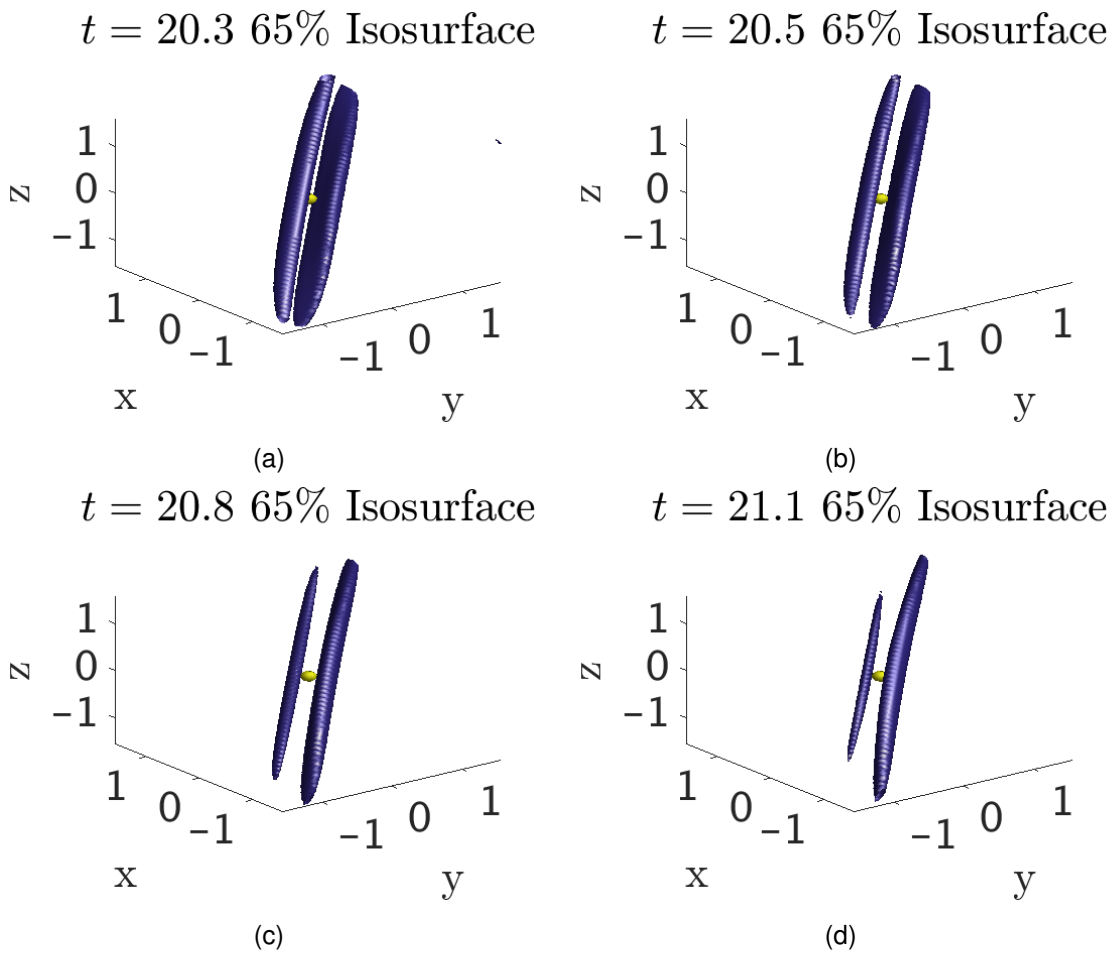

(a) (b) (c) (d)

Figure 4.39: 65% isosurfaces of $|\mathbf{B}|$ and 10% isosurface of $|\mathbf{u}|$ as a peak in H_2 is approached. We see that one of the magnetic field cigars shrink considerably.

In figure 4.40 I show times $21.2 - 21.6$ which correspond to moving off of the maxima of H_2. Here the small magnetic field cigar becomes stretched out in the direction perpendicular to the principle direction of the cigar. As we enter the relatively flat section of the plot of H_2 between the two maxima (figure 4.41) the small cigar then becomes stretched out along its main axis until it becomes approximately the same length as the other cigar. Finally as we approach the second maxima (figure 4.42) we again see one of the cigars shrink.

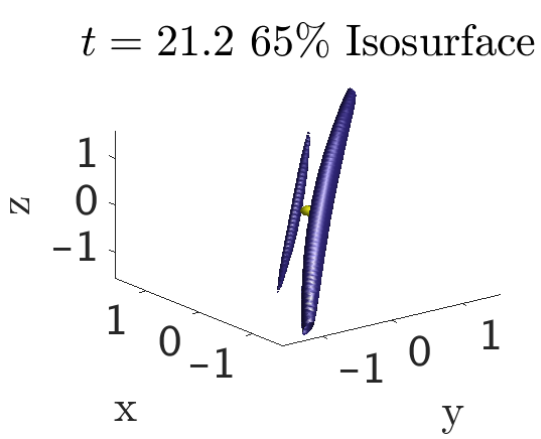

(a) The small cigar is no longer shrinking in length.

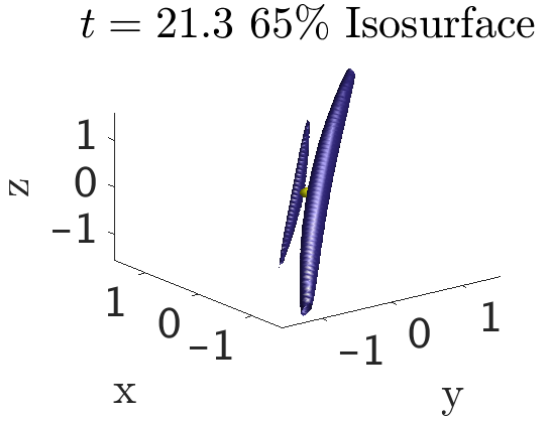

(b) The smaller cigar begins to be stretched in the direction perpendicular to the main direction of the cigars.

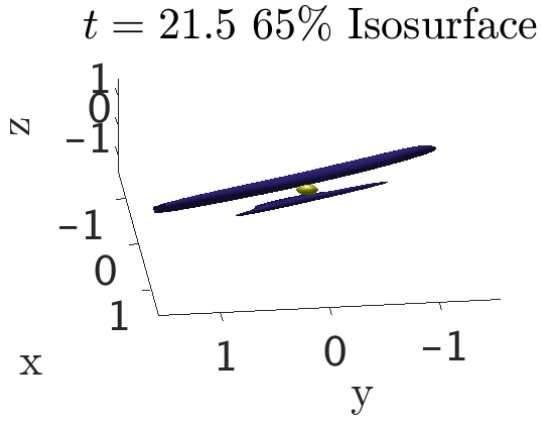

(c) The smaller cigar is seen to stretch perpendicular to the principle direction of the cigars.

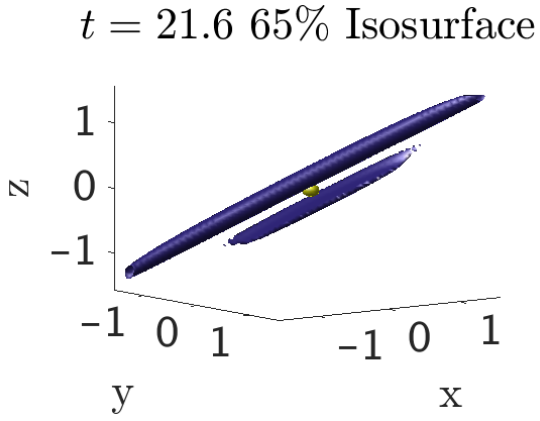

(d) The smaller cigar is seen to stretch perpendicular to the principle direction of the cigars.

Figure 4.40: 65% isosurfaces of $|\mathbf{B}|$ and 10% isosurface of $|\mathbf{u}|$ as the value of H_2 moves off of a peak.

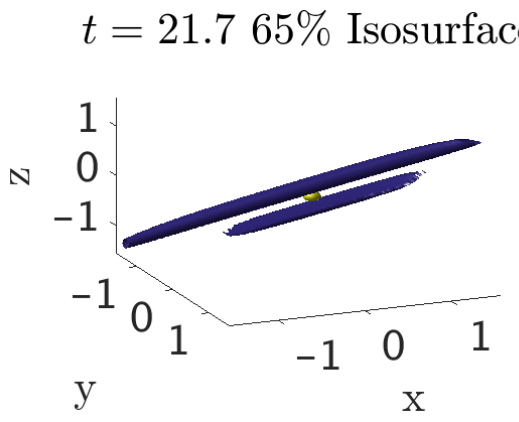

(a) The smaller cigar maintains its thickness and begins to increase in length.

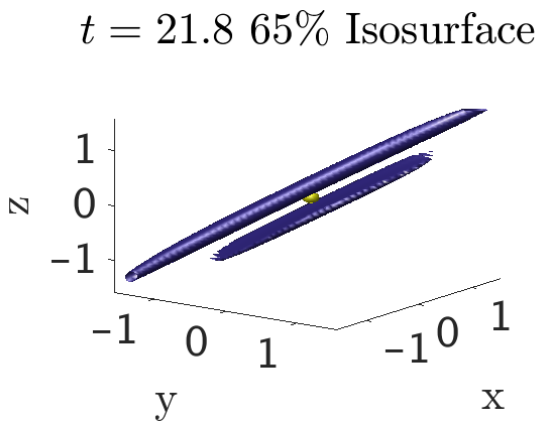

(b) The smaller cigar continues to increase in length.

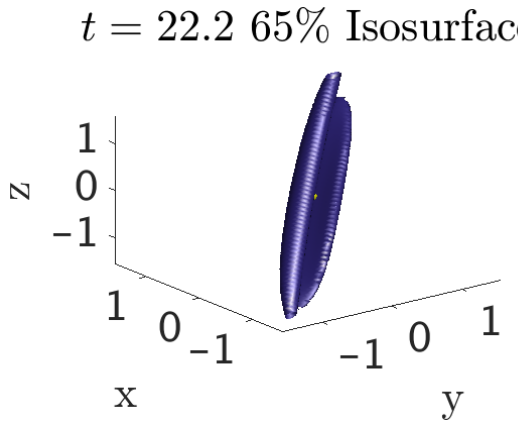

(c) The smaller cigar continues to increase in length.

Figure 4.41: 65% isosurfaces of $|\mathbf{B}|$ and 10% isosurface of $|\mathbf{u}|$. The second smaller cigar begins to grow in length again.

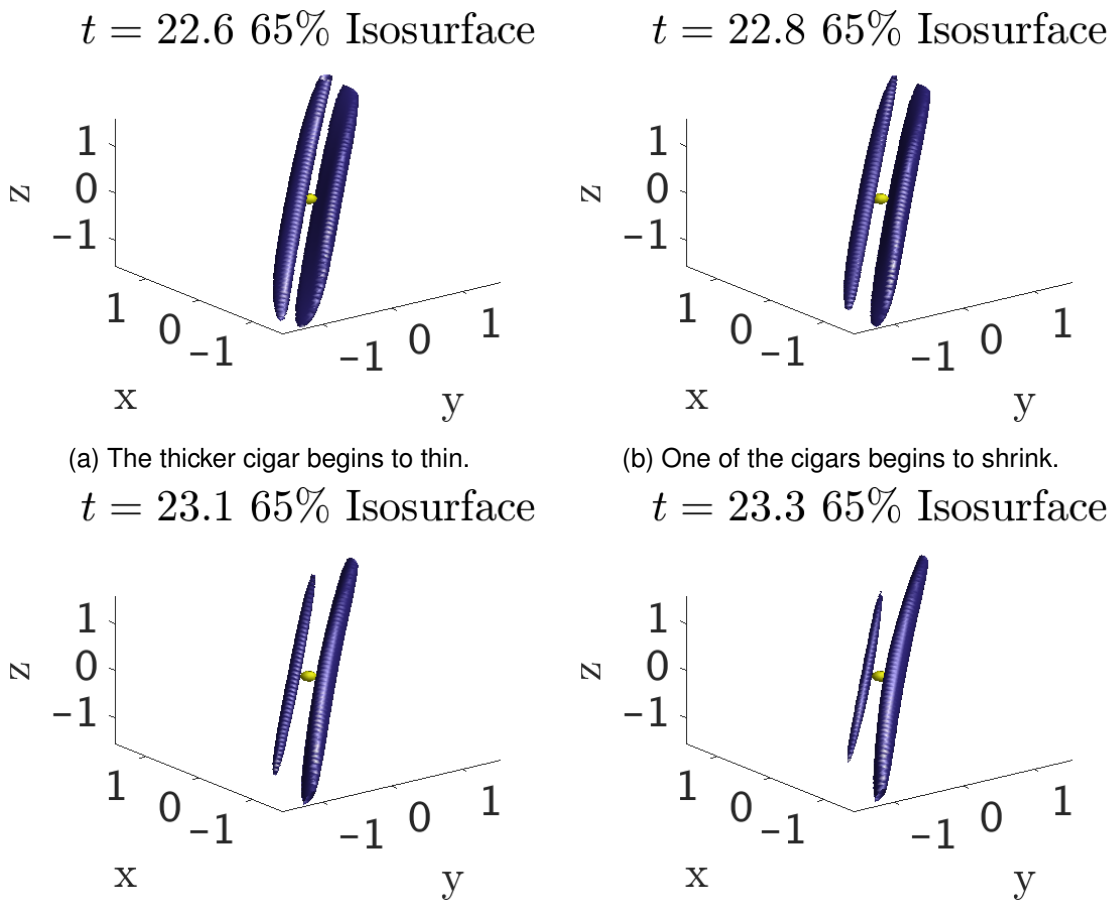

(a) The thicker cigar begins to thin.

(b) One of the cigars begins to shrink.

(c) The smaller cigar continues to shrink..

(d) The smaller cigar shrinks.

Figure 4.42: 65% isosurfaces of $|\mathbf{B}|$ and 10% isosurface of $|\mathbf{u}|$ as we again approach a maxima of H_2.

The isosurfaces thus give us a clear idea of how the morphology changes. We see that one cigar periodically shrinks, becomes stretched in the direction perpendicular to the principle direction of the cigar and then gets stretched back to the length of the other cigar. This periodic shrinking of one of the cigars is captured by the oscillations in H_2 where maxima correspond to the point where the small cigar is at its smallest. Whilst H_1 also shows this feature it also shows a number of other maxima which did not correspond to any obvious magnetic field structure changes. The cyclic amplification and decay of the cigars is similar to that identified for the ABC flow [35]. As such we can infer that the periodic shrinking of one of the flux cigars occurs due to less flux being supplied than the other cigar with the flux being generated elsewhere in the domain by chaotic advection [44] and magnetic reconnection between the two cigars replenishing field elsewhere in the domain.

To understand why measures of alignment relate to the magnetic field structure I show

65% isosurfaces of h_2

$$h_2 = \frac{\mathbf{u}\cdot\mathbf{B}}{\sqrt{ME}\sqrt{KE}} \tag{4.46}$$

along with $|\mathbf{B}|$ and $|\mathbf{u}|$ at 65% and 10% respectfully in figure 4.43. From the isosurfaces of h_2 we see that there is significant alignment between $\mathbf{u}$ and $\mathbf{B}$ at the ends of the cigars. This is logical. The cigars are aligned along the unstable eigendirection of the α type stagnation point in the direction of two β type stagnation points. Magnetic field thus converges onto the cigars from the plane perpendicular to the cigars (the plane of the two stable eigendirections) but diverges in the unstable direction (referred to as the direction of elongation within [44]) as it gets stretched out by the flow and as such becomes aligned here. As the cones of strong h_2 appear to wrap around the end of the cigars it is feasible that their cross section might be related to the cross section of the magnetic field cigars, and thus also their size. As such the size of H_2 oscillating and being linked to the size of the cigars makes sense.

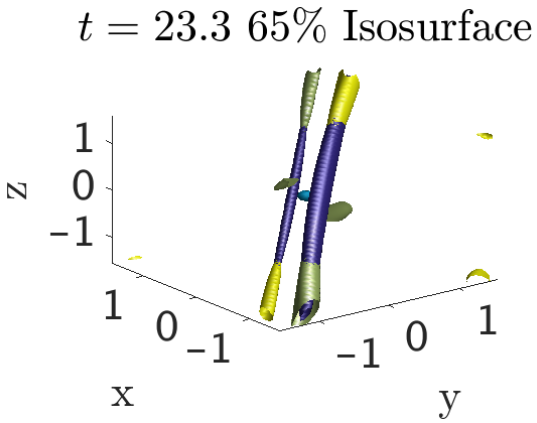

Figure 4.43: 65% Isosurfaces of $|\mathbf{B}|$ (purple), $h_2 = (\mathbf{u}\cdot\mathbf{B})/(\sqrt{KE}\sqrt{ME})$ (yellow and green) and 10% isosurface of the flow (blue). Each is divided by the maximum value so as to obtain isosurfaces.

To conclude, this section has shown that examining the alignment of the flow and magnetic field is again useful in identifying changes to magnetic field structure. In particular oscillations in H_2 can be linked to changes in the structure of the cigar shaped regions of strong magnetic field. Thus H_2 is a useful tool for examining the magnetic field evolution within any 3D kinematic dynamos which operate in a similar manner. An example would be ABC flows with stagnation points where the magnetic field also forms into cigar like structures.

An examination of H_2 would give an estimate of the frequency at which the cigars grow and shrink and would be a useful first step for examining the magnetic field morphology. As such we have again seen that alignment is a useful quantity to examine within kinematic dynamo theory and that this usefulness extends to fully three dimensional flows as well as 2.5D ones.

4.5 Relationship Between Alignment and Fluid Helicity For a Family of Time Dependent Flows

In this section I examine the relationship between alignment of the flow and magnetic fields and the fluid helicity (4.47).

$$H_{F\alpha} = \int_V \mathbf{u} \cdot \nabla \times \mathbf{u} dV \tag{4.47}$$

To do this I make use of a family of 2.5D time dependent flows. The family of flows is constructed so as to be able to vary fluid helicity between its maximal and minimal values. The flows are an extension of those examined within [55] by Hughes et al. and have a periodic time dependence.

4.5.1 Defining the Flow and Growth Rate Optimisation

As with all sections the two measures of alignment examined are H_1 and H_2.

$$H_1 = \frac{1}{V}\int_V \frac{|\mathbf{u}\cdot\mathbf{B}|}{|\mathbf{u}||\mathbf{B}|}dV \tag{4.48a}$$

$$H_2 = \frac{\int_V |\mathbf{u}\cdot\mathbf{B}|dV}{\sqrt{\int_V \mathbf{u}^2 dV \int_V \mathbf{B}^2 dV}} \tag{4.48b}$$

The starting points for constructing the family of flows are the maximally helical flow (4.49a) and the zero helicity flow (4.49b) from [55]. In both $X = x + \cos(t)$ and $Y = y + \sin(t)$.

$$\mathbf{u_1} = \sqrt{1.5}\begin{pmatrix} \cos(Y) \\ \sin(X) \\ \cos(X) + \sin(Y) \end{pmatrix} \tag{4.49a}$$

$$\mathbf{u_0} = \sqrt{1.5}\begin{pmatrix} \cos(Y) \\ \sin(X) \\ 2\sin(X)\cos(Y) \end{pmatrix} \tag{4.49b}$$

From these two flows I am able to construct a family of flows with identical x and y components, identical kinetic energy but different fluid helicity. I define this family, $\mathbf{u}_\alpha$

$$\mathbf{u}_\alpha = \beta\big(\alpha\mathbf{u_1} + (1-\alpha)\mathbf{u_0}\big) \tag{4.50}$$

where α is the parameter that controls the fluid helicity. The parameter α is varied in the interval $[0,1]$ with $\alpha = 0$ corresponding to $\mathbf{u_0}$ and $\alpha = 1$ corresponding to $\mathbf{u_1}$. The parameter β is found numerically for each value of α so that the kinetic energy is the same for all parameter values.

I now give the fluid helicity of the flows. First noting that $\nabla \times \mathbf{u}_1 = \mathbf{u}_1$ we have (4.51)

$$H_{F1} = 2\int_{-\pi}^{\pi}\int_{-\pi}^{\pi} \frac{|\mathbf{u_1}|^2}{2} dxdy \tag{4.51}$$

The fluid helicity for $\mathbf{u_1}$ is therefore equivalent to twice the kinetic energy and is maximal. The flow $\mathbf{u}_0$ has the property that $\mathbf{u}_0 \cdot (\nabla \times \mathbf{u}_0) = 0$ therefore the fluid helicity for this flow is both locally and globally zero. The local fluid helicity for $\mathbf{u}_\alpha$ is given by (4.52).

$$\mathbf{u}_\alpha \cdot \nabla \times \mathbf{u}_\alpha = \beta^2\left(\alpha^2|\mathbf{u_1}|^2 + \alpha(1-\alpha)\big(\mathbf{u_0}\cdot\mathbf{u_1} + \mathbf{u_1}\cdot\nabla\times\mathbf{u_0}\big)\right) \tag{4.52}$$

The $\mathbf{u_0}\cdot\mathbf{u_1} + \mathbf{u_1}\cdot\nabla\times\mathbf{u_0}$ term simplifies to $|\mathbf{u}_1|^2$ therefore from (4.53) we see that if we fix the kinetic energy the amount of fluid helicity can be controlled simply by varying the parameters α and β.

$$\begin{aligned} H_{F\alpha} &= \int_{-\pi}^{\pi}\int_{-\pi}^{\pi} \beta^2\left(\alpha^2|\mathbf{u_1}|^2 + \alpha(1-\alpha)\big(\mathbf{u_0}\cdot\mathbf{u_1} + \mathbf{u_1}\cdot\nabla\times\mathbf{u_0}\big)\right) dxdy \\ &= \beta^2\alpha\int_{-\pi}^{\pi}\int_{-\pi}^{\pi} |\mathbf{u_1}|^2 dxdy \\ &= 2\alpha\beta^2 \times \text{kinetic energy} \end{aligned} \tag{4.53}$$

The kinetic energy of $\mathbf{u}_0$ and $\mathbf{u}_1$ are both $6\pi^2$. The numerical value of β is therefore chosen to yield a time averaged kinetic energy of $6\pi^2$. I calculate the kinetic energy from equation (4.54) and then select β so that the energy has a value of $6\pi^2$. The results are shown in Table 4.1.

$$\int_V \frac{|\mathbf{u}_\alpha|^2}{2} dV = \beta^2\alpha^2 \int_V \mathbf{u}_1^2 dV + \beta^2(1-\alpha)^2 \int_V \mathbf{u}_0^2 dV + 2\beta^2\alpha(1-\alpha) \int_V \mathbf{u}_1 \cdot \mathbf{u}_0 dV \quad (4.54)$$

Value of α	0	0.2	0.4	0.6	0.8	1
Value of β	1	$\sqrt{1.191}$	$\sqrt{1.316}$	$\sqrt{1.316}$	$\sqrt{1.191}$	1
Value of $\alpha\beta^2$	0	0.2382	0.5264	0.7896	0.9528	1

Table 4.1: Table of values of α and β in order to keep the kinetic energy fixed. The value of $\alpha\beta^2$ is also shown.

As the vertical wavenumber k_z is a free parameter, variation in the magnetic field as k_z varies also needs to be accounted for. Where only one value of k_z is considered for each α I will use the common convention of selecting the value with the highest growth rate. For all values of α I perform a parameter scan of k_z. This is done using the numerical methods outlined in section 2.4.1. I use a magnetic Reynolds number of $R_m = 3620$. This value of R_m is used within [55] for the case of the flow with no fluid helicity ($\mathbf{u}_0$) and is sufficiently large such that an increase in R_m does not result in an increase in growth rate for any value of α. 50 points between 0.1 and 5 are used.

The results are shown in Table 4.2. The growth rates for all k_z are shown later in figures 4.46 and 4.47. I note the difficulty in obtaining the dominant growth rate for $\mathbf{u}_0$ due to many of them being of similar values.

Value of α	0	0.2	0.4	0.6	0.8	1
Optimal value of k_z	3.5	2.2	2.3	1.1	0.7	0.5
Corresponding growth rate	0.23	0.29	0.27	0.32	0.34	0.3
Fluid Helicity (H)	0	$0.24H_{max}$	$0.53H_{max}$	$0.79H_{max}$	$0.95H_{max}$	H_{max}

Table 4.2: Optimal wavenumbers with corresponding growth rates.

To look at the amount of chaos present within each of $\mathbf{u}_\alpha$ I plot Poincare sections as outlined in section 2.6. Figure 4.44 shows Poincare sections for each of the $\mathbf{u}_\alpha$. As figure

4.44f is simply the circularly polarised flow of [45] I may compare it with the results shown in [27] where the results are in good agreement. By looking at the size and location of the integrable regions in 4.44a-4.44f minus small differences attributable to different random initial conditions we see that the Poincare sections are almost identical and thus all $\mathbf{u}_\alpha$ have almost equal amounts of chaos and stretching properties.

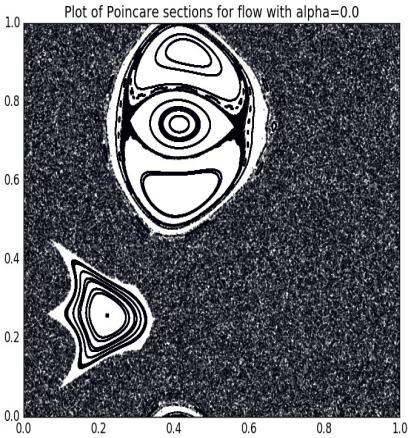

(a) Poincare section for $\alpha = 0$

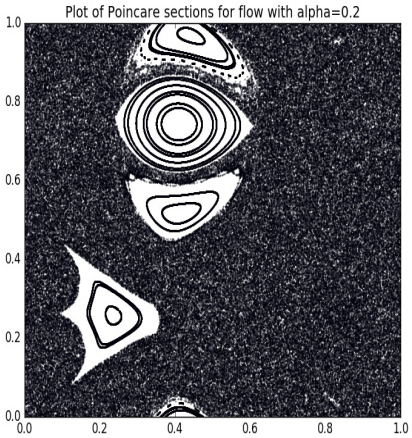

(b) Poincare section for $\alpha = 0.2$

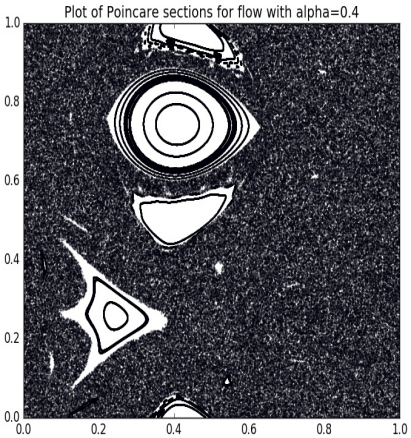

(c) Poincare section for $\alpha = 0.4$

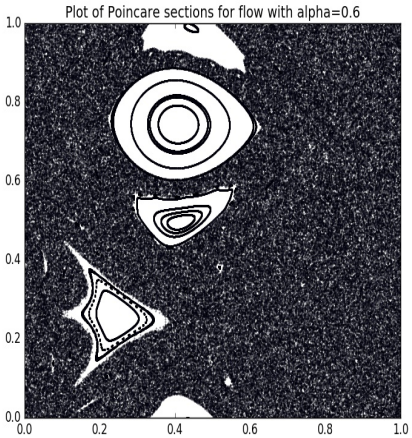

(d) Poincare section for $\alpha = 0.6$

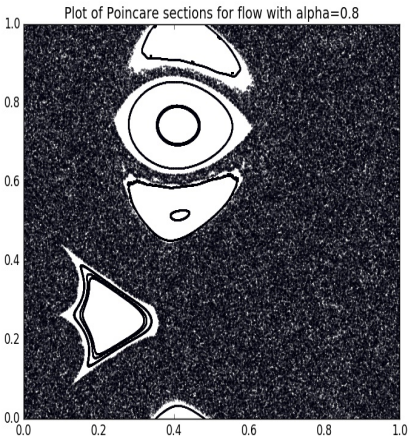

(e) Poincare section for $\alpha = 0.8$

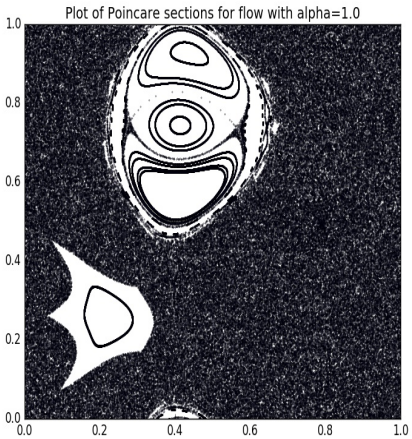

(f) Poincare section for $\alpha = 1$

Figure 4.44: Poincare sections for flows with varying fluid helicity. Each has two integrable regions surrounded by a web of chaotic regions.

For comparison figure 4.45 shows Poincare sections of (a) the Robert's flow multiplied by a factor of $\sqrt{1.5}$ and looked at in section 4.2 and (b) the Cat's eye flow of [30] and

looked at in section 4.3. What we see is that for each of these flows, which are both steady, all trajectories lie on closed curves and thus the whole domain is integrable. As a result of this we expect the flows to be worse at generating magnetic field than the flows of figure 4.44 with their large areas of chaos and indeed I have shown that growth rates are lower for these flows. The Poincare sections thus show that as well as having identical kinetic energy the family of flows $\mathbf{u}_\alpha$ also appears to have identical chaotic properties. This makes any difference between the dynamos more likely to be due to differences in their fluid helicities.

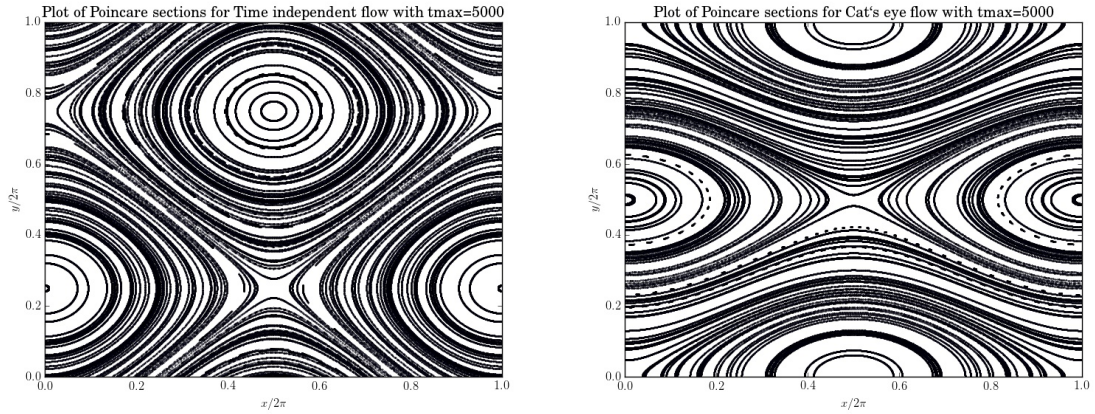

(a) Poincare section for the Roberts flow

(b) Poincare section for Cat's eye flow of [30]

Figure 4.45: Poincare sections of steady 2.5D flows. There are no chaotic regions unlike when time dependence is added (see figure 4.44) and so the flow is less able to stretch and enhance a magnetic field.

4.5.2 Relation Between Alignment and Fluid Helicity

Upon calculation of H_1 and H_2 in the kinematic dynamo for each α it is found that the value of each oscillates in time for each k_z. Examples of H_1 and H_2 are shown for $\alpha = 0.2$ and $\alpha = 0.8$ in figures 4.46 and 4.47. We see that for all α both are highly time dependent but in a periodic fashion. As such a time average is required to be able to compare runs.

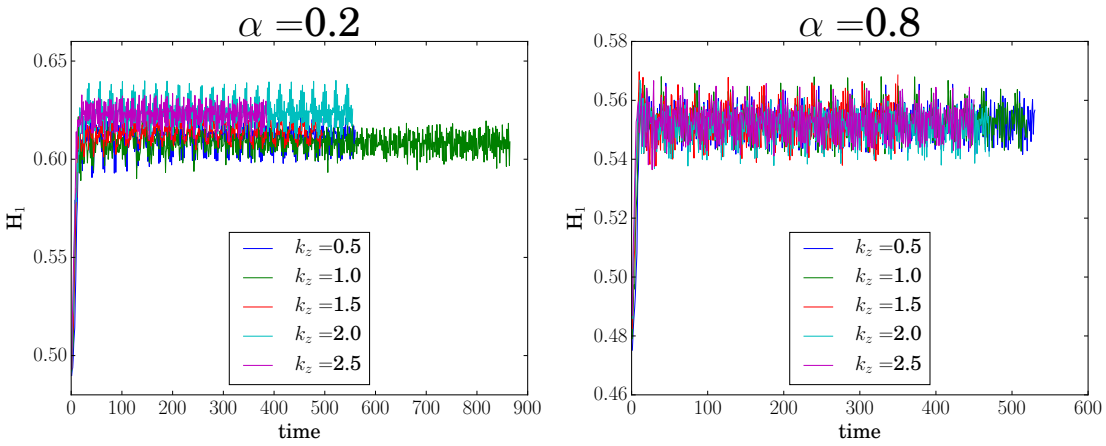

(a) (b)

Figure 4.46: Plot of H_1 vs time for $\alpha = 0.2$ and $\alpha = 0.8$ and $k_z \in (0.1, 3)$. All time series oscillate and there is little variation in the average.

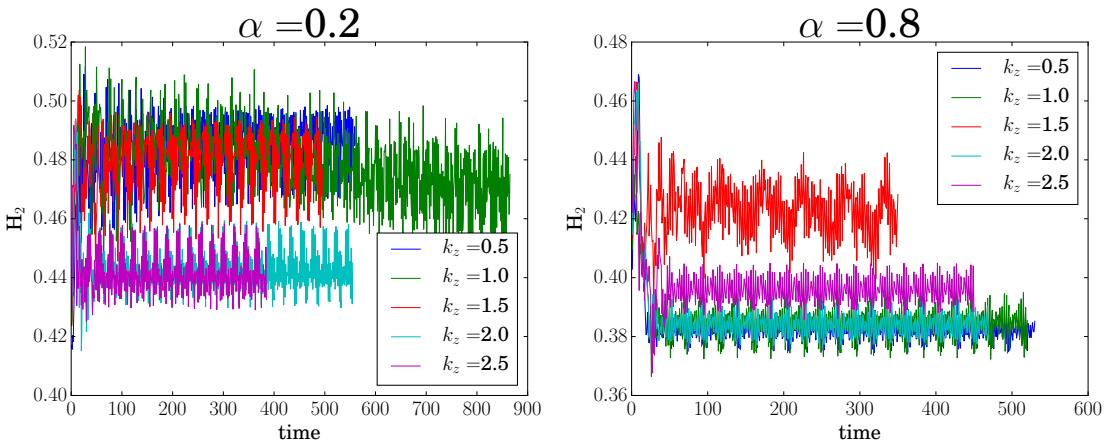

(a) (b)

Figure 4.47: Plot of H_2 vs time for $\alpha = 0.2$ and $\alpha = 0.8$ and $k_z \in (0.1, 3)$. All time series oscillate and there is some change in the value of H_2.

In figure 4.48 I show time averages of H_1 and $1/H_2$ (left axis, blue curves) against growth rate (right axis, red curves) for all k_z and α. I note two things. First, there is very little variation in the value of H_1 as k_z is varied for individual α. The reason for this will be explored later. Secondly, plots of $1/H_2$ show that there appears to be some inverse correlation between growth rate and H_2. This becomes more pronounced for larger fluid helicity.

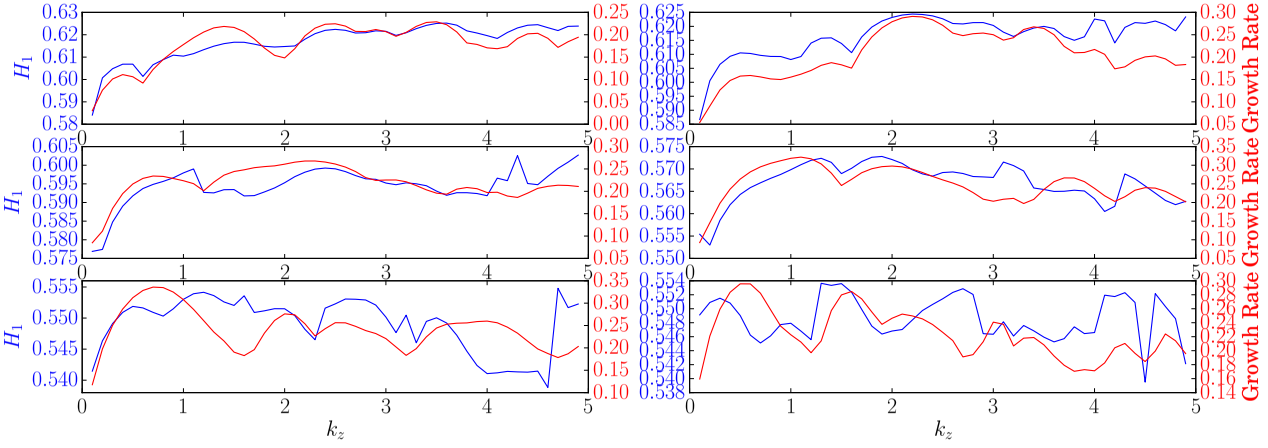

(a) There is very little variation in H_1 over k_z

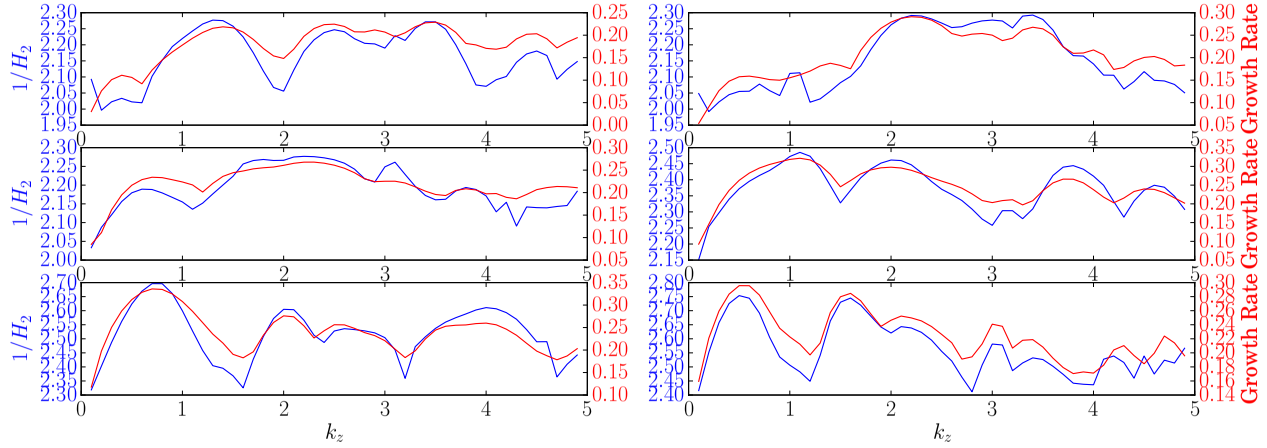

(b) There appears to be some inverse correlation between H_2 and Growth rate.

Figure 4.48: H_1 and H_2 (left axes) and growth rate (right axes) against k_z for all α.

To see why H_1 and H_2 show only a small amount of variation in k_z I plot a number of contours of $B_z/\max_{x,y,z}\{B_z\}$ for two values of α in figures 4.49 and 4.50. In sections 4.2 and 4.3 I showed how variation in H_1 and H_2 can give insights into changes in the magnetic field structure. The small amount of change in both H_1 and H_2 that we see in figure 4.48 would therefore lead us to assume that the magnetic field structure changes very little for each α. From the contours in figures 4.49 and 4.50 we see this to be true. At each k_z the magnetic field is strong only in small elongated structures which appear not to be present in the main center region of the Roberts flow (see figure 4.1). There is some variation in the width and length of the small strong regions, which leads to the variation in H_1 and H_2, but in general contours for a variety of k_z look similar. This is also seen for B_x and B_y contours (not shown).

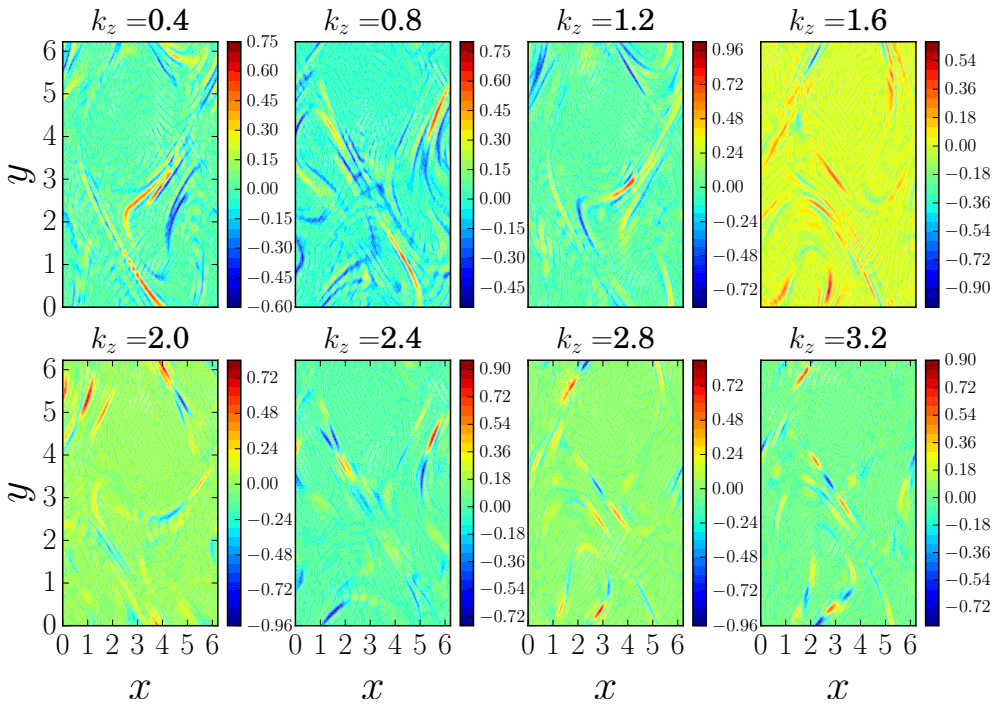

Figure 4.49: $B_z/\max_{x,y,z}\{B_z\}$ for $\alpha = 0.2$. We see that the magnetic field is small scale and only strong in small regions of the domain which appear to correlate with the channels of the Roberts flow (see figure 4.1). This is also seen for B_x and B_y which are a similar magnitude to B_x also.

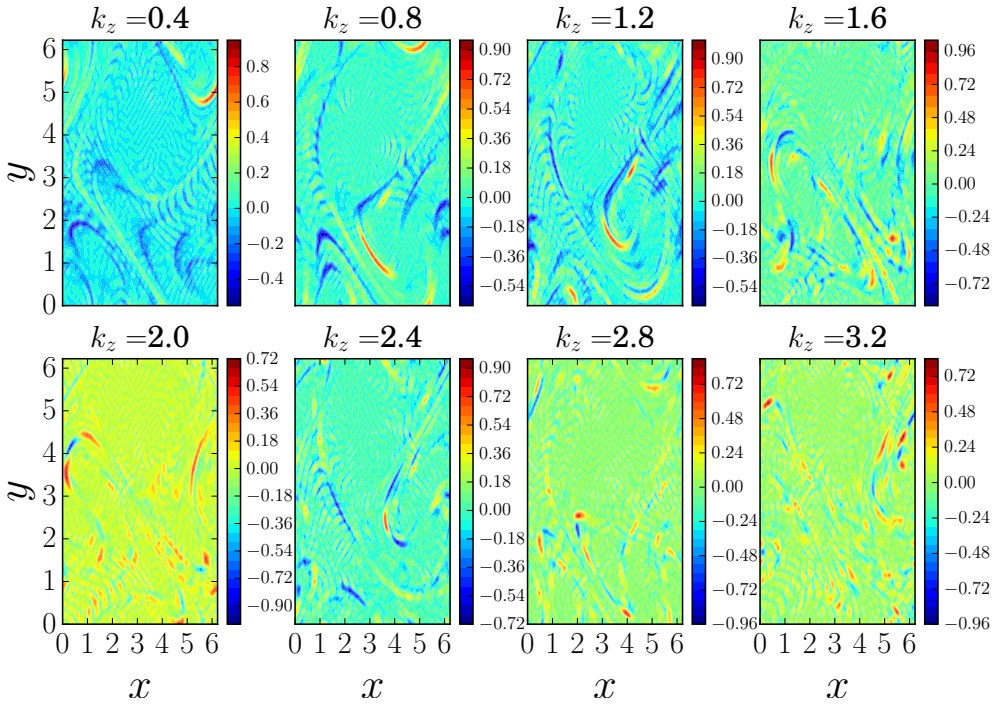

Figure 4.50: $B_z/\max_{x,y,z}\{B_z\}$ for $\alpha = 0.8$. We see that the magnetic field is small scale and only strong in small regions of the domain. As with $\alpha = 0.2$ the center at $(x,y) = (\pi, 3\pi/2)$ appears to be devoid of any strong magnetic field. The Roberts flow (see figure 4.1). This is also seen for B_x and B_y which are a similar magnitude to B_x also.

I now examine a possible link between alignment and fluid helicity by examining variation with α. To do this I compare the k_z where the growth rate is maximal. I plot the value of growth rate, H_1 and H_2 all against α in figure 4.51. There is a clear trend of increasing growth rate as fluid helicity increases. This supports the result within [55] that more fluid helicity is generally better at amplifying weak field. Secondly, both measures of alignment decrease as the flow becomes more helical. An increase in fluid helicity therefore appears to decrease the amount of alignment between the flow and magnetic field for our particular family of flows.

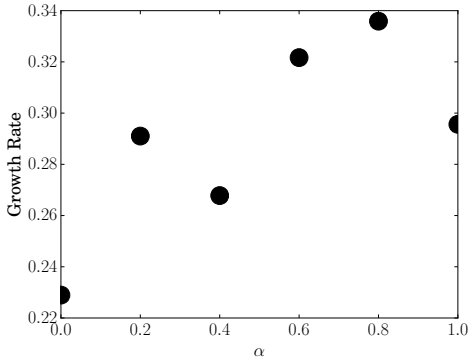

(a) Growth rate vs α. Broadly, more fluid helicity results in a higher growth rate.

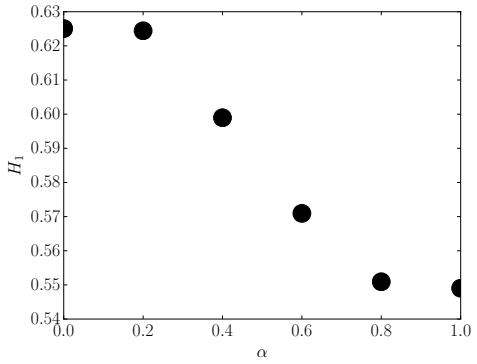

(b) H_1 vs α. Broadly more fluid helicity results in less alignment by this measure.

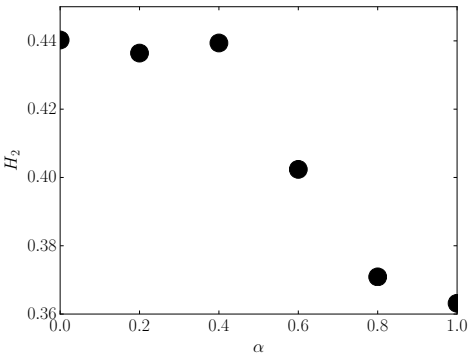

(c) H_2 vs α. More fluid helicity results in less alignment but this only begins for $\alpha > 0.4$ here.

Figure 4.51: Plot of Growth rate, H_1 and H_2 against α at the value of k_z with the largest growth rate. The trend is for a higher growth rate and less alignment as α increases. There is, however, very little change in value of H_1 and H_2 across all α.

It is important to note that the volume average is important here. The integrals are normalised by multiplying by $(k_z)^{max}/8\pi^3$ where $(k_z)^{max}$ is the value of k_z where the growth rate is largest. Due to $(k_z)^{max}$ becoming smaller as α increases if we did not volume average then H_1 would show an increase in alignment with fluid helicity as shown in figure 4.52.

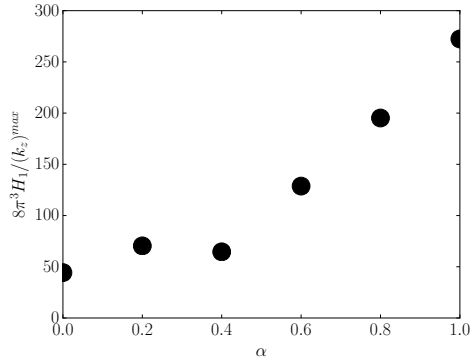

Figure 4.52: $8\pi^3 H_1/(k_z)^{max}$ by not averaging over the z direction we would incorrectly get an increase in alignment with increasing fluid helicity.

To summarise; in this section a family of time dependent 2.5D flows was created with fixed kinetic energy and almost identical chaotic regions (as measured by Poincare sections). In going from $\mathbf{u}_0$ to $\mathbf{u}_1$ the value of fluid helicity increased from minimal to maximal values. I have found a number of interesting results. The first is that there is very little change in magnetic field structure as k_z varies. The fact that H_1 and H_2 subsequently vary very little as k_z is varied at each α is therefore consistent with the other results in this section that alignment can be used as an indicator for changes in magnetic field structure. Secondly, I have found that for both of the measures considered alignment decreases as fluid helicity increases.

4.6 Discussion of Kinematic Dynamo Results

I will now refer back to the aims outlined at the beginning of the chapter and highlight what has been shown within the section. I then give possible avenues of future research.

- **To study alignment in 2.5 kinematic dynamos.**

  In this section I have examined two alignment quantities, H_1 and H_2, for two steady 2.5D flows. I have found that as k_z is varied the value of both H_1 and H_2 changes as the structure of the magnetic field changes. I have found that examining plots of H_1 and H_2 against vertical wavenumber, k_z, is a useful method of identifying where the structure of the magnetic field changes.

- **To study alignment in 3D kinematic dynamos**

In this section I have examined alignment in the Kolmogorov flow. I have found that oscillations in H_2 matched well with the lengthening of the magnetic field's cigar structures. This section showed how H_2 can be used in 3D kinematic dynamos to identify periodic morphology changes. It suggests that H_2 is a useful quantity to calculate in 3D kinematic dynamo simulations as it quickly yields information on changes in the magnetic field structure without having to examine numerous 3D plots.

- **To examine the relationship between alignment and fluid helicity in kinematic dynamos.**

  In this section I constructed a family of flows with varying fluid helicity. I showed that alignment decreases with increased fluid helicity. As this result is specific to a specific group of flows it is only a first step in examining the relation between these two quantities but due to the importance of the fluid helicity in kinematic dynamos I believe it is worth further investigation. This section also supported the results of the other two sections by showing that very little change in magnetic field structure accompanies very little change in H_1 and H_2.

Each of the flows examined have established a link between the magnetic field structure and H_1 and H_2. This is not unexpected. The flow remains unchanged during the runs and therefore change in alignment must be due to change in $\mathbf{B}$.

The results show that calculating a volume measure of alignment frequently during a kinematic dynamo simulation and when performing a parameter scan can be a useful first step to examining how the magnetic field structure evolves. Out of the two measures of alignment examined I believe that H_2 is more useful. The first reason is that as we can see in (4.55)

$$\begin{aligned} H_2 &= \frac{\int_V |\mathbf{u}\cdot\mathbf{B}|dV}{\sqrt{\int_V \mathbf{u}^2 dV \int_V \mathbf{B}^2 dV}} \\ &= \frac{\int_V |\mathbf{u}||\mathbf{B}||\cos(\theta)|dV}{\sqrt{\int_V \mathbf{u}^2 dV \int_V \mathbf{B}^2 dV}} \end{aligned} \tag{4.55}$$

H_2 explicitly weights the amount of alignment at a point by the strength of the aligning fields. As such spurious contributions from weak $\mathbf{u}$ and $\mathbf{B}$ make less of a contribution to the integral. Secondly, it was shown in section 4.4 that small oscillations in H_2 match better with the evolving field structure than oscillations in H_1, although this result is specific to the Kolmogorov flow at present.

The final reason is that H_1 frequently required more grid points to integrate. A standard procedure when running kinematic dynamo simulations is to increase the number of grid points until the growth rate no longer increases (to a set tolerance). In all of the flows examined in this chapter the value of H_2 saturated at the same resolution as the growth rate. However, H_1 frequently required much higher resolution before saturating. As such, obtaining a reliable value of H_1 would require increasing the resolution of the runs and would therefore be inefficient to calculate.

A logical next step to this work is to consider a wider group of flows with varying fluid helicity to examine whether or not decreasing alignment with increasing fluid helicity is a general trend. In particular, it would be interesting to examine this in 3D flows. The main next step, however, would be to use the link between alignment and the structure of $\mathbf{B}$ to identify where changes in this structure occur. This will be most useful when $\mathbf{u}$ remains approximately unchanged. As such it is most useful in either kinematic dynamos or the kinematic phase of nonlinear dynamos.

Chapter 5

Nonlinear Dynamos Involving an Alignment Mechanism

5.1 Introduction

In this chapter, motivated by questions that remain unanswered, I examine a nonlinear dynamo, which I will refer to as the Archontis dynamo. Motivations and existing literature are outlined in Chapter 3. In nonlinear dynamo theory both the equation of motion (5.1) for the flow and the induction equation (5.2) for the magnetic field are solved simultaneously for both $\mathbf{u}$ and $\mathbf{B}$ given a prescribed forcing $\mathbf{F}$.

$$\frac{\partial \mathbf{u}}{\partial t} = -\nabla P - (\mathbf{u}\cdot\nabla)\mathbf{u} + (\mathbf{B}\cdot\nabla)\mathbf{B} + \nu\nabla^2\mathbf{u} + \mathbf{F} \tag{5.1}$$

$$\frac{\partial \mathbf{B}}{\partial t} = (\mathbf{B}\cdot\nabla)\mathbf{u} - (\mathbf{u}\cdot\nabla)\mathbf{B} + \eta\nabla^2\mathbf{B} \tag{5.2}$$

An outline of how these equations are solved and the numerical methods employed can be found within Chapter 2. The forcing that I am concerned with is the Archontis forcing

$$\mathbf{F}_A = \nu \begin{pmatrix} \sin(z) \\ \sin(x) \\ \sin(y) \end{pmatrix}. \tag{5.3}$$

My aims are as follows:

- **To Explain the Two Statistically Steady States of the Archontis Dynamo**

  As outlined during the motivations for this work, in particular section 3.4, the reason for the existence of the two statistically steady states (SSS) of the energies (shown in figure 5.1)

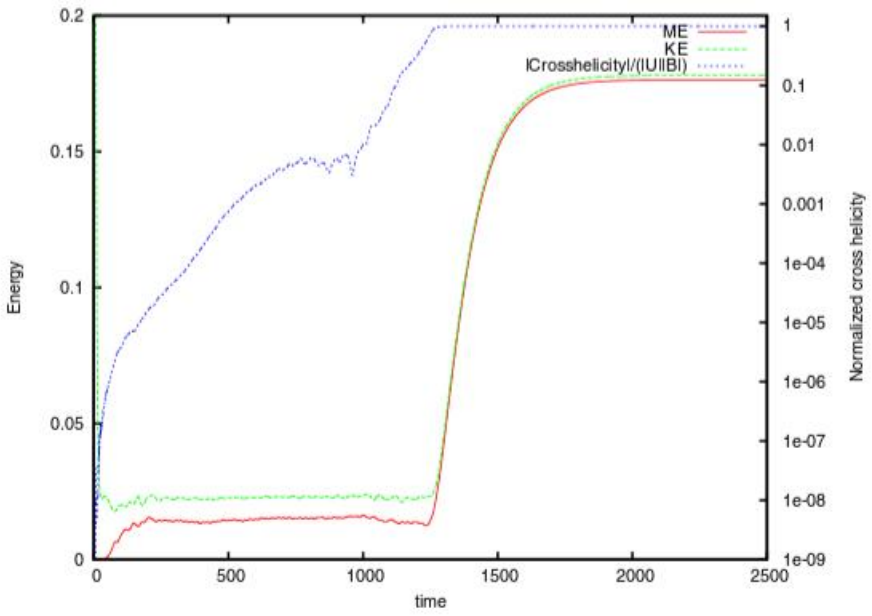

Figure 5.1: Figure 19 from [22] showing multiple SSS of the energies.

when a seed magnetic field is used to initialise the run is still an open question. In this chapter I aim to provide an explanation for why the two states exist. I also aim to explain why alignment between the magnetic and flow fields is such a good indicator of a transition between the two SSS.

- **To Examine the Robustness of the Dynamo to Changes to $P_m = \nu/\eta$**

  Some information on the influence of P_m on the Archontis dynamo was reported by Cameron and Galloway [22] who examined changes to the energies within the Archontis dynamo when P_m is changed to 0.25 ($\nu = 1/400$, $\eta = 1/100$) or 4 ($\nu = 1/100$, $\eta = 1/400$). Exact alignment information was not reported, however they obtained significant values of magnetic energy. In this chapter I will examine a large number of values of ν and η where $\nu^{-1} < 100$ and $\eta^{-1} < 100$. I will explore how the energies and alignment relate to P_m. The aim is to explore how varying P_m influences the magnetic and kinetic energy budgets as well as the amount of alignment between

the two fields.

- **To Examine the Stability of the Final Aligned State to the Introduction of Time Dependence and Asymmetry to the Forcing**

  Little is known about what particular properties of the Archontis forcing are important to produce an aligned dynamo with kinetic and magnetic energies of approximately equal strength. In this chapter I will introduce both asymmetry and time dependence to the forcing. I have a number of aims in doing this.

  The first is to see how stable the aligned state is. By stable I mean; does the aligned state disappear as soon as we make a small change to the forcing? How much time dependence and asymmetry can be introduced before we no longer obtain an aligned dynamo? By introducing time dependence and asymmetry via a parameter which makes the forcing more time dependent (or asymmetric) I can measure the changes to the energies and alignment as well as how much deviation from the original forcing can be made before we no longer have an aligned dynamo.

  The second aim concerns the relationship between achieving magnetic energy comparable to the kinetic energy and the two fields being strongly aligned. Cameron and Galloway [22] showed that alignment occurs immediately prior to the energies becoming of comparable magnitude within the Archontis dynamo which suggests that the alignment is responsible for the fields eventually being at equipartition. If alignment continues to be seen when dynamo action occurs for forcings close to $\mathbf{F}_A$ this would strongly support the idea that alignment is crucial to the working of dynamos with forcings similar to $\mathbf{F}_A$.

  The final aim is to increase the number of forcings in the literature which produce an aligned dynamo as only a small number currently exist, which inhibits investigation of what produces the aligned state.

5.2 The Influence Of Initial Conditions On Obtaining Multiple Statistically Steady States Within The Archontis Dynamo

As noted in section 3.4 one outstanding question in the study of alignment within nonlinear dynamo theory pertains to the finding by Cameron and Galloway [22] of the existence of multiple statistically steady states (SSS) within the Archontis dynamo where the magnetic field is initialised with a random seed field. In this section I analyse the relationship between the existence of the first SSS and the choice of initial magnetic field. In particular I define an initial field within Fourier space and systematically vary the strength of its real and imaginary components and in doing so identify a relationship between this and the existence of the first SSS.

I define kinetic energy (KE) and magnetic energy (ME) within equations (5.4a) and (5.4b). I define the amount of alignment within (5.4c). This choice of alignment measure is taken as it is the probable measure used by Cameron and Galloway and is also simply a normalisation of the cross-helicity which is itself an ideal MHD invariant.

$$KE = \frac{1}{8\pi^3}\int_V \frac{\mathbf{u}^2}{2} dV \qquad (5.4a) \qquad ME = \frac{1}{8\pi^3}\int_V \frac{\mathbf{B}^2}{2} dV \qquad (5.4b)$$

$$H_0 = \frac{1}{8\pi^3}\frac{1}{\sqrt{ME}\sqrt{KE}}\left|\int_V \frac{\mathbf{u}\cdot\mathbf{B}}{2} dV\right| \qquad (5.4c)$$

I use the initial condition $\mathbf{u}_0 = \mathbf{F}_A/\nu$ for the flow field. The magnetic field is specified in terms of its Fourier modes, $\widehat{\mathbf{B}}_\mathbf{k} = \widehat{\mathbf{B}}^R_\mathbf{k} + i\widehat{\mathbf{B}}^I_\mathbf{k}$, where $\widehat{\mathbf{B}}^R_\mathbf{k}$ and $\widehat{\mathbf{B}}^I_\mathbf{k}$ are real functions and the magnetic field's Fourier components are defined as in (5.5).

$$\mathbf{B} = \sum_\mathbf{k} \widehat{\mathbf{B}}_\mathbf{k} \exp(i\mathbf{k}\cdot\mathbf{x}) \qquad (5.5)$$

The real and imaginary components of $\widehat{\mathbf{B}}_\mathbf{k}$ are separately assigned a value at each Fourier mode $\mathbf{k} = (k_x, k_y, k_z)$ according to a random normal distribution. $\widehat{\mathbf{B}}^R_\mathbf{k}$ and $\widehat{\mathbf{B}}^I_\mathbf{k}$ are then multiplied by a power of 10 so that the relative order of magnitudes of the real and imaginary parts can be altered resulting in the respective order of magnitudes shown in equations

(5.6a) and (5.6b). Values $-4, -5, -6, -7, -8$ and $-\infty$ were used for each of parameters a and b.

$$O\big(\widehat{\mathbf{B}}^R_{\mathbf{k}}\big) = 10^a \qquad (5.6a) \qquad\qquad O\big(\widehat{\mathbf{B}}^I_{\mathbf{k}}\big) = 10^b \qquad (5.6b)$$

For reasons that will become clear later I also define the real (5.7a) and imaginary (5.7b) components of the Fourier transformed magnetic field, corresponding to the even and odd components of the magnetic field respectively.

$$\widehat{\mathbf{B}}^R_{\mathbf{k}} = \Re\{\widehat{\mathbf{B}}_{\mathbf{k}}\} \qquad (5.7a) \qquad \widehat{\mathbf{B}}^I_{\mathbf{k}} = \Im\{\widehat{\mathbf{B}}_{\mathbf{k}}\} \qquad (5.7b)$$

$$E_R = \sum_{\mathbf{k}} |\widehat{\mathbf{B}}^R_{\mathbf{k}}|^2 \qquad (5.7c) \qquad E_{IM} = \sum_{\mathbf{k}} |\widehat{\mathbf{B}}^I_{\mathbf{k}}|^2 \qquad (5.7d)$$

where $\Re$ denotes the real component and $\Im$ denotes the imaginary component of the magnetic field within Fourier space. I thus define the energy within the even component of the magnetic field as (5.7c) and the energy within the odd component of the magnetic field as (5.7d). The final state of the magnetic field $\mathbf{B}$ has been shown in [22] to be close to $\mathbf{F}_A/2\nu = \big[\sin(z), \sin(x), \sin(y)\big]/2$. As such we expect that at large time $E_R \to 0$ and E_{IM} will tend to a fixed value of 0.375 due to:

$$\frac{1}{8\pi^3}\int_0^{2\pi}\int_0^{2\pi}\int_0^{2\pi} \frac{\sin^2(x) + \sin^2(y) + \sin(z)^2}{4} dxdydz = 0.375. \qquad (5.8)$$

A number of test runs found that evolution to the field's final SSS was found to depend upon the magnitude of the initial magnetic fields real and imaginary Fourier components. It was this that motivated the parameter scan of a and b. Individual runs for a given (a, b) were also found to yield a variety of different evolutions to the final state. Broadly, the runs can be split into three categories which I will denote A, B and C. Group A consists of initial conditions for which only the second steady state within figure 5.1 is reached and this occurs much faster than the final states of groups B and C. Group B consists of initial conditions which yield a first state which whilst not quite steady only varies by a small (but noticeable) amplitude. The second steady state is also reached for group B. Group C consists of initial conditions which yield both steady states. For ease of reference I bullet point these below:

- Group A: Only one statistically steady state (SSS)
- Group B: A short first SSS followed by a second, final, SSS

- Group C: Two SSS

Table 5.1 shows the result of 10 runs for each combination of real and imaginary magnitudes. A random uniform distribution was also tested, yielding virtually identical results. Where a cell contains multiple letters the most frequent to least frequent results from the 10 runs are from left to right respectively.

Order of Magnitude of imaginary component / Order of Magnitude of real component	-3	-4	-5	-6	-7	-8	$-\infty$	
-3		A	A	B	B	B	B	
-4	A	A	A	A	A	A B	B	C
-5	A	A	A	A	A	A	C	B
-6	A	A	A	A	A	A	C	B
-7	A	A	A	A	A	A	B	C
-8	A	A	A	A	A	A	B	A
$-\infty$	A	A	A	A	A	A		

Table 5.1: Table showing how the magnitude of the real and imaginary components of the initial condition impact the time evolution. Group A only achieve the second steady state. Group B yield a first state which whilst not quite steady only varies by a small (but noticeable) amplitude. The second steady state is also reached for Group B. Group C yield both steady states.

The majority of initial conditions yield solutions which only have the second steady state, indicated by a yellow A in table 5.1. An example of this is shown within figures 5.2a and 5.2b. What we see in 5.2a is that the magnetic and fluid fields quickly become aligned ($t \approx 100$) and converge to the final state with $KE = ME \approx 0.17$ and no intermediate SSS. Figure 5.2b shows the odd and even components of the magnetic energy as well as the kinetic and magnetic energies. We see that the even component of the solution quickly becomes negligible, $O(10^{-6})$ by $t \approx 200$, whereas the odd component saturates due to convergence to the steady state.

Figures 5.3a and 5.3b shows a typical example of the Group B type of solution. As with figures 5.2a and 5.2b the values of the magnetic and kinetic energies eventually saturate at a value close to 0.17. Furthermore the energy in the even and odd components of the magnetic fields at large time has the same behaviour as the Group A run. The evolution of the even and odd components of the magnetic energy is, however, more interesting than

in the Group A case. In particular we observe that rapid growth of the fluid and magnetic energies occurs immediately after the transition from the even component of the magnetic field having more energy than the odd to the reverse of this at approximately $t = 300$ where we also see alignment saturate to approximately one. During the time period $t \approx (50, 300)$ where E_{IM} is beginning to dominate E_R we see a brief almost statistically steady state in the magnetic and kinetic energies. The behaviour is therefore close to that observed by Cameron and Galloway but not as well defined.

Typical examples of a Group C run are shown in figures 5.4a and 5.4b. This run was initiated with an even initial condition for the magnetic field. In figure 5.4a we see that it is these runs which most closely match that seen when Cameron and Galloway evolved a seed field within [22] as here we see that both statistically steady states are present. The final energies and values of the even and odd components of the magnetic energy are the same as the Group A and Group B runs. We see in figure 5.4b that the first apparent steady state corresponds to a time independent phase for the even component of the magnetic field however the odd component grows rapidly during this phase. Once the odd component of the magnetic field exceeds the magnitude of the even component we again see rapid growth of the magnetic and kinetic energy to the second steady state where it is now the odd component of the magnetic field which becomes steady whereas the even component decays rapidly.

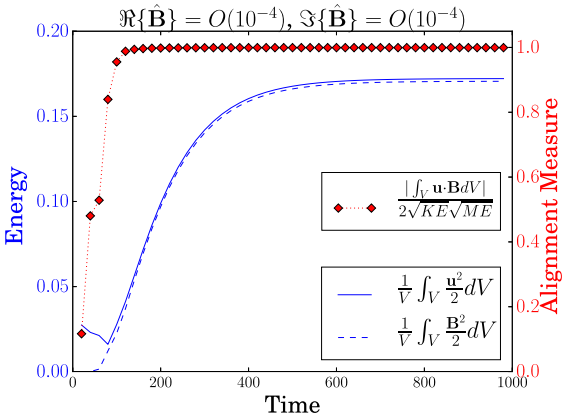

(a) Plot of the kinetic and magnetic energies vs various measures of alignment

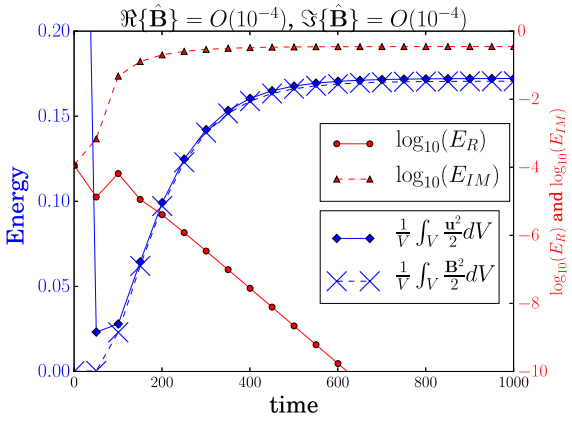

(b) Plot of the kinetic and magnetic energies vs the energies in the real and imaginary components of the magnetic field

Figure 5.2: Case A: $\mathbf{F}_A$ with $\mathbf{u}_0 = \mathbf{F}/\nu$, $1/\nu = 1/\eta = 100$ and a random Fourier magnetic field which has real and imaginary components of order $O(10^{-4})$.

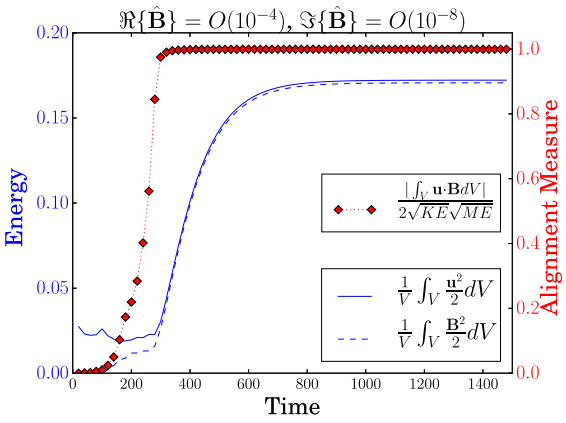

(a) Plot of the kinetic and magnetic energies vs various measures of alignment

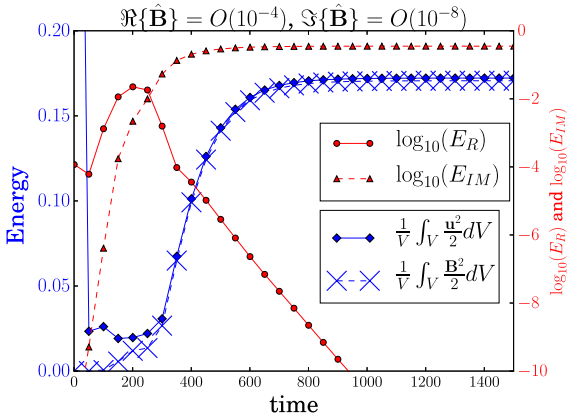

(b) Plot of the kinetic and magnetic energies vs the energies in the real and imaginary components of the magnetic field

Figure 5.3: Case B: $\mathbf{F}_A$ with $\mathbf{u}_0 = \mathbf{F}/\nu$, $1/\nu = 1/\eta = 100$ and a random Fourier magnetic field which has real component of order $O(10^{-4})$ and imaginary component of order $O(10^{-8})$.

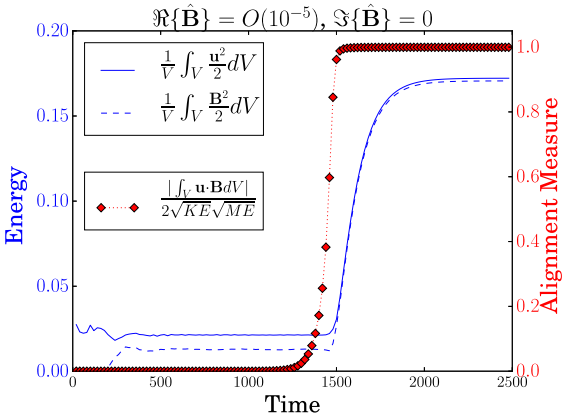

(a) Plot of the kinetic and magnetic energies vs various measures of alignment

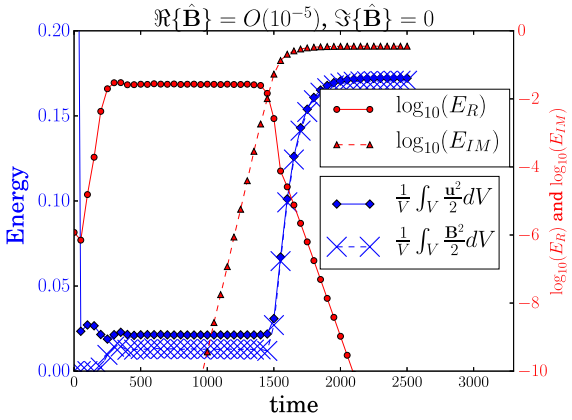

(b) Plot of the kinetic and magnetic energies vs the energies in the real and imaginary components of the magnetic field

Figure 5.4: Case C: $\mathbf{F}_A$ with $\mathbf{u}_0 = \mathbf{F}/\nu$, $1/\nu = 1/\eta = 100$ and a random Fourier magnetic field which only has a real component of order $O(10^{-5})$.

In plotting the energy in the even and odd components of the magnetic field we therefore see that sufficient energy in the odd component appears crucial to achieving the final state and that a lack of it initially is crucial to achieving two SSS. To explain this consider the MHD equations written in terms of their Fourier components in (5.9a) and (5.9b).

$$\frac{\partial \widehat{\mathbf{B}}_{\mathbf{k}}}{\partial t} + \eta \mathbf{k}^2 \widehat{\mathbf{B}}_{\mathbf{k}} = i\mathbf{k} \times \sum_{\mathbf{m}} (\widehat{\mathbf{u}}_{\mathbf{k}-\mathbf{m}} \times \widehat{\mathbf{B}}_{\mathbf{m}}) \tag{5.9a}$$

$$\frac{\partial \widehat{\mathbf{u}}_{\mathbf{k}}}{\partial t} + \nu \mathbf{k}^2 \widehat{\mathbf{u}}_{\mathbf{k}} = i\widehat{\mathbf{F}}^R_{\mathbf{k}} + i\mathbf{P} \sum_{\mathbf{m}} \left(\widehat{\mathbf{u}}_{\mathbf{k}-\mathbf{m}} \times (\mathbf{m} \times \widehat{\mathbf{u}}_{\mathbf{m}}) - \widehat{\mathbf{B}}_{\mathbf{k}-\mathbf{m}} \times (\mathbf{m} \times \widehat{\mathbf{B}}_{\mathbf{m}}) \right) \tag{5.9b}$$

Here use is made of incompressibility to define the projection operator $\mathbf{P}$ which in index notation is given by $P_{ij} = \delta_{ij} - k_i k_j/(k_l k_l)$. The forcing $\mathbf{F}_A$ in Fourier space is also written in terms of a real function $\widehat{\mathbf{F}}^R_{\mathbf{k}}$. The general form of $\widehat{\mathbf{u}}_{\mathbf{k}}$ and $\widehat{\mathbf{B}}_{\mathbf{k}}$ are given by $\widehat{\mathbf{u}}_{\mathbf{k}} = \widehat{\mathbf{u}}^R_{\mathbf{k}} + i\widehat{\mathbf{u}}^I_{\mathbf{k}}$ and $\widehat{\mathbf{B}}_{\mathbf{k}} = \widehat{\mathbf{B}}^R_{\mathbf{k}} + i\widehat{\mathbf{B}}^I_{\mathbf{k}}$ respectively with all functions being real. Substitution of $\widehat{\mathbf{u}}_{\mathbf{k}}$ and $\widehat{\mathbf{B}}_{\mathbf{k}}$ into (5.9a) and (5.9b) then yields evolution equations for $\widehat{\mathbf{u}}^R_{\mathbf{k}}$, $\widehat{\mathbf{u}}^I_{\mathbf{k}}$, $\widehat{\mathbf{B}}^R_{\mathbf{k}}$ and $\widehat{\mathbf{B}}^I_{\mathbf{k}}$. Substitution of the initial conditions of the Group C run, $\widehat{\mathbf{u}}_{\mathbf{k}} = i\widehat{\mathbf{u}}^I_{\mathbf{k}}$ and $\widehat{\mathbf{B}}_{\mathbf{k}} = \widehat{\mathbf{B}}^R_{\mathbf{k}}$, into these equations then yields equations (5.10a)-(5.10d).

$$\frac{\partial \widehat{\mathbf{B}}^R_{\mathbf{k}}}{\partial t} + \eta \mathbf{k}^2 \widehat{\mathbf{B}}^R_{\mathbf{k}} = -\mathbf{k} \times \sum_{\mathbf{m}} (\widehat{\mathbf{u}}^I_{\mathbf{k}-\mathbf{m}} \times \widehat{\mathbf{B}}^R_{\mathbf{m}}) \tag{5.10a}$$

$$\frac{\partial \widehat{\mathbf{B}}^I_{\mathbf{k}}}{\partial t} = 0 \tag{5.10b}$$

$$\frac{\partial \widehat{\mathbf{u}}^R_{\mathbf{k}}}{\partial t} = 0 \tag{5.10c}$$

$$\frac{\partial \widehat{\mathbf{u}}^I_{\mathbf{k}}}{\partial t} + \nu \mathbf{k}^2 \widehat{\mathbf{u}}^I_{\mathbf{k}} = \widehat{\mathbf{F}}^R_{\mathbf{k}} - \mathbf{P} \sum_{\mathbf{m}} \left(\widehat{\mathbf{u}}^I_{\mathbf{k}-\mathbf{m}} \times (\mathbf{m} \times \widehat{\mathbf{u}}^I_{\mathbf{m}}) + \widehat{\mathbf{B}}^R_{\mathbf{k}-\mathbf{m}} \times (\mathbf{m} \times \widehat{\mathbf{B}}^R_{\mathbf{m}}) \right) \tag{5.10d}$$

From equations (5.10b) and (5.10c) we see that if $\widehat{\mathbf{B}}_{\mathbf{k}}$ is initially real and $\widehat{\mathbf{u}}_{\mathbf{k}}$ is initially imaginary then they will remain so. I further note that if our initial conditions are $\widehat{\mathbf{u}}_{\mathbf{k}} = i\widehat{\mathbf{u}}^I_{\mathbf{k}}$ and $\widehat{\mathbf{B}}_{\mathbf{k}} = i\widehat{\mathbf{B}}^I_{\mathbf{k}}$ then we obtain similar evolution equations however here it is $\widehat{\mathbf{u}}^R_{\mathbf{k}}$ and $\widehat{\mathbf{B}}^R_{\mathbf{k}}$ that cannot grow. The Group C evolution that we see can therefore be explained as follows. Initially the magnetic field is even and the flow is odd and so the system does not evolve to the solution observed for the other initial conditions as the odd component of the magnetic field cannot grow. The fields thus evolve to the first SSS and remain there for a large number of timesteps. During this period the dot product of the flow and magnetic fields is odd and so H_0 is necessarily zero. However as the numerical simulation evolves numerical rounding errors cause the imaginary component of $\widehat{\mathbf{B}}$ to become non-zero and it subsequently grows in time. When this happens a symmetry breaking occurs and the

magnetic field transitions to a second state where it is now odd. This transition is captured by H_0 due to the quantity increasing from zero as the imaginary component of $\widehat{\mathbf{B}}$ grows, hence the quantities ability to pre-empt the second growth phase.

The short, close to statistically steady, state observed within Group B occurs due to the weakness of the imaginary component of $\widehat{\mathbf{B}}$ however the symmetry break is expedited due to it being initially non-zero and the system settles quickly onto the solution with $\widehat{\mathbf{B}}$ odd. For Group A the energy in the odd component already exceeds that of the even component and so the system converges immediately to the odd solution.

Within a Group C run both energies as well as H_0 on visual inspection (see figure 5.5) show changes that are potentially exponential in nature.

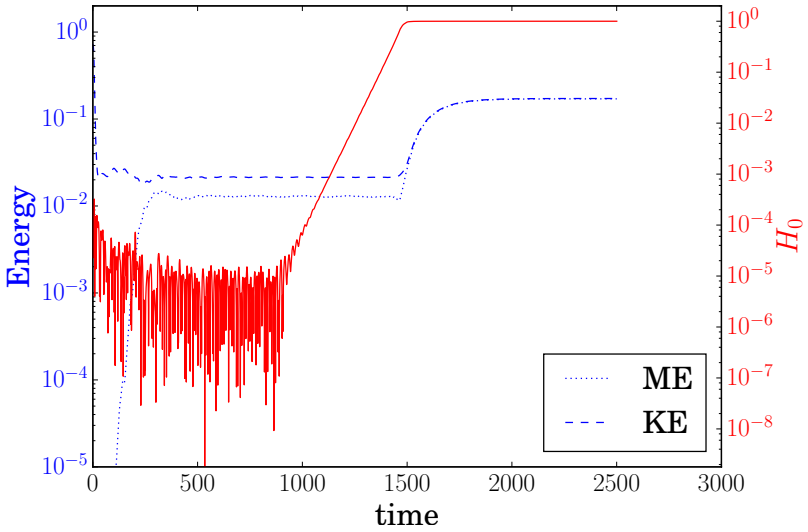

Figure 5.5: Energies (left axis) and H_0 (right axis) against growth rate. The initial ME, ME and KE in the second growth phase and the rapid growth rate of alignment all potentially appear to grow exponentially in time.

To examine this I perform a linear least squares fit on $\ln(ME)$, $\ln(KE)$ and $\ln(H_0)$ during a number of time intervals. I find that the initial growth of the magnetic energy is exponential with a growth rate, σ of 0.053. I also find that the alignment grows exponentially with a growth rate of 0.02. In both cases the r^2 value is 0.99 showing that the quantities fit well to an exponential. I find however that the second growth phase of ME and KE results in too small an increase in the energies to be able to discern between exponential and linear growth of the energies as both have a similar r^2 value. In figure 5.6 I show the growth rates

and the regions where they were measured for the initial ME and the exponential growth phase of H_0.

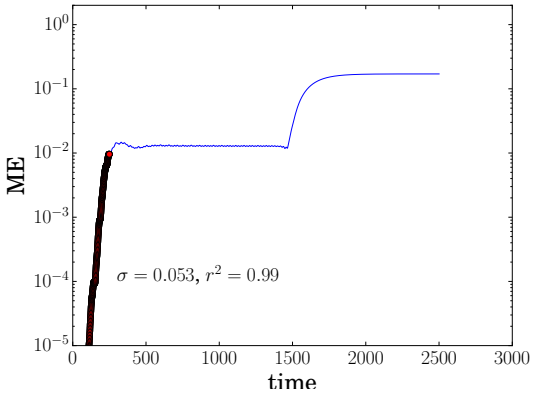

(a) Plot of the magnetic energy and its exponential growth rate during the kinematic phase of the dynamo.

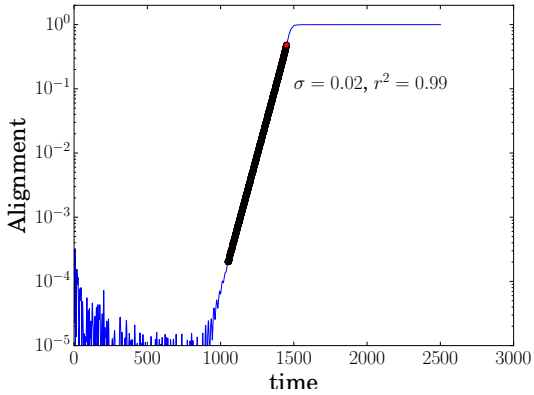

(b) Plot of the alignment quantity, H_0, and its exponential growth rate before the second growth phase of the dynamo.

Figure 5.6: Case A: $\mathbf{F}_A$ with $\mathbf{u}_0 = \mathbf{F}/\nu$, $1/\nu = 1/\eta = 100$ and a random Fourier magnetic field which has real and imaginary components of order $O(10^{-4})$.

The exponential nature of the initial ME is well explained by the theory of kinematic dynamos. The magnetic energy has however already saturated prior to the exponential growth of the alignment and therefore it cannot be growth of the magnetic field's magnitude that is driving the exponential growth of alignment. A clue as to where this originates can be seen in figure 5.4b and the growth of the energy in the odd component of the magnetic field, E_{IM}. I take the energy in the even and odd component of the magnetic field as in equations (5.7c) and (5.7d) and the energy in the even and odd components of the flow as in equations (5.11c) and (5.11d).

$$\widehat{\mathbf{u}}^R_{\mathbf{k}} = \Re\{\widehat{\mathbf{u}}_{\mathbf{k}}\} \qquad (5.11a) \qquad \widehat{\mathbf{u}}^I_{\mathbf{k}} = \Im\{\widehat{\mathbf{u}}_{\mathbf{k}}\} \qquad (5.11b)$$

$$E_{UR} = \sum_{\mathbf{k}} |\widehat{\mathbf{u}}^R_{\mathbf{k}}|^2 \qquad (5.11c) \qquad E_{UIM} = \sum_{\mathbf{k}} |\widehat{\mathbf{u}}^I_{\mathbf{k}}|^2 \qquad (5.11d)$$

These quantities are plotted for the time period where H_0 is growing exponentially in figure 5.7. We see that the growth rate, σ, of H_0 is half that of E_{UR} and E_{IM}. The growth rate of the alignment is therefore due to the exponential growth of $\widehat{\mathbf{u}}^R_{\mathbf{k}}$ and $\widehat{\mathbf{B}}^I_{\mathbf{k}}$.

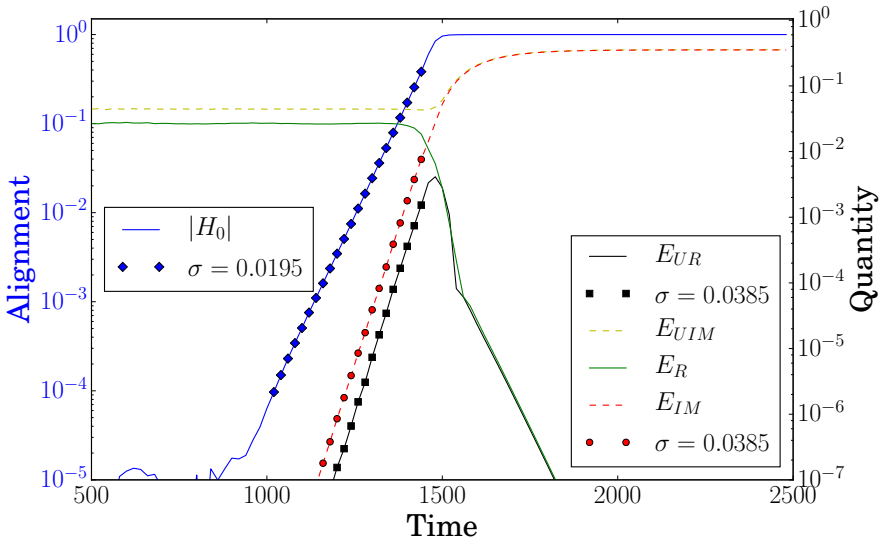

Figure 5.7: Plot of the exponential growth of H_0. This coincides with exponential growth of the energy within $\widehat{\mathbf{u}}_{\mathbf{k}}^R$ and $\widehat{\mathbf{B}}_{\mathbf{k}}^I$. The growth of H_0 is half that of the energies.

To see why this is the case I assume that the small parts of the magnetic and flow field are multiplied by an exponential, as shown in equations (5.12a) and (5.12b).

$$\widehat{\mathbf{B}}_{\mathbf{k}} = \widehat{\mathbf{B}}_{\mathbf{k}}^R + i\widehat{\mathbf{B}}_{\mathbf{k}}^I \exp(\sigma t) \qquad (5.12a) \qquad \widehat{\mathbf{u}}_{\mathbf{k}} = \widehat{\mathbf{u}}_{\mathbf{k}}^R \exp(\sigma t) + i\widehat{\mathbf{u}}_{\mathbf{k}}^I \qquad (5.12b)$$

The magnetic and kinetic energies are then shown in equations (5.14) and (5.15), where $\star$ denotes a complex conjugate.

$$\begin{aligned} ME &= \frac{1}{2}\sum_{\mathbf{k}} \widehat{\mathbf{B}}_{\mathbf{k}} \left(\widehat{\mathbf{B}}_{\mathbf{k}}\right)^{\star} \\ &= \frac{1}{2}\sum_{\mathbf{k}} \left[\widehat{\mathbf{B}}_{\mathbf{k}}^R \widehat{\mathbf{B}}_{\mathbf{k}}^R + \widehat{\mathbf{B}}_{\mathbf{k}}^I \widehat{\mathbf{B}}_{\mathbf{k}}^I \exp(2\sigma t)\right] && (5.13) \\ &\approx \frac{1}{2}\sum_{\mathbf{k}} \widehat{\mathbf{B}}_{\mathbf{k}}^R \widehat{\mathbf{B}}_{\mathbf{k}}^R && (5.14) \\ KE &\approx \frac{1}{2}\sum_{\mathbf{k}} \widehat{\mathbf{u}}_{\mathbf{k}}^I \widehat{\mathbf{u}}_{\mathbf{k}}^I && (5.15) \end{aligned}$$

The imaginary term is neglected in (5.13) due to it being much smaller than the other term for the times considered. I can now calculate H_0. This is shown in equation (5.16) where use has been made of the fact that odd functions are zero over the domain.

$$\begin{aligned} H_0 &= \frac{1}{16\pi^3\sqrt{ME}\sqrt{KE}} \left| \sum_{\mathbf{k}} \widehat{\mathbf{u}}_{\mathbf{k}} \left(\widehat{\mathbf{B}}_{\mathbf{k}}\right)^{\star} \right| \\ &= \frac{\exp(\sigma t)}{16\pi^3\sqrt{ME}\sqrt{KE}} \left| \sum_{\mathbf{k}} \left(\widehat{\mathbf{u}}_{\mathbf{k}}^R \widehat{\mathbf{B}}_{\mathbf{k}}^R + \widehat{\mathbf{u}}_{\mathbf{k}}^I \widehat{\mathbf{B}}_{\mathbf{k}}^I\right) \right| && (5.16) \end{aligned}$$

From (5.16) we therefore see that exponential growth of $\widehat{\mathbf{u}}^R_{\mathbf{k}}$ and $\widehat{\mathbf{B}}^I_{\mathbf{k}}$ directly leads to exponential growth of alignment. This approximation then holds until the neglected terms, $\widehat{\mathbf{B}}^I_{\mathbf{k}}\widehat{\mathbf{B}}^I_{\mathbf{k}}\exp(2\sigma t)$ and $\widehat{\mathbf{u}}^R_{\mathbf{k}}\widehat{\mathbf{u}}^R_{\mathbf{k}}\exp(2\sigma t)$, within the approximations (5.14) and (5.15) are no longer negligible.

In summary, I have shown that obtaining the first statistically steady state within the Archontis dynamo is a consequence of choice of initial conditions. Achieving the final state of the Archontis dynamo requires the growth of the odd component of the magnetic field. If an initial magnetic field is chosen such that the odd component cannot grow then the energies saturate at a first SSS where they stay until numerical imperfections cause the growth of the odd component of the energy. A symmetry break with the magnetic and flow fields then transitions the fields to a second SSS which corresponds to the final state found for a more general random initial condition. The first statistically steady state is therefore not necessary to obtain the final state when beginning with a random seed field and is not expected to be a general property of other aligned dynamos that may be found.

5.3 Local and Global Quantities Within a Group C Run of the Archontis Dynamo

In this section I examine the evolution of the Archontis dynamo where multiple SSS are present in greater detail. The initial conditions used are those used for the Group C run in section 5.2. This section is divided into two: In section 5.3.1 I look at the local values of both alignment and field strength with the aim of shedding light on the distribution of these quantities within the domain. In section 5.3.2 I then examine a number of volume average quantities taken from the evolution equations of ideal invariants.

5.3.1 Evolution of Local Quantities

I begin by looking at $z = 0$ contours of the magnetic and flow fields. Figure 5.8 shows the positions on the kinetic and magnetic energy curves that I will subsequently plot and discuss. The times chosen were $t = [220, 600, 1200, 1460, 1500, 1540, 1700, 2100]$. The first

three times were chosen to show typical magnetic and kinetic energy structures during the initial magnetic field growth period and the subsequent statistically steady state and are shown within figures 5.9a-5.10a respectively. Figures 5.10b-5.12b then show the initiation of the exponential growth phase followed by the subsequent saturation to a second statistically steady state.

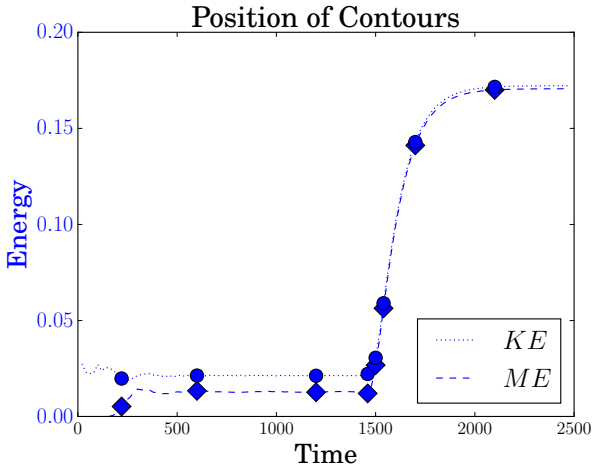

Figure 5.8: Plot of positions of contours in figures 5.9a-5.12a.

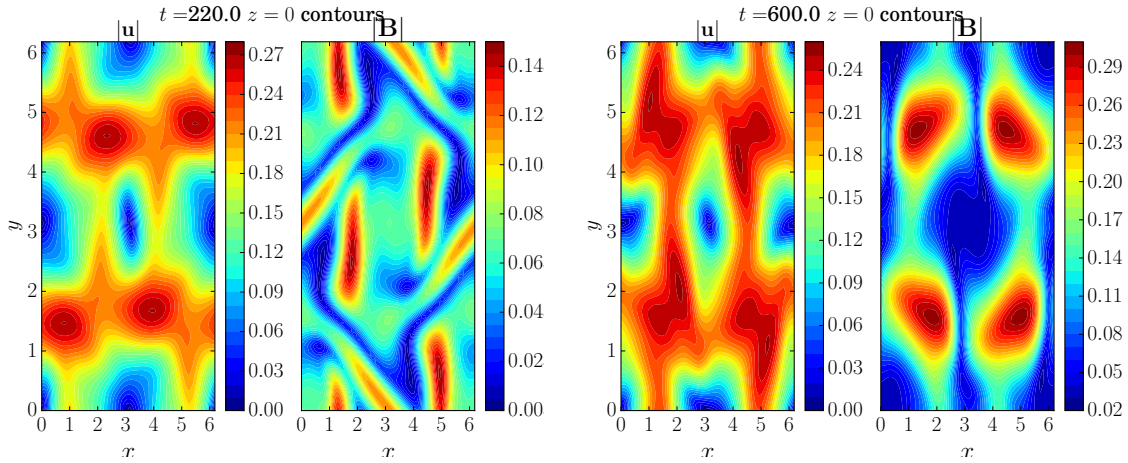

(a) $t = 220$ (b) $t = 600$

Figure 5.9: Plot of $|\mathbf{B}|$ and $|\mathbf{u}|$ at $z = 0$.

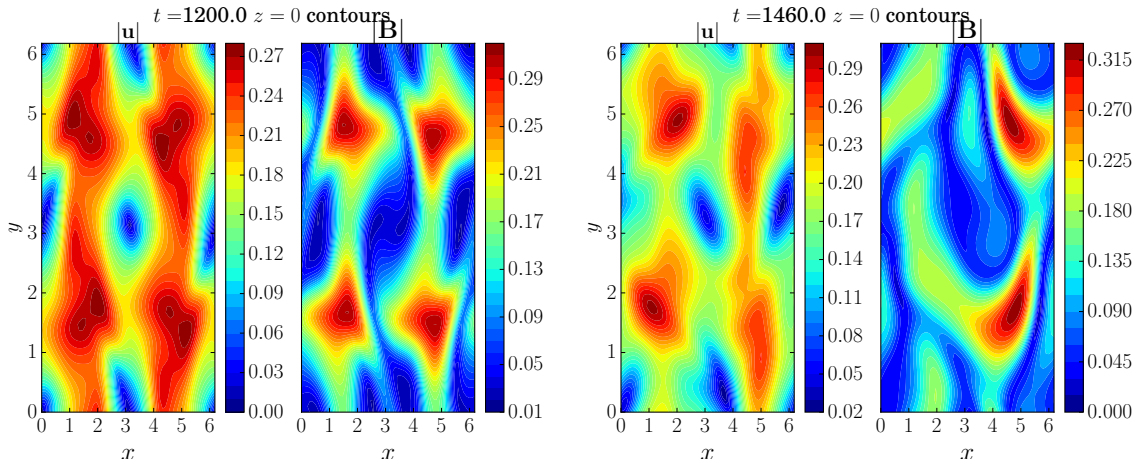

(a) $t = 1200$ (b) $t = 1460$

Figure 5.10: Plot of $|\mathbf{B}|$ and $|\mathbf{u}|$ at $z = 0$.

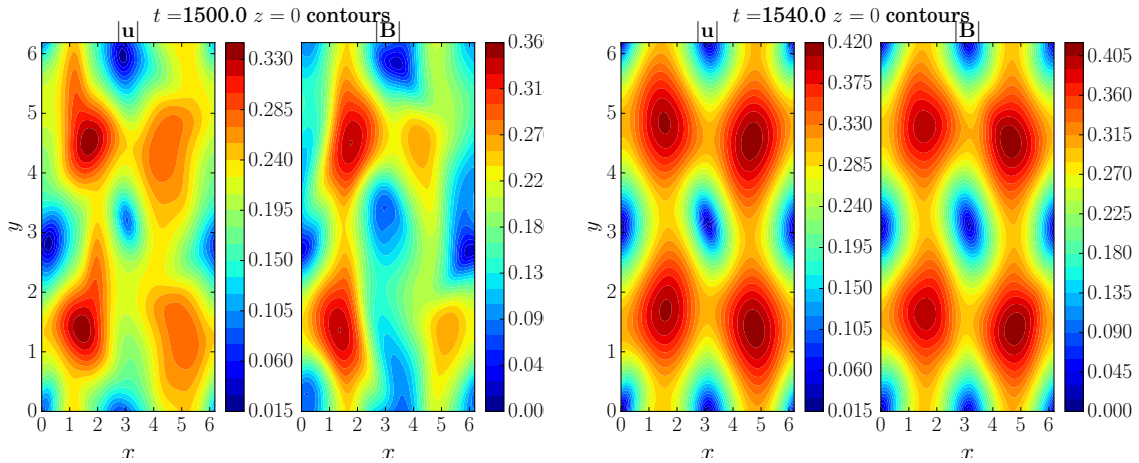

(a) $t = 1500$ (b) $t = 1540$

Figure 5.11: Plot of $|\mathbf{B}|$ and $|\mathbf{u}|$ at $z = 0$.

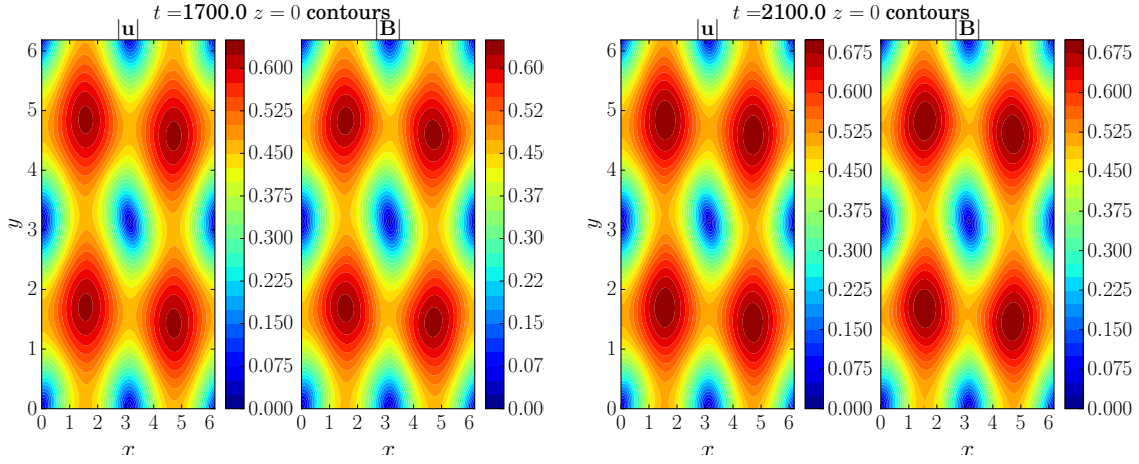

(a) $t = 1700$ (b) $t = 2100$

Figure 5.12: Plot of $|\mathbf{B}|$ and $|\mathbf{u}|$ at $z = 0$.

During the first statistically steady state we can see that the magnetic and velocity fields are still highly time dependent therefore the apparent saturation of the energies is somewhat misleading as the field structures continue to evolve. Both of the fields are made up of large eddies of strong field similar to the structures in the second statistically steady state. Figures 5.11a and 5.11b show contours immediately before and immediately after the structure begins to converge to the final state. The magnetic field structure appears to settle immediately before the second rapid growth phase of the flow and magnetic field, a result which agrees with the observation that alignment becomes maximal prior to the second growth phase.

One problem with examining contours of $|\mathbf{u}|$ and $|\mathbf{B}|$ is that they remove any information about the sign of the respective fields. One question that may be asked concerns the nature of the weak volume average of alignment observed within the first SSS of a Group C run (shown in figure 5.4a). This has already been shown to be linked to the fact that here the magnetic field is even however a number of different scenarios may produce a weak volume average, for example small values of alignment locally everywhere or almost equal amounts of positive and negative alignment of the same magnitude everywhere. Which of these is the case here is this question that I will now address.

I define the point-wise normalised cross-helicity H_c to be

$$H_c = \frac{\mathbf{u} \cdot \mathbf{B}}{|\mathbf{u}||\mathbf{B}|} \tag{5.17}$$

$$= \cos(\theta) \tag{5.18}$$

where θ is the angle of alignment between $\mathbf{u}$ and $\mathbf{B}$. In figures 5.13 and 5.14 I plot $z = 0$ contours of the angle θ. I also plot histograms of θ as well as the current stage of the kinetic and magnetic energies in the particular Group C run so as to illustrate where in the run the histograms and contours are taken.

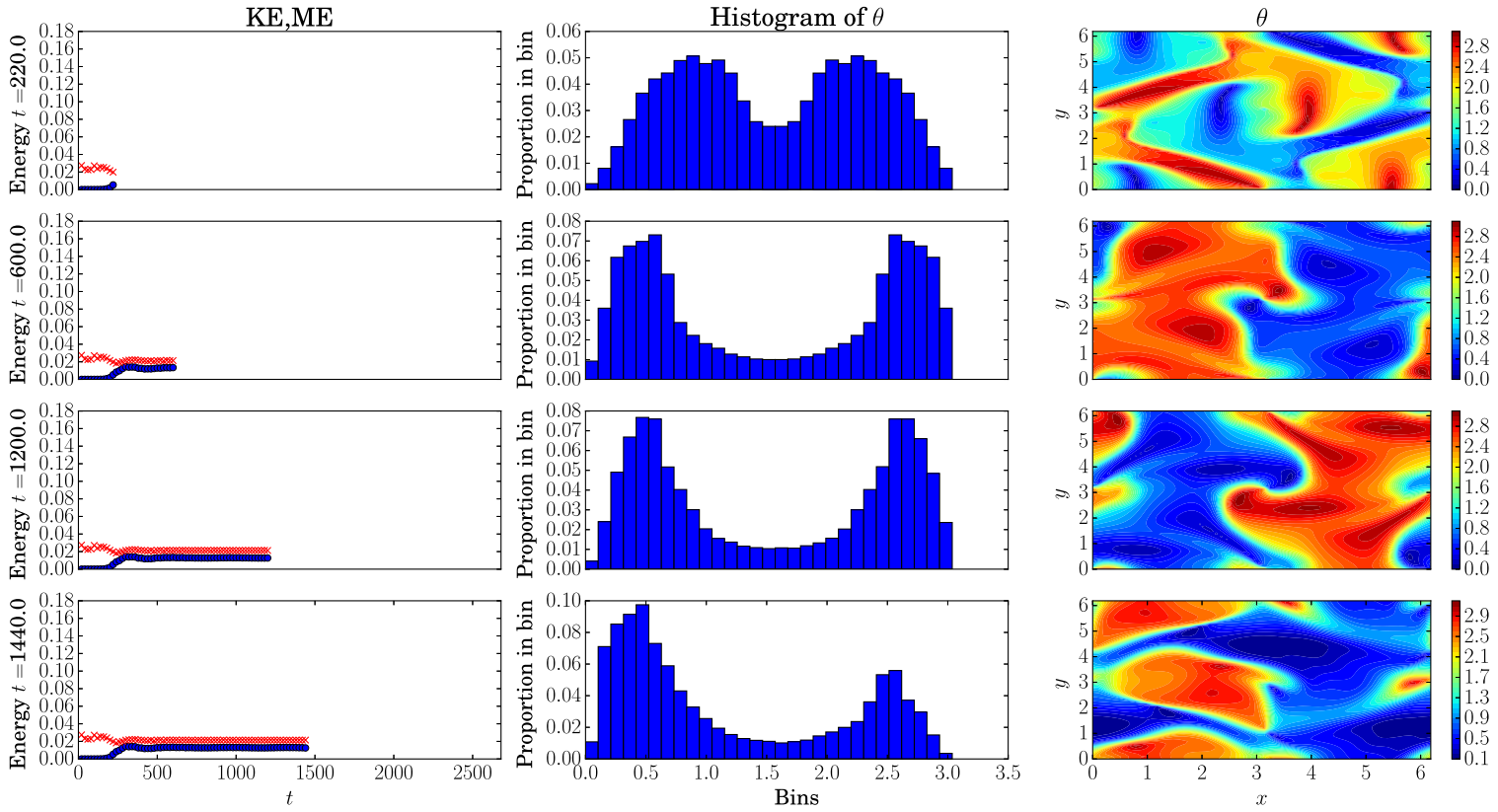

Figure 5.13: Energy, histograms of angle in radians and $z = 0$ contours of angle of alignment (radians) for $t = [220, 600, 1200, 1440]$. We see that during the first SSS the domain is made up of an almost equal amount of alignment and anti-alignment with the result being a volume average of approximately 0. Towards the end of the first SSS the balance between aligned and anti-aligned field becomes skewed towards positively aligned.

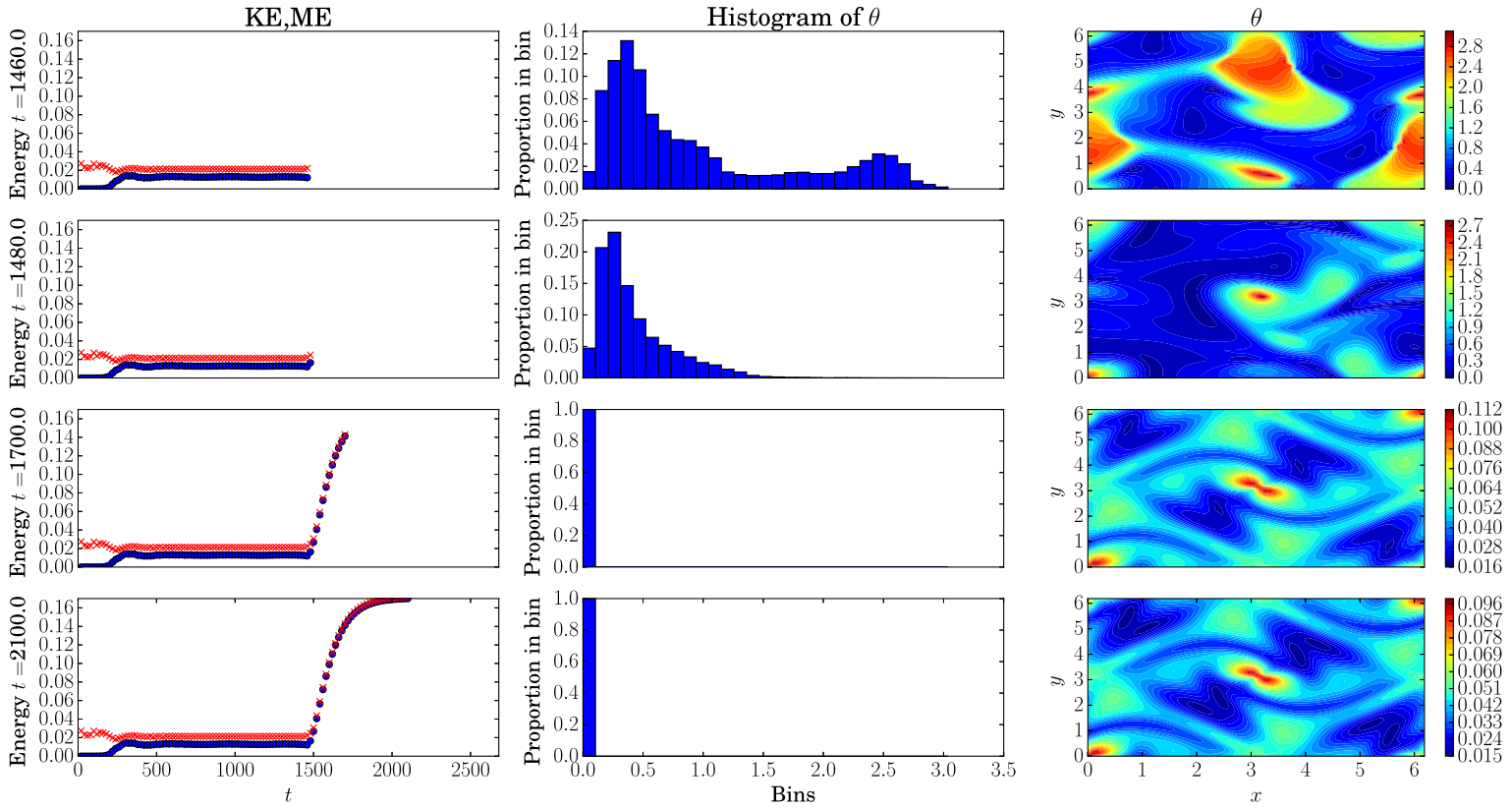

Figure 5.14: Energy, histograms of angle in radians and $z = 0$ contours of angle of alignment (radians) for $t = [1460, 1480, 1700, 2100]$. Plot shows that as we enter the second rapid growth phase the magnetic and fluid fields become entirely positively aligned.

Figure 5.13 shows the histograms and contour plots at $t = [220, 600, 1200, 1440]$. These times range from arrival at the first SSS ($t = 220$) to the end of the first SSS ($t = 1500$). We see that during most of the first SSS there is a roughly equal balance of aligned and anti-aligned field with θ being concentrated at $(0, 0.3)$ and $(2.6, 2.8)$. Furthermore we observe within the contour plots that the alignment is concentrated into large regions of alignment and large regions of anti-alignment rather than small chaotic regions of each.

We see that as we reach the end of the first SSS ($t = 1440$) an imbalance forms with the ratio of aligned to anti-aligned field increasing. This is not quite so apparent in the contour plots. However, as they are only a slice they do not show the complete picture. In figure 5.14 I then show $t = [1460, 1480, 1700, 2100]$ showing the time immediately prior to onset of the second rapid growth phase until saturation at the second SSS. We observe that the second growth phase occurs once alignment is almost entirely positive within the domain, although $t = 1460$ does show that some small regions of anti-alignment are present at this time.

Figure 5.14 further shows that during the second growth phase and the proceeding saturated state the entire domain is made up of positive alignment. The results within figures 5.13 and 5.14 therefore show that it is incorrect to view the first SSS as having no alignment. What we actually have is a domain made up of approximately equal amounts of large regions of strong positive and negative alignment. Rather than an increased magnitude of alignment within the domain the alignment mechanism instead changes the sign of the regions of anti-alignment. If the amount of absolute alignment within the domain rather than the average positive or negative amount is what we are interested in we may define an alternate measure H_2,

$$H_2 = \frac{1}{2} \frac{\int_v |\mathbf{u} \cdot \mathbf{B}| dV}{\sqrt{KE}\sqrt{ME}} \tag{5.19}$$

which does not allow for cancellation of positive and negative field and so gives a measure of the absolute alignment present. Figure 5.15 shows this measure of alignment as well as the old measure (both in red) with the kinetic and magnetic energies in blue.

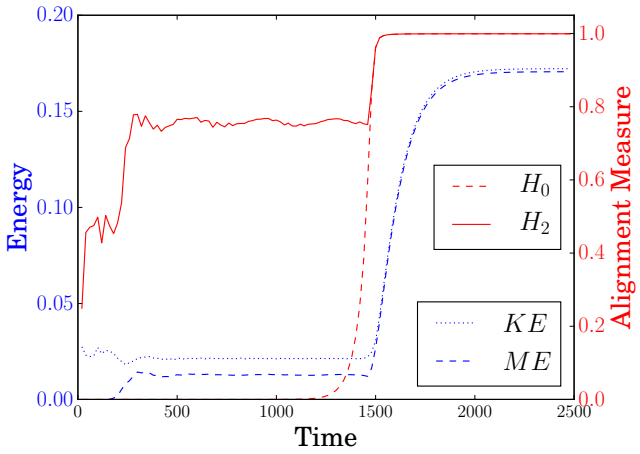

Figure 5.15: ME and KE (left axis), H_0 and H_2 (right axis). We see that H_2 reaches a value of 0.8 immediately prior to saturation of the energies to the first SSS and that this remains approximately steady until the second rapid growth phase. H_0 is weak during the first SSS. From figures 5.13 and 5.14 we see that this is in fact due to the amount of positive and negative alignment within the domain being approximately equal. Immediately prior to the second rapid growth phase the absolute alignment and the alignment become equal. This occurs due to an increase in the proportion of alignment within the domain that is positive over the proportion that is negative.

We see that upon entering the first SSS H_2 saturates to a value of approximately 0.8 where it stays until it increases again when the alignment increases immediately prior to the second growth phase. By this new measure therefore the change in alignment prior to the second growth phase is much more modest.

Examination of local quantities has therefore shown that the negligible alignment observed during the first SSS of a Group C run is a result of cancellation of significant quantities of alignment and anti-alignment. This balance of aligned and anti-aligned fields in the first SSS has been shown in section 5.2 to be a result of the flow being odd and the magnetic field being even. As such the Group C run behaves in a similar manner to the other initial conditions in that the flow and magnetic field rapidly become strongly aligned, as shown by H_2. However, due to the magnetic field being even in the first SSS, the strong alignment is split evenly between regions of strongly positive alignment and regions of strongly negative alignment. A zero average H_0 within Group C runs therefore masks the rapid alignment of the fields when, in fact, the Group C runs share this property with all initial conditions in the Archontis dynamo.

5.3.2 Evolution of Volume Average Quantities

In this section I examine the components of the evolution equations for cross-helicity and total energy for a Group C run from section 5.2. I investigate how the forcing and dissipation terms in each evolution equation evolve and, at particular times, cause either saturation or growth of the quantity.

By taking the dot product of the equation of motion with $\mathbf{u}$ and the induction equation with $\mathbf{B}$, summing the two, and volume averaging whilst assuming periodic boundary conditions we can construct the evolution equation for the total energy of the system. This equation is shown in (5.20), where $V = 8\pi^3$, and the nomenclature for each term within (5.20) is shown within equation (5.21).

$$\begin{aligned} V^{-1}\frac{d}{dt}\int_v \frac{\mathbf{u}^2+\mathbf{B}^2}{2}dV =& V^{-1}\int_v \mathbf{u}\cdot(\mathbf{B}\cdot\nabla)\mathbf{B}dV + V^{-1}\int_V \mathbf{B}\cdot\nabla\times(\mathbf{u}\times\mathbf{B})dV \\ &+ V^{-1}\nu\int_v \mathbf{u}\cdot\nabla^2\mathbf{u}dV + V^{-1}\eta\int_V \mathbf{B}\cdot\nabla^2\mathbf{B}dV \\ &+ V^{-1}\int_V \mathbf{u}\cdot\mathbf{F}dV \end{aligned} \tag{5.20}$$

$$V^{-1}\frac{d}{dt}\int_v \frac{\mathbf{u}^2+\mathbf{B}^2}{2}dV = T_L + T_I + T_\nu + T_\eta + T_F \tag{5.21}$$

$$= T_L + T_I + T_D + T_F \tag{5.22}$$

$$= T \tag{5.23}$$

By making use of a number of vector identities as well as Gauss' theorem to remove integrals of divergences across the periodic boundaries the following can be shown to be true:

$$\int_v \mathbf{u}\cdot(\mathbf{B}\cdot\nabla)\mathbf{B}dV = -\int_v \mathbf{J}\cdot(\mathbf{u}\times\mathbf{B})dV \tag{5.24}$$

$$\int_V \mathbf{B}\cdot\nabla\times(\mathbf{u}\times\mathbf{B})dV = \int_v \mathbf{J}\cdot(\mathbf{u}\times\mathbf{B})dV \tag{5.25}$$

Where $\mathbf{J} = \nabla \times \mathbf{B}$. In theory we should therefore find that T_I and T_L cancel. However due to numerical accuracy we find this to not be the case and we must therefore take this into account during our analysis.

Evolution of the total energy in the system is therefore governed by energy transfer to the flow by the Lorentz force and energy transfer to the magnetic field by induction (which should cancel over the volume), dissipation of both the flow and magnetic field and an injection of energy into the system from the forcing. Figure 5.16 shows each of these quantities. Each quantity has been normalised by the maximum of T_F, T_ν and T_η at each time step so as to give a sense of size for each of the components. These quantities will be useful in interpreting how the energies evolve.

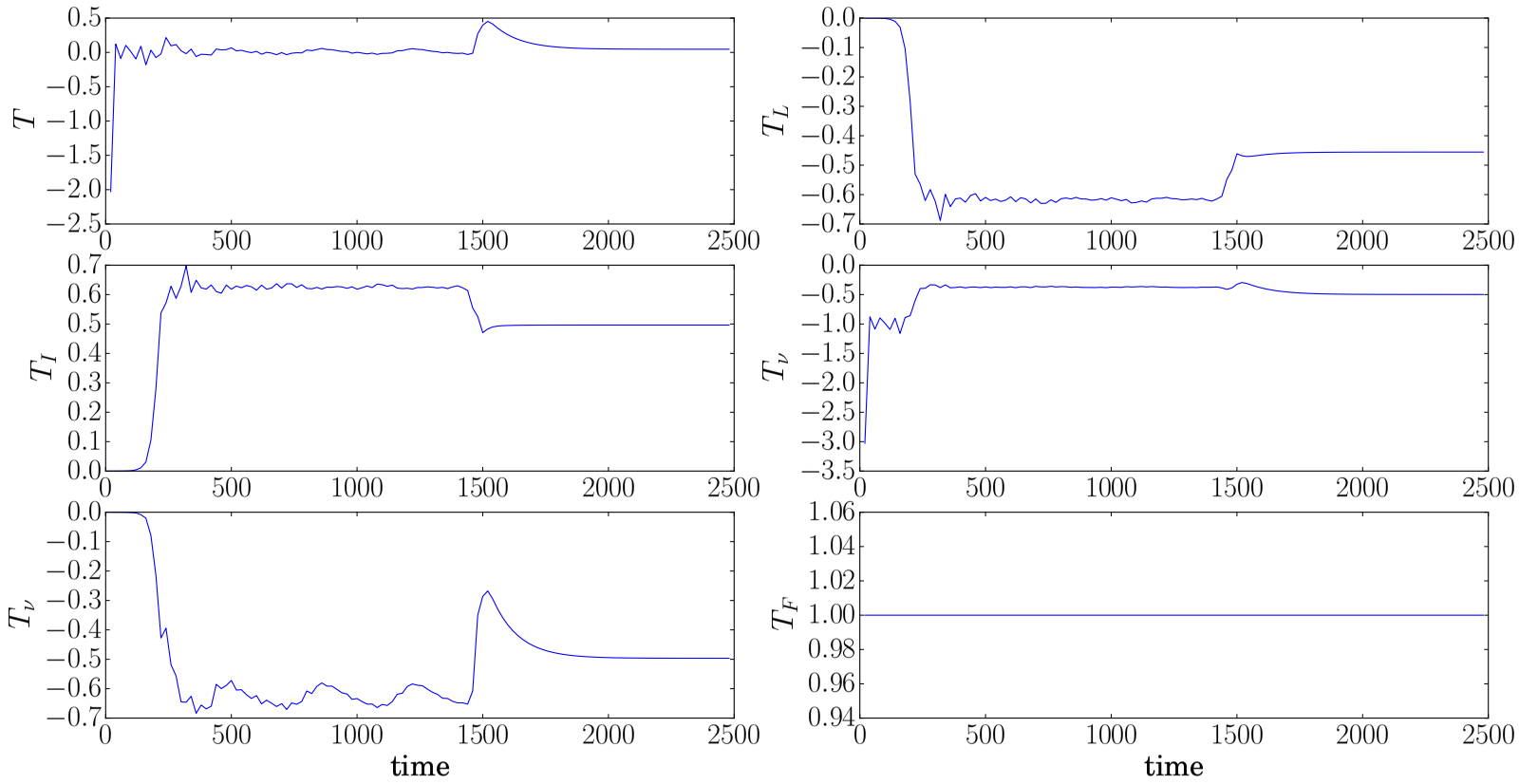

Figure 5.16: Components of energy evolution equation normalised by the largest value out of T_F, T_ν and T_η at each timestep. We see that T_F is the largest component throughout. The small value of T shows that significant cancellation of components occurs at each timestep.

During this discussion I divide the energy evolution into four sections. These are shown in figure 5.17.

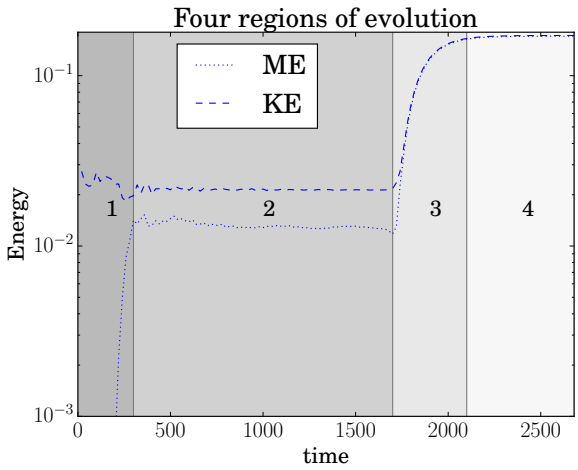

Figure 5.17: Plot KE and ME subdivided into four regions.

Section 1 is the first growth phase where the magnetic field grows to a size comparable to that of the flow field. Section 2 is the first statistically steady state (SSS). Section 3 is the second growth phase. Finally section 4 is the second SSS.

Figure 5.18 shows the magnetic and kinetic energies as well as the total energy change, the sum of the Lorentz force and induction components and the sum of the forcing and dissipative components. In region 1 (the kinematic growth phase) we see that the total energy change is governed by the difference between forcing and diffusion terms. We also see that in this section the errors, as a result of a non-zero $T_L + T_I$, are increasing as the magnetic field grows. By looking at figure 5.16 we can see how saturation to the first statistically steady state occurs. We see that a balance is achieved by force balancing the two dissipation terms through an increase in magnetic dissipation but a decrease in fluid dissipation, both relative to the forcing term.

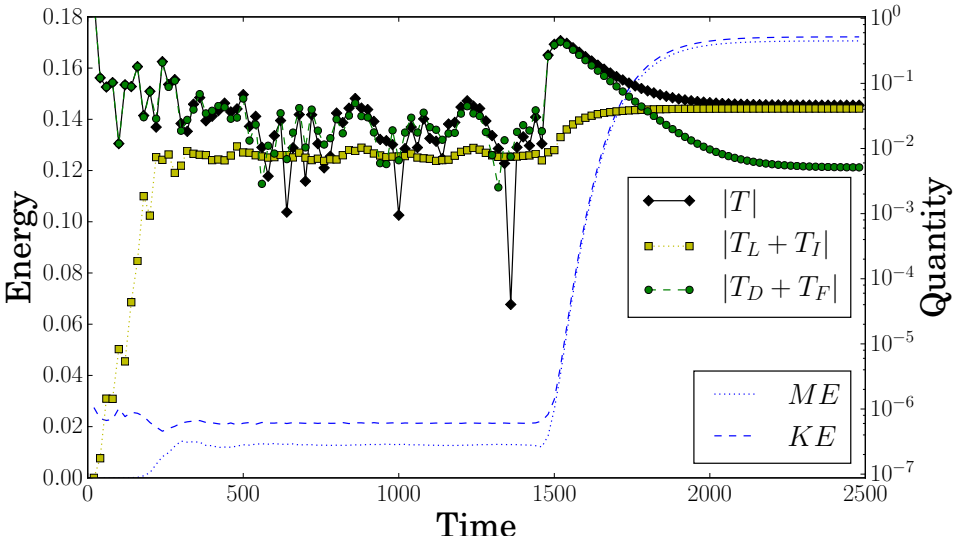

Figure 5.18: Components of the energy evolution equation and the energy. These are normalised by the maximum of T_ν, T_η and T at each timestep.

During the first statistically steady state a forcing and dissipation balance keeps the change in energy small. During this phase $T_L + T_I$ is weaker than the force dissipation balance but is not negligible. We see that at a number of times $T_L + T_I$ exceeds the force dissipation balance and therefore influences the change in energy. Region 3, the second growth phase, then occurs through a reduction in the magnitude of both the magnetic and fluid dissipation terms allowing the forcing to drive the system once more. This can be seen in figure 5.16. Saturation to a final SSS is then achieved by the dissipation terms growing in relative strength again to cancel the contribution from the forcing. For large time we then see that the total energy is almost completely controlled by the errors due to incomplete cancellation of T_L and T_I and therefore we can conclude that the kinetic and magnetic energies have saturated. Finally I note that the maxima of $T_F + T_D$ is achieved during region 3 immediately prior to the alignment becoming maximal.

I now discuss how alignment evolves. As shown in section 3.4 we may define an evolution equation for the alignment

$$V^{-1}\frac{d}{dt}\int_v \mathbf{u}\cdot\mathbf{B}dV = V^{-1}\int_v \mathbf{B}\cdot\mathbf{F}dV + V^{-1}\nu\int_v \mathbf{B}\cdot\nabla^2\mathbf{u}dV + V^{-1}\eta\int_v \mathbf{u}\cdot\nabla^2\mathbf{B}dV \quad (5.26)$$

$$= T_{AF} + T_{A\nu} + T_{A\eta} \quad (5.27)$$

$$= T_A \quad (5.28)$$

this then allows us to examine the role of each of the contributing terms in the increase in alignment seen prior to the second growth phase. The result is shown in figure 5.19. We see that T_{AF} is positive whereas the diffusive terms are negative. The result is that significant cancellation between the two occurs with cancellation being the reason that alignment saturates rather than each term individually becoming weak.

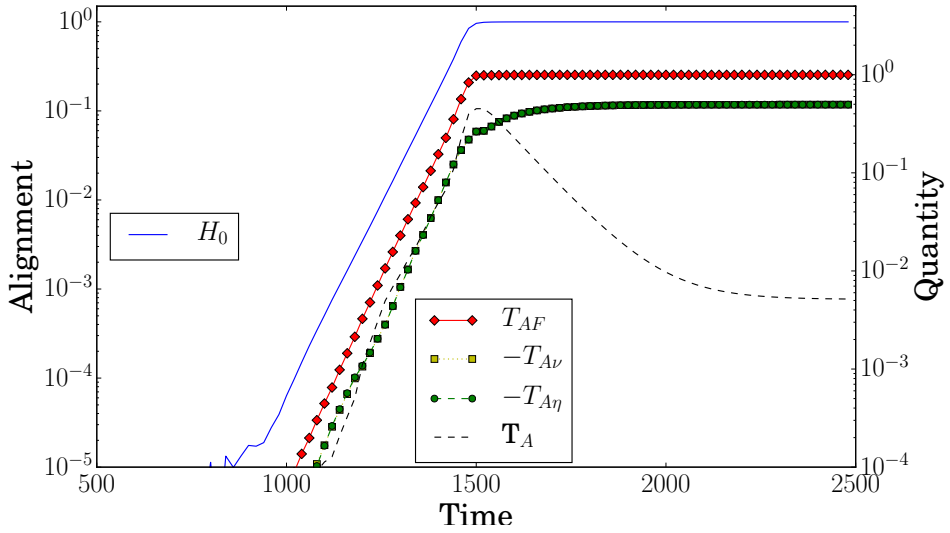

Figure 5.19: Each of the alignment evolution quantities plotted against time and with alignment. The alignment quantities values correspond to those on the right hand axis. The evolution curve of $T_{A\nu}$ is obscured by the curve for $T_{A\eta}$ due to them being almost identical

In the same vein as the work within section 5.3.1 we can also examine the distributions of the integrands within equation (5.26) at specific times using histograms. This is shown within figure 5.20a at $t = 1000$ with the initial structure of a normalised $\mathbf{B} \cdot \mathbf{F}$ also shown in figure 5.20b as a reference. We see that the forcing component has a different distribution to the diffusive components. Whereas the forcing has values concentrated at the extreme ends of the possible values the diffusive values are spread over a much larger range of values (note the low value on the y axis for the diffusive components). The symmetry about 0 in all three cases ensures that we obtain an integral of approximately 0 for each. When we sum the three we see that the distribution is then centrally distributed.

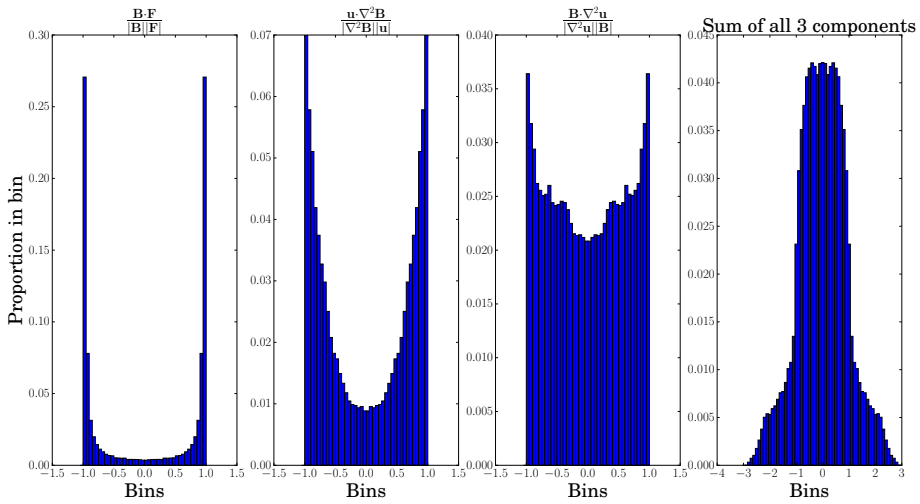

(a) Histograms at $t = 1000$. They show that T_{AF} is weak during region 2 of figure 5.17 due to a balance of strongly positive and negative whereas the other two components have a significantly more spread out distribution of values.

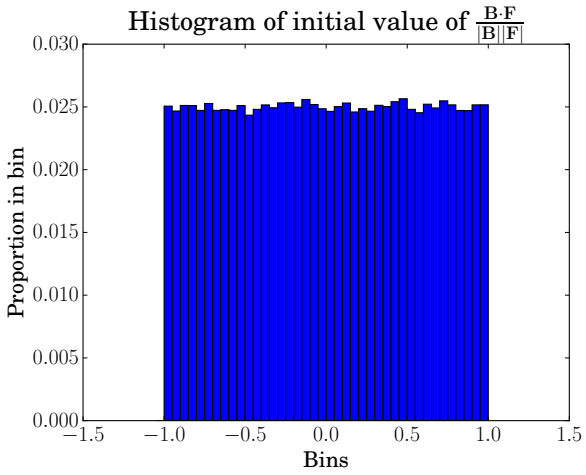

(b) Histogram of initial distribution of T_{AF}. We see that there is no preference for any values but that there is a balance between positive and negative.

Figure 5.20: Histograms of components of the cross-helicity evolution equation.

The alteration of $\mathbf{B}\cdot\mathbf{F}$ from an apparent uniform distribution to peaks at ± 1 shows that by the first SSS the magnetic energy is dominated by the component parallel (and anti-parallel) to the forcing.

To summarise, in this section a number of interesting developments in the Archontis dynamo have been found. First is that the distribution of alignment consists of large regions of aligned and large regions of anti-aligned field during the first SSS. This shows that throughout the bulk of the dynamo's evolution there is large scale organisation between the two fields. Secondly I have shown that when this is taken into account the growth in absolute alignment within the domain in going from the first SSS to the second is much

more modest. Furthermore in examining evolution of various terms in the energy evolution equation it was found that the second growth phase occurs through a reduction in diffusion, relative to the strength of the forcing term.

5.4 Varied Diffusivity within the Archontis Dynamo

In this section I consider the variation in final energy and field structures when η and ν are varied. I consider both the case where the magnetic Prandtl number $P_m = \nu/\eta$ is one as well as fixing either of η, ν and varying the other. As the forcing is of the form $\mathbf{F}_A = \nu[\sin(z), \sin(x), \sin(y)]$ the effect of varying ν becomes additionally important as the diffusivity directly influences the amplitude of the forcing as well as the contribution of diffusion to the system.

I first consider the case where $\nu = \eta$. I run a large number of simulations to obtain the smallest possible value of $1/\eta$ below which dynamo action is no longer possible. I begin all simulations using a random seed field for the Fourier transformed magnetic field $\widehat{\mathbf{B}}$ with real and imaginary components of $O(10^{-4})$. I find that the critical value for the onset of an aligned dynamo is $1/\nu = 1/\eta \geq 7$. For $1/\nu < 7$ the magnetic energy decays away to zero and as such the flow field evolves kinematically in that the magnetic field appears to play a negligible role in the evolution of the flow. Above this threshold the final flow and magnetic fields are highly aligned.

As $1/\nu$, $1/\eta$ are increased the difference between the magnetic and kinetic energies decreases, this is shown within figure 5.21 where I show both a plot of the energies as well as their difference as a percentage of the KE. Figure 5.21b also shows results of a run began with the set initial condition $\mathbf{u} = \mathbf{B} = \mathbf{F}_A/\nu$ up to $\nu = 1/50$. The agreement between the set initial condition and the seed field initial condition illustrates that the final state found is identical. The results match well with those of Cameron and Galloway within [22] who increased $1/\nu = 1/\eta$ from 100 up to 800 and showed that the difference between the kinetic and magnetic energies continued to decrease.

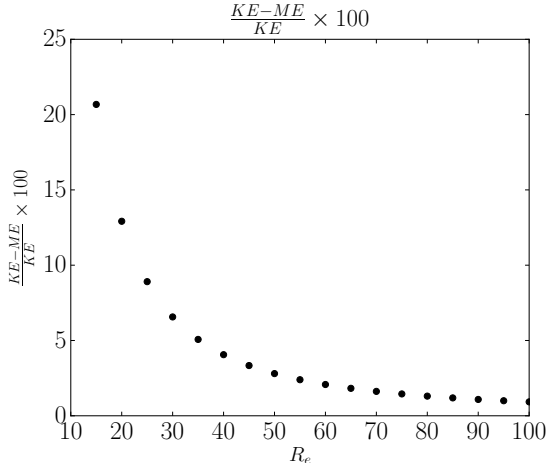

(a) Difference in energy as a percentage of the KE decreases as $1/\nu$,$1/\eta$ increase.

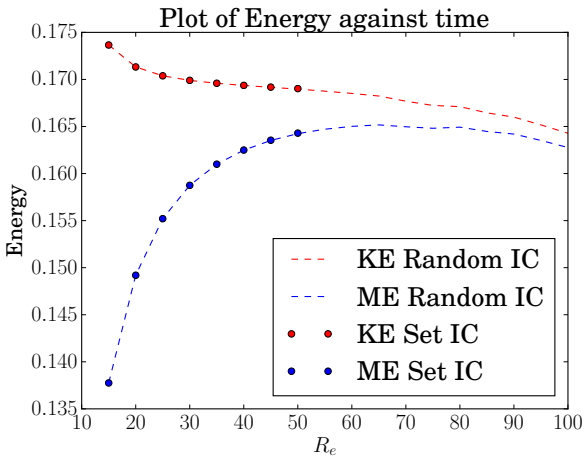

(b) Saturation values of KE and ME

Figure 5.21: $1/\nu = 1/\eta \in (15, 100)$ showing the value of the kinetic and magnetic energies, as well as their difference.

Calculation of the energy of the fields within the same mode as the Archontis forcing $\mathbf{F}_A$ as well as the alignment of the flow and magnetic field, quantified by (5.4c), is shown in figure 5.22. The percentage of the energy of $\mathbf{u}$, $\mathbf{B}$ contained within the Archontis mode is approximately 99.9% over the range of diffusivities considered and the alignment asymptotes to 1 as $1/\eta$ is increased. The main conclusion from these $\nu = \eta$ results is therefore that whilst the energies may change as the diffusivities are varied the field structures change very little.

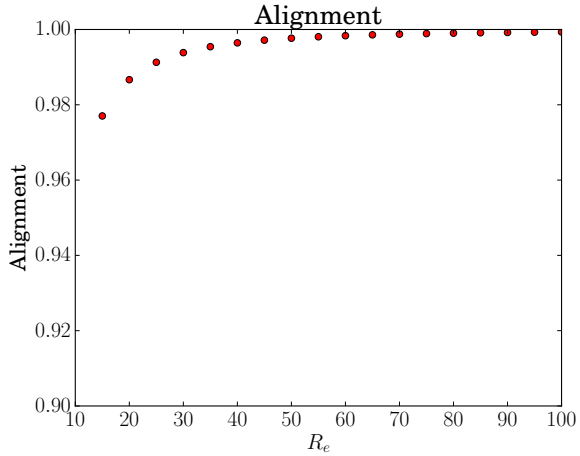

(a) Alignment quantity in equation (5.4c)

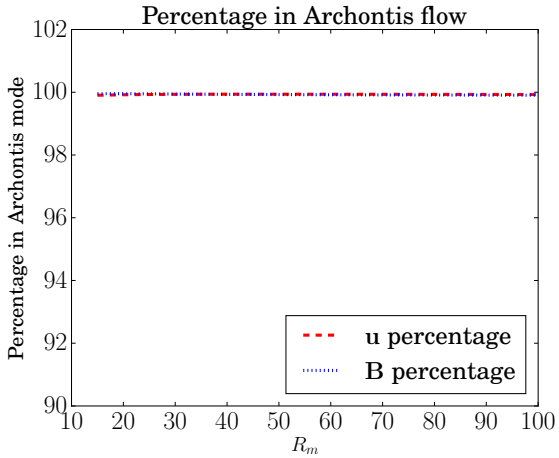

(b) Percentage in the Archontis mode

Figure 5.22: $1/\nu = 1/\eta \in (15, 100)$ showing the percentage of the energy within $\mathbf{F}_A$ and the alignment quantity in equation (5.4c).

I now consider $\nu \neq \eta$. In particular I test the assumption that the flow and magnetic field

structures will change very little as the diffusivities are varied. To do this I assume that $\mathbf{u}$, $\mathbf{B}$ are of the form $\alpha\big(\sin(z),\sin(x),\sin(y)\big)$ for some constant α and compare the resulting predicted energies against results from simulations. I set

$$\mathbf{u} = \alpha_1 \begin{pmatrix} \sin(z) \\ \sin(x) \\ \sin(y) \end{pmatrix} \qquad (5.29a) \qquad \mathbf{B} = \alpha_2 \begin{pmatrix} \sin(z) \\ \sin(x) \\ \sin(y) \end{pmatrix} \qquad (5.29b)$$

$$\mathbf{F} = \nu \begin{pmatrix} \sin(z) \\ \sin(x) \\ \sin(y) \end{pmatrix} \qquad (5.29c)$$

and note that

$$\frac{1}{V}\int_0^{2\pi}\int_0^{2\pi}\int_0^{2\pi} \sin(x)^2+\sin(y)^2+\sin(z)^2 dV = \frac{3}{2} \qquad (5.30)$$

the evolution equation for total energy is

$$\frac{d}{dt}\int_V \frac{\mathbf{u}^2+\mathbf{B}^2}{2} dV = \int_V \mathbf{F}\cdot\mathbf{u} dV + \eta\int_V \mathbf{B}\cdot\nabla^2\mathbf{B} dV + \nu\int_V \mathbf{u}\cdot\nabla^2\mathbf{u} dV \qquad (5.31)$$

and the evolution equation for cross-helicity is

$$\frac{d}{dt}\int_V \mathbf{u}\cdot\mathbf{B} dV = \int_V \mathbf{F}\cdot\mathbf{B} dV + \eta\int_V \mathbf{u}\cdot\nabla^2\mathbf{B} dV + \nu\int_V \mathbf{B}\cdot\nabla^2\mathbf{u} dV. \qquad (5.32)$$

Substituting equations (5.29a)-(5.29c) into (5.31) and (5.32) and assuming that $\alpha_1, \alpha_2 \neq 0$ we obtain

$$\nu(\alpha_1-\alpha_1^2)-\eta\alpha_2^2 = 0 \qquad (5.33a) \qquad \nu(1-\alpha_1)-\eta\alpha_1 = 0 \qquad (5.33b)$$

(5.33b) immediately yields α_1 and substituting this into (5.33a) yields α_2 provided $\eta \neq 0$.

$$\alpha_1 = \frac{\nu}{\nu+\eta} \qquad (5.34a) \qquad \alpha_2 = \pm\alpha_1 \qquad (5.34b)$$

Thus if the magnetic and fluid fields are sufficiently close to the forms shown in equations (5.29a) and (5.29b) then their energies will be at equipartition and can be shown to be

$$E = \frac{3\alpha^2}{4} \tag{5.35}$$

$$= \frac{3}{4}\left(\frac{\nu}{\eta+\nu}\right)^2 \tag{5.36}$$

I now compare this theoretical result to simulations by fixing one of either ν or η whilst varying the other over a range of values. Figure 5.23 shows the case where I fix $\nu = 1/100$ and vary η. Below approximately $\eta = 1/25$ no dynamo action is found within the simulations, the magnetic field decays to zero and the flow is then free to evolve hydrodynamically. As $1/\eta$ is increased above this minimum threshold both the magnetic and kinetic energies increase and this behaviour continues up until the largest $1/\eta$ examined, $\eta = 1/100$. For the values where dynamo action is achieved the flow and magnetic fields are highly aligned with the alignment asymptotically approaching 1 as $1/\nu$ is increased. Furthermore, comparing the theoretical results to the numerical simulations (figure 5.23a) shows that the theoretical and numerical results are in good agreement at the lowest $1/\eta$ but begin to differ at the larger values.

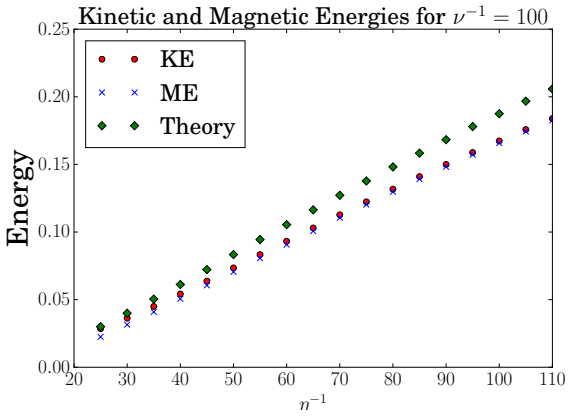

(a) Energy increases as $1/\eta$ increases

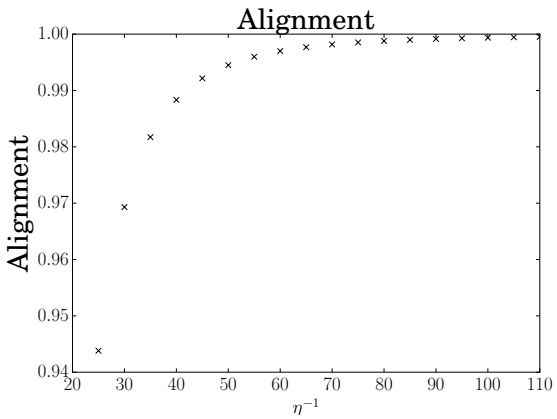

(b) Once a dynamo is achieved the alignment rapidly becomes almost perfect.

Figure 5.23: $\nu = 1/100$ and $1/\eta \in (25, 100)$.

In figure 5.24 I show kinetic and magnetic energy saturation values for values of $1/\nu$ from 5 to 100 as well as alignment. The energies are seen to decrease as $1/\nu$ increases. In figure 5.24b I show the predicted energies against the theoretical values. As with the results for varying η we see that the simulation results appear to agree well with the simulation

results.

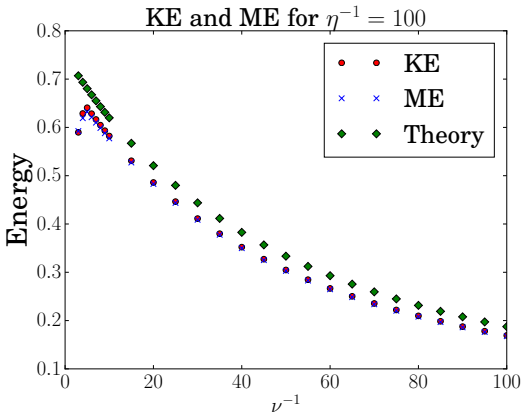

(a) Energies decrease with increasing $1/\nu$

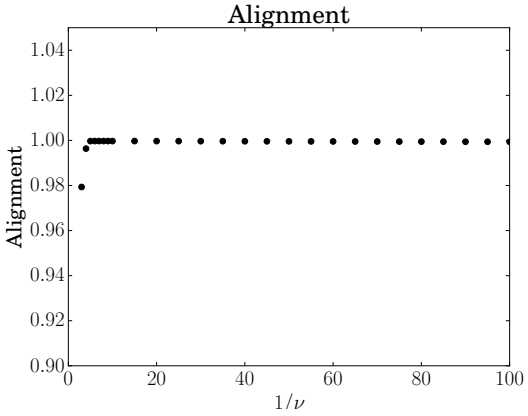

(b) Alignment is approximately one for all values of $1/\nu$ examined.

Figure 5.24: $1/\eta = 1/100$ and $1/\nu \in (5, 100)$.

In conclusion, variation of ν and η whilst keeping the other fixed results in a change in the energy in the final SSS. By making assumptions about the form of the magnetic and fluid fields I have been able to estimate the amount of energy for a given (ν, η) and I have shown that these estimates agree well with the values produced during numerical simulations. As an additional finding we see that alignment appears to be remarkably robust to a change in $1/\nu$, $1/\eta$ and that dynamo action only occurs when there is a high degree of alignment.

5.5 Evolution of a Passive Vector Field in the Archontis Dynamo

In this section I examine the ability of the final statistically steady state of the Archontis dynamo to amplify a seed field. Analysis of if and how the flow field amplifies a seed magnetic field can yield information on the chaotic and stretching properties of the flow. Following a similar method as that within [25] and [104] I define a passive vector field, $\mathbf{Q}$, which is a solution to the induction equation for the passive field

$$\frac{\partial \mathbf{Q}}{\partial t} = \nabla \times (\mathbf{u}_t \times \mathbf{Q}) + \eta \nabla^2 \mathbf{Q} \tag{5.37}$$

and where $\mathbf{u}_t$ is the flow once it has reached its final statistically steady state (SSS) in

the Archontis dynamo. The induction equation (for $\mathbf{B}$) and equation of motion are solved simultaneously until the SSS, for $\mathbf{u}$ and $\mathbf{B}$, is reached. Once the SSS is reached (5.37) is initialised with a week seed field for $\mathbf{Q}$ whilst the equation of motion and induction equation continue to be evolved. At all times, $\mathbf{Q}$ remains divergence free.

Figure 5.25 shows a single simulation for the case of $1/\nu = 1/\eta = 100$. We see that the passive vector field grows exponentially with a well defined growth rate. We see that the growth of the magnetic field during its kinematic phase is much faster (approximately double) that of the passive field.

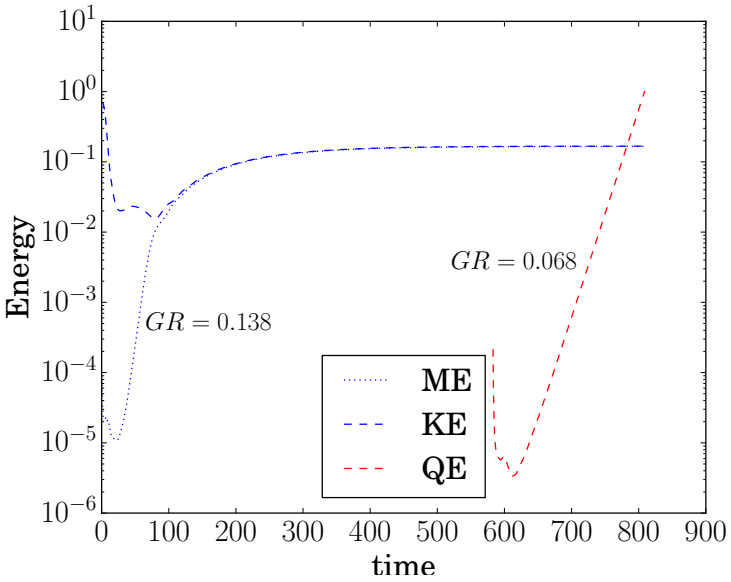

Figure 5.25: $1/\nu = 1/\eta = 100$, $\mathbf{Q}$ grows exponentially. The growth rate is much weaker (approximately half) than that of the magnetic field during its kinematic phase.

The significance of obtaining strong growth rates for a passive field during the nonlinear regime of a dynamo is that it illustrates that saturation of the velocity field to the statistically steady state does not remove the properties that allow it to amplify a seed magnetic field. This is in contrast to dynamos which saturate via a reduction in the chaotic properties of the flow, such as within [24]. The alignment mechanism for this specific case is thus able to saturate a dynamo without compromising the velocity fields ability to amplify seed fields at subsequent timesteps.

Figures 5.26 and 5.27 show $z = 0$ contours during the initial kinematic phase for $\mathbf{B}^2$ and $\mathbf{Q}^2$ respectively. We see that as the magnetic energy saturates the strong magnetic field

coalesces into 4 large eddies. The passive field, $\mathbf{Q}^2$, on the other hand coalesces into cigars with field structures almost identical to those seen in the kinematic runs for the Kolmogorov flow seen in section 4.4.

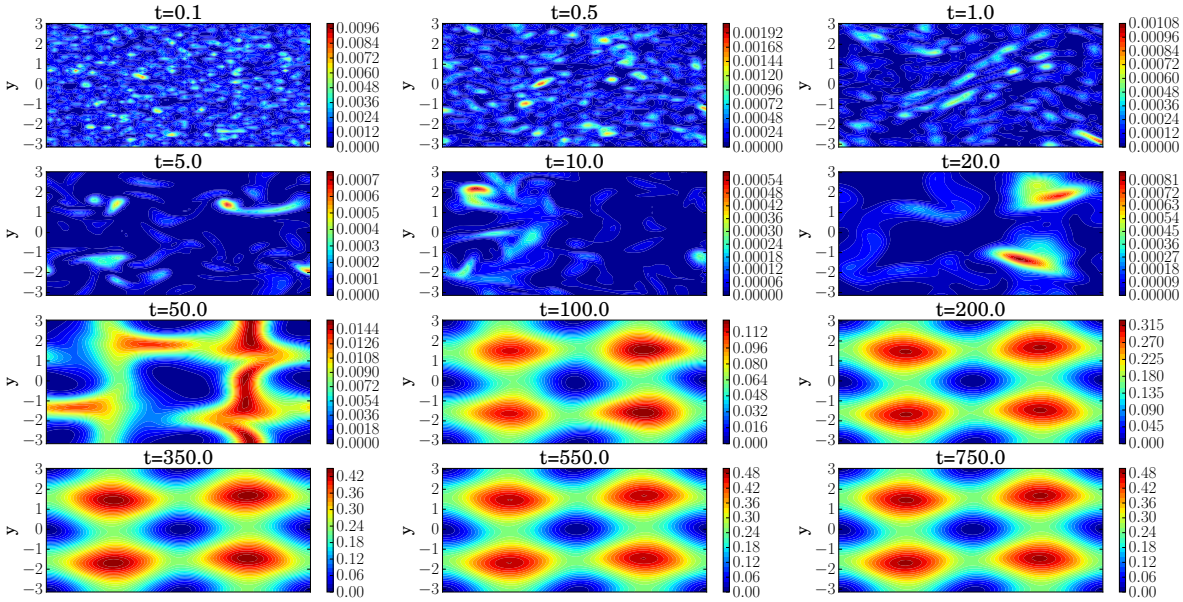

Figure 5.26: $z = 0$ contours for $\mathbf{B}^2$. We see that the magnetic field is concentrated in four large eddies.

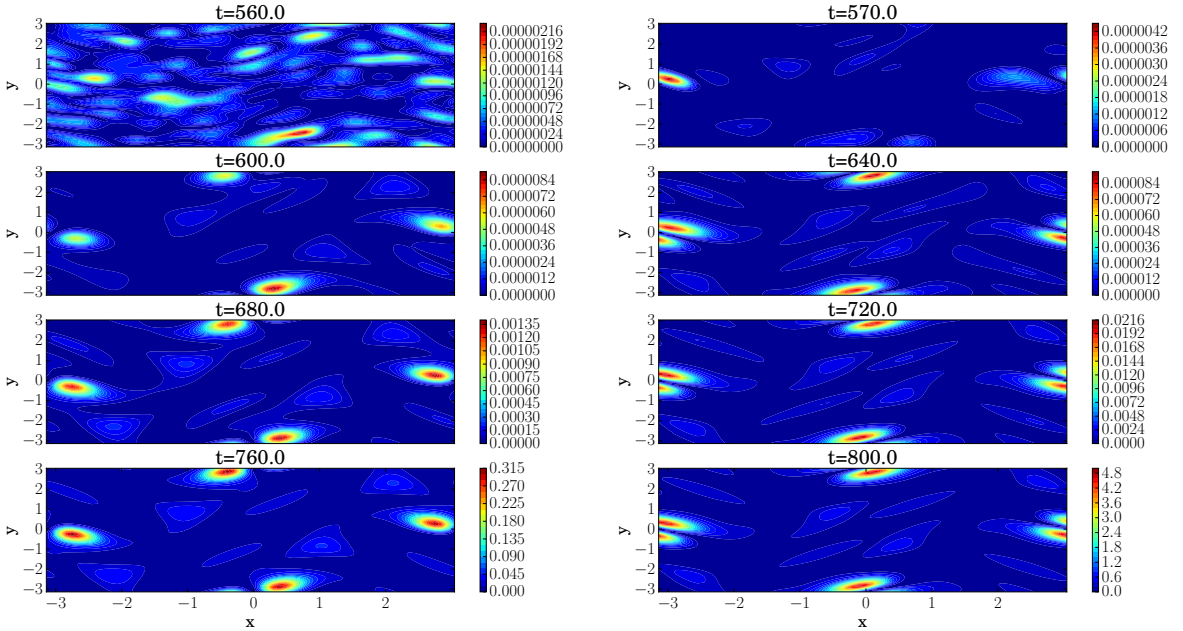

Figure 5.27: $z = 0$ contours for $\mathbf{Q}^2$. We see that the passive field is predominantly weak (in this particular slice) but has strong field in four extremely small regions nearby $[0, \pm\pi]$ and $[\pm\pi, 0]$.

In figure 5.28 I show 65% isosurfaces of $|\mathbf{Q}|/\max_{x,y,z}\{|\mathbf{Q}|\}$ as well as 15% isosurfaces of $|\mathbf{u}|/\max_{x,y,z}\{|\mathbf{u}|\}$. We see that the cigars point in the direction of stagnation points and are situated at other stagnation points. The reason for this is explained in section 4.4. Figures 5.27-5.28 therefore show that the passive vector field evolves in a similar manner as if the flow in the SSS was identical to $\mathbf{F}_A/2\nu$. As such the small differences between the flow in the SSS and $\mathbf{F}_A/2\nu$ make no difference to the structure of the passive field it amplifies.

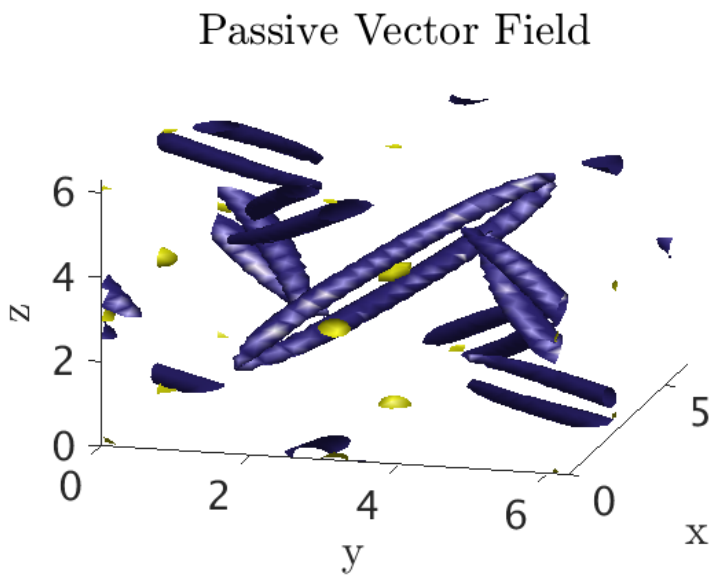

Figure 5.28: Plot of 65% isosurfaces of $|\mathbf{Q}|$ (purple) and 15% isosurfaces of the flow (yellow). We see that the structures are identical to those seen for the kinematic dynamo of the Kolmogorov flow in section 4.4.

Examination of the field amplification properties of both the initial flow and the saturated flow for the Archontis dynamo has shown that the flow amplifies a seed field differently in each of these states. The probable reason for this can be seen in the initial evolution of the KE in figure 5.25. We see that the kinetic energy quickly transitions away from its initial structure of $\mathbf{F}_A/\nu$ and as such the way it amplifies a seed field is different from that of the Kolmogorov flow.

I have further shown that once the kinetic and magnetic energies saturate the flow is still capable of amplifying a seed field and so does not lose its amplification mechanism upon saturation. I have shown that the differences between the flow and $\mathbf{F}_A/2\nu$ do not significantly alter how the flow amplifies a seed field as the final structure found for the passive field is identical to that seen for the Kolmogorov flow in section 4.4.

5.6 Variations on the Archontis Dynamo

In this section I examine a number of different forcings close to the Archontis forcing. The aim is to see how robust obtaining an aligned state is to both time dependence and increasing asymmetry in the forcing. By varying a parameter in each of the flows I am able to make the forcing increasingly different to the Archontis forcing, and in doing so test whether an aligned state can be found for an increasingly complex forcing.

Furthermore, as there is no a priori method for obtaining an aligned flow and magnetic field given a forcing and only a small number of forcings which produce aligned $\mathbf{u}$ and $\mathbf{B}$ have been found this work has the additional benefit of yielding a number of other forcings which produce aligned fields.

5.6.1 A Circularly Polarised Archontis Dynamo

In this section I consider an Archontis dynamo with oscillations of increasing radius in the $x-y$ plane. The forcing is given by

$$\mathbf{F}_{CP} = \nu \begin{pmatrix} \sin(z) \\ \sin(x + R\cos(t)) \\ \sin(y + R\sin(t)) \end{pmatrix}. \tag{5.38}$$

The addition of time dependence here is similar to the approach adopted in [45] to add time dependence to the Roberts flow in that the time dependence corresponds to "circular polarisation" [45] where the forcing rotates anti-clockwise with radius R in planes of constant z (see figure 5.29). As such, I will refer to $\mathbf{F}_{CP}$ as the circularly polarised Archontis forcing, abbreviated as the CP forcing.

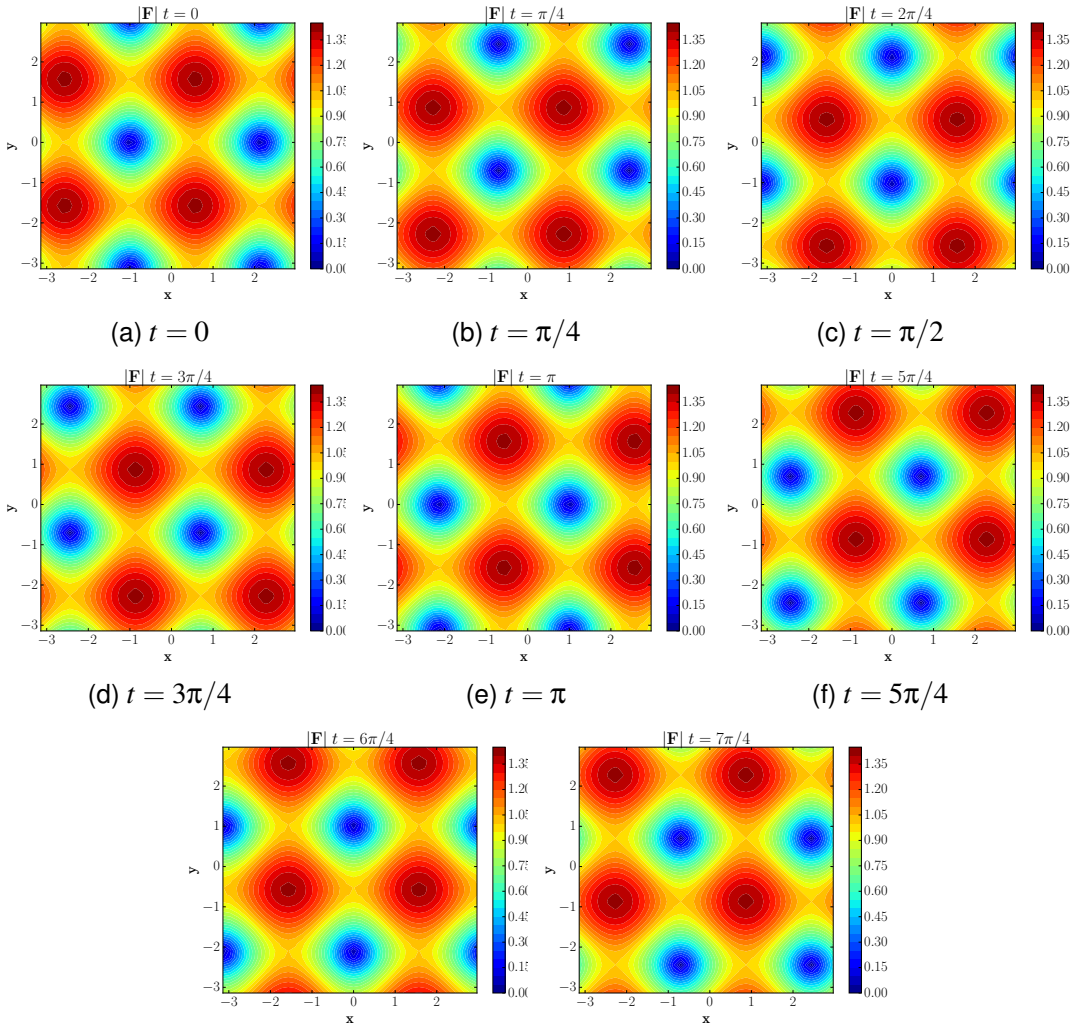

(a) $t = 0$ (b) $t = \pi/4$ (c) $t = \pi/2$

(d) $t = 3\pi/4$ (e) $t = \pi$ (f) $t = 5\pi/4$

(g) $t = 3\pi/2$ (h) $t = 7\pi/4$

Figure 5.29: Contours of $|\mathbf{F}_{CP}|\Big|_{z=0}$ at various times and for $R = 1$ showing the effect of the time dependence. The regions of strong force rotate anticlockwise.

As the saturation of the magnetic energy (ME) and kinetic energy (KE) to their statistically steady state (SSS) in the Archontis dynamo is preceded by alignment of $\mathbf{u}$ and $\mathbf{B}$ it is of interest to examine whether introducing circular polarisation to the forcing can disrupt the alignment mechanism enough that it influences whether or not dynamo action occurs.

I consider two sets of runs: one with $1/\nu = 100$, $1/\eta = 100$ and one with $1/\nu = 100$ and $1/\eta = 50$. I increase R from $R = 0.1$ in steps of 0.1 until dynamo action no longer occurs and the ME decays to negligible values. In both cases I take as initial condition $\mathbf{u} = \mathbf{F}_A/\nu$ and begin $\mathbf{B}$ with a random seed field within Fourier space which has real and imaginary components of $O(10^{-4})$. Figures 5.30-5.33 shows the result for $1/\nu = 1/\eta = 100$.

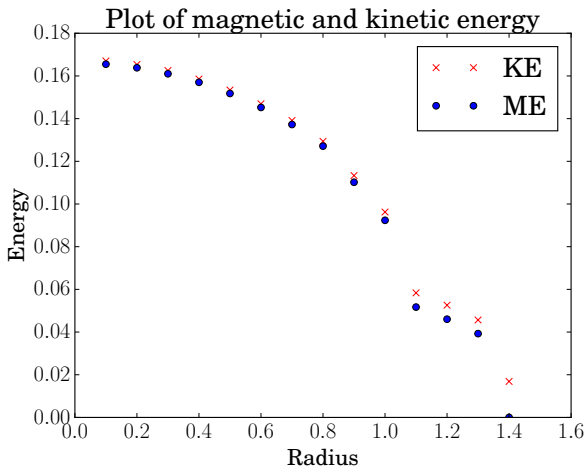

Figure 5.30: Kinetic and magnetic energy in the final statistically steady state. We see that both energies decrease with increasing radius, but remain approximately at equipartition.

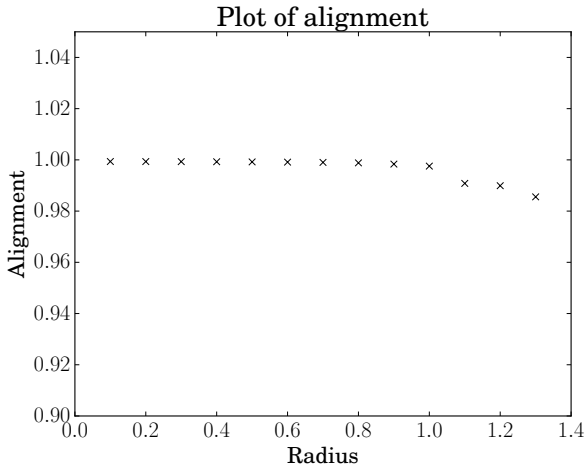

Figure 5.31: Alignment in the final statistically steady state. Alignment is seen to decrease slightly beyond $R = 1$. For all forcings where the ME does not decay, $\mathbf{u}$ and $\mathbf{B}$ are strongly aligned.

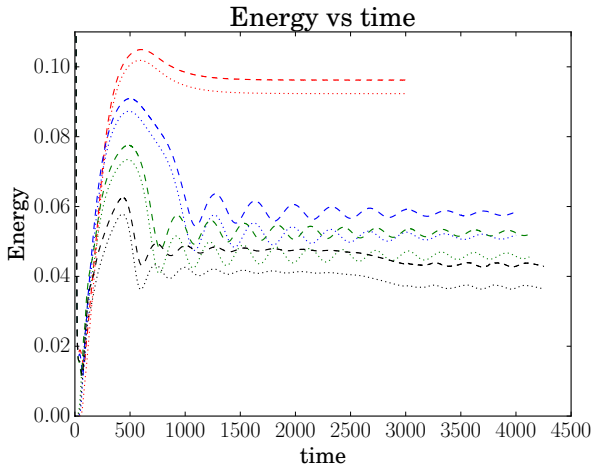

Figure 5.32: KE (dashed) and ME (dotted). $R = 1.0$ is red, $R = 1.1$ is blue, $R = 1.2$ is green and $R = 1.3$ is black.

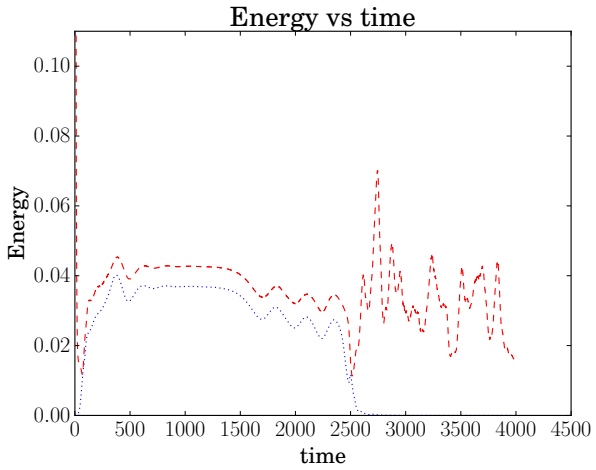

Figure 5.33: KE (red) and ME(blue) for $R = 1.4$. We see that the ME eventually decays however it takes a long time to do so.

In figure 5.30 I show the kinetic and magnetic energies against radius. Where the energy asymptotes to a constant value this value is taken but where oscillations are present a time average over a suitable period of time is taken. In all cases a negligible amplitude oscillation of 2π is present in both the kinetic and magnetic energy due to the periodicity of the forcing. We see that both KE and ME decrease monotonically as R is increased up to $R = 1.3$. For $R > 1.3$ the ME becomes negligible and the system becomes hydrodynamic. This continued up to the largest R tested which was 1.7.

Figure 5.31 shows alignment (measured by H_0) against radius. We see that above $R = 1$ a small decrease in alignment is observed. The figure also shows that all values of R which produce dynamo action do so with values of alignment close to 1. The aligned dynamo therefore appears to be remarkably robust in that all values of R which produce dynamo action also produce strong alignment.

In figure 5.32 I show that for $R > 1$ oscillations with a constant mean are seen within the time series of both the KE and the ME. These dampen after a large time however their presence must be taken into consideration when comparing the energies at various R. Figure 5.33 shows the first value of R found to not yield dynamo action. Of interest is that during the simulation the dynamo quickly becomes highly aligned and had an approximately steady KE and ME for a large time before the ME eventually decayed to zero. This result was checked with multiple initial conditions.

In figure 5.34 I show how energy and alignment vary with radius for $1/\nu = 100$ and $1/\eta = 50$.

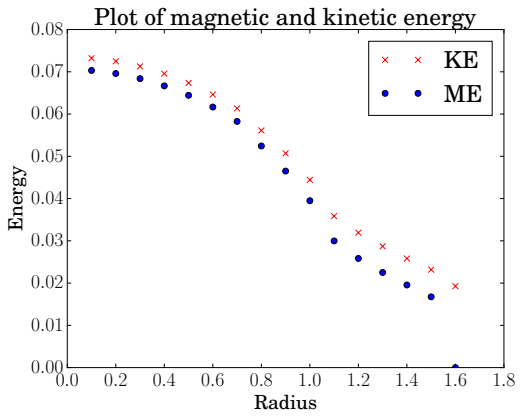

(a) Kinetic and magnetic energies decrease with increased R

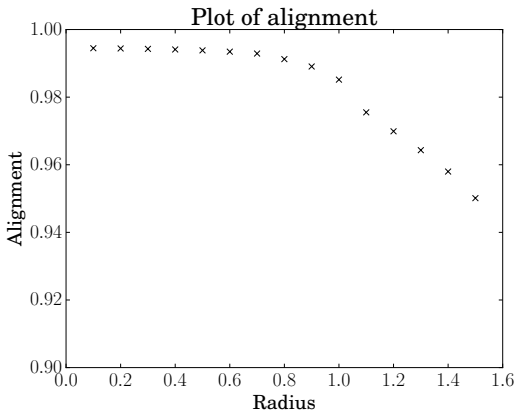

(b) Plot of alignment quantity (5.4c) against radius

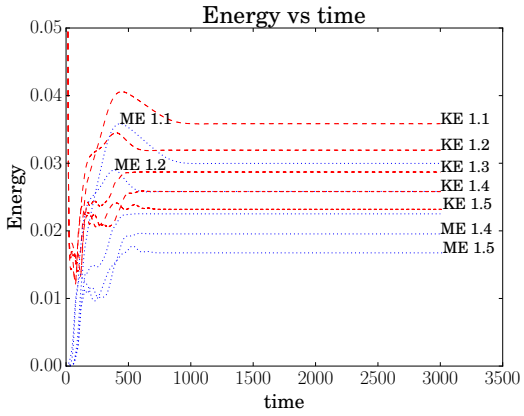

(c) Plot of ME and KE against radius. No oscillations in the SSS are found.

Figure 5.34: $1/\eta = 50$ and $1/\nu = 100$.

We see that there are a number of similarities to the $1/\nu = 1/\eta = 100$ case shown in figures 5.30-5.33. In both cases we see that the energies are at their largest at small R and monotonically decrease in value as R is increased. We also see a small decrease in the alignment between the magnetic and fluid fields as R is increased. Finally, in both cases, we observe that for radii where the magnetic field does not decay away the flow and magnetic fields have high amounts of alignment.

The two sets of parameter values also have a number of differences. Firstly, the value of R at which dynamo action no longer occurs differs between the two. We observe that a dynamo is achieved at a higher R for the $\eta = 50$ case than the $\eta = 100$ case. Another difference is the behaviour for $R > 1$. In the $1/\eta = 100$ case there appears to be almost

two separate behaviours exhibited, one for $R \leq 1$ and one for $R > 1$ with a large drop in energy at $R = 1.1$. This can be seen in figure 5.32 to be due to a bifurcation to an oscillating state with the oscillations shrinking in amplitude at large time. In contrast, for $1/\eta = 50$ the decrease in the energies appears to be much smoother. If we plot the ME and KE against time for $\eta = 50$ and $R > 1$, as I have in figure 5.34c, we see that the statistically steady state of the system has no oscillations and has not greatly decreased in value.

Both sets of runs therefore show that dynamo action is achieved for significant circular polarisation of the Archontis dynamo. It also shows that achieving dynamo action appears to be strongly linked to whether or not the flow and magnetic field are strongly aligned with dynamo action only being achieved when this is the case. For the rest of this section I focus on the $\nu^{-1} = \eta^{-1} = 100$ simulations.

Whilst the volume averaged quantities enable us to gain an overview of the system they tell us very little about how the structure of the magnetic and velocity fields change as R is increased. Figures 5.35 and 5.36 show how $z = 0$ contour plots of the magnetic and fluid fields respectively differ as the radius is varied (for $1/\eta = 1/\nu = 100$) with $z = 0$ being a representative example. We see that the four regions of large magnetic field become significantly deformed for $R > 1$. Comparing figure 5.35 to figure 5.36 we see that the contours for $\mathbf{u}$ and $\mathbf{B}$ look similar for $R < 1$ due to the fields being almost aligned and equal in magnitude, which is further supported by figures 5.31. Beyond $R = 1$ the structures of the two fields exhibit clear differences as shown by the contour plots, although each has the strongest field within similar regions of the domain, hence the high degree of alignment between the two for $R < 1.4$.

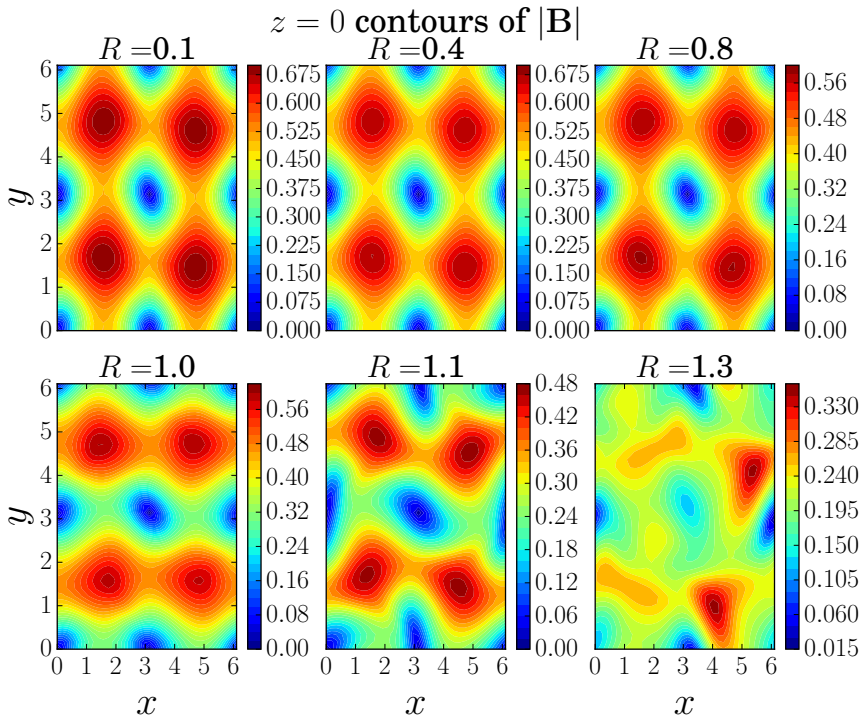

Figure 5.35: Contours of $|\mathbf{B}|\Big|_{z=0}$ for a number of radii and $1/\eta = 1/\nu = 100$. These are similar to that of $R = 0$ up to $R = 1$ beyond which the field becomes distorted and eventually ($R > 1.3$) becomes negligible.

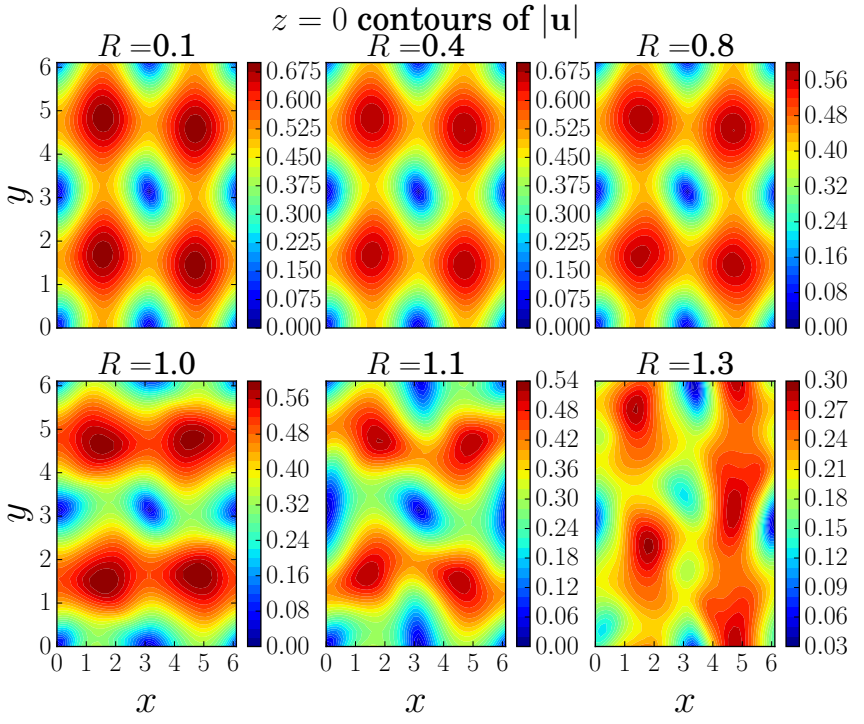

Figure 5.36: Contours of $|\mathbf{u}|\Big|_{z=0}$ for a number of radii and $1/\eta = 1/\nu = 100$. These are similar to that of $R = 0$ up to $R = 1$ beyond which the field becomes distorted and eventually ($R > 1.3$) evolves hydrodynamically due to the weak magnetic field.

As the initial condition for the flow $\mathbf{u}_0 = \mathbf{F}_{CP}/\nu$ is not an exact solution to the hydrodynamic equation

$$\frac{\partial \mathbf{u}}{\partial t} = -\nabla P - (\mathbf{u}\cdot\nabla)\mathbf{u} + \nu\nabla^2\mathbf{u} + \mathbf{F}_{CP} \tag{5.39}$$

the initial flow that amplifies the magnetic field is not $\mathbf{F}_{CP}/\nu$ but rather what it evolves to. To better understand the evolution that the flow undergoes upon introduction of the magnetic field I run a set of hydrodynamic simulations begun with $\mathbf{u} = 0$. The final flow field structure is shown in figure 5.37.

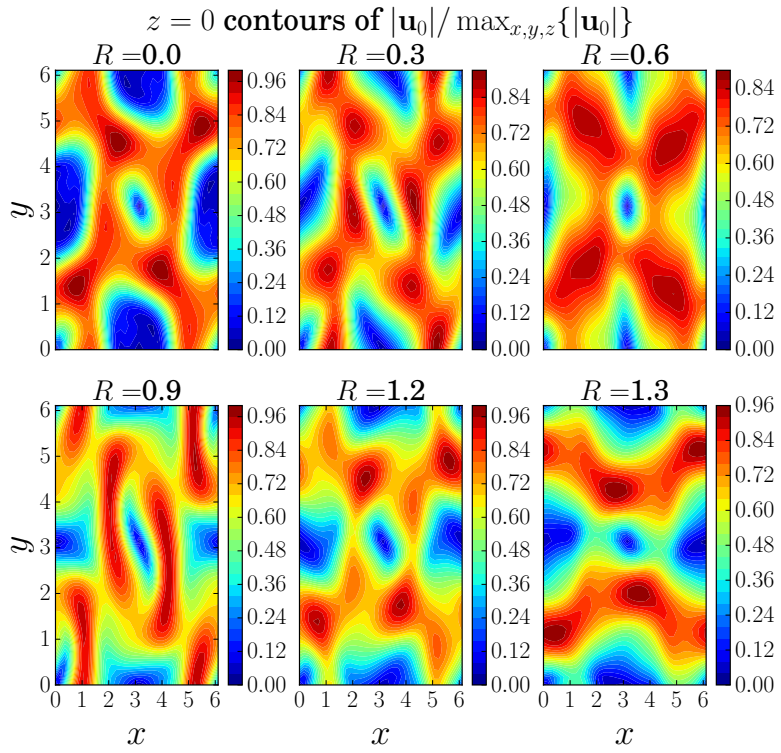

Figure 5.37: Result of solving (5.39) beginning with $\mathbf{u} = \mathbf{0}$.

The flow is concentrated in large structures and bears some resemblance to the contours of the forcing however the symmetrical structure has been disrupted. To see whether or not a change in initial conditions for the flow changes the final state of $\mathbf{u}$ and $\mathbf{B}$ I now run full nonlinear MHD simulations beginning $\mathbf{u}$ with the final field from the hydrodynamic simulations and compare them to the results where this is not done. In figure 5.38 I show the kinetic and magnetic energies with subscript H being for runs where hydrodynamic simulations are first performed. The hydrodynamic runs final energies are obscured by the other runs due to the closeness of their agreement and so it appears that the initial choice

of $\mathbf{u}$ makes no difference on the final energy obtained.

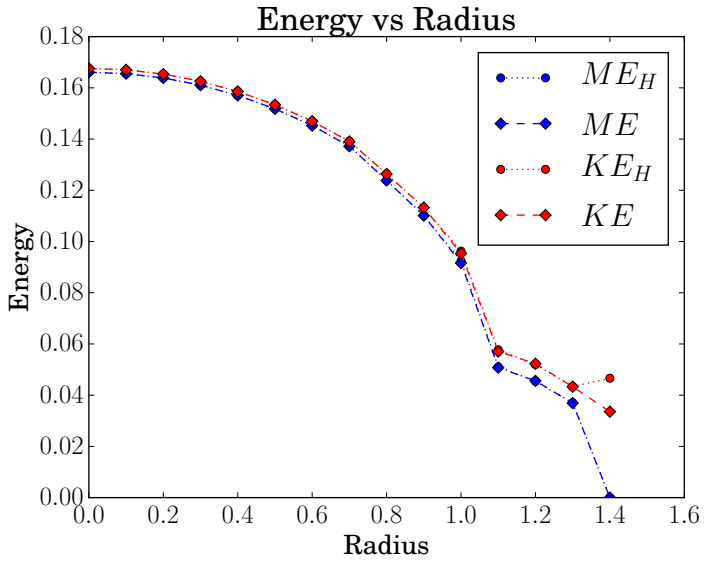

Figure 5.38: ME and KE for runs where the initial $\mathbf{u}$ is either the result of a hydrodynamic simulation (those with subscript H) or $\mathbf{u} = \mathbf{F}_{CP}/\nu$. We see that the initial choice of $\mathbf{u}$ makes no difference.

In figures 5.39 and 5.40 I compare $z = 0$ contours of $|\mathbf{B}|$ for runs began with and without a hydrodynamic simulation. We see that the resulting magnetic field's contours are identical except at $R = 1.3$ where the time dependence of the field means that we are seeing the field at different times.

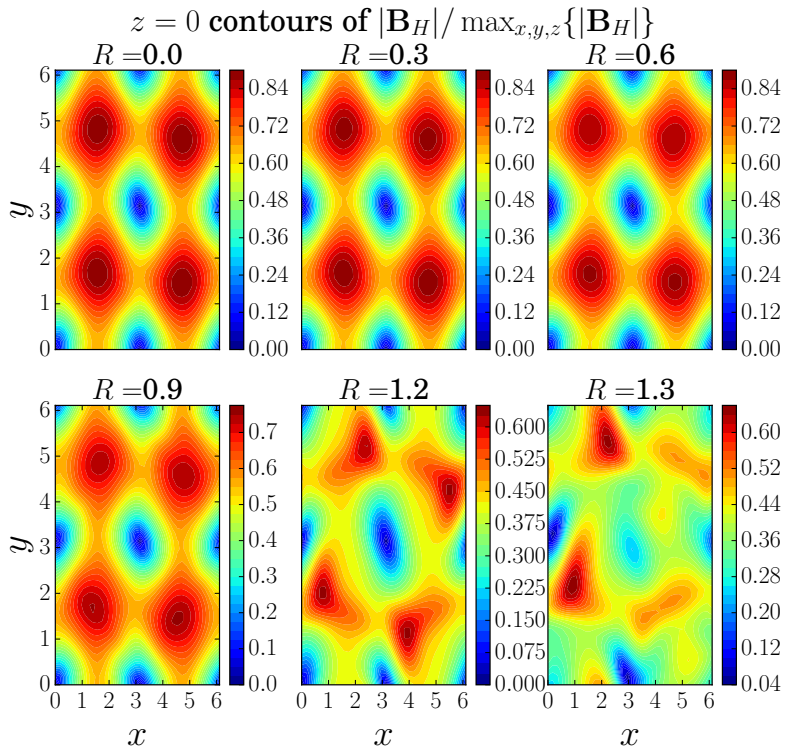

Figure 5.39: $z = 0$ contours of $|\mathbf{B}|$ began with a hydrodynamic solution for $\mathbf{B}$.

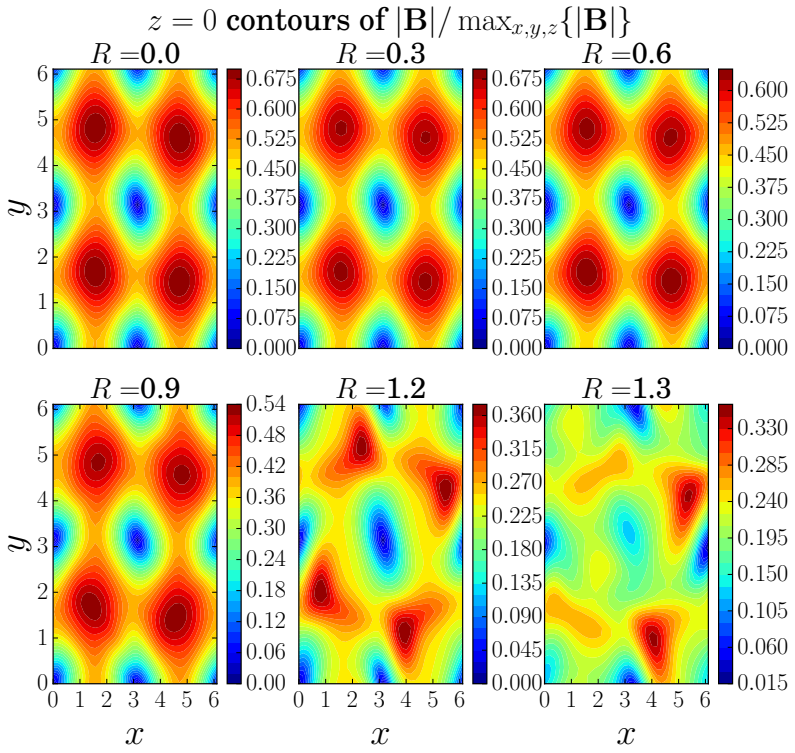

Figure 5.40: $z = 0$ contours of $|\mathbf{B}|$ not began with a hydrodynamic solution for $\mathbf{B}$.

We therefore see that allowing the flow to settle to a hydrodynamic solution to the equation of motion before adding a seed magnetic field has not altered either the critical R for obtaining dynamo action, the energies or the final magnetic field structure. Thus we see that the flow being a solution to the equation of motion before the simulation begins does not affect the final fields that we obtain.

I now return focus to the results where no hydrodynamic runs were performed. Figure 5.41 shows 90% isosurfaces of the magnetic and fluid fields for $1/\eta = 1/\nu = 100$. The strongest field is initially confined to 8 regions which are centred at $\mathbf{x} = \pm\pi/2$ due to the field structures close resemblance to $\mathbf{F}_A$ however these become deformed as R increases. Finally at high enough R a number of the regions disappear altogether.

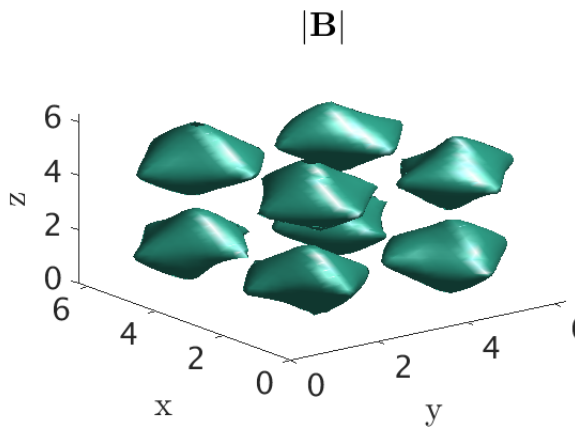

(a) 90% isosurface of $|\mathbf{B}|$ for $R = 0.2$

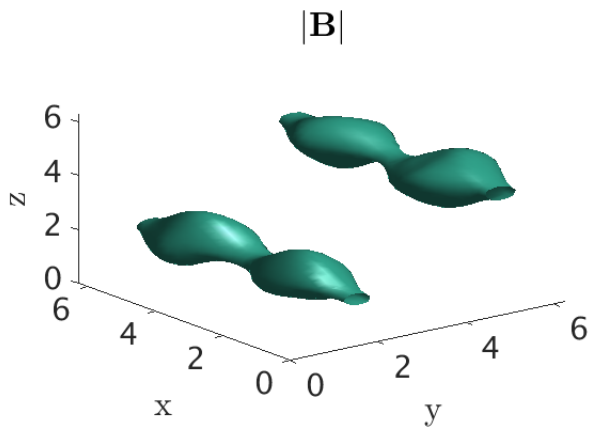

(b) 90% isosurface of $|\mathbf{B}|$ for $R = 0.8$

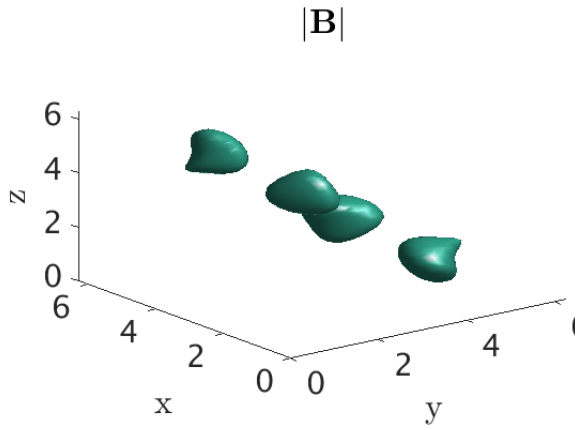

(c) 90% isosurface of $|\mathbf{B}|$ for $R = 1.1$

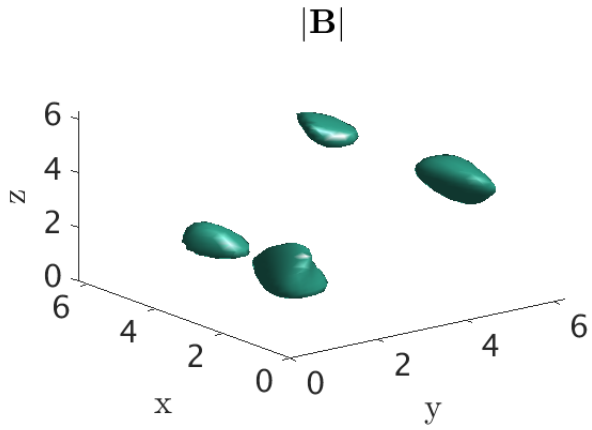

(d) 90% isosurface of $|\mathbf{B}|$ for $R = 1.3$

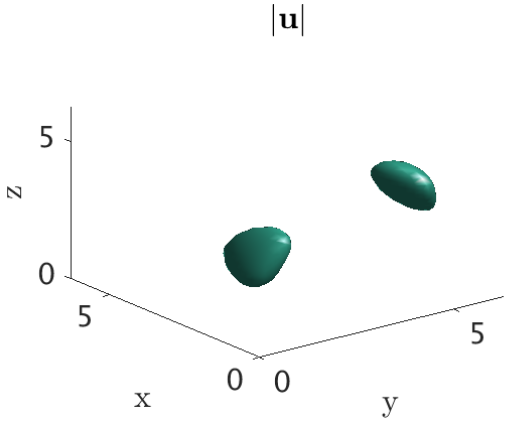

(e) 90% isosurface of $|\mathbf{u}|$ for $R = 1.3$

Figure 5.41: 90% isosurfaces for a number of radii and showing how the regions of strong field become distorted as R is increased.

A more complete visualisation of the magnetic field structure is shown in figure 5.42 for two values of R. I show three isosurfaces, 40% (purple), 70% (green) and 90% (yellow)), of the L_2 norm of the magnetic field, $|\mathbf{B}| = \sqrt{B_x^2 + B_y^2 + B_z^2}$, normalised by dividing by the infinity norm $||\mathbf{B}||_\infty = \max_{\mathbf{x},\mathbf{y},\mathbf{z}} \left(|\mathbf{B}|\right)$. For $R = 0.2$, we observe that the strong and weak field occupy particular regions of the domain separated by a network of magnetic field

with strengths between 65 and 90% of the maximum value. For $R = 1.2$, we observe that the number of regions of strongest field have halved and that a much larger proportion of the domain is made up of weaker field. What is also noticeable is the reduction in the symmetry of the magnetic field. At $R = 0.2$ we see that our domain can be split into 8 identical sub-domains by inserting planes at $\mathbf{x} = 0$, however this is no longer the case for $R = 1.2$.

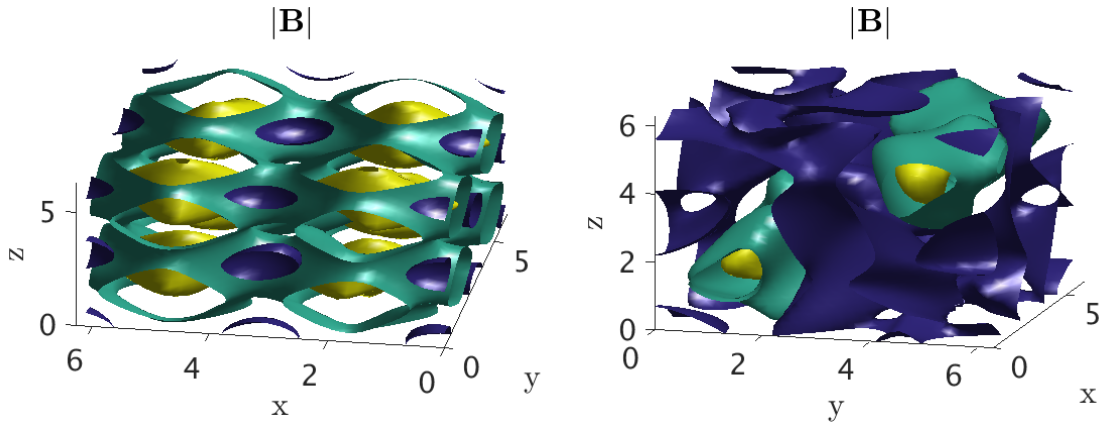

(a) 40%(purple), 70%(green) and 90%(yellow) isosurfaces of $|\mathbf{B}|/\max_{\mathbf{x},\mathbf{y},\mathbf{z}}(|\mathbf{B}|)$ for $R = 0.2$ which illustrate the distribution of the magnetic field

(b) 40%(purple), 70%(green) and 90%(yellow) isosurfaces of $|\mathbf{B}|/\max_{\mathbf{x},\mathbf{y},\mathbf{z}}(|\mathbf{B}|)$ for $R = 1.2$ which illustrate the distribution of the magnetic field.

Figure 5.42: Isosurfaces at varying strengths for $R = 0.2$ and $R = 1.2$. These illustrate the differences in magnetic field structure.

Figure 5.43 shows histograms of the values of the magnetic and fluid fields for an $R = 0$ run overlaid with the idealised $R = 0$ solution $\mathbf{u} = \mathbf{B} \approx \mathbf{F}_A/2\nu$. These have been normalised by their infinity norm, as illustrated in equations (5.40a)-(5.40c).

$$B_N = \frac{|\mathbf{B}|}{\max_{\mathbf{x},\mathbf{y},\mathbf{z}}(|\mathbf{B}|)} \qquad (5.40a) \qquad U_N = \frac{|\mathbf{u}|}{\max_{\mathbf{x},\mathbf{y},\mathbf{z}}(|\mathbf{u}|)} \qquad (5.40b)$$

$$F_N = \frac{|\mathbf{F}_A|}{\max_{\mathbf{x},\mathbf{y},\mathbf{z}}(|\mathbf{F}_A|)} \qquad (5.40c)$$

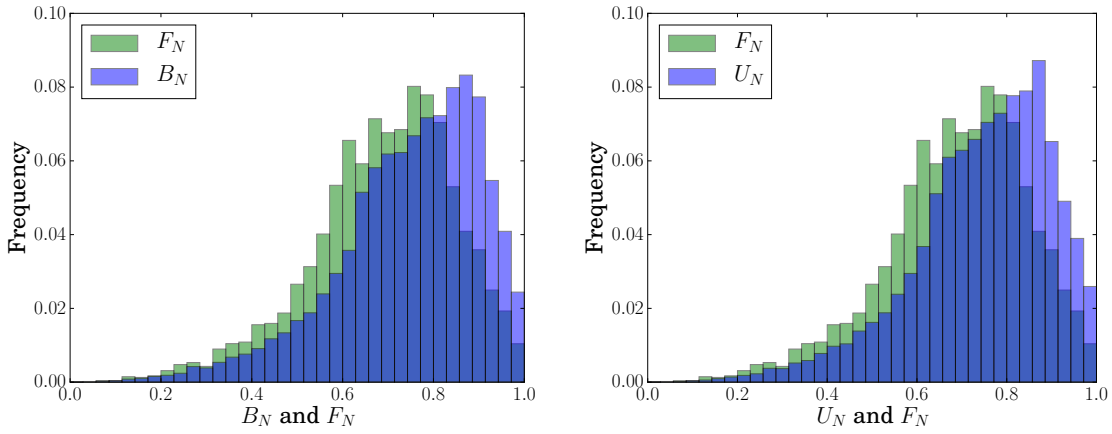

Figure 5.43: Histograms of B_N and U_N overlaid with a histogram of F_N for $R = 0$.

We see that the solutions obtained for the magnetic and fluid fields have a slightly higher proportion of strong field (relative to their respective fields) than the approximate solution. Figures 5.44 and 5.45 show histograms of the values of the magnetic and flow fields within the domain plotted for various illustrative R. Again these are overlaid with F_N. We see that the peak migrates to lower B_N as R increases. This shows that the regions of strong field are becoming smaller in size (as was seen in figure 5.41) and that an increasing majority of the domain is being made up of field less than half this strength. We also see that the proportions of relative field strength within the domain increasingly do not resemble the forcing as R increases.

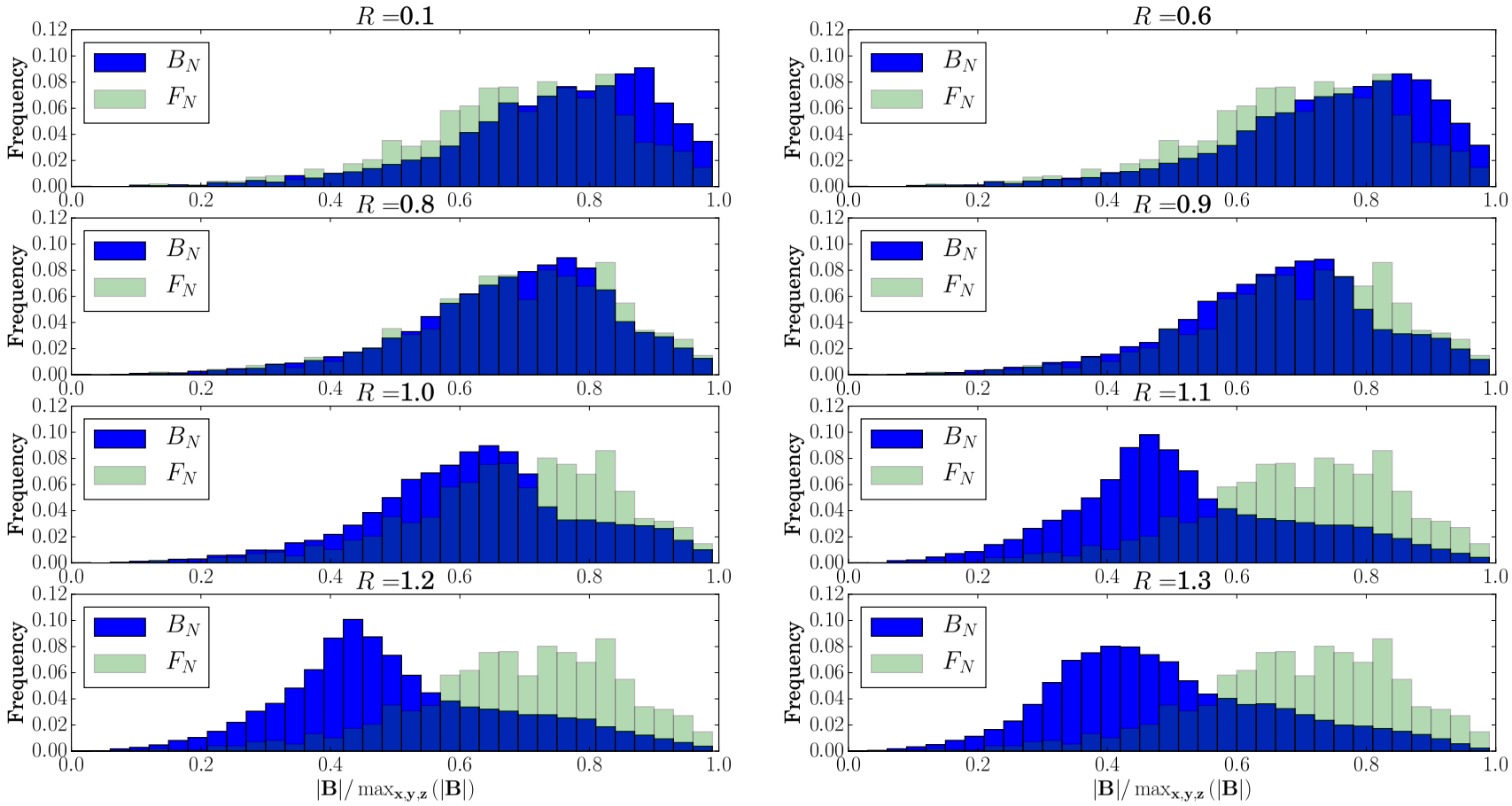

Figure 5.44: Histograms of the value of $|\mathbf{B}|/\max_{\mathbf{x},\mathbf{y},\mathbf{z}}\left(|\mathbf{B}|\right)$ for various radii. We see that as R increases the proportion of the domain made up of the strongest field decreases.

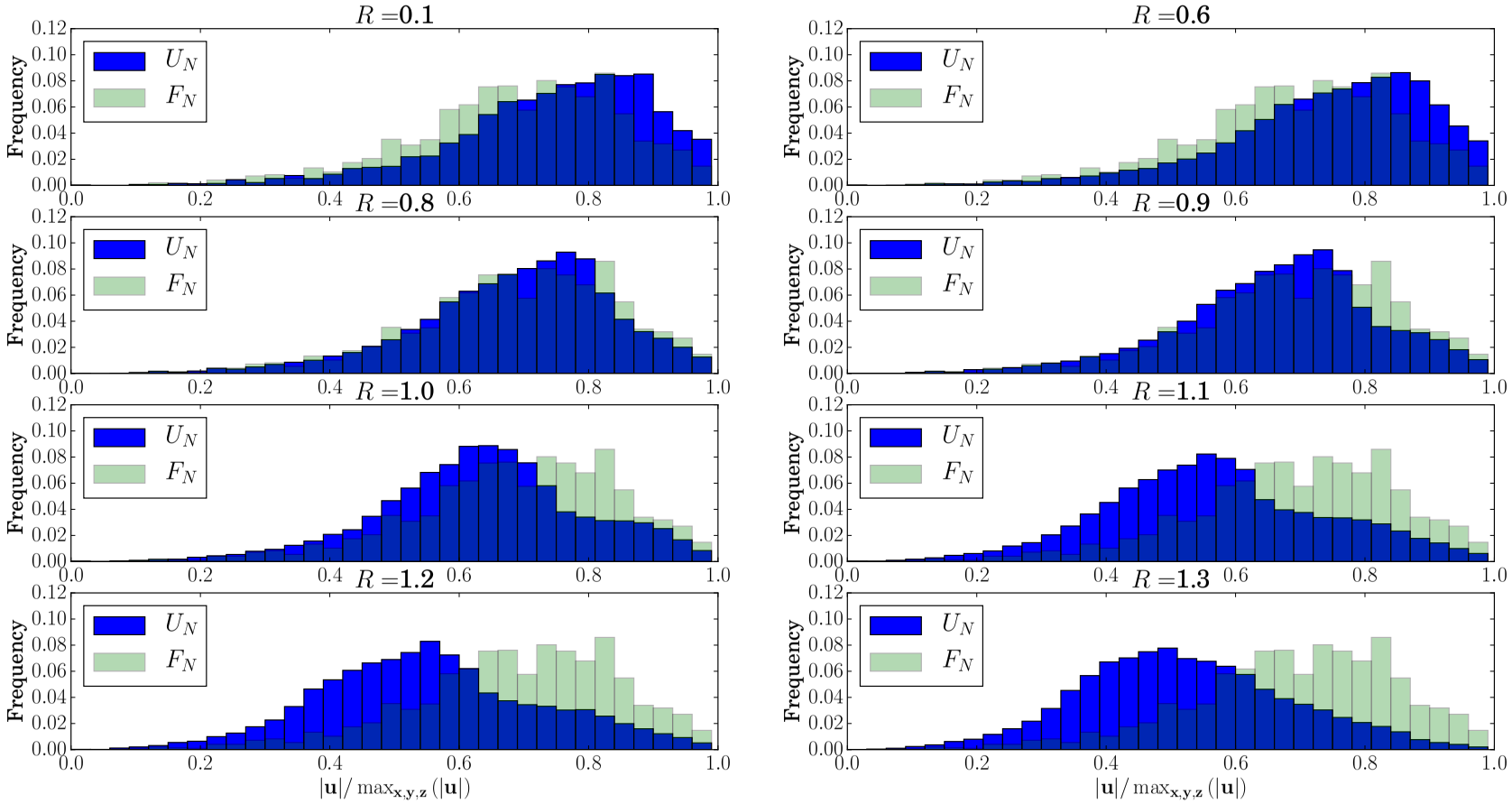

Figure 5.45: Histograms of the value of $|\mathbf{u}|/\max_{\mathbf{x},\mathbf{y},\mathbf{z}}\left(|\mathbf{u}|\right)$ for various radii. We see that as R increases the proportion of the domain made up of the strongest field decreases.

Consider the 90% isosurfaces shown within figure 5.41. We observe that as the radius increases the number of regions of strong field (both $\mathbf{u}$ and $\mathbf{B}$) decrease. An increase in the radius of oscillation of the forcing therefore appears to have the effect of hindering the accumulation of regions of strong field within the domain. The regions of strong field are also seen to reduce in size and become more elongated in the y direction as R is increased. The reduction in size as well as the reduction in number as well as the histograms in figures 5.44 and 5.45 therefore help us to understand the reduction of energy seen within figure 5.30. We see that the reduction in the energy in the domain is due to a reduction in the size and amount of regions of strong field within the domain as it begins to differ in structure to $\mathbf{F}_A/2\nu$. Beyond $R \approx 1.0$ the decrease is made more pronounced by the magnetic and fluid fields becoming weaker throughout a larger bulk of the domain.

I now examine possible reasons why the dynamo fails. It is clear from the isosurfaces in figure 5.41 that as we approach the critical radius at which dynamo action no longer occurs increasingly less strong field accumulates in the regions where it occurs for $R = 0$. The reason for this can be explained as follows. Consider a time averaged forcing $\tilde{F}_{CP}$

$$\tilde{F}_{CP}(x,y,z) = \int_0^{2\pi} \frac{|\mathbf{F}_{CP}(x,y,z,t)|}{\max_{x,y,z}\left\{|\mathbf{F}_{CP}(x,y,z,t)|\right\}} dt \tag{5.41}$$

The spatial distribution of $\tilde{F}_{CP}$ then gives information on the regions in which the forcing is operating on average over time. This is shown in figure 5.46 where I show $z = 0$ contours of $\tilde{F}_{CP}$ for a number of R.

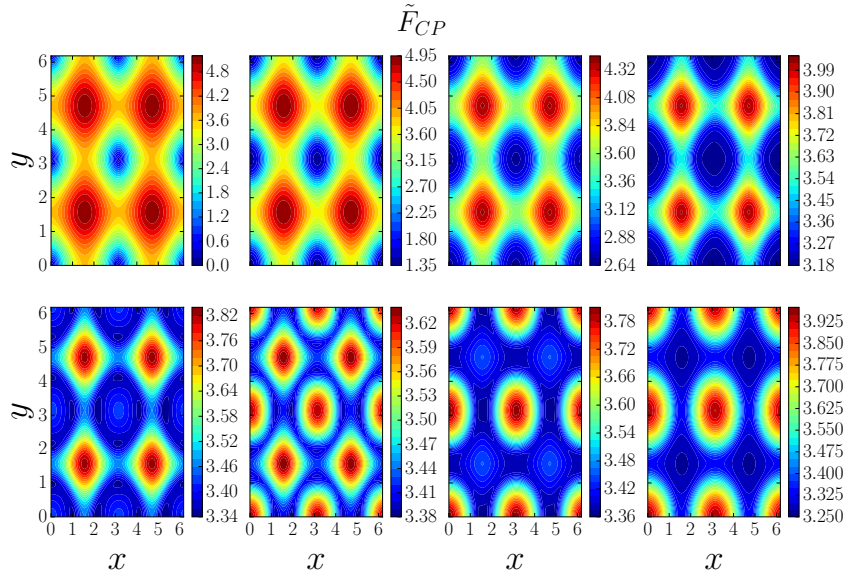

Figure 5.46: $\tilde{F}_{CP}$ for a number of radii. As R increases the strongest forcing becomes in the regions where it was weakest for $R = 0$. Note the colorbar changes so that as R increases to 1.2 the difference between strong and weak field decreases. It then decreases again for $R > 1.2$.

Figure 5.46 shows that an increasing proportion of the forcing occurs in the regions between the strong $\mathbf{F}_A$ regions as R increases with a corresponding decrease in the amount of forcing within the regions of strong field. Figure 5.46 therefore shows that as R increases the average forcing increasingly does not resemble the distribution of the fields. As such rather than reinforcing the field structures the forcing disrupts them by adding energy to other regions of the domain. This then disrupts the alignment and subsequently, for large enough R, the fields can not maintain alignment and the dynamo fails.

To summarise: examples for two different magnetic diffusivities, $\nu = 100$, $1/\eta = [50, 100]$ have shown how adding a circular polarisation to the forcing alters the final states of the magnetic and flow fields. We see that an increase in circular polarisation results in a decrease of magnetic and kinetic energy up to a critical radii beyond which no dynamo action is achieved. Plots of isosurfaces have shown that the reduction in energy is a result of inhibition of the growth of the regions of strong field with the symmetry of the final state also being disrupted. Plots of alignment for both values of η show that for all values of R for which dynamo action occurs the magnetic and fluid fields are highly aligned. This shows that the alignment mechanism is remarkably robust to the circular polarisation.

5.6.2 An Asymmetrical Archontis Dynamo F_ξ

The addition of a circular polarisation has shown that the final magnetic and fluid field structures are remarkably robust to a small time dependent periodic change to the forcing. In particular, for small enough radii the fields saturate to a field structure similar to that of the time independent forcing.

In this section I build upon the Archontis and CP dynamo work by considering a group of forcings, close to the Archontis forcing, with spatial asymmetry. The aim is to understand whether obtaining an aligned dynamo requires the large amount of symmetry present within the Archontis forcing. Additionally, the results within section 5.6.1 showed that obtaining significant magnetic energy only occurred for parameters where strong alignment was also present. This suggests that dynamo action for forcings close to the Archontis dynamo require strong alignment and I will examine this further here.

I define a forcing $\mathbf{F}_\xi$

$$\mathbf{F}_\xi = \nu \begin{pmatrix} \sin(z) \\ (1+\xi)\sin(x) \\ \sin(y) \end{pmatrix}. \tag{5.42}$$

This forcing is the Archontis forcing but with a deviation in the x dependent y component. In figure 5.47 I show $z = 0$ contours of $|\mathbf{F}_\xi|$. Moving from negative ξ to positive ξ the forcing transitions from stretching in $y-z$ to becoming elongated in x. Varying ξ therefore results in substantial stretching out of the forcing. As such, if the exact symmetries present within the Archontis forcing are crucial to reaching an aligned state then even a small disruption to them will result in no aligned state.

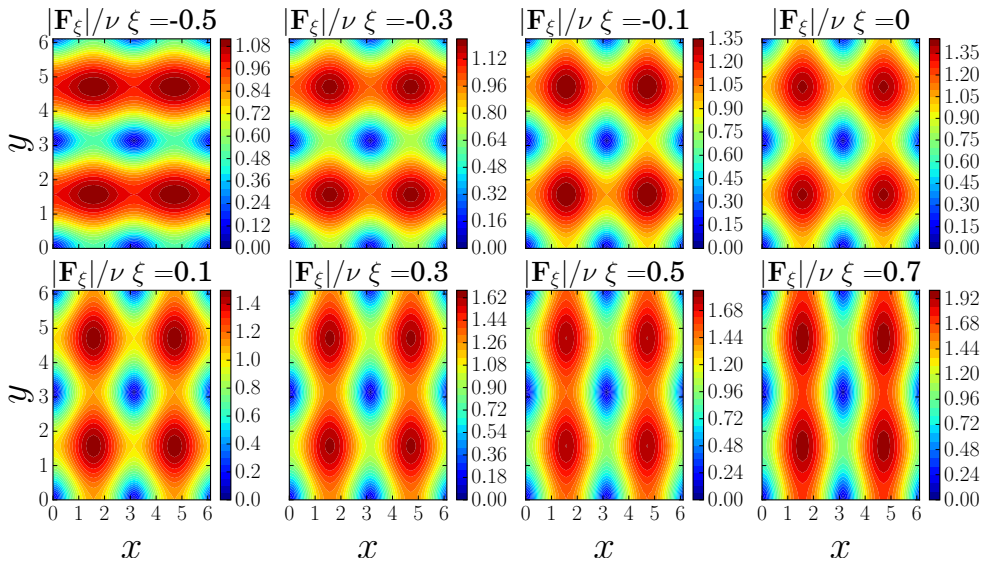

Figure 5.47: $z = 0$ Contours of $|\mathbf{F}_\xi|$. The direction of asymmetry changes in moving from negative to positive ξ.

In keeping with my work on $\mathbf{F}_A$ and $\mathbf{F}_{CP}$ I take $\eta = \nu = 1/100$. I use the initial condition $\mathbf{u}_0 = \mathbf{B}_0 = \mathbf{F}_\xi/\nu$. This initial condition is used for speed of convergence. I vary ξ in increments of 0.1 away from 0 until a parameter value shows no dynamo action, at which point I do not increase $|\xi|$ further.

The definitions of the energies and the alignment (H_0) are the same as in the Archontis and CP sections and are shown in equations (5.43a), (5.43b) and (5.43c) for ease of reference.

$$KE = \frac{1}{8\pi^3}\int_V \frac{\mathbf{u}^2}{2} dV \qquad (5.43a) \qquad ME = \frac{1}{8\pi^3}\int_V \frac{\mathbf{B}^2}{2} dV \qquad (5.43b)$$

$$H_0 = \frac{1}{8\pi^3}\frac{1}{\sqrt{ME}\sqrt{KE}}\left|\int_V \frac{\mathbf{u}\cdot\mathbf{B}}{2} dV\right| \qquad (5.43c)$$

In figure 5.48a I show the kinetic and magnetic energy. Starting from $\xi = 0$ the energy decreases as $\xi \to -0.6$ beyond which no dynamo action occurs. Above $\xi = 0$ the energies increase until $\xi = 0.3$ where they begin to decrease. Comparing the energies to $z = 0$ contours of the flow and magnetic fields (figures 5.49 and 5.50) as well as the forcing contours (figure 5.47) shows that the ξ above and below zero where smooth changes to the energies occur result in magnetic and flow field structures that resemble the forcing i.e. $\xi \in (-0.3, 0.5)$. For ξ outside of this range the general structure of the contours remains similar, however the regions of strong field become distorted.

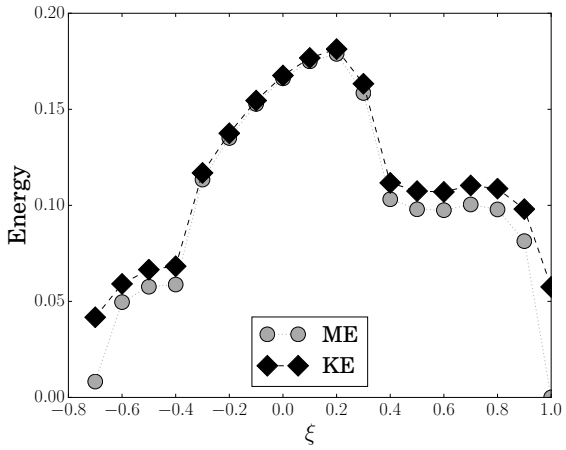

(a) ME and KE for the forcing (5.42). As the forcing becomes less symmetrical we see a decrease in the energies although there is a slight increase from $\xi = 0$ to $\xi = 0.3$. Note that more dynamo action is seen for positive than negative ξ.

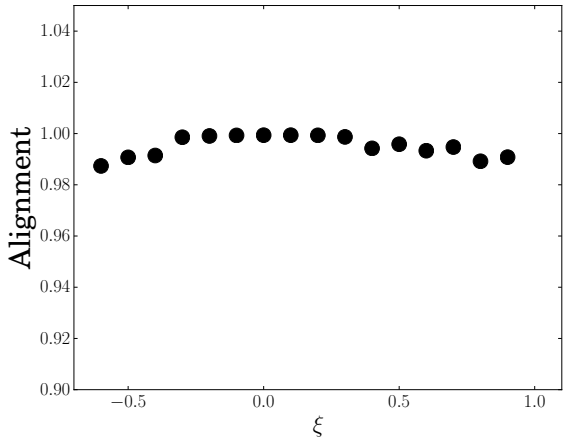

(b) Alignment (H_0) vs ξ for the values where dynamo action occurs. For all values where dynamo action occurs the two fields are strongly aligned. This further supports the idea that for forcings similar to $\mathbf{F}_A$ alignment is crucial.

Figure 5.48

In figure 5.48b I show the alignment. For all ξ where dynamo action was achieved $\mathbf{u}$ and $\mathbf{B}$ are strongly aligned. As such $\mathbf{u} \propto \mathbf{B}$. As figure 5.48a shows the KE and ME to be approximately the same $\mathbf{u} \approx \mathbf{B}$. This is the same result as that seen for both $\mathbf{F}_A$ and $\mathbf{F}_{CP}$. Further support is therefore seen for alignment being crucial to the working of these dynamos and that this dynamo is operating via a similar mechanism to $\mathbf{F}_A$. Reaching an aligned state even with significant deformation of the forcing also shows that the precise symmetries of $\mathbf{F}_A$, outlined in [48], are not necessary to achieve an aligned dynamo.

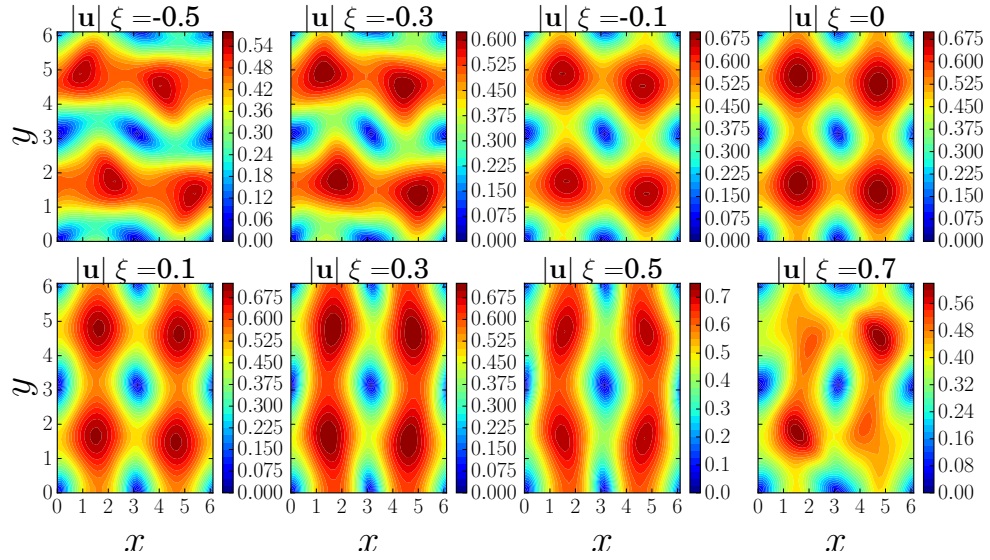

Figure 5.49: $z = 0$ Contours of $|\mathbf{u}|$. The direction of asymmetry changes in moving from negative to positive ξ with symmetry being lost at $\xi = 0.6$. The field largely resembles $|\mathbf{B}|$ for $\xi < 0.6$ (see figure 5.50) with the two fields being strongly aligned.

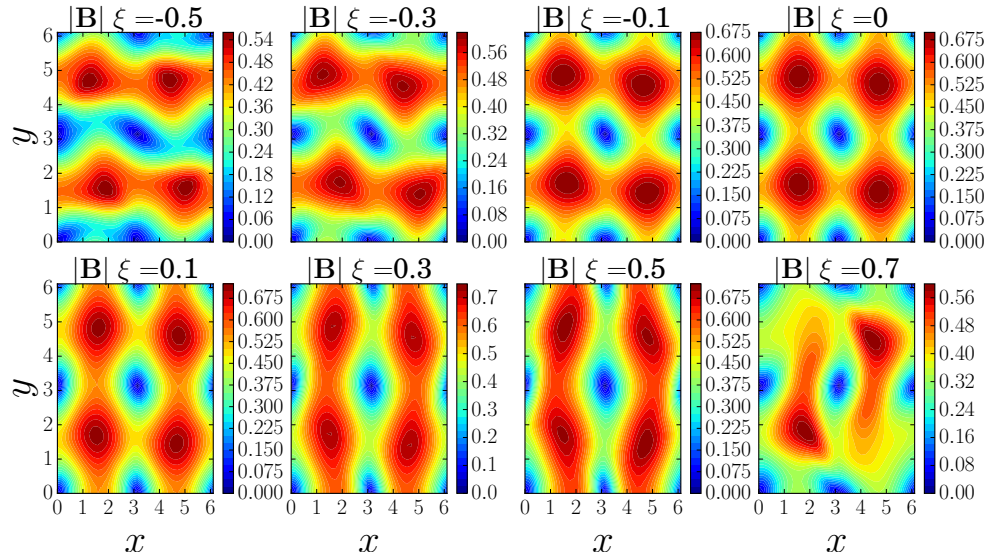

Figure 5.50: $z = 0$ Contours of $|\mathbf{B}|$. The direction of asymmetry changes in moving from negative to positive ξ with symmetry being lost at $\xi = 0.6$.The field largely resembles $|\mathbf{u}|$ for $\xi < 0.6$ (see figure 5.49) with the two fields being strongly aligned.

In figures 5.51 and 5.52 I show the regions of strong $|\mathbf{B}|$ and strong $|\mathbf{F}_\xi|$ for negative and positive ξ. . For negative ξ up to -0.3 the magnetic field deforms in a similar manner to the forcing however beyond this the strong regions become much smaller than the regions of strong forcing. For positive ξ the magnetic field deforms similarly to the forcing until 0.2. For $\xi = 0.3$ half of the regions of strong field disappear, correspondingly we see a drop in the magnetic energy within figure 5.48. This reduction in the number of regions of

strong field and the corresponding decrease in energy was previously seen within the CP dynamo. Finally, $\xi = 0.9$ behaves differently to the other values in that we see the return of 8 regions of strong field.

These isosurfaces reveal a number of things. Firstly, a decrease in energy as $|\xi|$ increases is again due to a reduction in the size and/or number of the regions of strongest field. Secondly the regions of strongest magnetic field most closely resemble the forcing's structure for $\xi \in (-0.3, 0.2)$. Outside of this range $|\mathbf{u}|$ and $|\mathbf{B}|$ resemble each other but due to the reduction in symmetries that occurs they no longer as closely resemble the forcing. I will return to this point later.

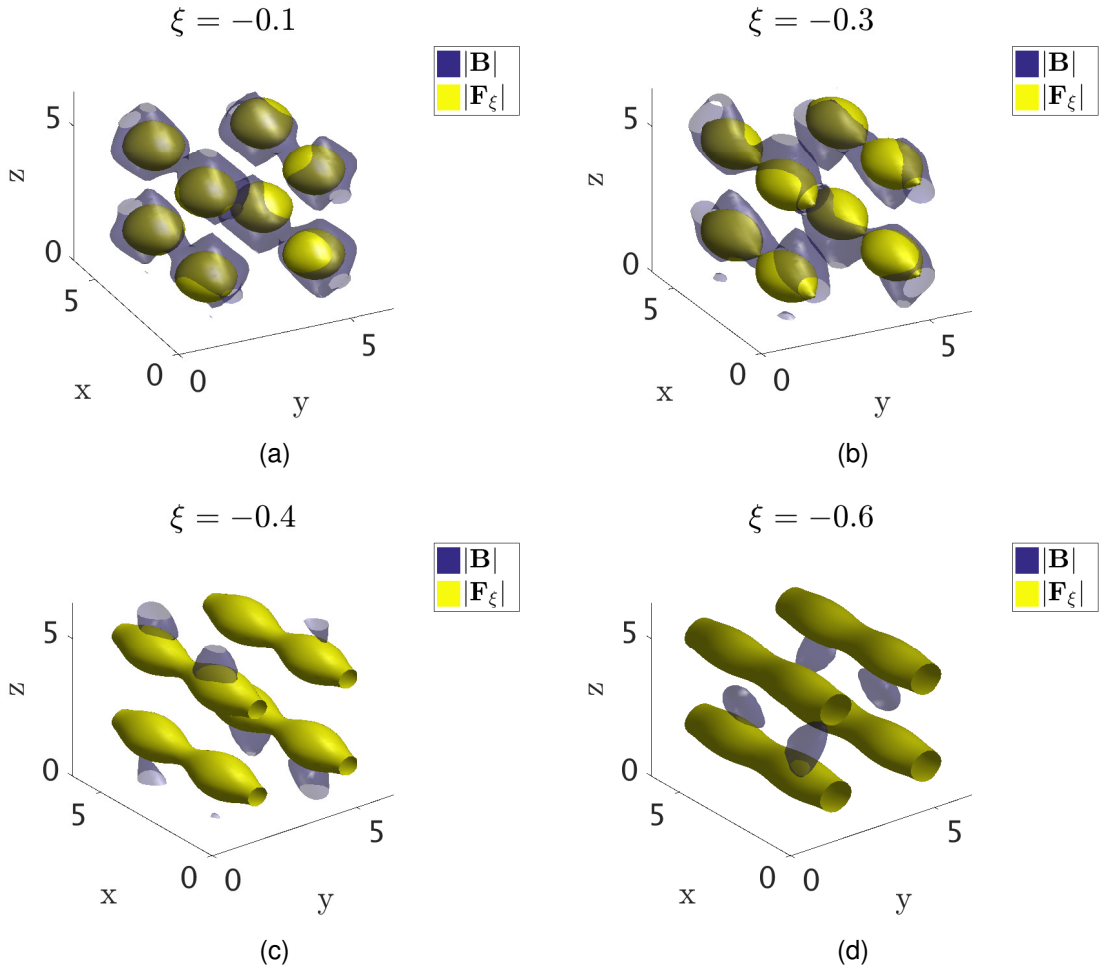

Figure 5.51: 90% isosurface of $|\mathbf{B}|$ and 80% isosurface of $|\mathbf{F}_\xi|$ for negative ξ. The magnetic field becomes increasingly elongated until $\xi = -0.4$ when the build up of strong field becomes disrupted and we see a significant reduction in the size of the strong field regions.

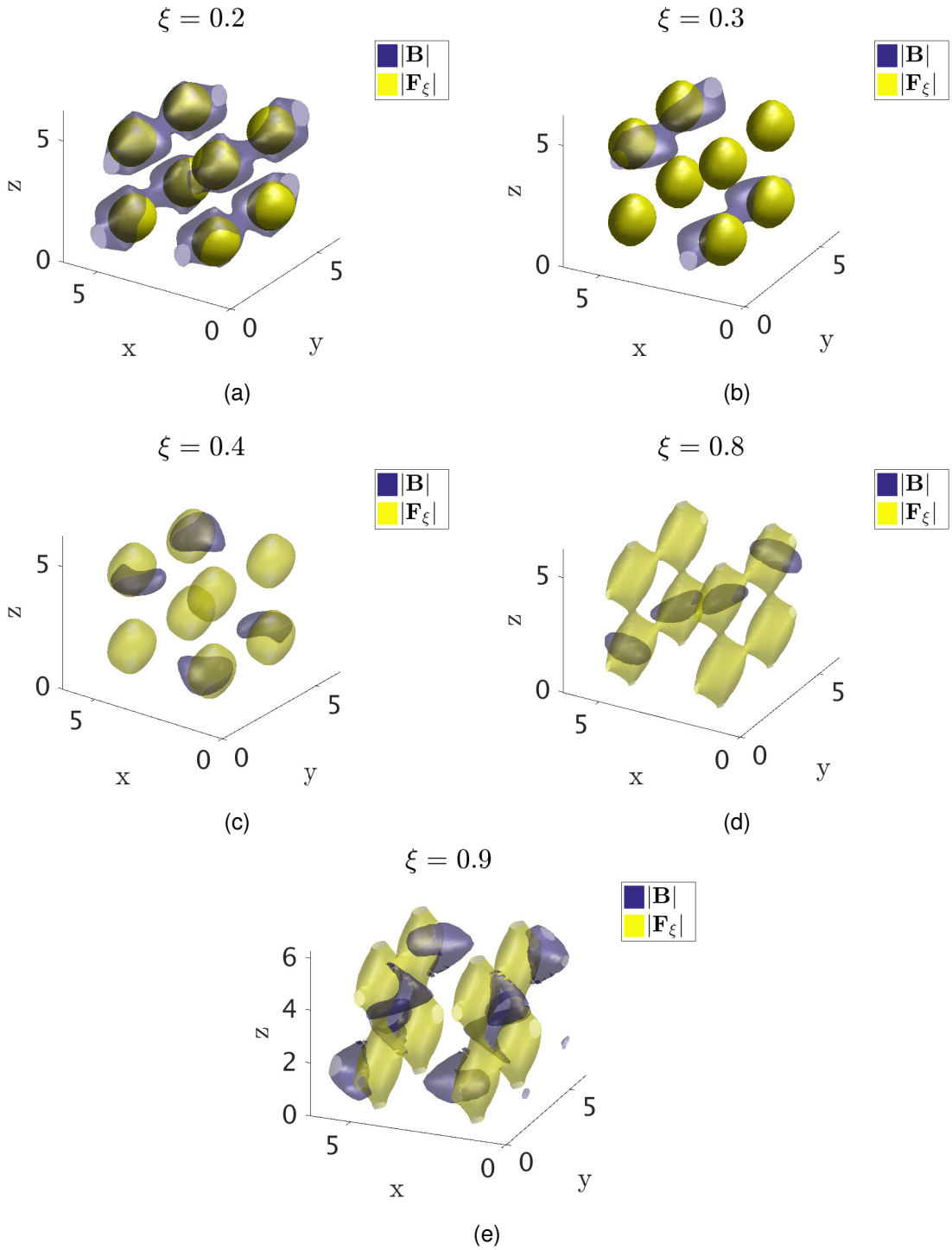

Figure 5.52: 90% isosurface of $|\mathbf{B}|$ and 80% isosurface of $|\mathbf{F}_\xi|$ for positive ξ. A number of features stand out. The first is that the regions of strong $|\mathbf{B}|$ become increasingly elongated until $\xi = 0.4$ where they become smaller. The second feature is that for $\xi \in (0.4, 0.8)$ half of the strong field regions disappear. This is similar to the behaviour seen for the CP forcing in section 5.6.1.

In figures 5.53-5.56 I show isosurfaces of varying strength for a number of ξ to illustrate how field of all strengths is distributed. In figure 5.53 I show $|\xi| = 0.1$. The magnetic field structure closely resembles what we expect for $\xi = 0$ with 8 regions of strong field

surrounded by channels of medium strength field and weak field at the stagnation points. A strong symmetry is present with the 8 regions being approximately identical. For $|\xi| = 0.3$ (figure 5.54) all of the field becomes elongated and subsequently we see that the symmetry is broken. In particular for $\xi = 0.3$ we see that the loss of two of the regions of strong field has broken the magnetic fields symmetrical structure. We also see that it is field of all strengths that become distorted due to the forcing asymmetry. This distortion then increases as $|\xi|$ increases with $|\xi| = 0.5$ (figure 5.55) showing that the magnetic field structure for $\xi = 0.5$ has become much more complex. For $\xi = -0.5$ we also see significant changes from the symmetrical structure we previously had with the elongation now being the most obvious morphological feature. Finally, for the last values of ξ that produce dynamo action, figure 5.56, we see that the dominant behaviour is an elongation of the field.

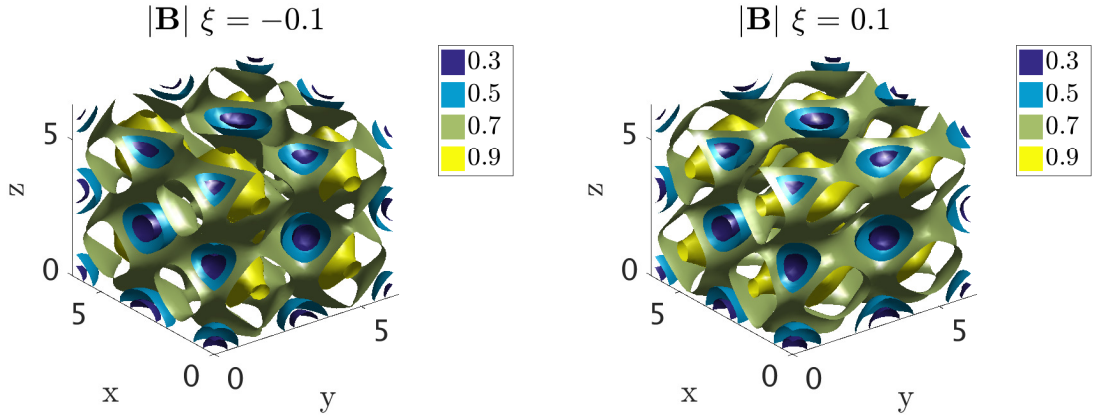

(a) (b)

Figure 5.53: Isosurfaces of $|\mathbf{B}|$ for a variety of field strengths. For $\xi = \pm 0.1$ we see that the structures are elongated however they remain relatively symmetrical.

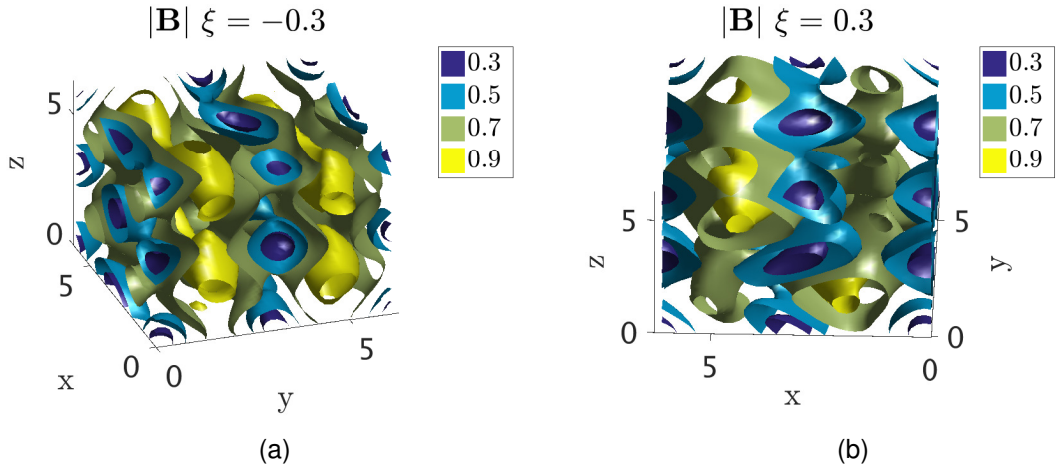

(a) (b)

Figure 5.54: Isosurfaces of $|\mathbf{B}|$ for a variety of field strengths. For $\xi = -0.3$ we see that the structures are elongated however they remain relatively symmetrical with a high amount of symmetry. For $\xi = 0.3$ the structures are again elongated but half of the strong regions not being present disrupts the magnetic field's symmetry.

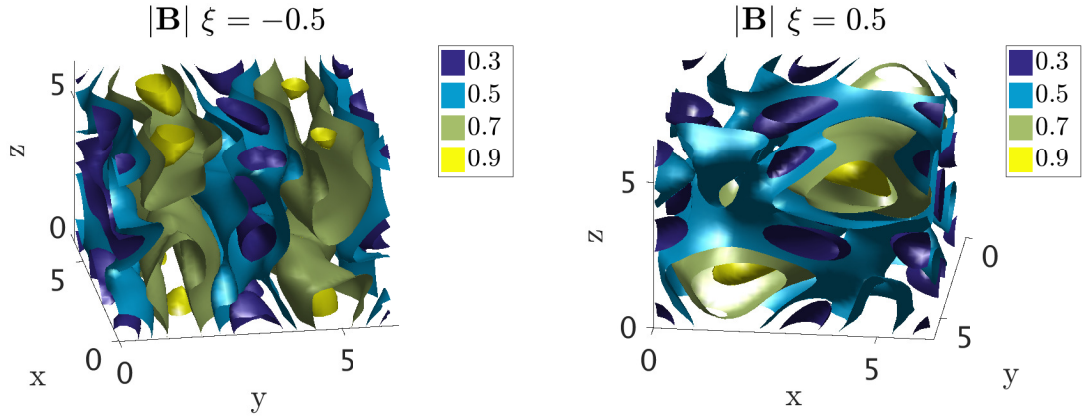

(a) (b)

Figure 5.55: Isosurfaces of $|\mathbf{B}|$ for a variety of field strengths. The figures are similar to those for $\xi = \pm 0.3$, however, the symmetries have become increasingly disrupted. Elongation of the field in the x ($\xi = -0.5$) or y ($\xi = 0.5$) direction continues to be a distinctive feature.

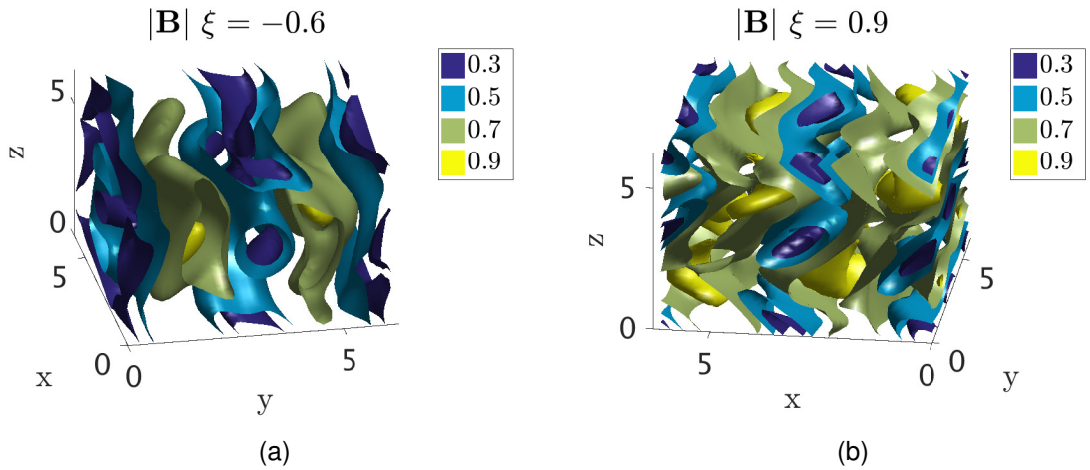

(a) (b)

Figure 5.56: Isosurfaces of $|\mathbf{B}|$ for a variety of field strengths. The values of ξ are the last before the dynamo fails. Elongation of the field in the x ($\xi = -0.5$) or y ($\xi = 0.5$) direction continues to be a distinctive feature.

Isosurfaces of $|\mathbf{u}|$ predominantly resemble those of $|\mathbf{B}|$ and as such are not examined. The exceptions to this are $\xi = [-0.4, -0.5, 0.9]$ which are shown in figure 5.57. In each case the strong field regions of $\mathbf{u}$ are much larger than those of $\mathbf{B}$. I note that these are towards the end of the ξ where dynamo action is achieved and so the asymmetry of the forcing is beginning to significantly disrupt the alignment.

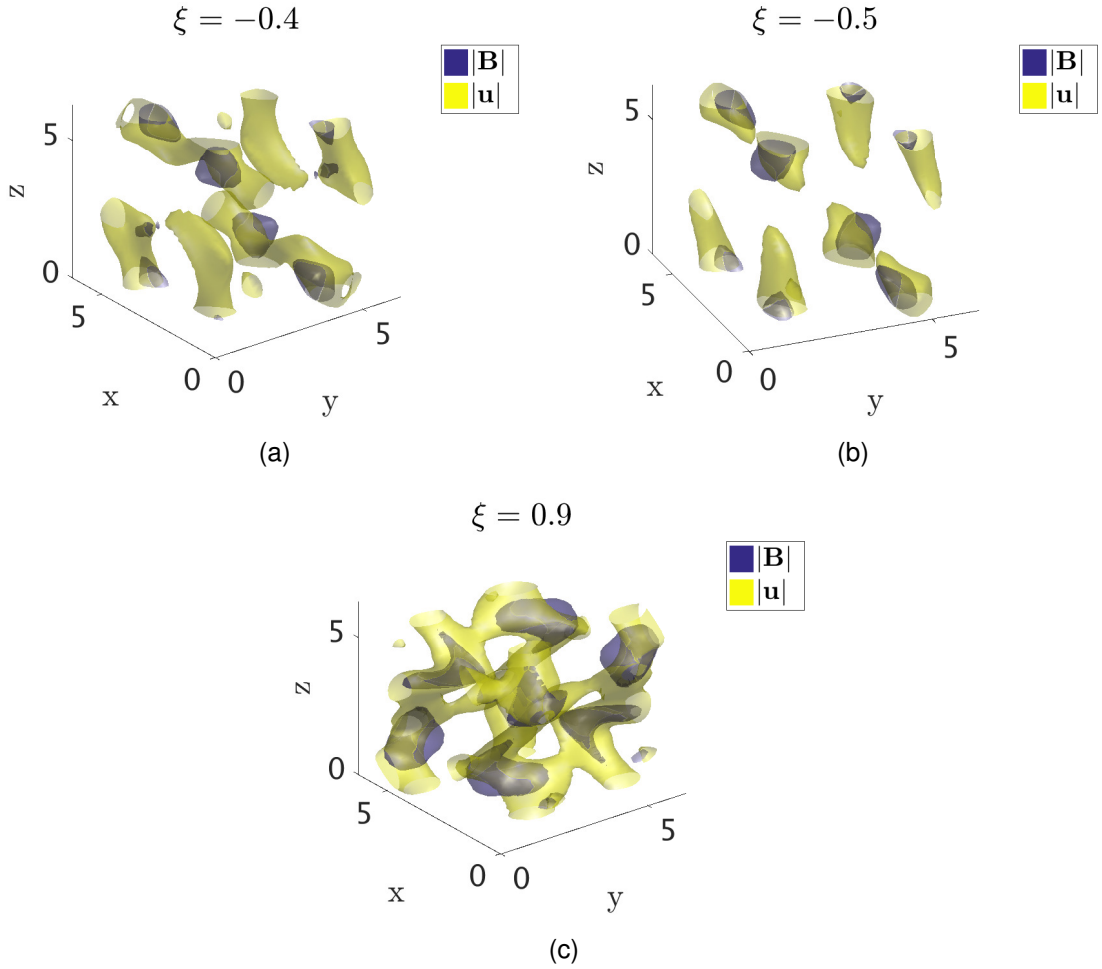

Figure 5.57: 90% isosurfaces of $|\mathbf{B}|$ and $|\mathbf{u}|$ for the values of ξ where there are differences in the field structures. We see that for these values the strong field regions of $\mathbf{u}$ are much larger than those of $\mathbf{B}$.

The last thing that I will examine with regards to the magnetic field structure is how the distribution of the field strength changes as $|\xi|$ increases. To examine this I follow a similar method as in figure 5.44 of the CP section by defining B_N and F_N as in equations (5.44a) and (5.44b).

$$B_N = \frac{|\mathbf{B}|}{\max_{\mathbf{x},\mathbf{y},\mathbf{z}}\left(|\mathbf{B}|\right)} \qquad (5.44a) \qquad F_N = \frac{|\mathbf{F}_\xi|}{\max_{\mathbf{x},\mathbf{y},\mathbf{z}}\left(|\mathbf{F}_\xi|\right)} \qquad (5.44b)$$

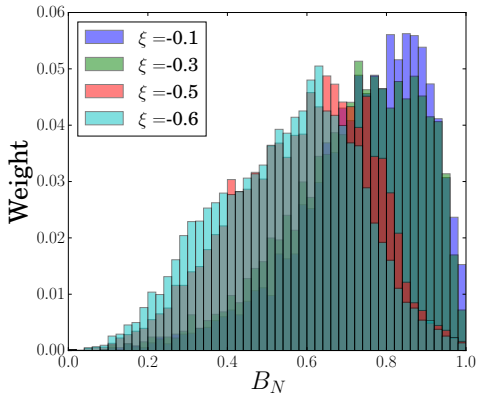

(a) B_N for negative values of ξ

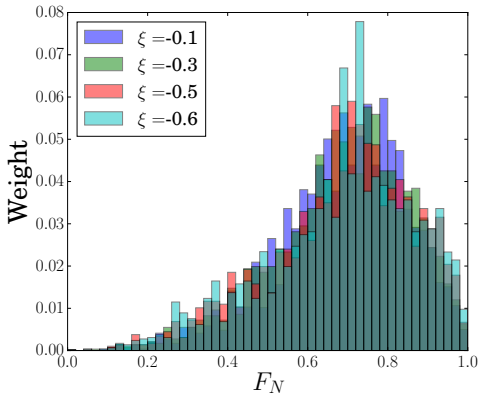

(b) F_N for negative values of ξ

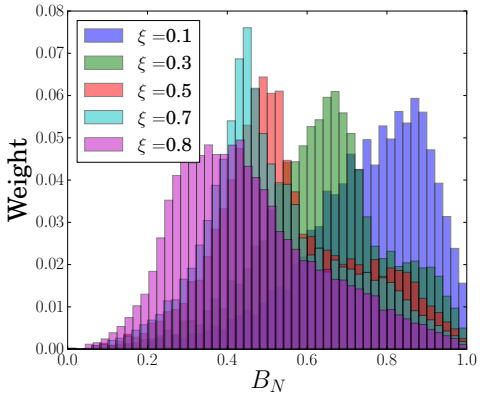

(c) B_N for positive values of ξ

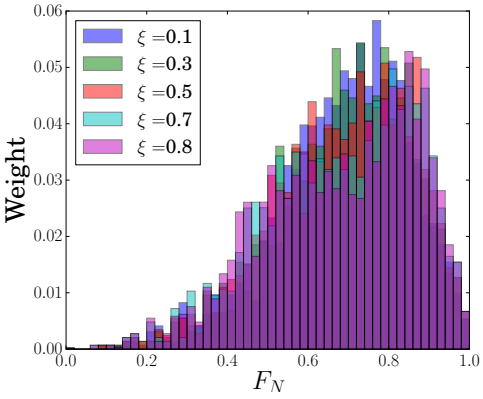

(d) F_N for positive values of ξ

Figure 5.58: Histograms of B_N (equation (5.44a)) and F_N (equation (5.44b)) for negative (a,b) and positive (c,d) values of ξ. For all ξ B_N tends to smaller values as $|\xi|$ increases. The exception is the two values immediately before no dynamo action (-0.6 and 0.9) which do not follow this trend.

Figures 5.58a and 5.58b show B_N and F_N for negative values of ξ. We see that as ξ becomes more negative the peak of the field strength migrates to lower values. The histograms of F_N in figure 5.58b however show very little change in the distribution as ξ increases. This is due to the fact that as the structures become elongated rather than smaller. Figures 5.58c and 5.58d show B_N and F_N for positive values of ξ. We see that as ξ increases the peak of B_N again migrates to lower values. The magnetic field becoming weaker on average in the domain is therefore a general property of $\mathbf{F}_\xi$ dynamos. In examining the isosurfaces this appears to be due to a reduction in the size of the regions of the strongest field with medium strength field occupying the regions in the domain it had previously. I note that $\xi = 0.9$ is an exception to the above trend. To see why consider figure 5.52e which shows the isosurfaces of the strongest $|\mathbf{B}|$ for $\xi = 0.9$. We see that

this value has again got 8 regions of strong field and as such the histograms for this value skew back to higher values.

As I have shown, the magnetic and fluid fields are highly aligned (greater than 98% of the maximum value). However isosurfaces of the magnetic field have shown that its structure differs somewhat from $\mathbf{F}_\xi$ at higher values of $|\xi|$. To examine how different than the forcing the flow and magnetic field are I define an equivalent to H_0 for the pairs $[\mathbf{u}, \mathbf{F}_\xi]$ and $[\mathbf{B}, \mathbf{F}_\xi]$ in equations (5.45b) and (5.45c) respectively. These quantities then measure how aligned to the forcing the flow and magnetic fields are respectively.

$$FE = \frac{1}{8\pi^3}\int_V \frac{\mathbf{F}_\xi^2}{2} dV \tag{5.45a}$$

$$A_{UF} = \frac{1}{8\pi^3}\frac{1}{\sqrt{FE}\sqrt{KE}}\left|\int_V \frac{\mathbf{u}\cdot\mathbf{F}_\xi}{2} dV\right| \tag{5.45b}$$

$$A_{BF} = \frac{1}{8\pi^3}\frac{1}{\sqrt{FE}\sqrt{ME}}\left|\int_V \frac{\mathbf{B}\cdot\mathbf{F}_\xi}{2} dV\right| \tag{5.45c}$$

Figure 5.60a then shows the result. Both $\mathbf{u}$ and $\mathbf{B}$ behave similarly so I will detail their results together. Both show that for $\xi \in (-0.3, 0.5)$ there is strong alignment between the field and the forcing but that this decreases as ξ gets further from zero with large jumps at $\xi = -0.4$ and $\xi = 0.6$. The jump at -0.4 occurs due to the drastic reduction in the size of the regions of the strong field. This can be seen within figure 5.51. The large decrease from 0.5 to 0.6 appears to be related to the change in the location of the remaining four regions of strong field. This can be seen in figure 5.59. We see that the regions of strong field have been reflected about the $x = \pi$ plane. For $\xi = [0.3, 0.4, 0.5]$ the four strong regions present are positioned identically and for $\xi = [0.6, 0.7, 0.8]$ the four strong regions present are positioned identically.

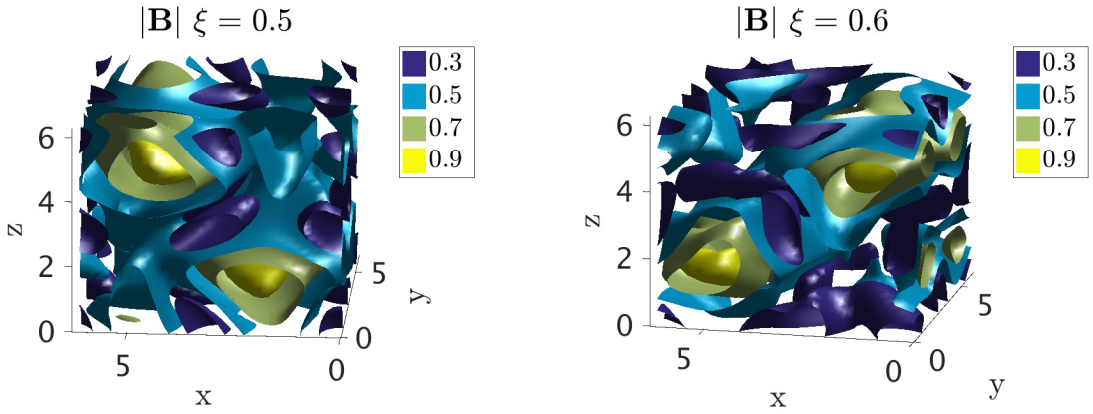

(a) (b)

Figure 5.59: Isosurfaces of $|\mathbf{B}|$ for $\xi = 0.5$ and $\xi = 0.6$. The position of the regions of strong field have been reflected in the $x = \pi$ plane.

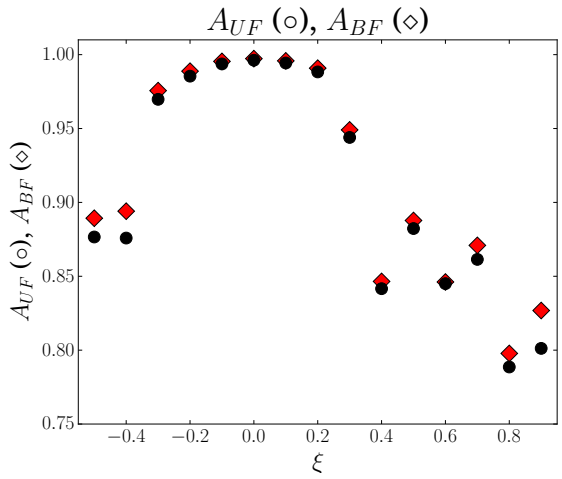

(a) Quantities (5.45b) and (5.45c) that show the alignment of the flow and magnetic field with the forcing $\mathbf{F}_\xi$. Whilst the alignment isn't as good as between $\mathbf{u}$ and $\mathbf{B}$ it is still strong. This shows that close to $\xi = 0$ $\mathbf{u} \propto \mathbf{F}_\xi$ and $\mathbf{B} \propto \mathbf{F}_\xi$.

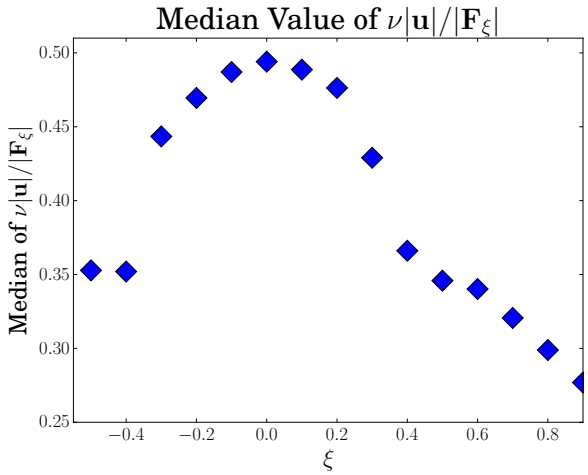

(b) Median value for the ratio $\nu|\mathbf{u}|/|\mathbf{F}_\xi|$. For the ξ whose $|\mathbf{u}|$ and $|\mathbf{B}|$ contours resemble the forcing the ratio is close to 0.5 which is the $\xi = 0$ value. The median value decreases as the asymmetry increases.

Figure 5.60

As $\mathbf{u} \approx \mathbf{B}$ and $\mathbf{B} \propto \mathbf{F}_\xi$ for $\xi \in (-0.3, 0.5)$ I now estimate the value of the constant of proportionality to compare it to the dynamo forced by $\mathbf{F}_A$. For the Archontis dynamo this is found to be 0.5. In figure 5.60b I show the median value of the ratio $\nu|\mathbf{u}|/|\mathbf{F}_\xi|$. Histograms (not shown) show that this median value is representative of the value of the ratio over the domain as a whole. We see that for $\xi \in (-0.3, 0.5)$ the ratio is close to its value for $\xi = 0$ ($\mathbf{F}_A$). Furthermore as ξ is increased or decreased away from 0 $\mathbf{u}$ and $\mathbf{B}$ become weaker compared to the forcing.

In summary, I have shown that an asymmetric Archontis forcing $\mathbf{F}_\xi$, does indeed produce a dynamo over a range of ξ. This dynamo has $\mathbf{u}$ and $\mathbf{B}$ strongly aligned however as $|\xi|$ becomes larger the alignment becomes marginally less and significant morphology differences occur between the fields and the forcing. The work in this section further illustrates the robustness of the aligned state as alignment is achieved for significant deviation from the Archontis dynamo.

5.6.3 A Time Dependent and Asymmetric Archontis Dynamo

In this section I build upon the work done in sections 5.6.1 and 5.6.2 by defining a forcing $\mathbf{F}_\chi$

$$\mathbf{F}_\chi = \nu \begin{pmatrix} \sin(z) \\ \left(1 + \chi\cos(t)\right)^2 \sin(x) \\ \left(1 + \chi\sin(t)\right)^2 \sin(y) \end{pmatrix}. \tag{5.46}$$

which is both asymmetric and time dependent. The structure of the forcing changes dramatically over time. Figure 5.61 shows the ratio of the y and z component of the forcing. We see that from $\pi/4$ to π the amplitude of the z component is much stronger then that of the y component and the opposite is true as time approaches $3\pi/2$.

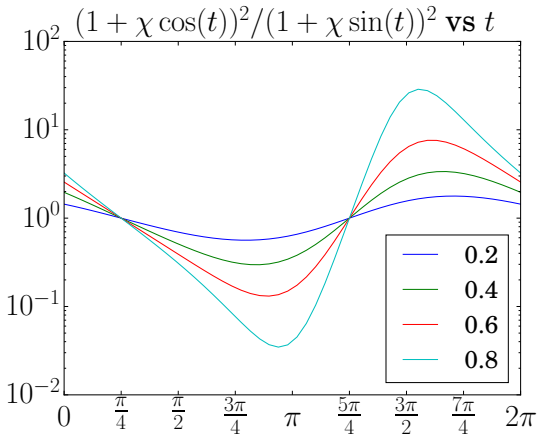

Figure 5.61: Ratio of the amplitude of the y and z components. As time approaches π the z component of the forcing has a much larger amplitude than the y component. As time is increased to 1.5π this then reverses with the y component of the forcing now having a much larger amplitude than the z component.

The effect of the changing amplitude can best be visualised using isosurfaces. In figure 5.62 I show isosurfaces of $|\mathbf{F}_\chi|^2$ for $\chi = 0.5$. Figure 5.62a shows 90% isosurfaces at four times, $t = \pi/4$, $3\pi/4$, $5\pi/4$ and $7\pi/4$. In figure 5.62b I then show 60% isosurfaces at the same times. In both figures we see that as time approaches π the field becomes constant in the x direction. To see why this is the case consider $(\mathbf{F}_\chi)^2$ at $t = \pi$

$$|\mathbf{F}_\chi|^2/\nu^2 = \sin(z)^2 + (1-\chi)^4\sin(x)^2 + \sin(y)^2 \tag{5.47}$$

we see that, for $\chi \in (0,1)$, the x dependent component provides less of a contribution to the total forcing. This can be seen in the blue isosurfaces in figure 5.62 which are clearly independent of x. Similarly for $t \in (1.25\pi, 2\pi)$ the y dependent sine function has a weak amplitude and as a result we see in the isosurfaces in figure 5.62 that the field becomes invariant in y.

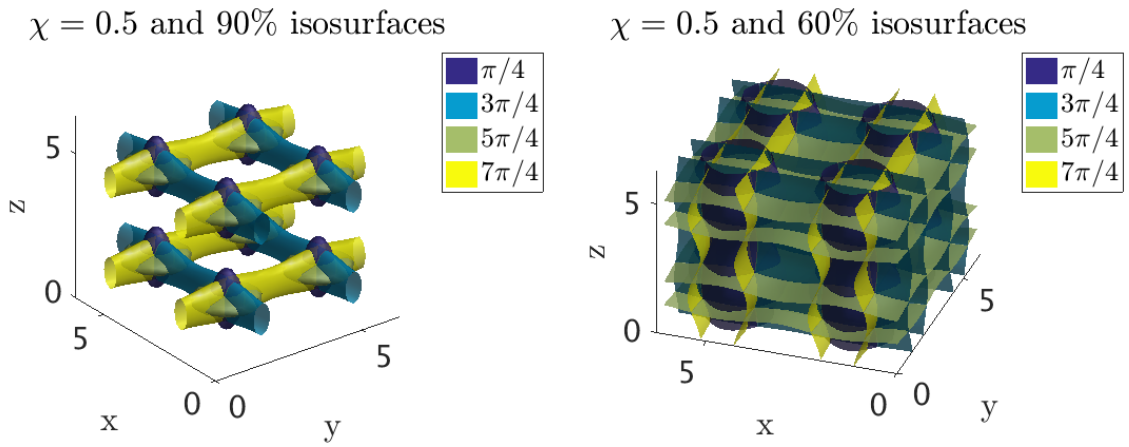

(a) (b)

Figure 5.62: Isosurfaces of $|\mathbf{F}_\chi|^2$ for $\chi = 0.5$.

Figure 5.63 illustrates the effect of increasing χ on the three dimensional structure of the forcing. For the strongest field we see that the cylindrical structures have increased the area of their $y-z$ cross-section with the isosurface at $t = 5\pi/4$ now too big to fit in the domain. For the mid strength field, represented by the 60% isosurfaces, there is much less difference in the field as χ increases. As such it is the changes to the strong field regions which must be playing the largest role in how the resulting flow and magnetic fields change as χ increases.

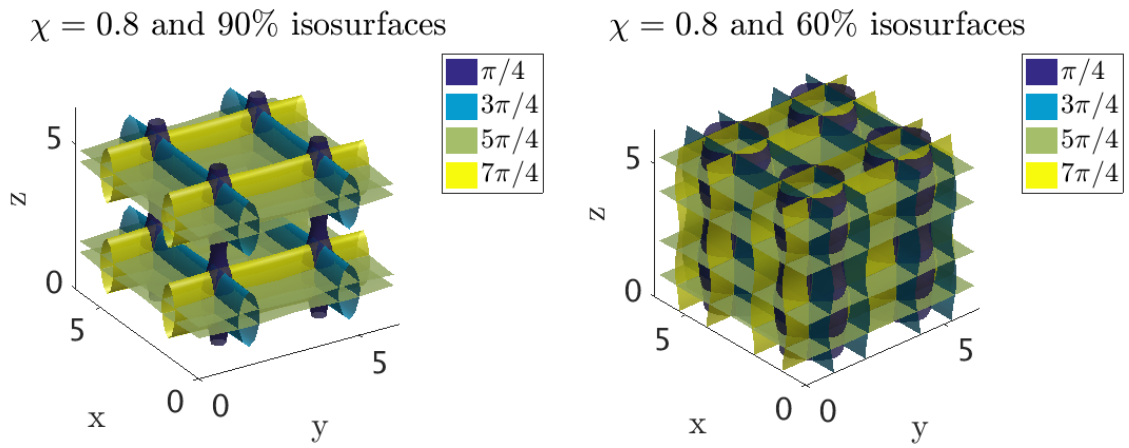

(a) (b)

Figure 5.63: Isosurfaces of $|\mathbf{F}_\chi|^2$ for $\chi = 0.8$.

I now show the results of a set of simulations where I increase χ from 0.1 in increments of 0.1. The code used to timestep the equations is a pseudo-spectral predictor-corrector code as outlined in Chapter 2. An initial condition for $\mathbf{B}$ is specified in Fourier space by assigning the imaginary parts of its Fourier modes $\widehat{\mathbf{B}}_\mathbf{k}$

$$\mathbf{B} = \sum_{\mathbf{k}} \widehat{\mathbf{B}}_{\mathbf{k}} \exp(i\mathbf{k}\cdot\mathbf{x}) \tag{5.48}$$

a value at each Fourier mode $\mathbf{k} = (k_x, k_y, k_z)$ according to a random normal distribution multiplied by 10^{-4}. The real part is chosen to be zero so as to speed up convergence to the final statistically steady state.

I calculate the KE, ME and H_0 regularly throughout the simulation. Above $\chi = 0.8$ the timeseries of the magnetic energy exhibits a number of different features which would require higher resolution than is feasible to ensure their reliability. As such I will examine only $\chi \leq 0.8$ here with larger values being left open for potential future work.

$$KE = \frac{1}{8\pi^3}\int_V \frac{\mathbf{u}^2}{2} dV \tag{5.49a}$$

$$ME = \frac{1}{8\pi^3}\int_V \frac{\mathbf{B}^2}{2} dV \tag{5.49b}$$

$$H_0 = \frac{1}{8\pi^3}\frac{1}{\sqrt{ME}\sqrt{KE}}\left|\int_V \frac{\mathbf{u}\cdot\mathbf{B}}{2} dV\right| \tag{5.49c}$$

In figure 5.64 I show the kinetic energy and the magnetic energy (with a shift in the vertical direction so it is visible) for a number of χ. We see that following a kinematic phase the magnetic energy saturates to a statistically steady state (SSS) with the kinetic energy also reaching a SSS with an almost identical mean value. Both energies have an oscillation with a period of 2π due to the time dependence of the forcing. Maxima of the KE correspond to minima of the ME and vice versa.

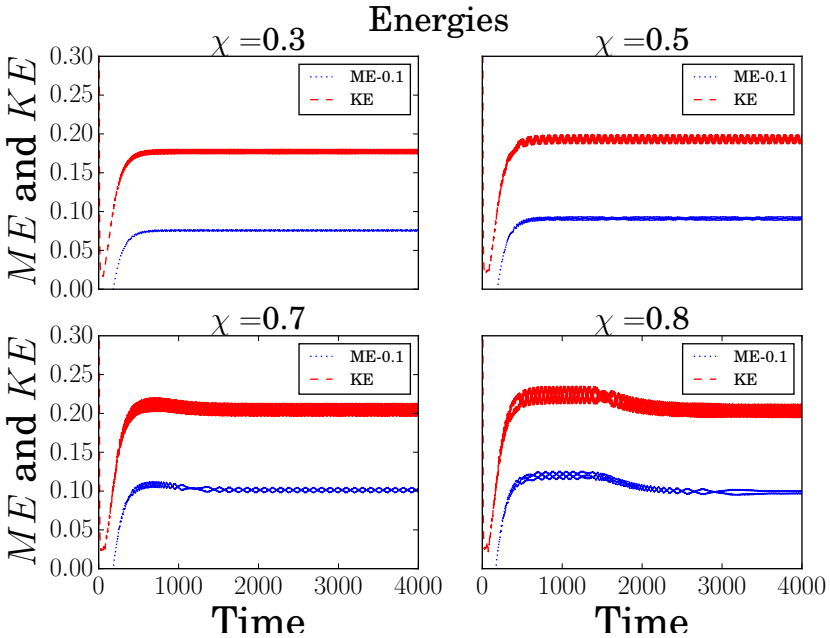

Figure 5.64: Kinetic energy (red) against magnetic energy (blue) where I have subtracted 0.1 from the ME so that it is not obscured by the KE. In both cases the energy becomes statistically steady with a 2π oscillation due to the oscillation in the forcing.

In figure 5.65 I show time averages of the two energies against χ as well as the alignment quantity H_0 against χ. In contrast to what we saw for $\mathbf{F}_{CP}$ and $\mathbf{F}_{\xi}$ an increase in χ appears to result in an increase in the amount of energy present. However, as we have seen in the other forcings examined the flow and magnetic fields remain highly aligned as χ is increased. This shows that the forcing operates in a similar manner to the others examined in that alignment is a necessity to achieve a saturated dynamo.

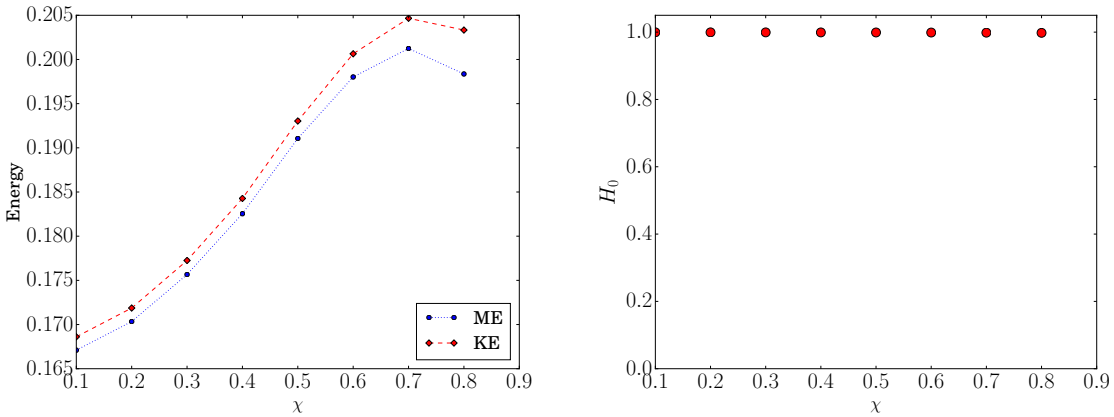

(a) Energy against χ. We see the energy increases until 0.7 when it starts to decrease.

(b) H_0 against χ. We see that all values of χ have strong alignment.

Figure 5.65

I will now examine how the magnetic field changes as the ME oscillates in the nonlinear

phase of the dynamo and seek to understand why the energy oscillates at all.

In figure 5.66 I show $z = 0$ contours of $\mathbf{B}^2$ at the last time during the simulation. There is very little difference as χ is increased, until we approach $\chi = 0.8$ where the regions of strong field begin to deform. These isosurfaces however do not show the complete picture.

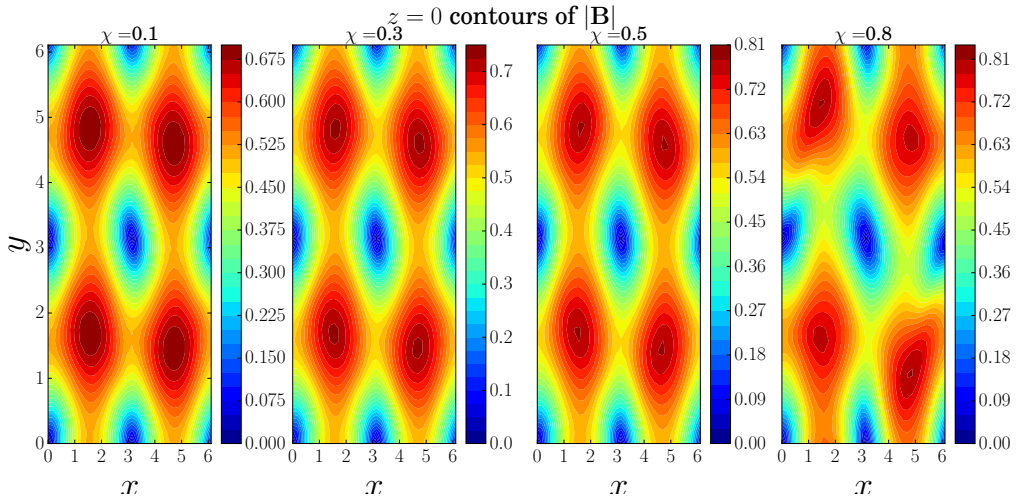

Figure 5.66: Contour plots of $\mathbf{B}^2$ at $z = 0$. There is very little difference up until $\chi = 0.8$.

In figure 5.67 I show 90% isosurfaces of $\mathbf{B}^2/\max_{x,y,z}\{\mathbf{B}^2\}$ at $\chi = 0.5$ and $\chi = 0.6$. For $\chi < 0.6$ 8 regions of strong field form however for $\chi \geq 0.6$ only half of these are present. This is similar to the behaviour seen for $\mathbf{F}_{CP}$ and $\mathbf{F}_{\xi}$ where we saw that, as the forcing deviated more from the Archontis forcing, half of the regions of strong field fail to form. Half of the strong fields not forming therefore appears to be the first step in the breakdown of the alignment, and subsequently the failure of the dynamo for these forcings close to $\mathbf{F}_A$.

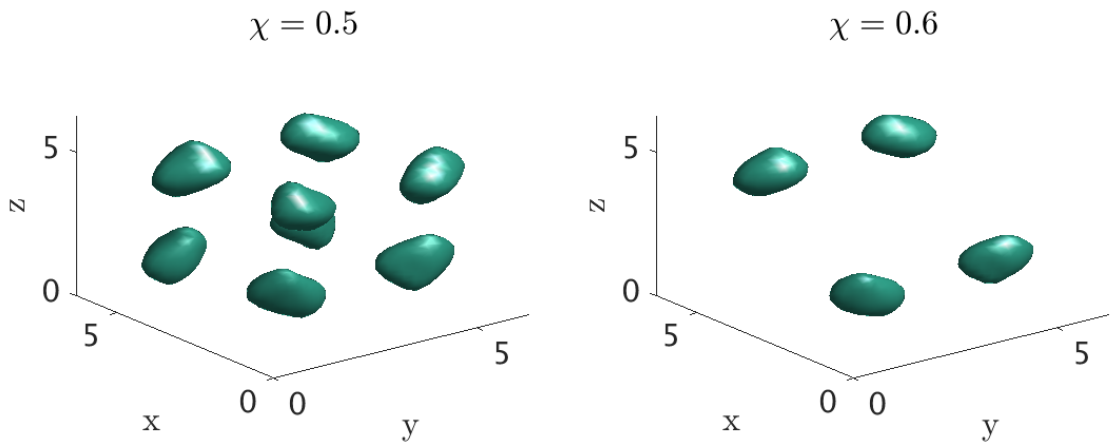

(a) 90% isosurfaces of $\mathbf{B}^2/\max_{x,y,z}\{\mathbf{B}^2\}$ for $\chi = 0.5$. We see that the strongest field is confined to 8 regions.

(b) 90% isosurfaces of $\mathbf{B}^2/\max_{x,y,z}\{\mathbf{B}^2\}$ for $\chi = 0.6$. We see that four of the 8 strong regions have not formed.

Figure 5.67

Examining these isosurfaces and figure 5.67a, where we see an increase in energy up until $\chi = 0.7$, shows that it must be the case that the field on average must be stronger for $\chi = 0.6$ then $\chi = 0.5$. In figure 5.68 I show histograms of $\mathbf{B}^2$ where we see that this is indeed the case. We also see that the field becomes skewed to its weaker values following $\chi = 0.5$. This is a direct result of only half of the regions of the strong field forming.

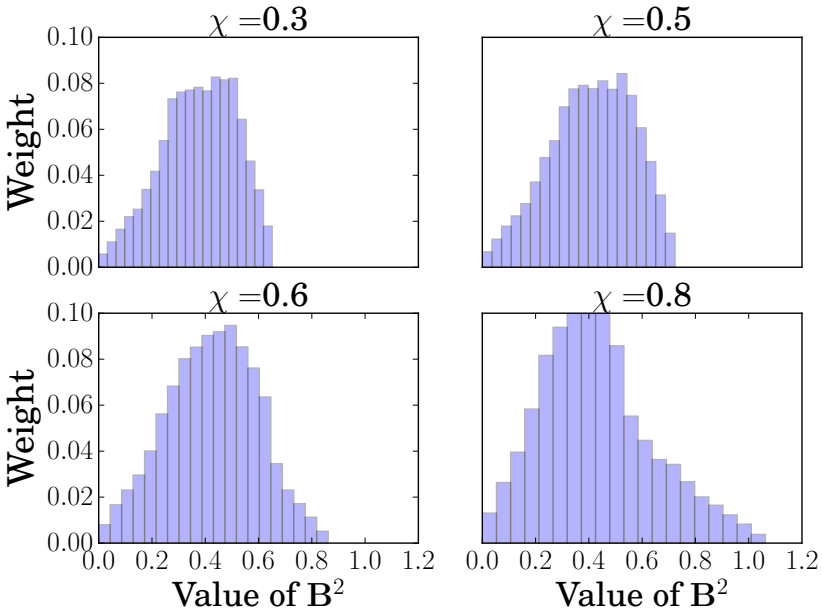

Figure 5.68: Histograms of the value of $\mathbf{B}^2$. We see that as χ increases the value of the strongest regions increases but the distribution becomes increasingly skewed towards weaker values. This is seen most prominently in going from $\chi = 0.5$ to $\chi = 0.6$ and occurs due to the fact that half of the regions of strongest field do not form.

In figure 5.69 I show how the distribution of $\mathbf{B}^2$ changes as the magnetic energy goes

from a minima (purple bar) to a maxima (green bar). For all χ we see a small increase in the proportion of strong field as the ME becomes maximal. This therefore shows that the regions of strong field become larger as the ME reaches a maxima.

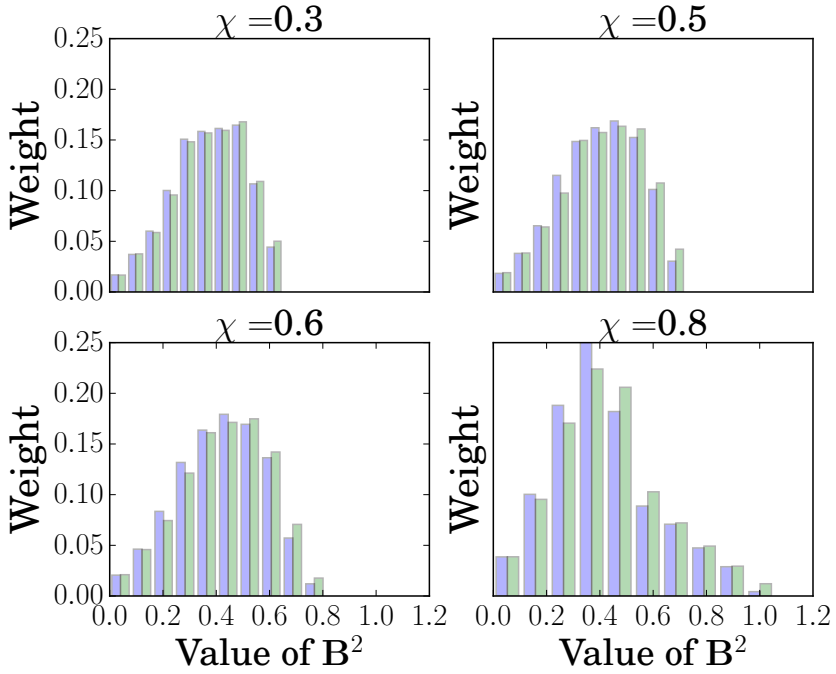

Figure 5.69: Histograms of the value of $\mathbf{B}^2$ at a minima (purple) and a maxima (green) of magnetic energy. We see that at the maxima their is an increase in the proportion of strongest field.

In figure 5.70 I show 90% isosurfaces of $\mathbf{B}^2$ during the nonlinear phase of the dynamo where both energies are oscillating. The isosurfaces show the change in the regions of strongest field going from the minima of ME ($t = 3213$), to the maxima ($t = 3216$). We see that there is very little change in structure unlike the forcing which changes its structure much more dramatically over time (see figure 5.63a). The same lack of change in structure is also seen for $\mathbf{u}^2$. We therefore see that the magnetic and flow fields have reached a state where they change very little. As such they do not resemble the forcing, which continues to evolve, but instead resemble something closer to the Archontis forcing, $\nu\big(\sin(z), \sin(x), \sin(y)\big)$.

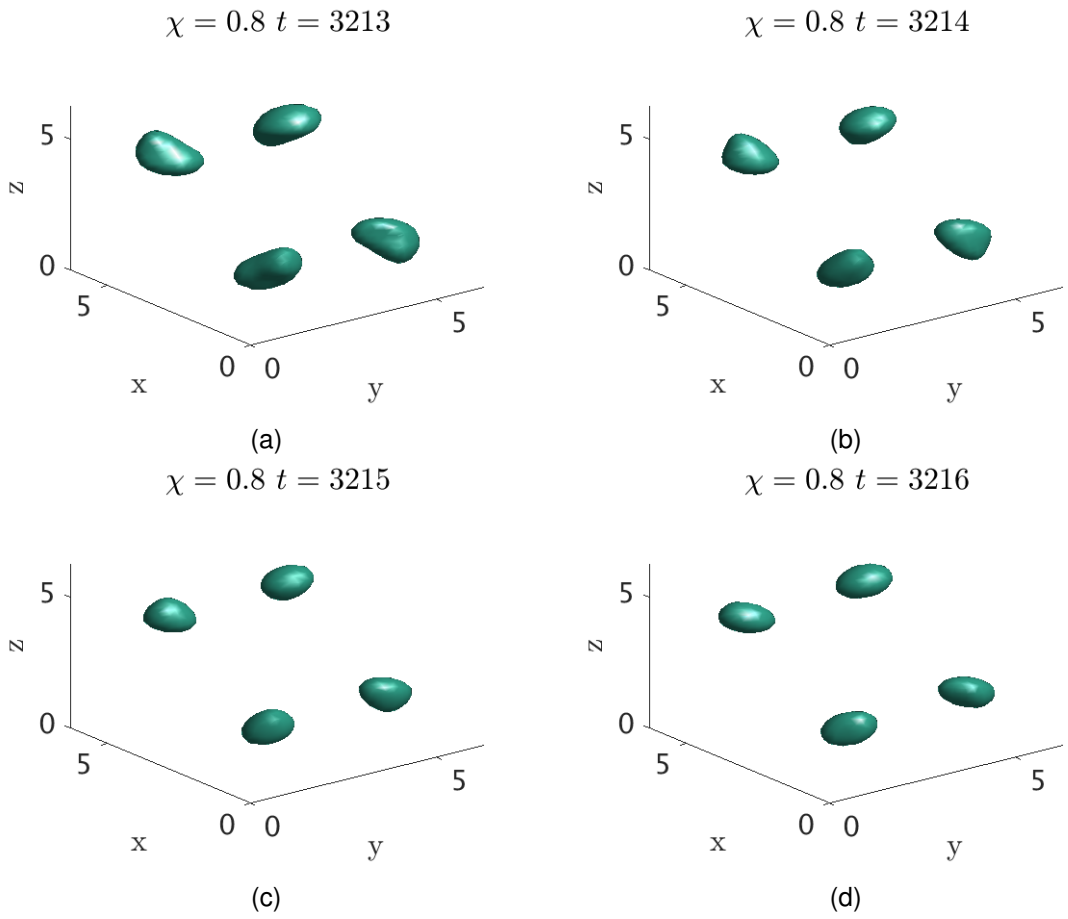

Figure 5.70: Isosurfaces of $\mathbf{B}^2$ for $\chi = 0.8$ as the ME goes from a minima (3213) to a maxima (3216). There is very little change in the structure of the magnetic field. This is in contrast to the change in the forcing structure shown in figure 5.63a where we see a dramatic change in magnetic field structure.

As the magnetic and flow fields do not change much over time once they reach the saturated state the oscillations in ME and KE must necessarily be due to the forcing. To see this consider the evolution equation for the total energy $E = ME + KE$ in equation (5.50). We see that if $\mathbf{u}$ and $\mathbf{B}$ remain approximately unchanged then it must be the injection of energy from the forcing which controls the oscillations.

$$\partial_t \int_V \frac{\mathbf{u}^2 + \mathbf{B}^2}{2} dV = \int_V \mathbf{u} \cdot \mathbf{F} dV + \nu \int_V \mathbf{u} \cdot \nabla^2 \mathbf{u} dV + \eta \int_V \mathbf{B} \cdot \nabla^2 \mathbf{B} dV \qquad (5.50)$$

To test this I calculate quantities (5.51b) and (5.51c) for 100 time units for each χ. The result is shown in figure 5.71

$$E = ME + KE \qquad (5.51a) \qquad T_F = \frac{1}{V} \int_V \mathbf{u} \cdot \mathbf{F}_\chi dv \qquad (5.51b)$$

$$T_D = \frac{1}{V} \int_V \nu \mathbf{u} \cdot \nabla^2 \mathbf{u} + \eta \mathbf{B} \cdot \nabla^2 \mathbf{B} dV \qquad (5.51c)$$

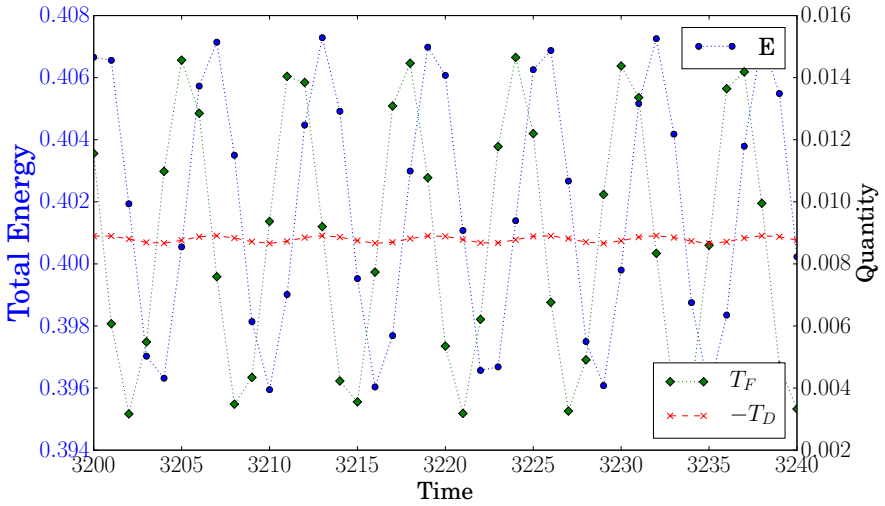

Figure 5.71: Total Energy (E) against rate of injection of forcing (T_F) and the negative of the sum of the effects of dissipation ($-T_D$). We see that the change in total energy is due to the forcing term in the evolution equation.

We see that T_D remains approximately constant. On the other hand the rate of injection of energy from the forcing oscillates. This clearly shows that the oscillations in energy are due to the forcing term in the evolution equation.

In summary, I have found that all of the magnetic and flow fields produced are close to equipartition ($\mathbf{u} \approx \mathbf{B}$) as was the case for the forcings previously examined. I have found that the structure of the magnetic and flow fields change very little once the nonlinear regime is entered with oscillations in the energy caused by an oscillation in the injection of energy from the forcing

Furthermore, I have found that the addition of an oscillating amplitude to the forcing successfully amplifies a seed magnetic field for a significant amount of oscillation. This further supports the results obtained for $\mathbf{F}_{CP}$ and $\mathbf{F}_{\xi}$ in that amplification of a seed magnetic field by first aligning the two fields appears to be a surprisingly robust process.

5.7 Discussion of Archontis Dynamo Results

I now refer back to the aims outlined at the beginning of the chapter and highlight what has been shown within the section. I then give possible avenues of future research.

- **To Explain the Two Statistically Steady States of the Archontis Dynamo**

In section 5.2 I showed that the first SSS is a result of choosing an initial seed field for $\mathbf{B}$ which is even. As the final state of the system is odd the odd component of $\mathbf{B}$ has to grow to exceed the even component. The first SSS of the two state dynamo is therefore a result of no growth in the, dominant, even component of $\mathbf{B}$ but exponential growth of the odd component. Once the odd component exceeds the even and the even becomes small a symmetry break occurs and the system transitions to the final state.

I have shown analytically that if the odd component of $\mathbf{B}$ is initially zero then it will remain so. The growth of this component therefore occurs due to small amounts of odd $\mathbf{B}$ being introduced by small numerical rounding errors. Furthermore I have shown that the reason that $\mathbf{H}_0$ is such a good indicator of the symmetry break is that, due to the properties of even and odd functions, only integrals of the exponentially growing weak components are non-zero. This was confirmed numerically by showing that the growth rate of $\mathbf{H}_0$ matches that of the odd component of $\mathbf{B}$ and the even component of $\mathbf{u}$.

- **To Examine the Robustness of the Dynamo to Changes to $P_m = \nu/\eta$**

  In section 5.4 I have shown that alignment and equipartition $\mathbf{u}$ and $\mathbf{B}$ persist over a broad range of P_m. Furthermore I showed that assuming $\mathbf{u} = \mathbf{B}$ and $\mathbf{u} \propto \mathbf{F}_A$ and calculating a predicted energy in terms of ν and η agrees well with results from numerical simulations. As such, $\mathbf{u} \propto \mathbf{F}_A$ and $\mathbf{B} \propto \mathbf{F}_A$ continues to be a good approximation over a broad range of P_m.

- **To Examine the Stability of the Final Aligned State to the Introduction of Time Dependence and Asymmetry to the Forcing**

  In section 5.6 I considered a number of different forcings with both asymmetry and time dependence. I have shown that obtaining statistically steady $\mathbf{u}$ and $\mathbf{B}$ which are strongly aligned is remarkably robust with an aligned dynamo being found for significant amounts of time dependence and asymmetry. This shows that the perfect symmetries present in $\mathbf{F}_A$ are not necessary to obtain an aligned dynamo.

  I have shown that for forcings close to $\mathbf{F}_A$ significant amounts of ME, relative to

KE, are only achieved when the two fields are strongly aligned. As such alignment appears to be crucial in achieving significant ME. Furthermore, in examining this relationship between energy and alignment I have considered a large number of different forcings, each with a different amount of asymmetry and time dependence. I have found a number of forcings which produce aligned dynamos and have therefore expanded the existing literature on aligned dynamos.

A number of different avenues for future research exist. The main aim of future work is to understand the mechanisms which drive the flow and magnetic field to an aligned and equipartition state. As such analytical work appears to be the most important. I have shown that if $\mathbf{u} = \mathbf{B}$ and $\mathbf{u} \propto \mathbf{F}_A$ initially then they remain so. One possible avenue for future research is therefore to expand this and show that given a generic initial condition for $\mathbf{B}$ the even component will decay. It would then be required to show that the odd component of $\mathbf{B}$ is necessarily equivalent to that of $\mathbf{u}$.

Considering whether aligned dynamos continue to exist for non-periodic boundary conditions is also a potential avenue for future research. As periodicity allows for the cancellation of a number of terms in the cross-helicity evolution equation, but is not a physical boundary condition, it is of astrophysical relevance to examine whether equipartition aligned dynamos still exist without periodic boundary conditions. Examining whether these dynamos exist for spherical geometries is also important in assessing whether this type of dynamo could amplify the seed magnetic field of an astrophysical body.

Chapter 6

Evolution of Field Structures in ABC Forced Nonlinear Dynamos

6.1 Motivation for Studying Structure in ABC Flows

In this section I give an overview of the existing literature on a body of flows known as the ABC flows. In doing so I highlight a gap in the literature which is worthy of study and is the focus of my work within this chapter.

ABC flows are a group of flows of the form

$$\mathbf{u}_{ABC} = \begin{pmatrix} A\sin(kz) + C\cos(ky) \\ B\sin(kx) + A\cos(kz) \\ C\sin(ky) + B\cos(kx) \end{pmatrix} \tag{6.1}$$

where I set $k = 1$. In this section I will replace A, B and C in the subscript of $\mathbf{u}_{ABC}$ and $\mathbf{F}_{ABC} = \nu\mathbf{u}_{ABC}$ by their respective values when I am talking about a specific ABC flow or forcing. The ABC flows are named after Arnold and Childress, for their papers [9] and [28] as well as for Beltrami due to the flows having the Beltrami property $\mathbf{u} = \nabla \times \mathbf{u}$. A useful property of $\mathbf{u}_{ABC}$ is that given a forcing, $\mathbf{F}_{ABC} = \nu\mathbf{u}_{ABC}$, the flow $\mathbf{u}_{ABC}$ is then an exact solution of the equation of motion (6.2).

$$\frac{\partial \mathbf{u}}{\partial t} = -\nabla P - (\mathbf{u}\cdot\nabla)\mathbf{u} + \nu\nabla^2\mathbf{u} + \mathbf{F}_{ABC} \tag{6.2}$$

The properties of the flow depend upon the values of A, B and C. If $A_1^2 > A_2^2 + A_3^2$ where A_1 is the largest of A, B and C and A_2 and A_3 are the remaining two then the flow has no stagnation points however if $A_1^2 \leq A_2^2 + A_3^2$ then the flow has stagnation points [34]. The magnetic field induced by the ABC flow in a kinematic dynamo is found to have a very different structure depending on whether or not stagnation points exist due to their role in influencing how magnetic field builds up within the domain and so it is natural to split kinematic and nonlinear dynamo work into parts where the flow/forcing has and doesn't have stagnation points.

A number of authors have examined ABC flows hydrodynamically. For example Dombre et al. within [34] performed a detailed analysis of the flows dynamical properties. They found that the flow in general consisted of helical streamlines surrounded by Kolmogorov-Arnoldi-Moser surfaces and regions of chaos. Stability of the ABC flows has also been examined. Galloway and Frisch within [43] and Podvigina and Pouquet within [84] both examine the stability of $\mathbf{u}_{111}$ to perturbations. They found that at high enough R_e the 111 flow becomes unstable to the perturbations and evolves into a different flow. This result is important as it is the amplification properties of the ABC flow we are concerned with and so we must ensure that the flow does not change to a different flow during the kinematic regime of a nonlinear dynamo (one where the flow field is evolved as well as the magnetic field). Of particular interest is the result in [84] that the 111 flow appears to transition to a flow close to the 522 flow.

The ABC flows were first examined within MHD as flows within kinematic dynamo work. Arnold and Korkina [10] and Galloway and Frisch [41] examined the 111 flow up to $R_m = 200$ and found two windows of dynamo action. These were given within [41] as being $R_m \in (8, 18)$ and $R_m \in (27, 200)$. These windows have been extended and refined in a number of papers since with [42] refining the first window to $(9, 17.5)$. Galloway and Frisch within [42] also examined the magnetic field structure of the 111 dynamo showing it concentrates in "cigar like structures" along heteroclinic field lines connecting stagnation points. These cigars were further examined within [44] by Galloway and O'Brian, [4] by Archontis and Dorch and [35] by Dorch. It was shown in [44], [4] and [35] that the magnetic

field in fact forms double cigars with the cigars being opposite in sign. Reconnection between these then acts to redistribute the magnetic field throughout the bulk of the domain and drives the growth of the magnetic energy. Archontis et al [6] further show that once symmetry breaking occurs for the $k = 2$ case the flux cigars within the domain then vary in size

Further research has been performed on the 111 kinematic dynamo by Bouya and Dormy ([19],[20]), Jones [57], Jones and Gilbert [58], Gilbert [47], Galanti et al [37] (a paper I return to later), and Shumaylova et al [98].

There has been much less work done on the non 111 kinematic ABC flows. Galanti et al within [37] examined growth rates for moderate R_m where they set $1 = A > B = C$ and vary $B = C \in (0, 1)$ whilst always ensuring that $A^2 + B^2 + C^2 = 3$. Figure 6.1 shows the result. The results show that the dynamo with the largest growth rate is close to parameter values 522 (normalised by dividing each by $\sqrt{11}$). A more detailed parameter scan was also performed by Alexakis within [3]. Alexakis showed that the 522 is indeed the parameter values with the largest growth rate as well as a number of other results pertaining to other criterion of “best kinematic dynamo” such as one with a positive growth rate at the lowest R_m.

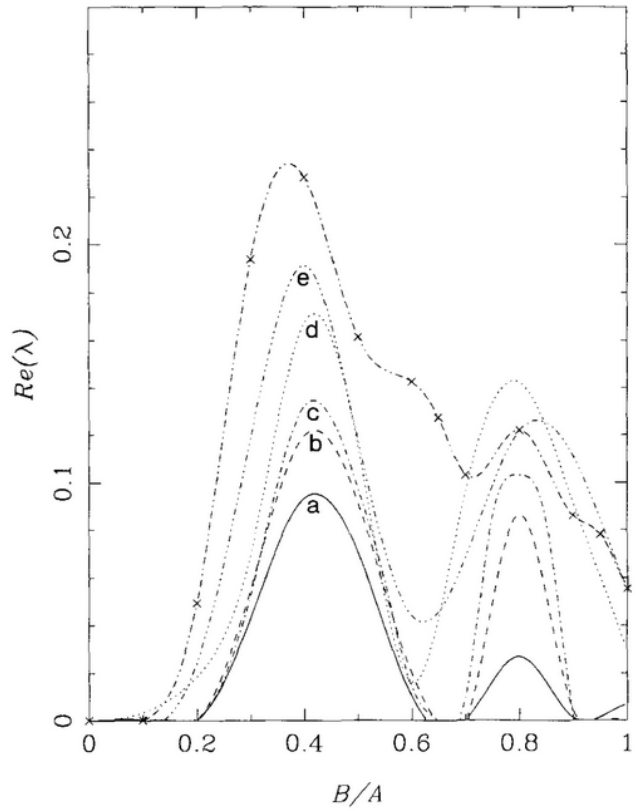

Figure 2 Rate of growth of the magnetic field generated by the ABC kinematic dynamo with $k_0 = 1$, as a function of B/A with the double condition that $B = C$ and $A^2 + B^2 + C^2 = 3$ for various magnetic Reynolds numbers: $R^M = 12$, (a); $R^M = 16$, (b); $R^M = 20$, (c); $R^M = 40$, (d); and $R^M = 80$, (e). The largest Lyapunov exponents in the regions where the magnetic field develops are indicated by $\times$-symbols.

Figure 6.1: Figure 2 from [37] showing kinematic growth rate against coefficient values in the ABC flow. We see that the 522 flow has the largest growth rate and that relative to the rest of the family the growth rate of the 111 is small.

As well as [37] a small number of other papers have looked specifically at kinematic ABC flows other than the 111. Galloway and Frisch within [42] looked at the 411 and 522 flows in particular finding a magnetic field that is flatter and wider than the cigar structures of the 111. Galloway and O'Brian within [44] further examined the 522 at $R_m = 300$ and showed that the magnetic field forms sheet like structures. The paper also showed that the 211 and 411 similarly formed sheet like structures and formed the conclusion that sheet like magnetic fields is a feature of dynamos driven by ABC flows without stagnation points. The sheets are investigated more thoroughly in [4] where it is shown that the magnetic field forms into double sheet like structures which replenish the magnetic field within the rest of the domain through a process of reconnection in much the same way that happens for flux cigars. Archontis further examines this within [5] where he calls the thin structures "ribbons" and shows that energy growth occurs through stretching and constructive folding

of the ribbons. This label of ribbons will be addressed during my analysis in a later section where in particular I will show that the use of this word aligns well with its interpretation as deformation of a sphere.

As with the non 111 kinematic results very little has been done to examine the full nonlinear system where the magnetic and fluid fields are timestepped together. One of the first papers to attempt this was [37] by Galanti et al. They showed that the 111 flow produces a nonlinear dynamo both at R_m where it produces a kinematic one as well as at an R_m where it does not.

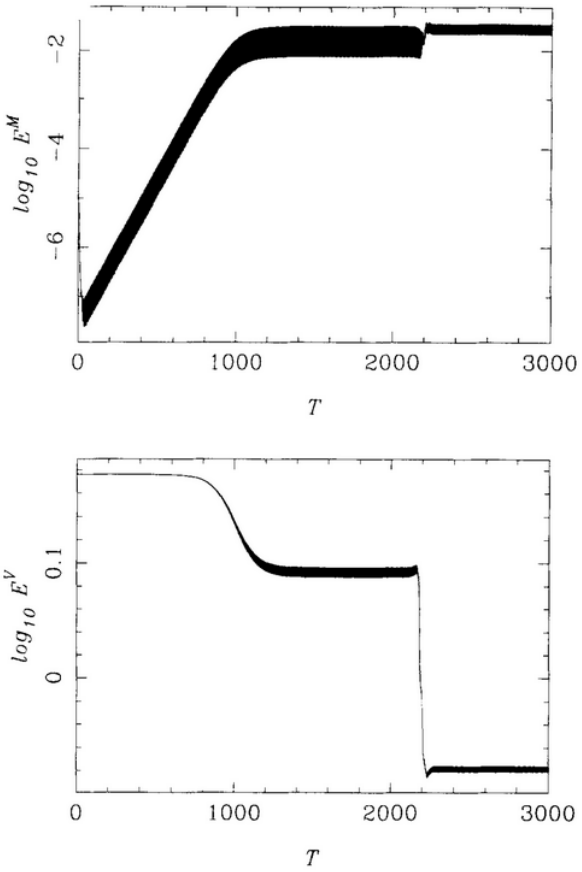

Figure 3 Time evolution of the magnetic (a) and kinetic (b) energies when the stirring force is given by equation (3.1) with $A = B = C = 1$, $k_0 = 1$, and $R^V = R^M = 12$.

Figure 6.2: Figure 3 from [37] showing magnetic and kinetic energies. Two saturation phases occur.

Figure 6.2 shows the kinetic and magnetic energies for an R_m which is a kinematic dynamo. Unusually we have two saturation phases to the dynamo. Brummell et al within [21] also examined flows in the ABC family in the nonlinear regime. In particular they took the 111 flow with a time dependent oscillation $\mathbf{x} \mapsto \mathbf{x} + \varepsilon \sin(\Omega t)$ and varied the frequency and

radius of oscillation.

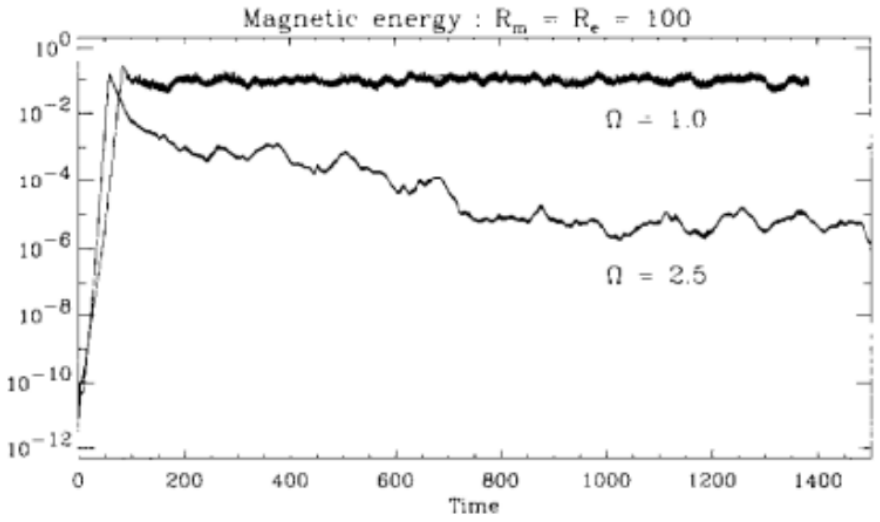

Fig. 3. Times series of the magnetic energy for the cases with forcing frequencies $\Omega = 1$ and $\Omega = 2.5$. Different nonlinear behaviors are apparent: $\Omega = 1$ equilibrates with a finite magnetic energy, whereas for $\Omega = 2.5$ the magnetic energy decays.

Figure 6.3: Figure 3 from [21] showing magnetic energy for two different frequencies. Interestingly the frequency with the highest kinematic growth rate $\Omega = 2.5$ is found to decay in the nonlinear regime.

Figure 6.3 shows the magnetic energy for two different frequencies. Interestingly the frequency with the highest kinematic growth rate $\Omega = 2.5$ is found to decay in the nonlinear regime. This result serves as a warning that exploring flows which would be considered strong dynamos within the kinematic regime may perform poorly once the flow and magnetic field begin to exchange energy. Archontis et al. [5] also considered an ABC forced flow (with parameter values $0.9 : 1 : 1$) which differs only slightly from the 111 flow. The paper considers the high R_m regime so as to examine a strongly turbulent dynamo. It is found that the amplification of the field occurs in the regions of weak magnetic field, a result also seen by Galanti et al. [37].

It is clear from the above literature that there exists a number of unanswered questions. In particular a nonlinear examination of the ABC flows remains predominantly unexplored. As $\mathbf{F}_{ABC}$ is an exact solution to the equation of motion it enables the study of a group of nonlinear dynamos whose kinematic phase is well understood and have existing literature. As such, links can be made between the saturated magnetic field and its kinematic properties.

As the variety of parameter choices enable us to have both flat and filamentary structures the family of flows can be used to examine how a variety of different magnetic field structures change upon saturation to the nonlinear regime. The study of the change in these structures in this relatively simple framework can then be used to aid in the understanding of more complex and realistic simulations.

At present there is no literature concerning nonlinear dynamos forced by flows with no stagnation points. How flat magnetic field structures behave upon saturation for the ABC forcings therefore remains to be explored. Furthermore as these flows have been conclusively shown by Alexakis [3] to be the fastest kinematic dynamos they are a natural choice to examine within the nonlinear regime as the magnetic field should grow sufficiently fast during the kinematic regime to produce magnetic energy suitably large so as to influence the flow field.

ABC forced nonlinear dynamos with stagnation points are also relatively unexplored as $\mathbf{F}_{111}$ and $\mathbf{F}_{0.911}$ are the only forcings with stagnation points which have been examined. As $\mathbf{u}_{ABC}$ with stagnation points behave similarly in the kinematic regime it is interesting to explore whether or not the similarities remain once we enter the nonlinear regime. In particular the discovery by Galanti [37] of a flattening out of the magnetic field structures of the 111 flow upon saturation then immediately draws comparisons to the kinematic 522 magnetic field's structure which motivates the study of whether or not the flattening out of the cigars occurs for all stagnation point forcings. If so this would have implications for all magnetic fields which have a filamentary structure during the kinematic regime as it would suggest that one manner in which they can achieve a saturated nonlinear dynamo is for the magnetic field to become stretched out in the perpendicular direction to the filament and thus "flattened". This flattening would then enable the dynamo to persist at high R_m as its magnetic field is no longer in filaments whose cross-sectional area would scale like $R_m^{-0.5}$ [38].

In order to quantify changes to magnetic field structure upon saturation, a method of measuring changes to structure is required. A convenient method for doing this is Minkowski Functions which give an objective measure of the planarity and filamentarity of the mag-

netic field structure. From these we then have quantities whose value changing tells us whether a structure is "flattening" and words such as planar, filamentary and ribbon-like have clear definitions as opposed to simply being used as descriptors as has predominantly been the case at present. Very little use has been made of Minkowski Functions within MHD. However, they have been successfully employed by Wilkin [108], Wilkin et al. [109] and Seta et al. [97] to examine the relationship between a turbulent dynamo's magnetic field structure and R_m. An overview of Minkowski Functions will be given in section 6.2.

In this chapter I examine the magnetic field structures within nonlinear dynamos forced by ABC flows. In section 6.2 I introduce the Minkowski Functions. In section 6.3 I lay the groundwork for the study of the 522 nonlinear dynamo in section 6.4 by examining the kinematic and hydrodynamic regimes of the 522 dynamo. In section 6.5 I compare the nonlinear regime morphologies of the 522 and 111 dynamos and finally in section 6.6 I examine the morphologies of nonlinear ABC dynamos whose forcings contain stagnation points. The main aims of this body of research are as follows:

- **To examine how magnetic field structures change when a dynamo saturates**.

  One of the main aims is to identify the changes that the saturation process has on the magnetic field structure. The simple geometry and the fact that the magnetic field has the same type of structure throughout the domain, in the kinematic regime, should help to provide a clearer picture of the impact of the saturation process on the magnetic field structure.

- **To apply morphology tools (the Minkowski Functions) to nonlinear dynamos to quantify structure changes in the magnetic field.**

  Relatively little use has been made within MHD dynamo theory of Minkowski Functions or any other morphological tools to examine the three dimensional structure of the magnetic field. A secondary aim of this work is therefore to show just how useful these can be in aiding our understanding of the dynamo process and the magnetic field's evolution.

- **To examine the suitability of the 522 flow as a nonlinear dynamo.**

  As there is no literature examining the suitability of $\mathbf{F}_{522} = \nu\mathbf{u}_{522}$ as a forcing whether or not a saturated regime will be achieved is unknown, however the large growth rate in the kinematic dynamo suggests that there is sufficient initial field amplification and is therefore encouraging.

- **To compare the magnetic field morphologies (in the saturated regime) of the 522 and 111 dynamos**.

  Initial work by Galanti et al. [37] has shown that the magnetic field of the 111 dynamo flattens upon entering the saturated regime. As the 522 dynamo's magnetic field during the kinematic regime is flat and the 111 dynamo's magnetic field is filamentary I am able to compare how the morphology changes during the saturation process for these two different initial magnetic field structures.

- **To examine whether the flattening of magnetic field structures is a broad feature of nonlinear stagnation point ABC dynamos.**

  I define stagnation point dynamos to be those forced by ABC forcings $\mathbf{F}_{ABC}$ which have stagnation points. I will investigate whether the flattening observed for the 111 dynamo is also a feature of other stagnation point dynamos. I note that the R_m and R_e that I examine will be small and so the results will be specific to small values of these parameters and as such the results may not apply to turbulent dynamos at higher R_m and/or R_e.

6.2 Calculation of Minkowski Functions

Minkowski Functions are a means by which we can gain an understanding of the shape of a scalar field within a domain by providing a quantitative measure of the structure. Given a scalar field $B(x,y,z)$ we can define an excursion set (see, for example, [49]) of B, F_ν, to be the set of points for which $B > \nu\sigma$ where $\sigma = \max_{x,y,z}\{B\}$ and ν is our threshold value. The closed boundary surfaces of the excursion set then define a number of different structures

within our domain which are also isosurfaces at the threshold value ν. These boundary surfaces thus enclose the regions of the domain where $B > \nu\sigma$, i.e. our excursion set.

The four Minkowski Functions which describe the geometry of these surfaces are then given by

$$V_0 = \int_V \Theta(B - \nu\sigma) dV \qquad (6.3a) \qquad V_1 = \int_{\partial F_\nu} ds_\nu \qquad (6.3b)$$

$$V_2 = \int_{\partial F_\nu} \frac{\kappa_1 + \kappa_2}{2} ds_\nu \qquad (6.3c) \qquad V_3 = \frac{1}{2\pi} \int_{\partial F_\nu} \kappa_1 \kappa_2 ds_\nu \qquad (6.3d)$$

where Θ is a Heaviside function and $\int_{\partial F_\nu}$ denotes a surface integral over the boundary of the excursion set. (6.3a) is therefore the volume, (6.3b) is the surface area, (6.3c) is the integrated mean curvature and (6.3d) is the Euler characteristic of the surface with a 2π normalisation so as to reproduce the correct Euler characteristic for a sphere i.e. 2. κ_1 and κ_2 are the principal curvatures of the surface. Detail on principle curvatures is omitted here but may be found within Chapter 13 of E.Abbena et al. [1]. Ratios of the four Minkowski Functions then give 3 measures of the shape of our structure, each of dimension of length;

$$T = \frac{3V_0}{V_1} \qquad (6.4a) \qquad W = \frac{V_1}{V_2} \qquad (6.4b)$$

$$L = \frac{V_2}{2\pi V_3} \qquad (6.4c)$$

these have been normalised to yield the radius r over a spherical surface by noting that Gaussian curvature $\kappa_1\kappa_2$ and mean curvature $(\kappa_1 + \kappa_2)/2$ are constants on a sphere and of values $1/r^2$ and $1/r$ respectively. Furthermore, as identified by Sahni, Sathyaprakash and Shandarin [93] we can make two dimensionless quantities out of T,W and L which give us a measure of the Planarity, P, and Filamentarity, F, of the field. These are;

$$P = \frac{W - T}{W + T} \qquad (6.5a) \qquad F = \frac{L - W}{L + W} \qquad (6.5b)$$

Between quantities T, W, L, P and F we are therefore able to attach a number to the relative dimensions of the excursion set. From this we can then make comparisons to a number of idealised structures; a perfectly flat pancake like structure $(P,F) = (1,0)$, a filament where L is much larger than the other two so that $(P,F) = (0,1)$, a sphere where $T = W = L$ so that $(P,F) = (0,0)$ and a ribbon where $L \gg W \gg T$ so that $(P,F) = (1,1)$.

6.2.1 Crofton's Method

To calculate Minkowski Functions I use Crofton's method. This method uses the counting of faces, edges and cubes of the scalar field at positions on a lattice grid to approximate the Minkowski Functions and is thus designed for use on a grid such as one used within numerical simulations. It is the most common method employed to calculate Minkowski Functions, used for example by Schmalzing and Buchert within cosmology [94] and later by Wilkin et al.[109] and Seta et al. [97] to analyse magnetic field structures from a small scale dynamo.

Define an *edge* to be the length dx between two neighbouring points, a face to be a collection of 4 points in any plane with coordinates (i, j), $(i+1, j)$, $(i+1, j+1)$ and $(i, j+1)$ and a cube to be the 3D extension of this. If n_0 is the total mesh points with values in the excursion set, n_1 is the total number of edges where each of the end points is in the excursion set, n_2 is the number of faces where each of the four points is in the excursion set and finally n_3 is the number of cubes where each of its 8 points is in the excursion set then we can approximate the four Minkowski Functions as

$$V_0 = \frac{n_3}{L} \tag{6.6}$$

$$V_1 = \frac{1}{dx \cdot L}\left[\frac{2n_2}{9} - \frac{2n_3}{3}\right] \tag{6.7}$$

$$V_2 = \frac{1}{(dx)^2 \cdot L}\left[\frac{2n_3}{3} - \frac{4n_2}{9} + \frac{2n_1}{9}\right] \tag{6.8}$$

$$V_3 = \frac{1}{(dx)^3 \cdot L}\left[n_0 - n_1 + n_2 - n_3\right] \tag{6.9}$$

where dx is the grid spacing and L is the total number of points that make up the cube $((2\pi/dx)^3)$. Tests with a number of cuboids produce the expected values of V_0-V_3. To test the code further I use the same approach as Wilkin [108] and consider the ellipsoid (6.10)

$$\alpha x^2 + \beta y^2 + z^2 = r^2 \tag{6.10}$$

Making α and β large then produces a long filament in the z direction (and so a small P

and large F) and making either α or β large produces a planar structure (large P and small F). To check that we produce values of P and F which do indeed correspond to filaments and planar structures I vary α and β between 1 and 4096 in such a way as to transition between the structures. This is done for $r = 120$ in a box of fixed size and a resolution of 256^3. The result is shown in figure 6.4 with the brackets next to the points indicating α and β respectively. We obtain the expected results with variation of α and β in that if one is much larger than the other two we obtain a flat planar structure and if two are much larger than the z direction we obtain a filament. Figure 6.5 shows typical examples of the structures using the full ellipsoidal equation (6.11). These enable us to have a clear image of what the numbers for P and F represent (see [109] for more examples).

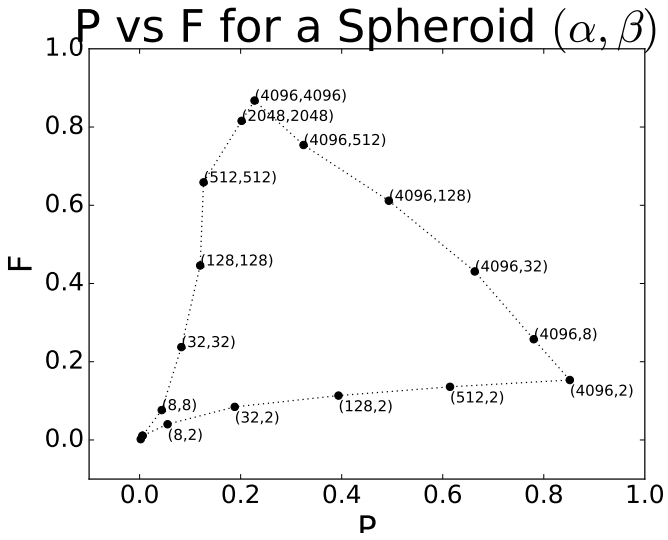

Figure 6.4: Variation of α and β.

$$r^2 = \left(\frac{x}{x_r}\right)^2 + \left(\frac{y}{y_r}\right)^2 + \left(\frac{z}{z_r}\right)^2 \tag{6.11}$$

$$(r, x_r, y_r, z_r) = (1, 100, 100, 1)$$

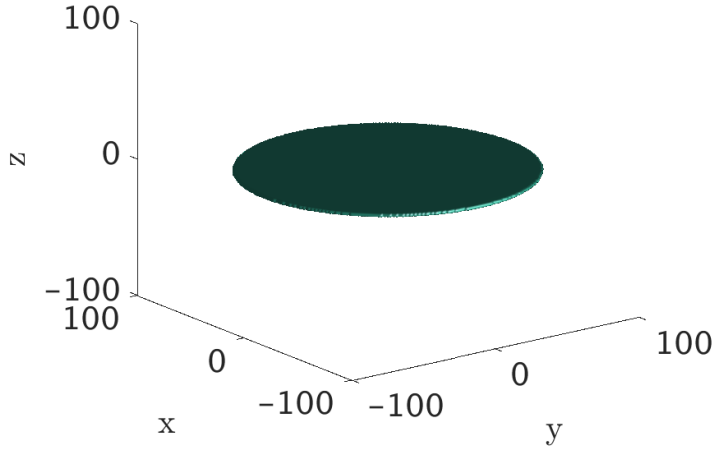

(a) Example of a pancake, the shape resembles a flat disk. The values used are $(x_r, y_r, z_r) = (100, 100, 1)$

$$(r, x_r, y_r, z_r) = (1, 100, 1, 1)$$

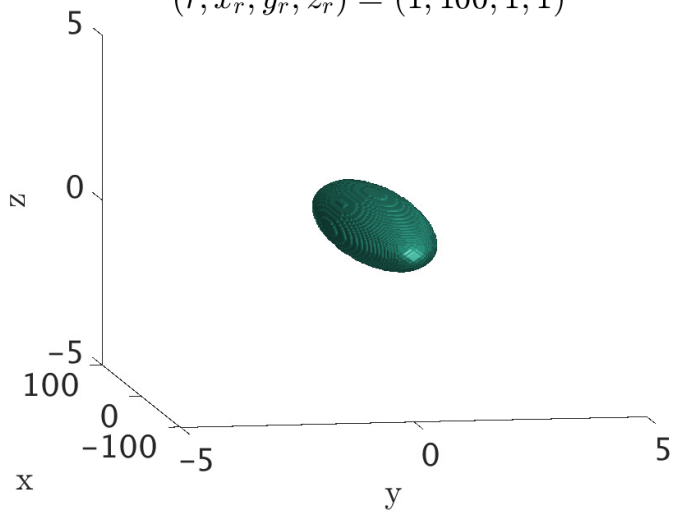

(b) Example of a filament, the structure is shaped like a cigar. The values used are $(x_r, y_r, z_r) = (100, 1, 1)$

$$(r, x_r, y_r, z_r) = (1, 100, 1, 0.01)$$

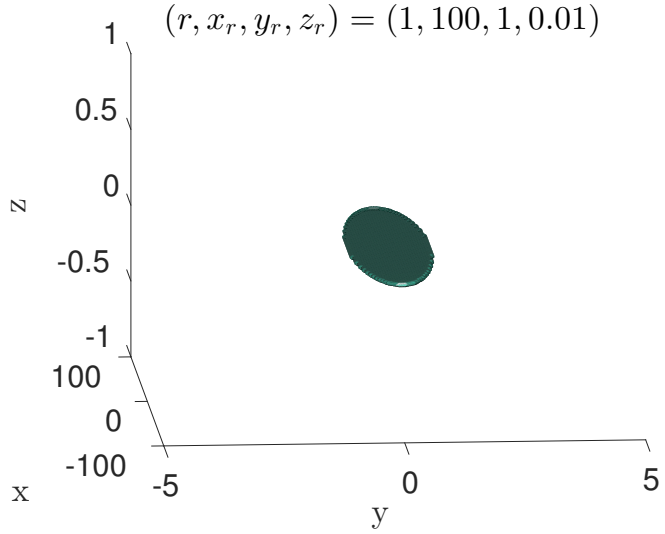

(c) Example of a ribbon, the structure is a flattened cigar. The values used are $(x_r, y_r, z_r) = (100, 1, 0.01)$

Figure 6.5: Prototypical examples of pancakes, filaments and ribbons using equation (6.11).

Some approximations to V_2 and V_3 becomes small at some timesteps due to the manner in which they are calculated. This can then skew the results and makes considering mean properties of the length measures impossible. To work around this problem a median filter is applied in these cases, see figure 6.6. Consider a time series X with components works by considering the interval $[X_{i-1}, X_i, X_{i+1}]$ of the time series at component i. The median of X_{i-1}, X_i and X_{i+1} is then found and given to the point i. This of course can be applied with an interval of arbitrary width however here I consider the smallest possible width due to the fact that if these high values persisted then this would itself be an interesting result warranting investigation.

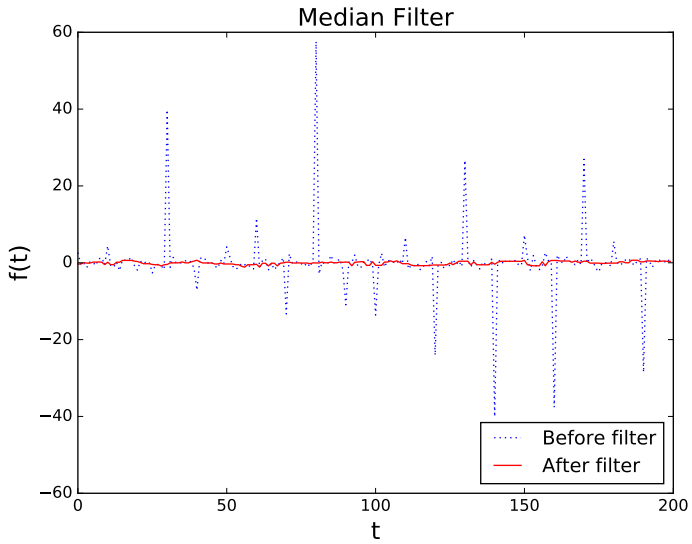

Figure 6.6: Example of how a median filter filters out sharp spikes.

6.3 Hydrodynamic and Kinematic Results for the 522 Dynamo

To examine the 522 dynamo in the nonlinear regime a number of results for its hydrodynamic and kinematic dynamo counterparts are required. By hydrodynamic results I mean that equation (6.12) is solved where $\mathbf{F}_{522}/\nu = (11)^{-\frac{1}{2}}[5\sin(z)+2\cos(y), 2\sin(x)+5\cos(z), 2\sin(y)+2\cos(x)]$

$$\frac{\partial \mathbf{u}}{\partial t} + (\mathbf{u}\cdot\nabla)\mathbf{u} = -\nabla p + \nu\nabla^2\mathbf{u} + \mathbf{F}_{522}. \tag{6.12}$$

By kinematic results I mean that the induction equation is solved for $\mathbf{u}_{522} = \mathbf{F}_{522}/\nu$. The aim of the hydrodynamic work is to identify which value of ν will be used within the non-linear simulations. The aim of the kinematic results is to establish its credentials as a successful kinematic dynamo and to show the 3D structure of the magnetic field.

6.3.1 Hydrodynamic Results for the 522 No Stagnation Point Flow

All ABC flows are exact solutions to the equation of motion (6.13). However their stability when (6.13) is solved numerically depends on the value of the kinematic viscosity ν. For values of ν above a critical value the ABC flow is a stable solution to the equation and simulations initialised with $\mathbf{u}_{ABC}$ will see no change in the flow. However below this critical value $\mathbf{u}_{ABC}$ is no longer the stable solution to the system. A transition will therefore occur from the ABC flow to a different flow which is also a solution to (6.13). As it is the aim of this work to examine amplification and subsequent saturation of the magnetic field by an ABC flow it is important that the flow remains the ABC flow during the kinematic phase of the dynamo. It is therefore important to identify the value of ν we must stay above in order to maintain an ABC flow.

$$\frac{\partial \mathbf{u}}{\partial t} + (\mathbf{u}\cdot\nabla)\mathbf{u} = -\nabla p + \nu\nabla^2\mathbf{u} + \mathbf{F}_{522} \tag{6.13}$$

To identify the value of ν I run hydrodynamic simulations where the flow is forced by $\mathbf{F}_{522}$

$$\mathbf{F}_{522} = \frac{\nu}{\sqrt{11}} \begin{pmatrix} 5\sin(z) + 2\cos(y) \\ 2\sin(x) + 5\cos(z) \\ 2\sin(y) + 2\cos(x) \end{pmatrix}. \tag{6.14}$$

and initialised by $\mathbf{u}_{522} = \mathbf{F}_{522}/\nu$. An Adams-Bashforth numerical scheme is used to timestep the equation of motion with the diffusion being treated exactly and the flow taken to be incompressible. A grid resolution of 36^3 is used. The values of ν^{-1} simulated range from 1 to 20 in increments of 0.5. Figure 6.7 shows some of the key findings. I find that the stable solution remains the 522 flow until $\nu^{-1} = 9$. Above this two transitions occur. Marginally above $\nu^{-1} = 9$ the flow transitions to a second steady flow and then at a larger ν^{-1} further transitions to a time dependent solution which oscillates with a well defined

period. This behaviour is similar to that observed for the 111 ABC flow by Zheligovsky and Pouquet [110].

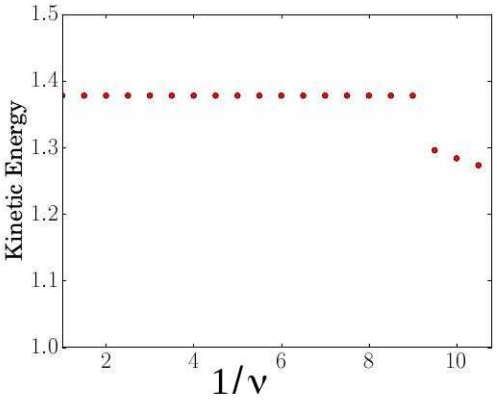

(a) Final kinetic energy vs ν^{-1} for a number of hydrodynamic runs. For $\nu^{-1} \leq 9$ the flow remains the ABC flow however above this the flow transitions to a different flow.

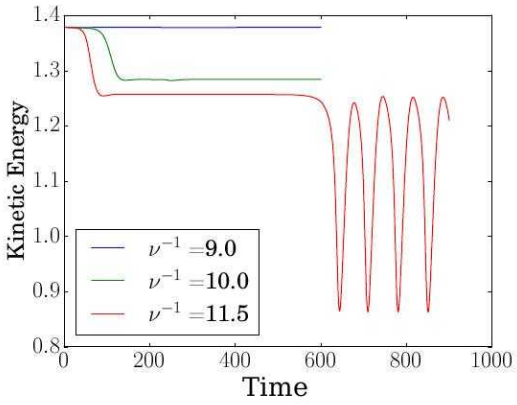

(b) Transitions in the flow as ν^{-1} is increased. Two transitions are seen to occur. Somewhere in the region of $\nu^{-1} = 9$ the flow becomes unstable and transitions to a second state which appears stable. Secondly a transition occurs at approximately $\nu^{-1} = 11$ from the second state to one that oscillates with a well defined period.

Figure 6.7

The results suggest that in order to maintain a 522 flow during the kinematic phase of the dynamo we need to keep ν^{-1} below 9. Furthermore they show that the 522 flow undergoes transitions with increasing ν^{-1} in a similar manner as the 111 was observed to by Zheligovsky and Pouquet. Further increase in ν^{-1} may result in further bifurcations in the flow field structure with a steady flow, a more time dependent flow or windows of both all being possible. It is anticipated that the introduction of a seed magnetic field may cause the flow to deviate from the 522 flow at a lower ν^{-1}. The deviation of the flow from the 522 flow will therefore be monitored during my nonlinear simulations within section 6.4 to ensure that it is the 522 flow which is causing the magnetic field amplification during the kinematic phase.

6.3.2 Kinematic Results for the 522 Flow

In this section I outline the results of running a kinematic simulation using $\mathbf{u}_{522} = \mathbf{F}_{522}/\nu$ as the kinematic flow. Investigations of the 522 flow within kinematic dynamo theory have been previously performed by Galloway and Frisch [42] and more recently by Alexakis [2].

I run simulations for $\eta^{-1} \in (5, 195)$ and monitor growth rates, energy evolution and the final magnetic field configuration. Figure 6.8 shows the exponential growth rate against η^{-1}.

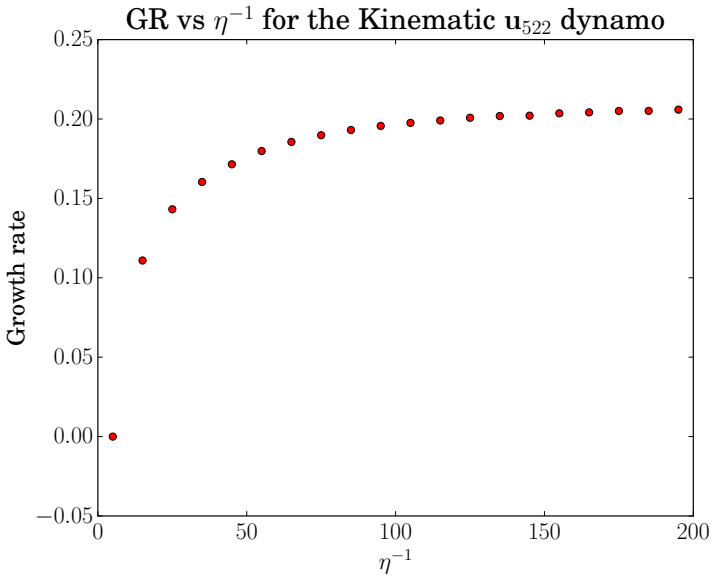

Figure 6.8: η^{-1} vs saturated growth rate for the 522 dynamo. The growth rate appears to be saturating at higher η^{-1}.

We see that for $\eta^{-1} = 5$ the flow is only marginally a dynamo however as we increase η^{-1} the growth rate becomes larger and then shows evidence of beginning to saturate at the largest η^{-1} examined. The positive growth rate shows that the flow is able to successfully amplify a seed magnetic field. As such the magnetic field is able to grow in strength until it reaches a field strength such that in a nonlinear regime it can act back upon the flow via the Lorentz force $(\nabla \times \mathbf{B}) \times \mathbf{B}$.

Isosurfaces of 40% of the maximum magnetic field strength are shown in figure 6.9 as a way of examining the magnetic field structure. We see that as η^{-1} increases the field becomes thinner with the width of the structures suggesting that they are ribbons.

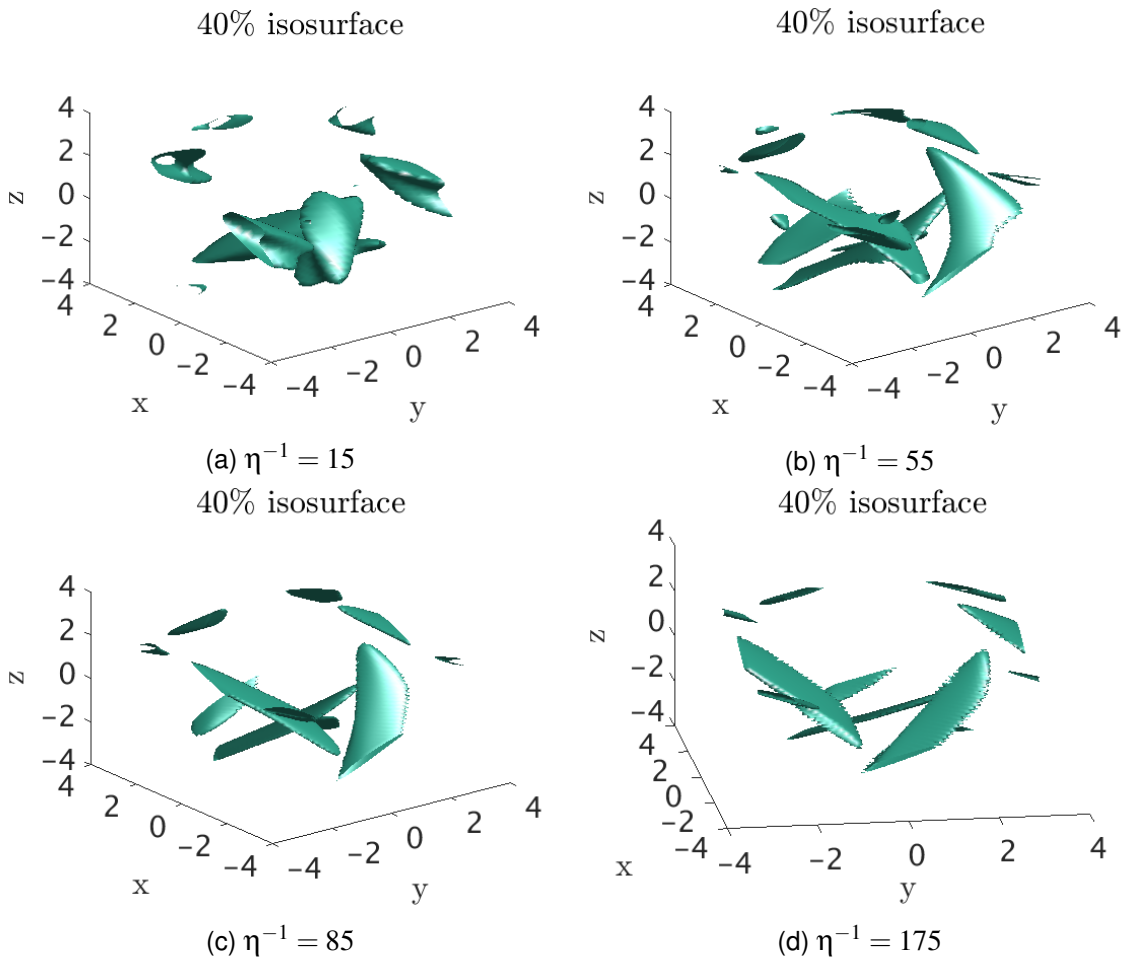

(a) $\eta^{-1} = 15$ (b) $\eta^{-1} = 55$

(c) $\eta^{-1} = 85$ (d) $\eta^{-1} = 175$

Figure 6.9: 40% isosurfaces of the 522 magnetic field. We see that the magnetic field is confined to thin "sheet-like" structures. We see that as η^{-1} increases the magnetic field are visibly smaller and thinner.

These kinematic results have shown that the 522 dynamo works well as a kinematic dynamo in that it has a strongly positive growth rate. Additionally we see that the magnetic field structure is concentrated in thin sheet like structures. The morphology differs greatly from that of the magnetic field for ABC flows with stagnation points where the magnetic field structure is filamentary within the kinematic regime.

6.4 The Nonlinear 522 ABC Dynamo

I now begin examination of the fully nonlinear MHD problem by examining the 522 nonlinear dynamo. Within the nonlinear MHD problem an additional Lorentz force term $(\nabla \times \mathbf{B}) \times \mathbf{B}$ is added to the right hand side of equation (6.13). Furthermore the induction equation (6.15) is solved simultaneously with both the magnetic and flow fields having a divergence

of zero.

$$\frac{\partial \mathbf{B}}{\partial t} = (\mathbf{B}\cdot\nabla)\mathbf{u} - (\mathbf{u}\cdot\nabla)\mathbf{B} + \eta\nabla^2\mathbf{B}. \tag{6.15}$$

The kinematic viscosity ν is chosen so as to ensure that the flow remains the 522 ABC flow during the kinematic phase of the dynamo calculation. Following the work within section 6.3.1 I take $\nu^{-1} = 7$. The inverse magnetic diffusivity is then taken to be one of the following five values; 7, 14, 28, 56 and 112. The values of η are chosen so that we may examine the impact of increasing the magnetic Prandtl number $P_m = \nu/\eta$. The magnetic Prandtl number thus varies from 1 to 16. Unless otherwise stated simulations are performed on a 64^3 grid with a timestep of 0.005 using an Adams-Bashforth timestepping scheme.

As stated previously there are a number of motivations for studying the 522 nonlinear dynamo. The first is to examine whether or not it can produce a nonlinear dynamo at all. The second is to examine how the magnetic field structure changes upon entering the nonlinear regime. Finally these results on the change in structure of the magnetic field will be used in conjunction with similar results from nonlinear dynamos with stagnation points to build up a picture of potential global properties of the saturation process.

I begin by examining the energies for the various η. Figure 6.10a shows the time average of the final 100 points (to average out oscillations) of both the kinetic (red) and magnetic (blue) energies plotted against η^{-1}. We see that for large η the kinetic energy is a couple of orders of magnitude larger than the magnetic energy however as the magnetic Prandtl number increases so does the ratio of magnetic to kinetic energy. By $P_m = 2$ the ratio of magnetic to kinetic energy is $O(10^{-1})$. These results therefore show that the 522 flow is capable of operating as a nonlinear dynamo particularly at high P_m.

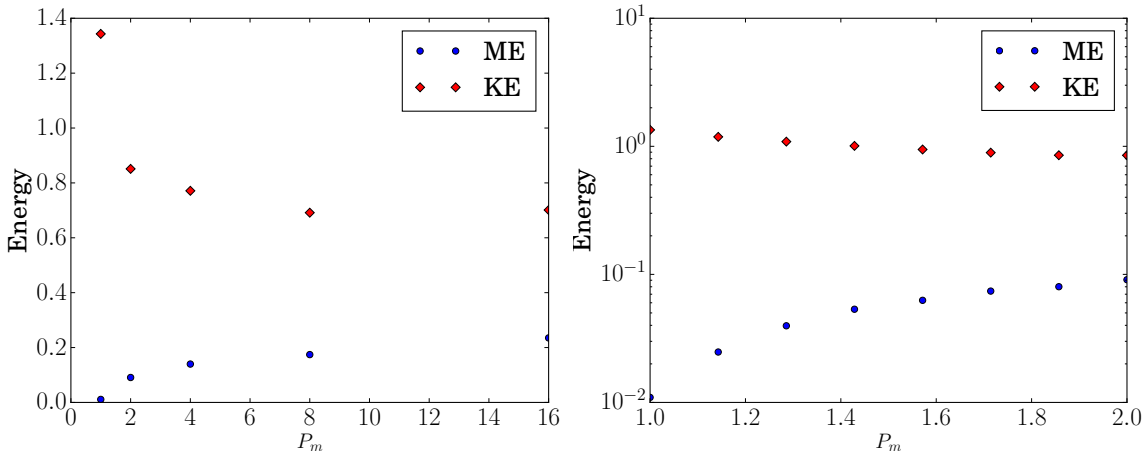

(a) Simulations of the 522 dynamo for increasing P_m. We see that the magnetic energy is the same order of magnitude as the kinetic energy above $P_m = 1$ with both the energies seemingly tending to a constant value at large P_m.

(b) Simulations of the 522 dynamo for P_m between 1 and 2 ($\nu^{-1} = 7$). We see that the magnetic energy increases towards the same order of magnitude as the kinetic energy as soon as P_m increases.

Figure 6.10: Energy as P_m is varied.

Figure 6.11 shows time series of the magnetic energy for each of the runs. We see that $\eta = 1/7$ takes much longer to reach the nonlinear state than the runs with higher P_m. For $\eta^{-1} = [56, 112]$ we see that the magnetic energy is highly time dependent but is no longer increasing in time.

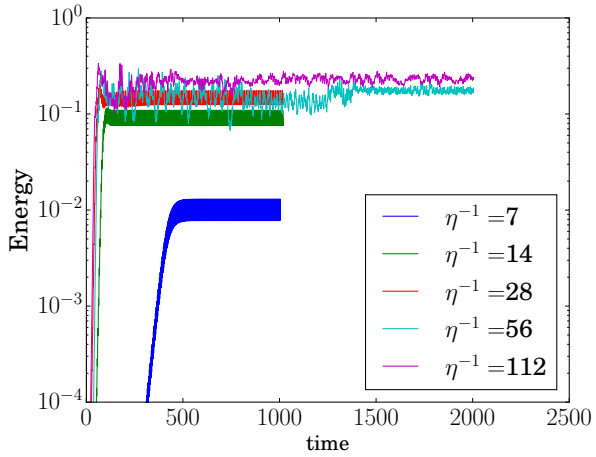

Figure 6.11: Plot of magnetic energy against time for the 5 different P_m examined. We see that $\eta^{-1} = [7, 14, 28]$ have a well defined, oscillatory, kinematic growth phase followed by an oscillatory statistically steady state. $\eta^{-1} = [56, 112]$ also have a well defined, oscillatory, kinematic growth phase however the statistically steady state is much more time dependent.

I now check that the flow remains the 522 flow during the kinematic phase of the dynamo. Figure 6.12 shows plots of the kinematic phase of the dynamo for the various η^{-1}. We see

that the kinetic energy remains constant throughout the entire kinematic growth phase and only transitions to a different flow once saturation to the nonlinear state begins. Further evidence that the flow remains unchanged from the 522 flow during the kinematic phase of the dynamo can be seen by calculating the quantity (6.16). Examples of this for three η are shown in figure 6.13. We see that for all of the η examined the flow stays within a fraction of a percent of the 522 flow at the point in the domain where it deviates most. This is seen for the other values not shown also. These plots further show that the flow deviates significantly from the 522 flow once the dynamo saturates.

$$\max_{x,y,z} \left\{ \frac{(\mathbf{u} - \mathbf{u}_{522})^2}{\mathbf{u}_{522}^2} \right\} \times 100 \tag{6.16}$$

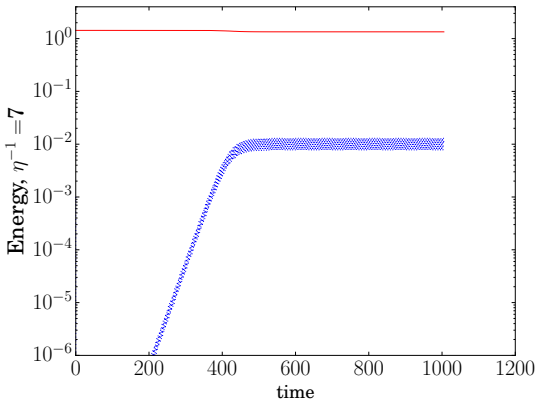

(a) $\eta^{-1} = 7$. Note that the flow oscillates during the nonlinear phase however the amplitude is too small to see on the scale shown here.

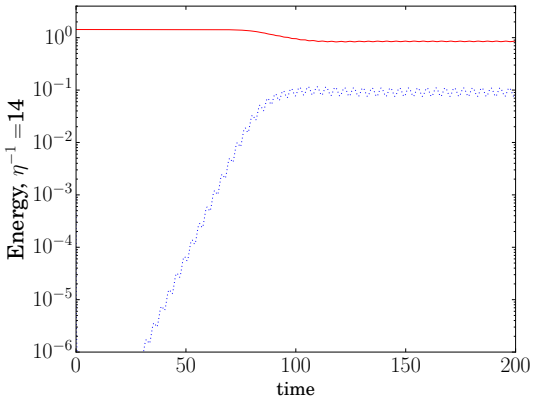

(b) $\eta^{-1} = 14$.Note that the flow oscillates during the nonlinear phase however the amplitude is too small to see on the scale shown here.

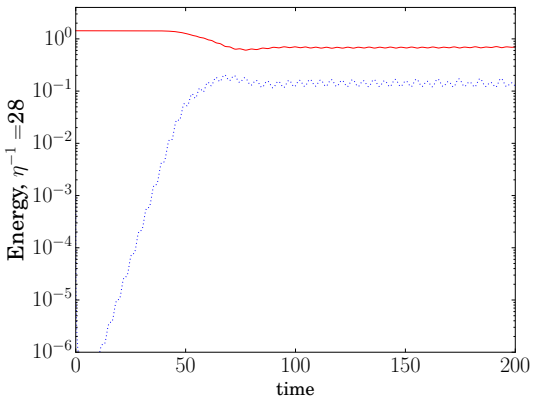

(c) $\eta^{-1} = 28$.

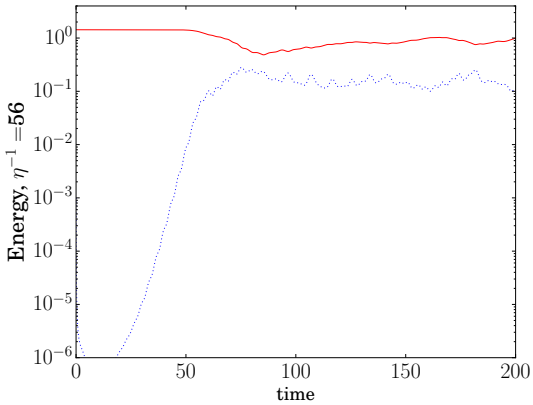

(d) $\eta^{-1} = 56$

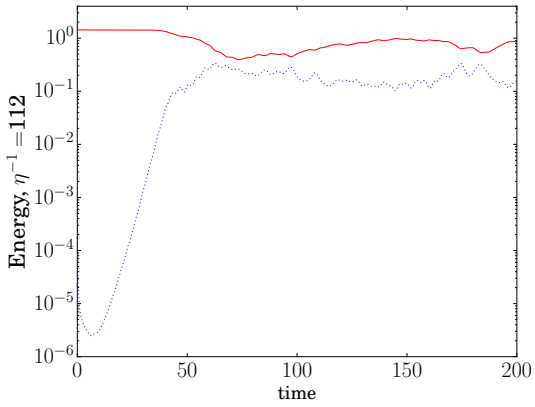

(e) $\eta^{-1} = 112$

Figure 6.12: Plot of the kinematic and saturated phases of the 522 dynamo for all ν examined. Red indicates kinetic energy and blue indicates magnetic energy. We see that the kinetic energy remains constant for the entire kinematic phase. Upon the saturation of the dynamo the flow then undergoes a transition away from the 522 flow. Note that due to the scale the flow appears steady during the nonlinear phase for $\eta^{-1} = [7, 14, 28]$. In fact it oscillates with maximas at minimas of the magnetic energy and vice versa.

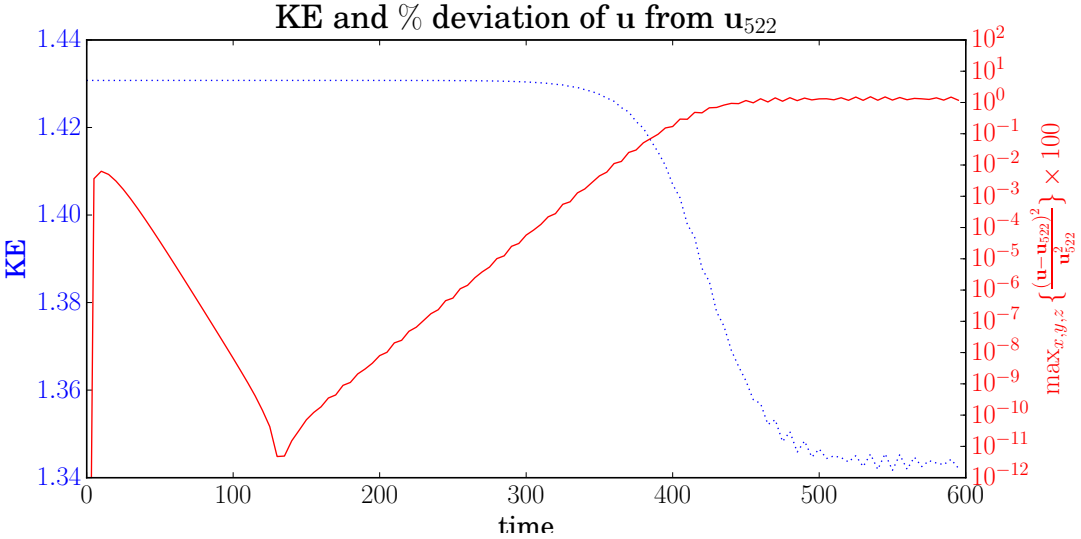

(a) $\eta^{-1} = 7$

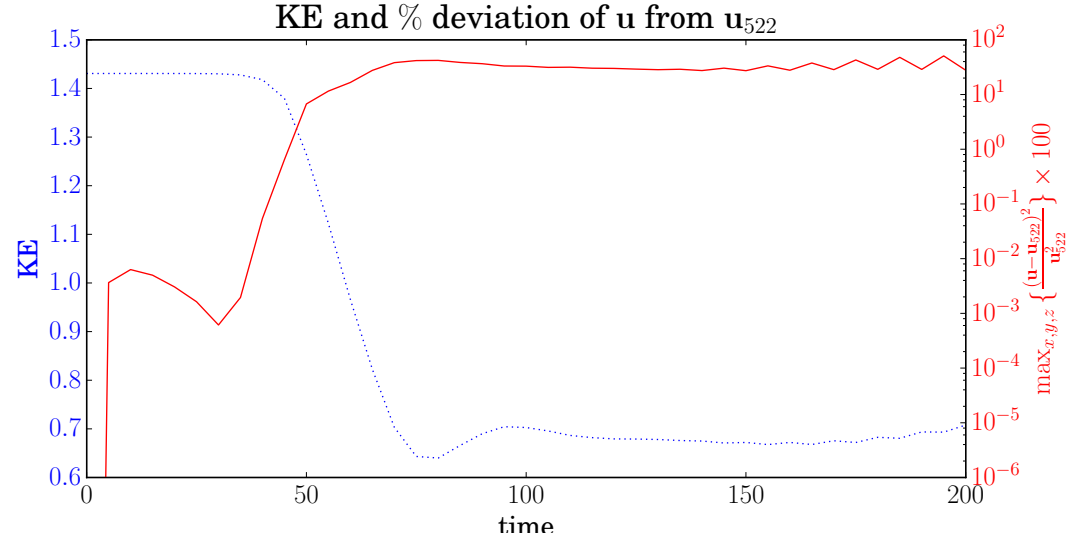

(b) $\eta^{-1} = 28$

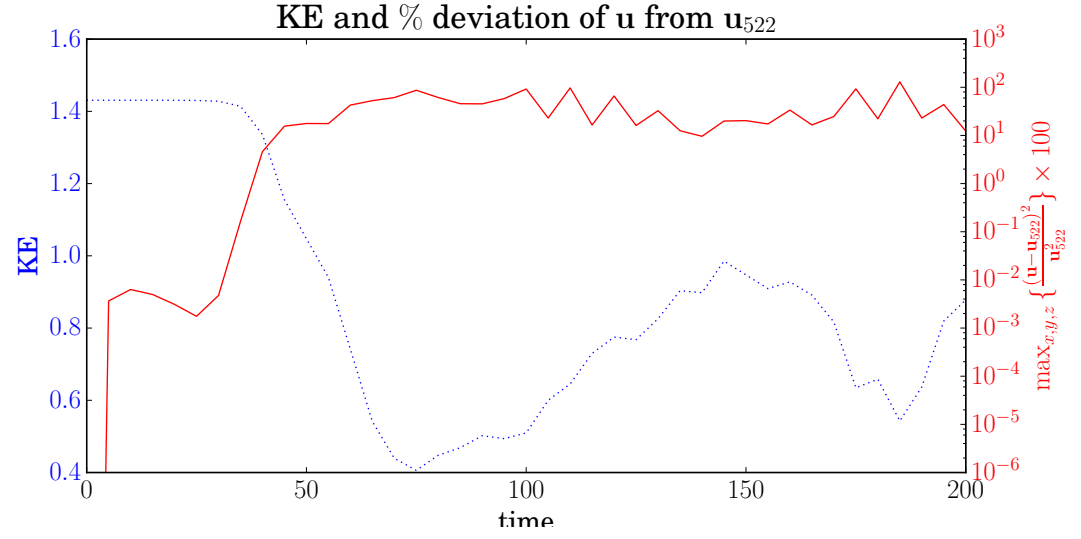

(c) $\eta^{-1} = 112$

Figure 6.13: $\max_{x,y,z}\left\{\frac{(\mathbf{u}-\mathbf{u}_{522})^2}{\mathbf{u}_{522}^2}\right\}\times 100$

6.4.1 Analysis of Field Structure Using Contour Plots

In this section I will examine the field structure of the magnetic and flow fields during the nonlinear dynamo runs. I begin by looking at the length scales of each. Given a field $\mathbf{Q}$ we may calculate its length scale via (6.17)

$$l_Q = \sqrt{\frac{\int_V \mathbf{Q}^2 dV}{\int_V |\nabla \times \mathbf{Q}|^2 dV}} \tag{6.17}$$

This is done for both the flow (denoted l_u) and the magnetic field (denoted l_B) in figure 6.14.

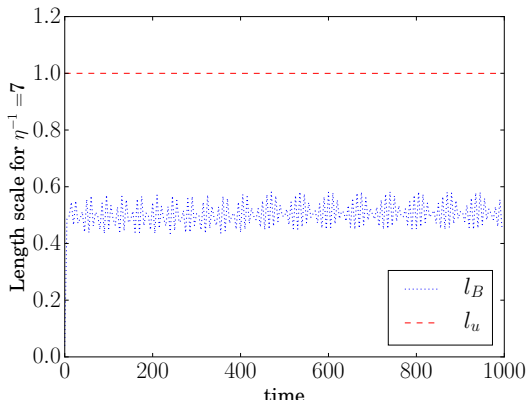

(a) $\eta^{-1} = 7$

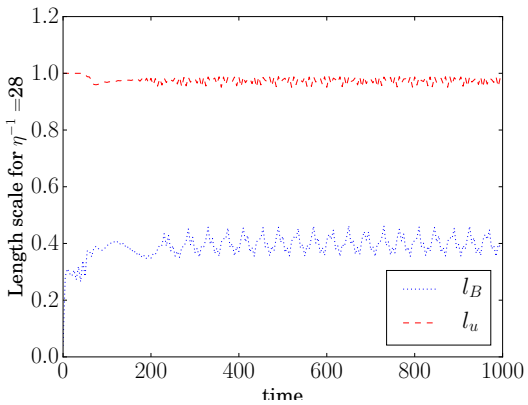

(b) $\eta^{-1} = 28$

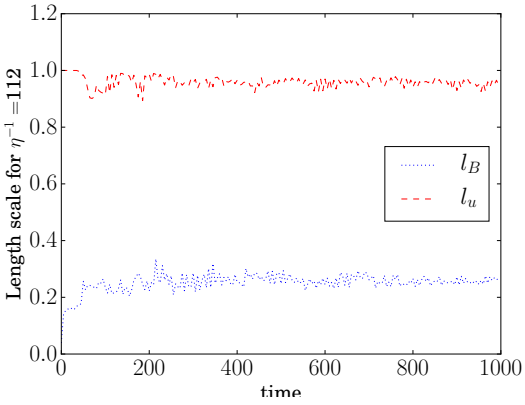

(c) $\eta^{-1} = 112$

Figure 6.14: Length scales of the flow and magnetic fields against time for a selection of η. We see that the length scale of the flow remains approximately unchanged at high η and that the length scale of the magnetic field continuously evolves during each run, even during the statistically steady state. $\eta^{-1} = 14$ behaviour is similar to $\eta^{-1} = 7$ and $\eta^{-1} = 112$ is similar to $\eta^{-1} = 56$.

A number of things are noticeable in figure 6.14. The most obvious being that the length scale of the magnetic field is always less than that of the flow and decreases with increas-

ing η^{-1}. Furthermore we see that for all η the length scale of the flow changes very little over time. As expected, due to the small scale random field we initialise $\mathbf{B}$ with, the length scale of the magnetic field grows from being extremely small to being of $O(10^{-1})$ during the kinematic phase of the dynamo for each η. Following this rapid growth it then appears to become statistically steady in all cases. For $\eta^{-1} = [7, 14, 28]$ the length scale of the magnetic field oscillates with a well defined period during the nonlinear stage of the dynamo. This is suggestive of a magnetic field which is periodically changing structure. This will be explored later within this section. A more complex evolution of the magnetic field structure is suggested by the length scale evolution of $\mathbf{B}$ in the case of $\eta^{-1} = [56, 112]$.

Galanti et al. [37] noted that the regions of strong magnetic field for the 111 nonlinear dynamo are contained within the regions of weak flow field. To test if this is the case for the 522 dynamo I plot contours of $\mathbf{u}^2$ and $\mathbf{B}^2$ at various z slices both during the kinematic phase and after saturation. The case of $\eta^{-1} = 28$ is shown as a representative example within figures 6.15 and 6.16. We see that the regions of strong magnetic field are indeed within regions of weak flow. This was found to be the case for all η. The small size of the regions of strong field supports the findings from the length scales in that the size of the magnetic field structures is smaller than that of the flow.

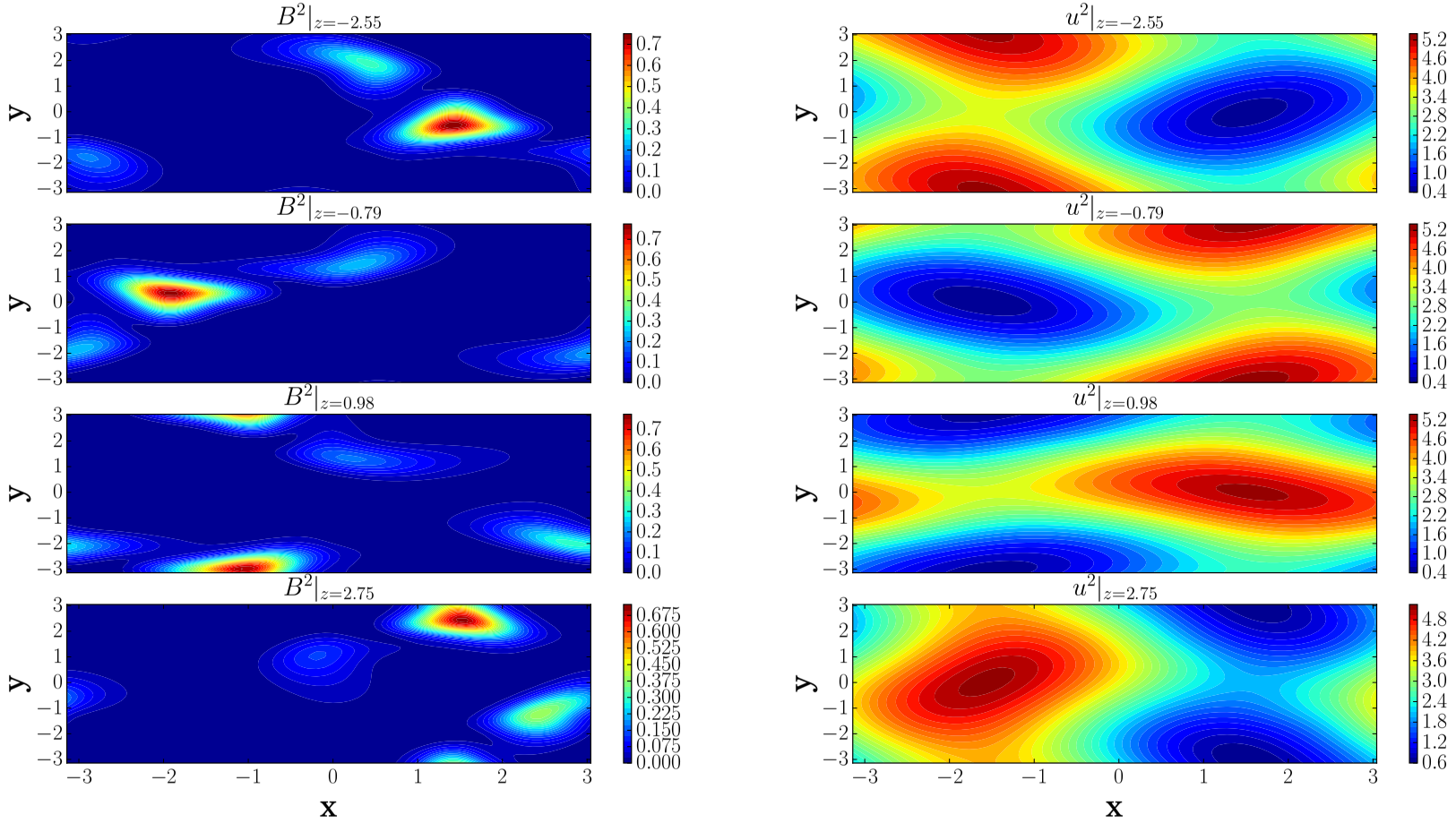

Figure 6.15: Plot of $\mathbf{B}^2$ and $\mathbf{u}^2$ at time $t = 50$ (during the kinematic phase of the dynamo) for the case of $\eta^{-1} = 28$. Note that the regions of strong magnetic field are contained within regions of weak flow.

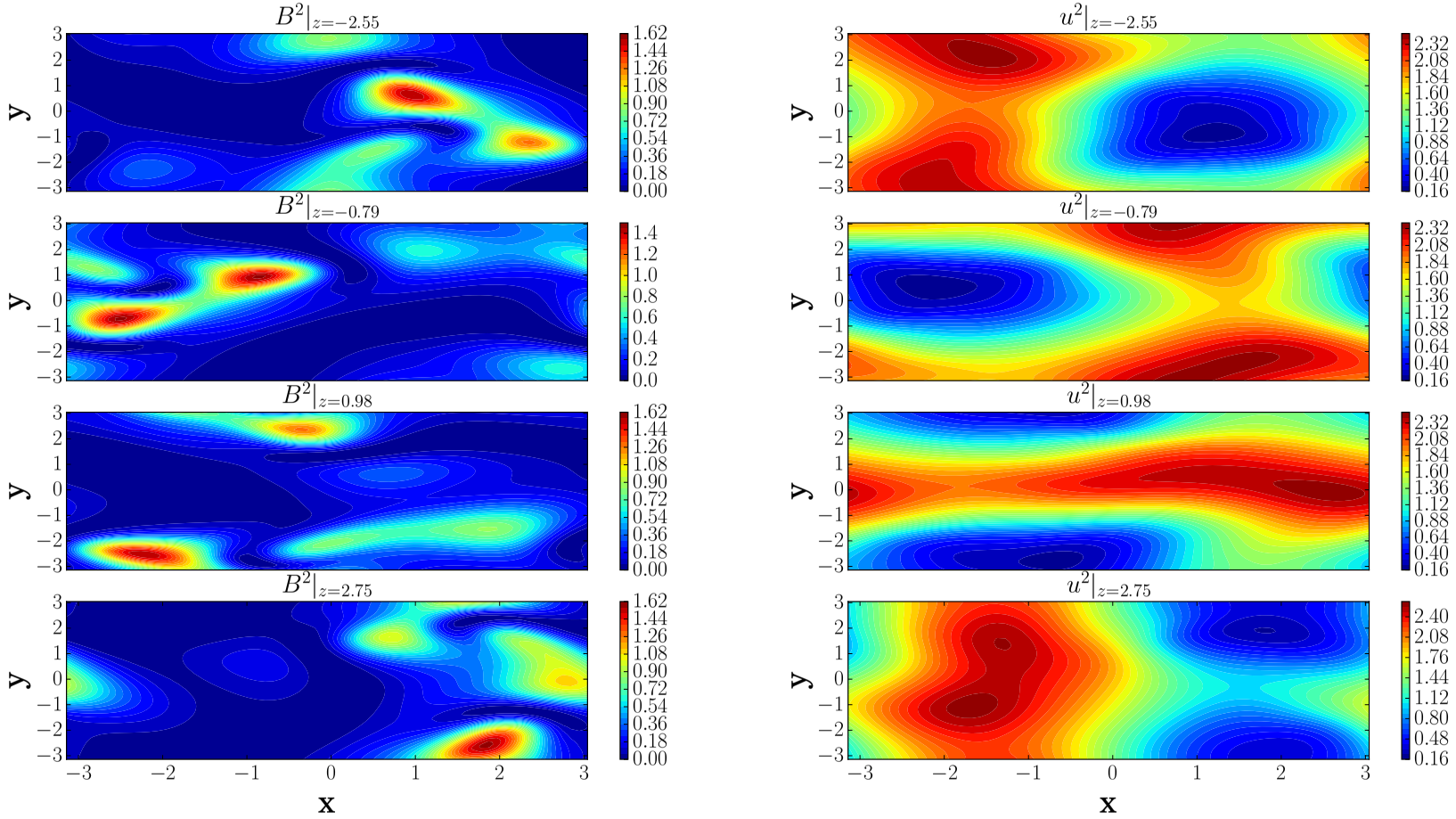

Figure 6.16: Plot of $\mathbf{B}^2$ and $\mathbf{u}^2$ at time $t = 100$ (after the dynamo has saturated) for the case of $\eta^{-1} = 28$. Note that the regions of strong magnetic field are contained within regions of weak flow.

To further the comparison with results for the 111 flow Archontis et al. [5] noted that a quantity they call the “external average work” (but do not define) is strongest in the regions where the magnetic field is weakest. If we note that the evolution of the total energy within the system is governed by (6.18)

$$\frac{1}{2}\frac{d}{dt}\int_v \mathbf{u}^2 + \mathbf{B}^2 dV = \int_V \mathbf{u}\cdot\mathbf{F} dV + \nu\int_V \mathbf{u}\cdot\nabla^2\mathbf{u} dV + \eta\int_V \mathbf{B}\cdot\nabla^2\mathbf{B} dV \tag{6.18}$$

then the contribution at each point within the domain to the total energy is given by

$$Q = \mathbf{u}\cdot\mathbf{F} + \nu\mathbf{u}\cdot\nabla^2\mathbf{u} + \eta\mathbf{B}\cdot\nabla^2\mathbf{B}. \tag{6.19}$$

Examining how the distribution of (6.19) evolves as the dynamo goes through its kinematic phase, saturates and enters the nonlinear regime produces a number of insights into the workings of the dynamo as it contains the information on the local contributions to the total energy in each stage.

Figures 6.17 and 6.18 show plots of Q, $\mathbf{B}^2$, $\mathbf{u}^2$ and $\mathbf{B}\cdot\nabla^2\mathbf{B}$ at various z slices which are representative of $\eta^{-1} = [7, 14, 28]$ in the kinematic and nonlinear regimes respectively. The results show that Q is only negative in the small regions where the magnetic field is strong. As growth must come from the regions where Q is positive growth of energy occurs within the regions where the magnetic field is weak. We can understand why this is the case by looking at the magnetic diffusion term. We see that this term is strongly negative in the same regions where the magnetic field is strong and thus Q is weakened in these regions. The results therefore show that energy growth for the 522 dynamo behaves in a similar manner as the 111 dynamo in that the majority of the energy growth is coming from the regions of weak magnetic field. This is therefore a feature that both dynamos share.

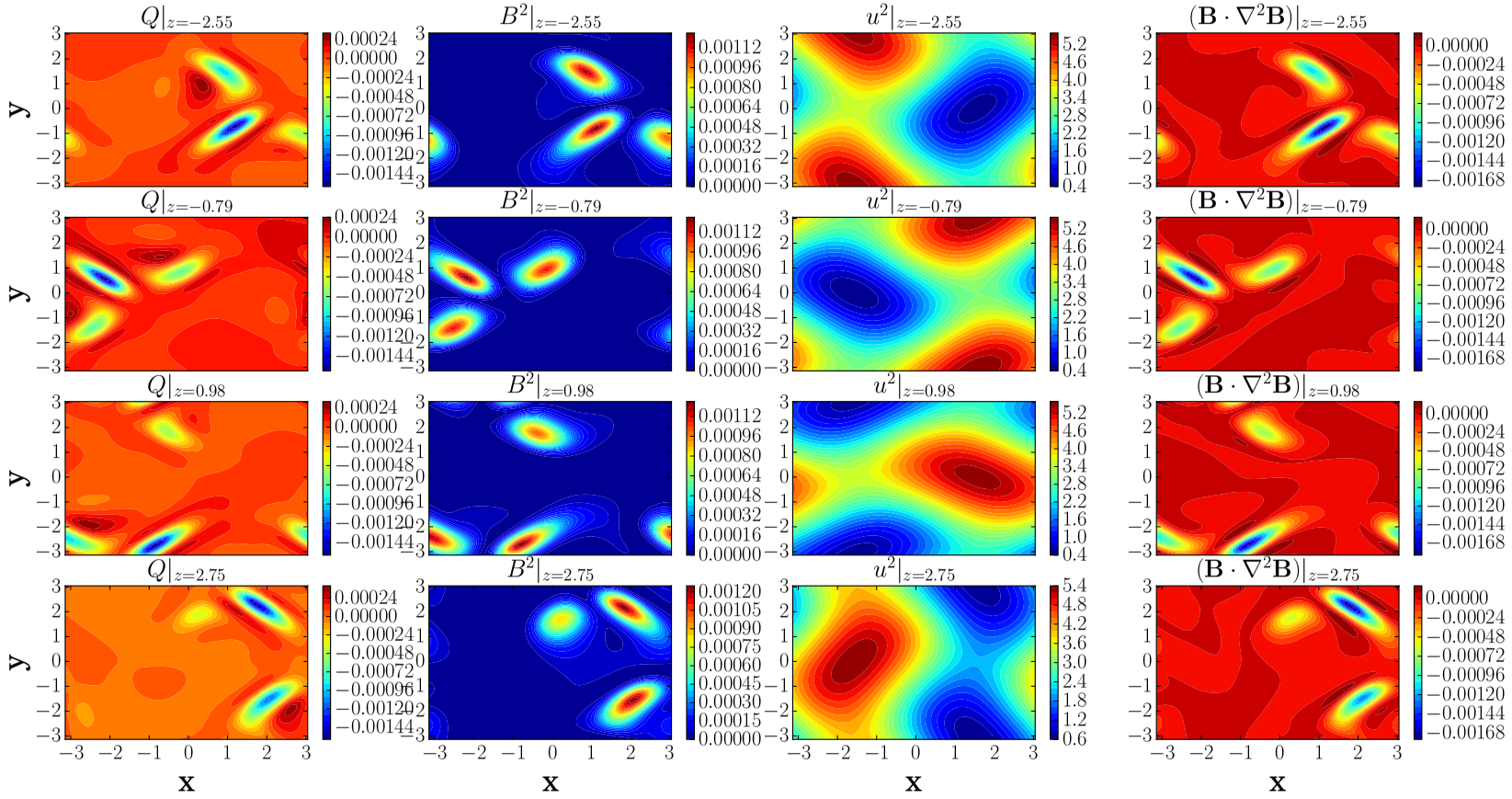

Figure 6.17: Plot of Q, $B^2 = B_x^2 + B_y^2 + B_z^2$, $u^2 = u_x^2 + u_y^2 + u_z^2$ and $\mathbf{B}\cdot\nabla^2\mathbf{B}$ at various z slices for $\eta^{-1} = 14$ at $t = 50$ (during the kinematic phase). We see that the gain in pointwise energy is within the regions of weak magnetic field. Second, we see that the regions where there is negative Q actually correspond to the strongest magnetic field. This is due to the increase in strength of $\mathbf{B}\cdot\nabla^2\mathbf{B}$ in these regions.

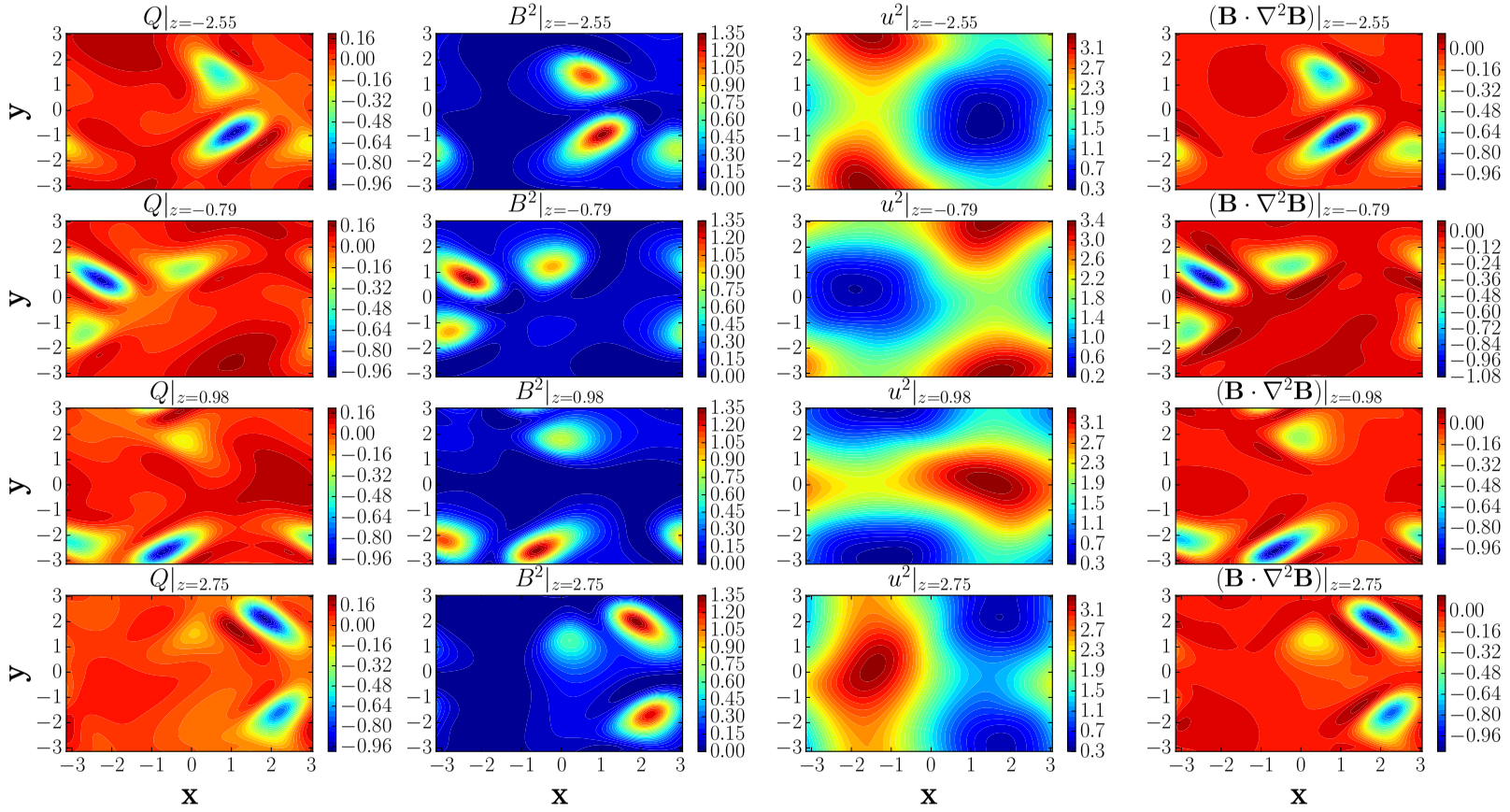

Figure 6.18: Plot of Q, $B^2 = B_x^2 + B_y^2 + B_z^2$, $u^2 = u_x^2 + u_y^2 + u_z^2$ and $\mathbf{B}\cdot\nabla^2\mathbf{B}$ at various z slices for $\eta^{-1} = 14$ at $t = 190$. We see that the gain in pointwise energy is within the regions of weak magnetic field. Second, we see that the regions where there is negative Q actually correspond to the strongest magnetic field. This is due to the increase in strength of $\mathbf{B}\cdot\nabla^2\mathbf{B}$ in these regions.

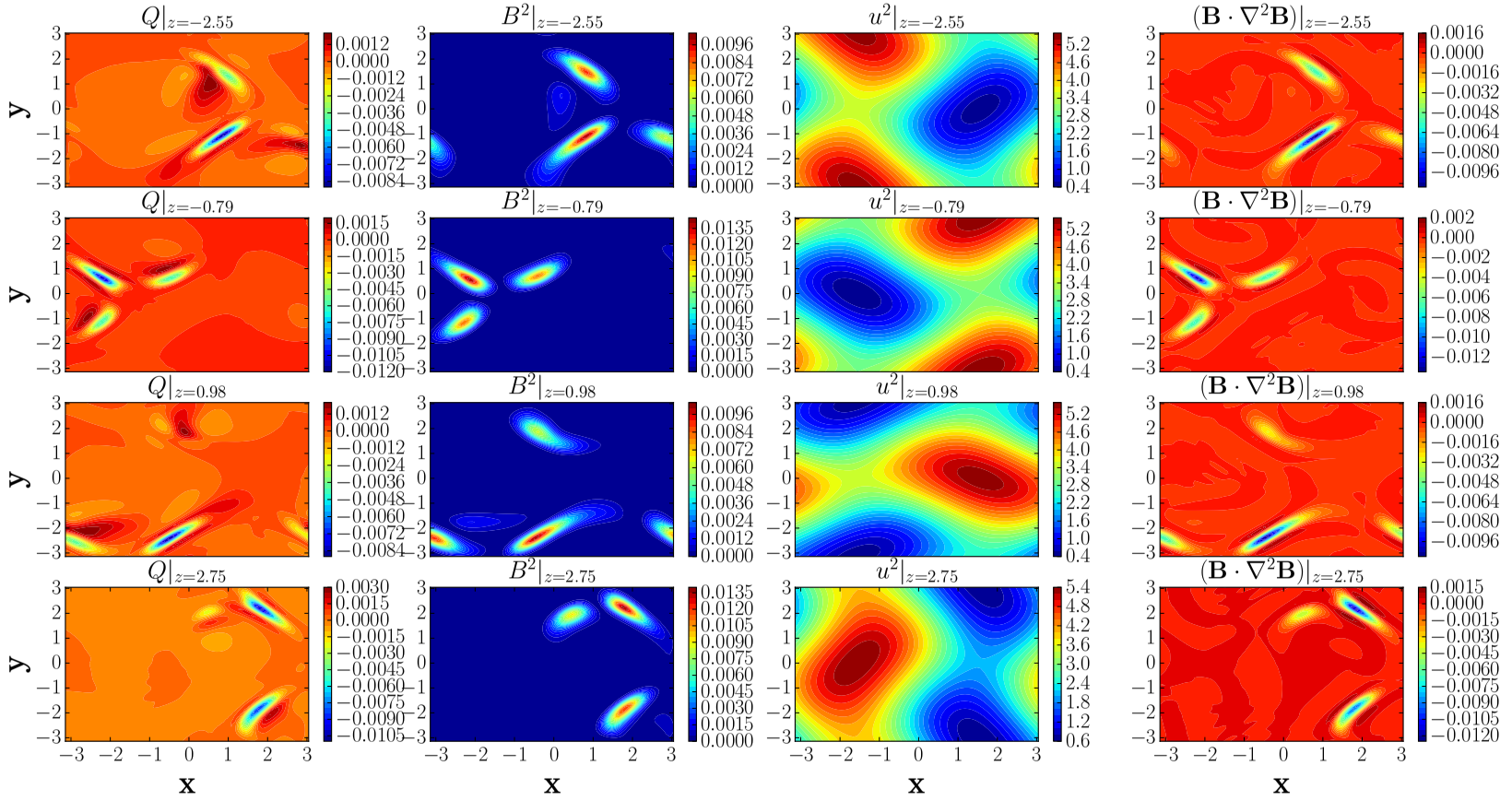

Figure 6.19: Plot of Q, $B^2 = B_x^2 + B_y^2 + B_z^2$, $u^2 = u_x^2 + u_y^2 + u_z^2$ and $\mathbf{B}\cdot\nabla^2\mathbf{B}$ at various z slices for $\eta^{-1} = 56$ at $t = 40$. We see that the gain in pointwise energy is within the regions of weak magnetic field. Second, we see that the regions where there is negative Q actually correspond to the strongest magnetic field. This is due to the increase in strength of $\mathbf{B}\cdot\nabla^2\mathbf{B}$ in these regions.

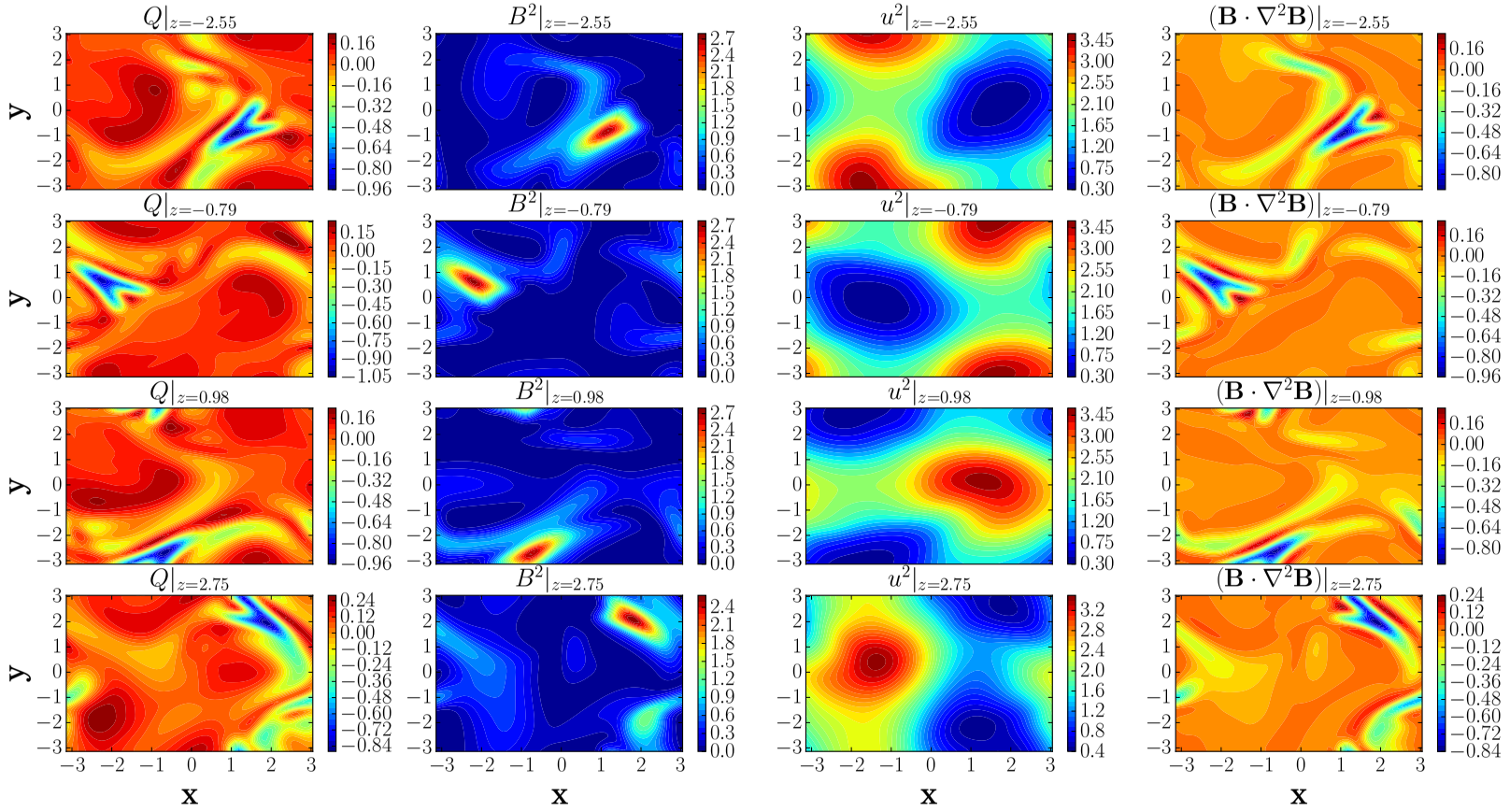

Figure 6.20: Plot of Q, $B^2 = B_x^2 + B_y^2 + B_z^2$, $u^2 = u_x^2 + u_y^2 + u_z^2$ and $\mathbf{B}\cdot\nabla^2\mathbf{B}$ at various z slices for $\eta^{-1} = 56$ at $t = 190$. We see that the gain in pointwise energy is within the regions of weak magnetic field. Second, we see that the regions where there is negative Q actually correspond to the strongest magnetic field. This is due to the increase in strength of $\mathbf{B}\cdot\nabla^2\mathbf{B}$ in these regions.

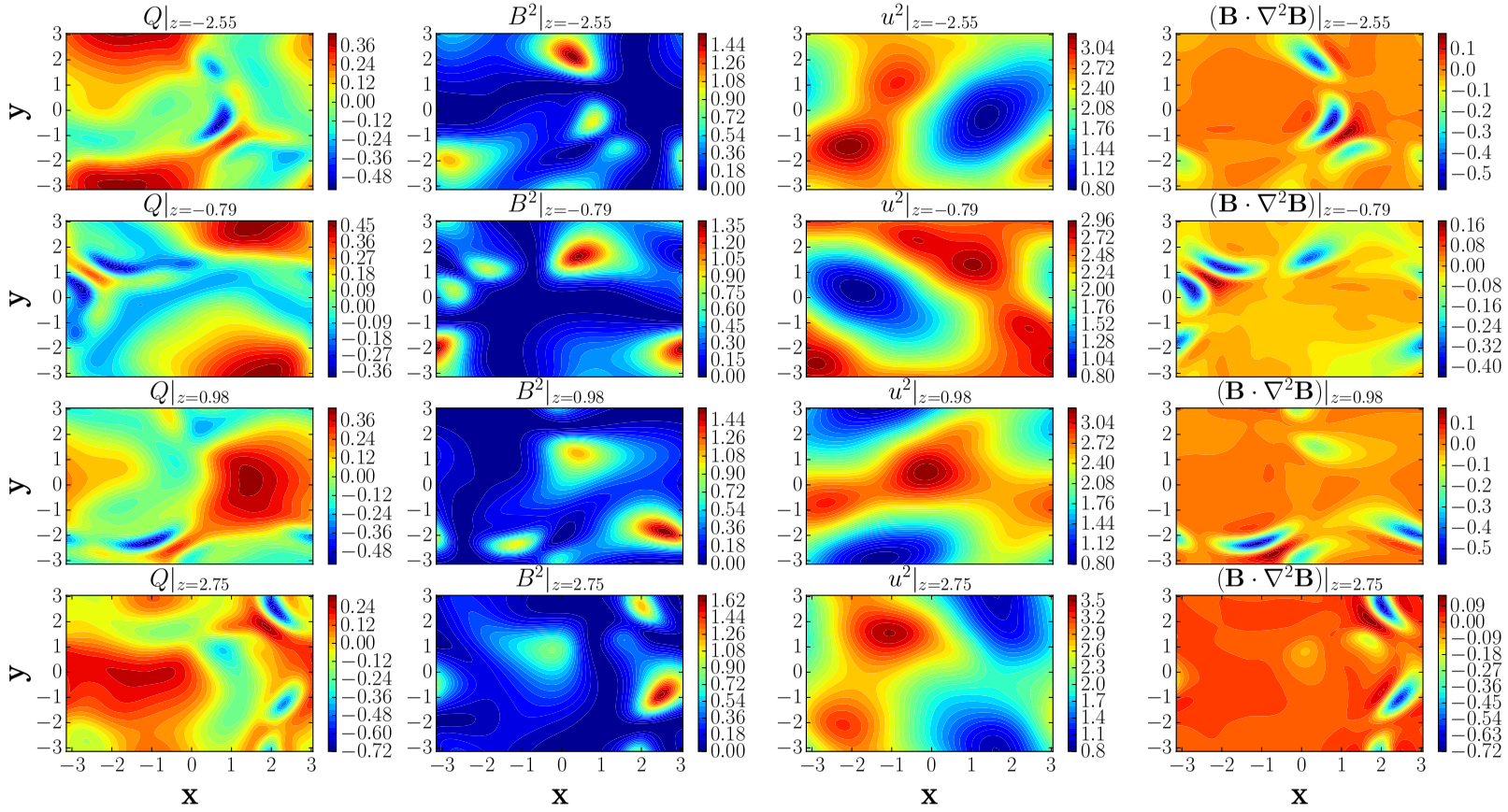

Figure 6.21: Plot of Q, $B^2 = B_x^2 + B_y^2 + B_z^2$, $u^2 = u_x^2 + u_y^2 + u_z^2$ and $\mathbf{B}\cdot\nabla^2\mathbf{B}$ at various z slices for $\eta^{-1} = 56$ at $t = 210$. For $\eta^{-1} = [56, 112]$the strength and polarity of Q at various z slices and timesteps is not as well correlated with the strength of the magnetic field.

For $\eta^{-1} = [56, 112]$ the results are broadly the same. Within figures 6.19 and 6.20 I show the same quantities as before in both the kinematic (t=40) and nonlinear (t=190) regimes for $\eta^{-1} = 56$. As was the case at higher η, negative contributions to Q only occur in the small regions where the magnetic field is strong. As such the energy growth again comes from the regions where the magnetic field is weak. This behaviour of energy growth in regions of weak magnetic field and strong magnetic fields in regions of weak flow is seen throughout the kinematic regime for all timesteps and for the vast majority of timesteps in the nonlinear regime. The reason for the difference is unknown however it is not unexpected that more complex results are produced when the system becomes more chaotic at high η^{-1}.

6.4.2 Analysis of Field Structure Using Isosurfaces

I now focus my attention on the three dimensional structures of the magnetic field. To do this I will make use of isosurfaces of the magnetic field where an $X\%$ isosurface is defined to be an isosurface where the values of the field are $X\%$ of the maximum value of the magnetic field within the domain. I begin by focussing on $\eta^{-1} = 7$. Figure 6.22 shows isosurfaces of increasing strength at t=45 during the kinematic phase of the dynamo. The weak magnetic field makes up a large proportion of the domain and consist of a large number of "thin" structures with two of their three dimensions much larger than the other. 40% and 70% isosurfaces also show field contained in flat structures, thus the field at all strengths has a flat structure. One particular structure, which I name the boomerang for its similarity in appearance, can be seen in all three isosurface plots for $y \in (-2, 2)$. This structure is present within a large number of the plots at various time and η.

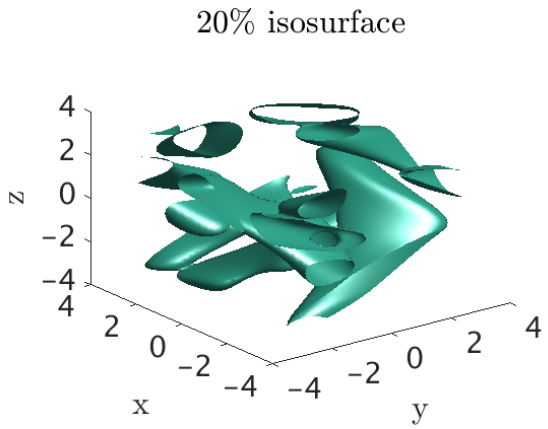

(a) 20% isosurface for t=45. The field is space filling but with structures that have a high aspect ratio.

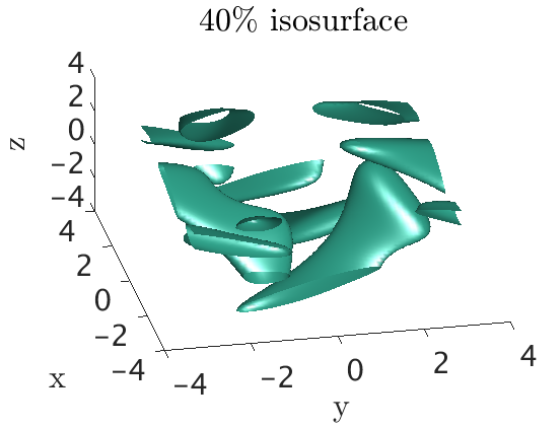

(b) 40% isosurface for t=45. Note the "boomerang" structure present for $y \in (-2, 2)$ as well as the high aspect ratio of all the structures present.

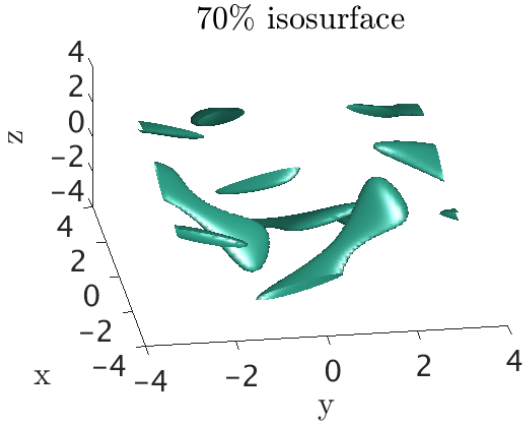

(c) 70% isosurface for t=45. $\mathbf{B}^2$ is confined to a number of long thin structures (high aspect ratio).

Figure 6.22: Isosurfaces of increasing strength at $t = 45$ (the kinematic regime of the dynamo). We note the "boomerang" like structure present at the front of the 40% isosurface picture and also seen in the other two images.

It was seen in figure 6.11 that upon saturating to a statistically steady state the magnetic energy then oscillates with a well defined period. To examine this oscillation I examine how the 3D structure of the magnetic field changes during the oscillation. I therefore select a small window in the nonlinear regime of magnetic energy where the regular storage of the magnetic field structures during my simulations has picked out maxima and minima of the oscillations (shown by red dots in figure 6.23f) and examine how the field structure changes during the oscillation. Figure 6.23 shows 40% isosurfaces of the magnetic field at various points during these oscillations as well as the energy at that time. We see that the structure of the magnetic field goes through a cyclic behaviour whereby the magnetic field becomes stretched at the minimas of the energy and then reforms back into smoother

structures at the peaks. Oscillations of the magnetic energy thus correspond to periodic stretching of the magnetic field.

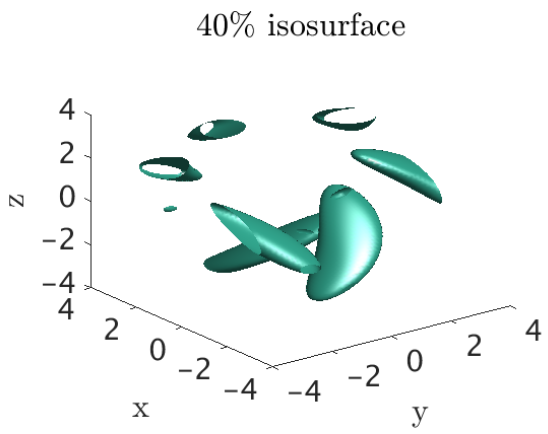

(a) t=700

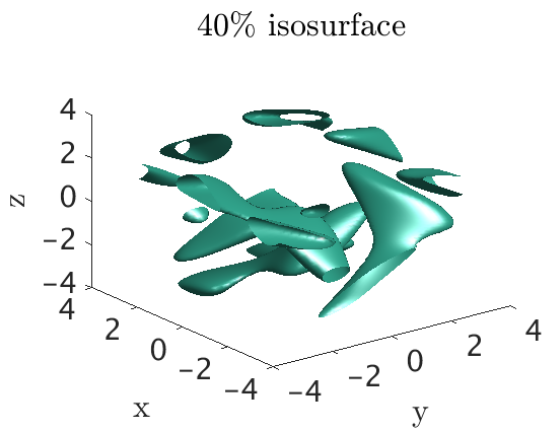

(b) t=705

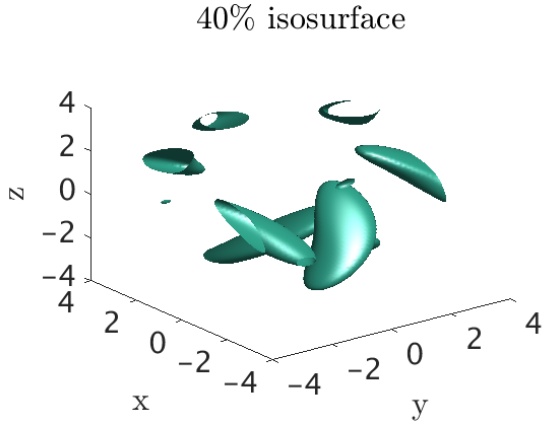

(c) t=710

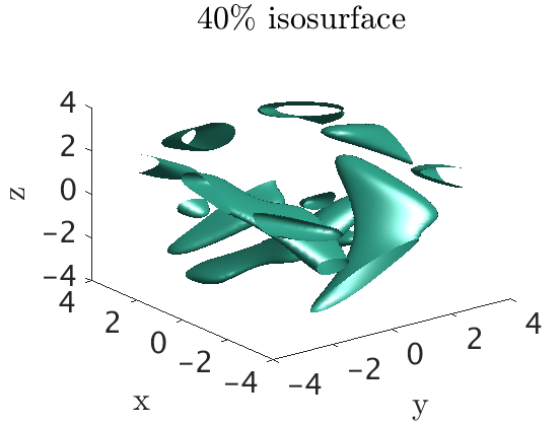

(d) t=715

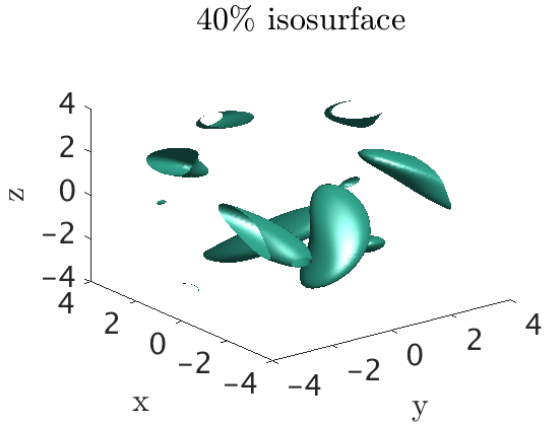

(e) t=720

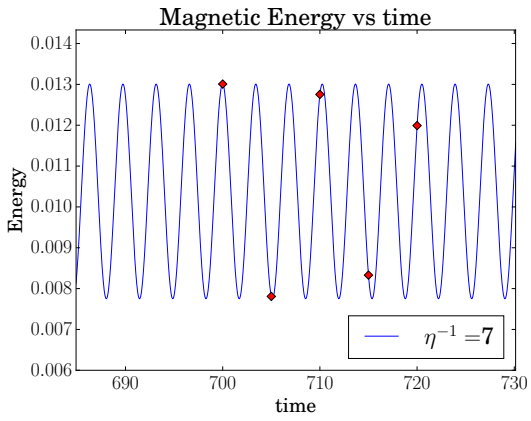

(f) Close view of the oscillations of the magnetic energy when the magnetic field structure is that within plots a-e (the red diamonds)

Figure 6.23: 40% isosurfaces of $\mathbf{B}^2$ at various timesteps during the statistically steady nonlinear regime for $\eta^{-1} = 7$. We see an oscillatory pattern where the magnetic field structure becomes elongated and deformed at [705,715] but then goes back to its original structure approximately 5 time units later.

Figure 6.24 shows the kinetic and magnetic energies for a short period in the nonlinear

regime for each of the three η^{-1} with oscillating magnetic fields during the nonlinear regime. For $\eta^{-1} = 7$ we see that as the magnetic energy increases we see a corresponding decrease in the kinetic energy and vice versa, indicating a transfer of energy between the two fields. The sum of the two energies is however not constant and therefore injection of energy by the forcing and diffusion must also contribute to the energy evolution. As I have already identified that the energy growth appears to be taking place in the regions of weak field the following heuristic description of the dynamo saturation follows. Energy growth occurs in the regions of weak magnetic field. This then increases the strength of the magnetic field which then transfers energy to the flow via the Lorentz force. As the magnetic field globally grows it also grows at the regions where it is strongest and these regions become larger in size. As they increase in size the regions of weak magnetic field correspondingly shrink and therefore less energy growth occurs. Eventually a critical point is reached whereby the energy produced is insufficient to enlarge the regions of strong field but is also only enough to balance diffusion and therefore the energy, and the dynamo saturates. Oscillations of the magnetic energy then occur as follows. Beginning at a peak magnetic energy is dissipated from the structures by diffusion as well as being transferred to the flow via the Lorentz force. This causes a reduction in their size and enlarges the regions where energy growth occurs. Energy growth then occurs causing the structures to regrow until they again reach a peak and the cycle restarts.

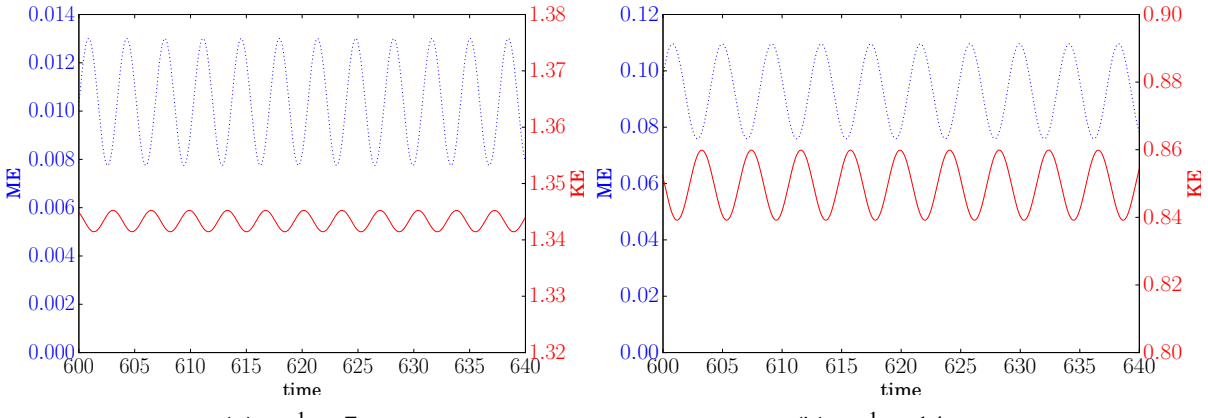

(a) $\eta^{-1} = 7$

(b) $\eta^{-1} = 14$

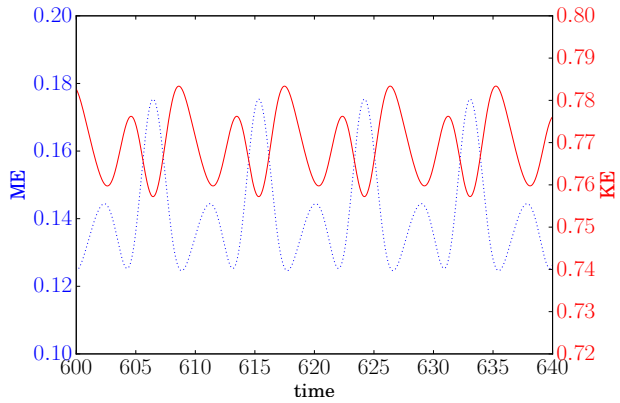

(c) $\eta^{-1} = 28$

Figure 6.24: Plot of oscillations in magnetic and kinetic energy during the nonlinear phase of the dynamo for $\eta^{-1} = [7, 14, 28]$. We see that as the magnetic energy is increased we see a corresponding decrease in kinetic energy. The changes in the magnetic field structure which occur due to these oscillations therefore can be seen to be caused by an exchange in energy between the two fields.

The structure of the magnetic field and its evolution for $\eta^{-1} = 14$ is similar to that seen for $\eta^{-1} = 7$ and therefore the heuristic description of the dynamo mechanism described above is also valid for $\eta^{-1} = 14$. $\eta^{-1} = 28$ exhibits a similar pattern however there are some differences. In figure 6.25 I show 40% isosurfaces of the magnetic field at various times as well as the kinetic and magnetic energy evolution during the window encompassed by the isosurfaces. Figure 6.25a shows plots of the energy with red dots indicating the isosurfaces shown in all of the other plots within figure 6.25. We see that the oscillating pattern has changed to a periodic oscillation where completion of a single period involves a larger and a smaller oscillation, each with the same frequency. Figures 6.25b-6.25e show how the structures become stretched. The plots have been arranged to show one cycle beginning from a large maxima and ending at the minima after the small maxima. Going

from the larger maxima (t=420, figure 6.25b) to the minima between a large and small maxima (t=440, figure 6.25c) we see that as with the lower η^{-1} cases the large magnetic field structures become stretched out. However as we then approach the small maxima the structure that is formed is not the one seen at the large maxima but a different one (t=460, see figure 6.25d). This then becomes stretched out as we again reach a minima (t=400, see figure 6.25e) although this minima has a different structure to that seen in the minima proceeding the large maxima. As such rather than the two step process that the magnetic field undergoes for $\eta^{-1} = [7, 14]$ the field instead here undergoes a 4 step periodic process.

From the 40% isosurfaces of the magnetic field for $\eta = [7, 14, 28]$ I have therefore been able to show that oscillations in the magnetic and kinetic energy correspond to periodic stretching of the magnetic field structures. This stretching occurs simultaneously with the transfer of energy between the magnetic and kinetic fields.

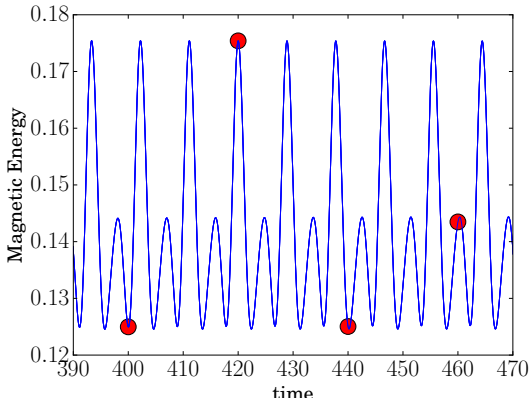

(a) Close view of the oscillations of the magnetic energy when the magnetic field structure is that within plots a-e (the red diamonds)

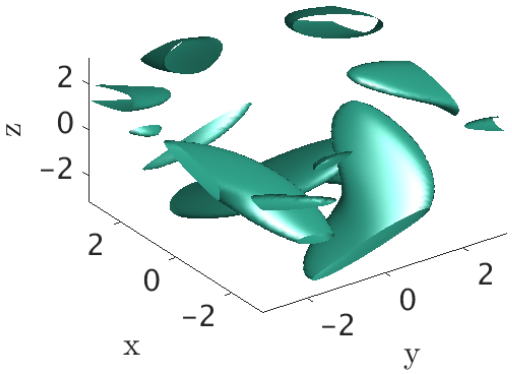

(b) t=420 at the maxima of the larger peak

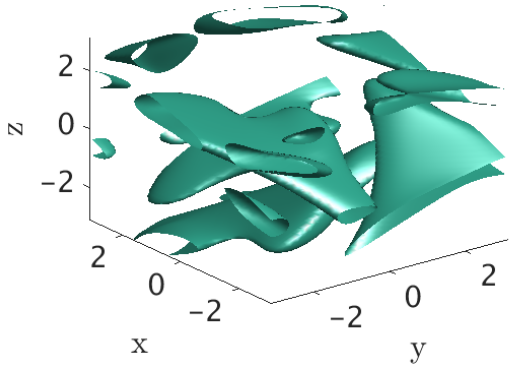

(c) t=440 the minima between the larger and smaller maxima

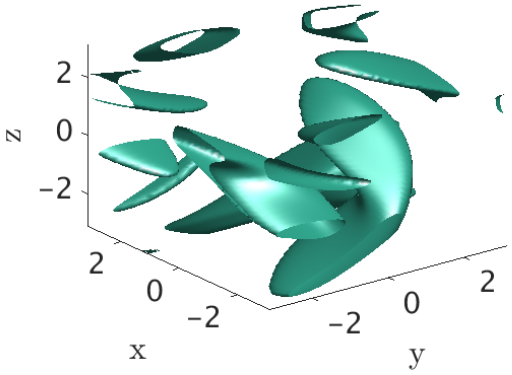

(d) t=460 At the smaller maxima.

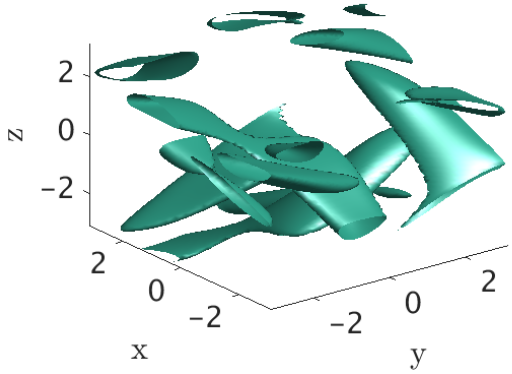

(e) t=400 the minima between the smaller and larger peak.

Figure 6.25: 40% isosurfaces of $\mathbf{B}^2$ at various timesteps during the statistically steady nonlinear regime for $\eta^{-1} = 28$.

For $\eta^{-1} = [56, 112]$ time series of the magnetic energy (see figure 6.12) lose their predictable periodic nature and instead behave somewhat chaotically whilst still being statistically steady. As such there is no periodic behaviour to examine. Figure 6.26 shows

40% isosurfaces for $\eta^{-1} = 56$ throughout the nonlinear regime. The morphology bears a resemblance to that seen for $\eta^{-1} = 28$ and consists of thin structures.

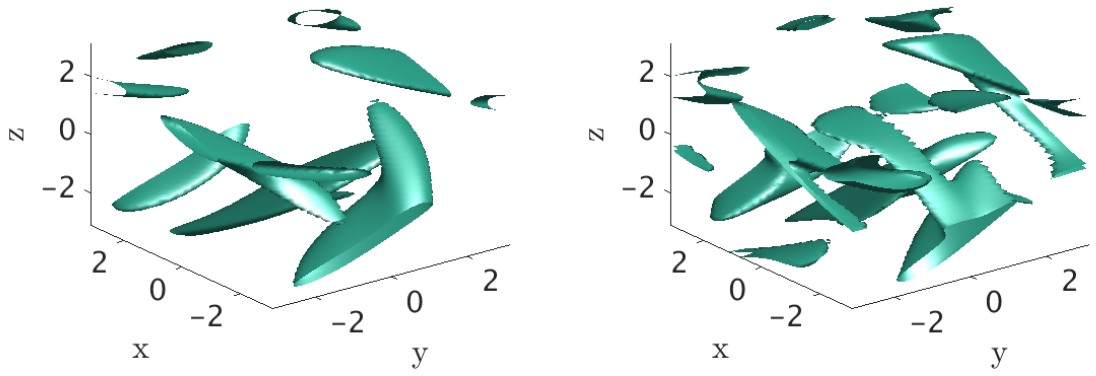

(a) $t = 800$ (b) $t = 860$

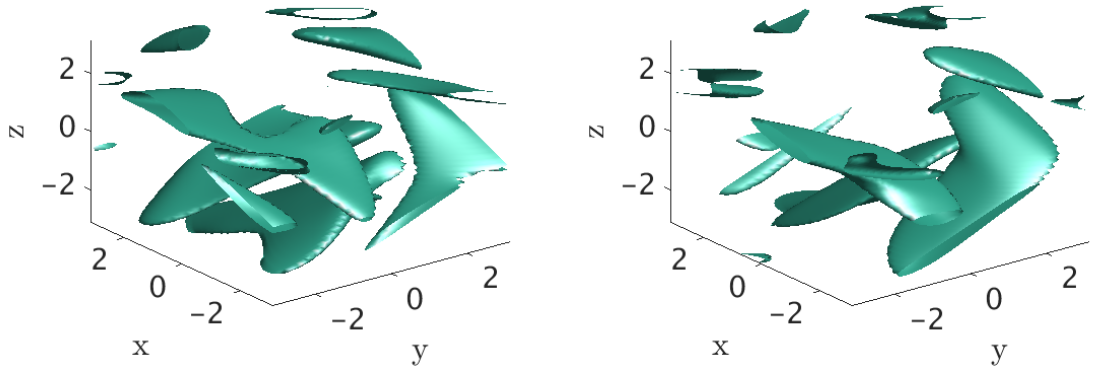

(c) $t = 1800$ (d) $t = 1860$

Figure 6.26: 40% isosurfaces of $\mathbf{B}^2$ for $\eta^{-1} = 56$. Whilst the evolution of the field is more chaotic the structures still have the characteristic thinness seen at lower η^{-1}.

The flow field also undergoes a number of changes. Figure 6.27 shows how the flow field evolves from its initial structure, through the kinematic phase (time=100), saturation (time=200) and then at a minima (time=370) and a maxima (time=370) of the oscillations of the magnetic energy during the nonlinear phase of the dynamo for $\eta^{-1} = 14$. One feature that appears to be present in all contours is that the separated regions of strong field appear to coalesce as the dynamo evolves. The flow field structure does not appear to change drastically going from a minima to a maxima however there are some noticeable differences, in particular at a minima the large regions of strong field appear more circular whereas at the maxima they have a more elongated appearance. Finally in figure 6.28 I show examples for $\eta^{-1} = 56$ with one time in the kinematic regime (70) and the other 3 spread out within the time dependent saturated state. The flow field structure has now

changed more drastically with the eddy like regions of strong field now being replaced by long thin structures. Furthermore regions of weak field have become deformed and themselves elongated.

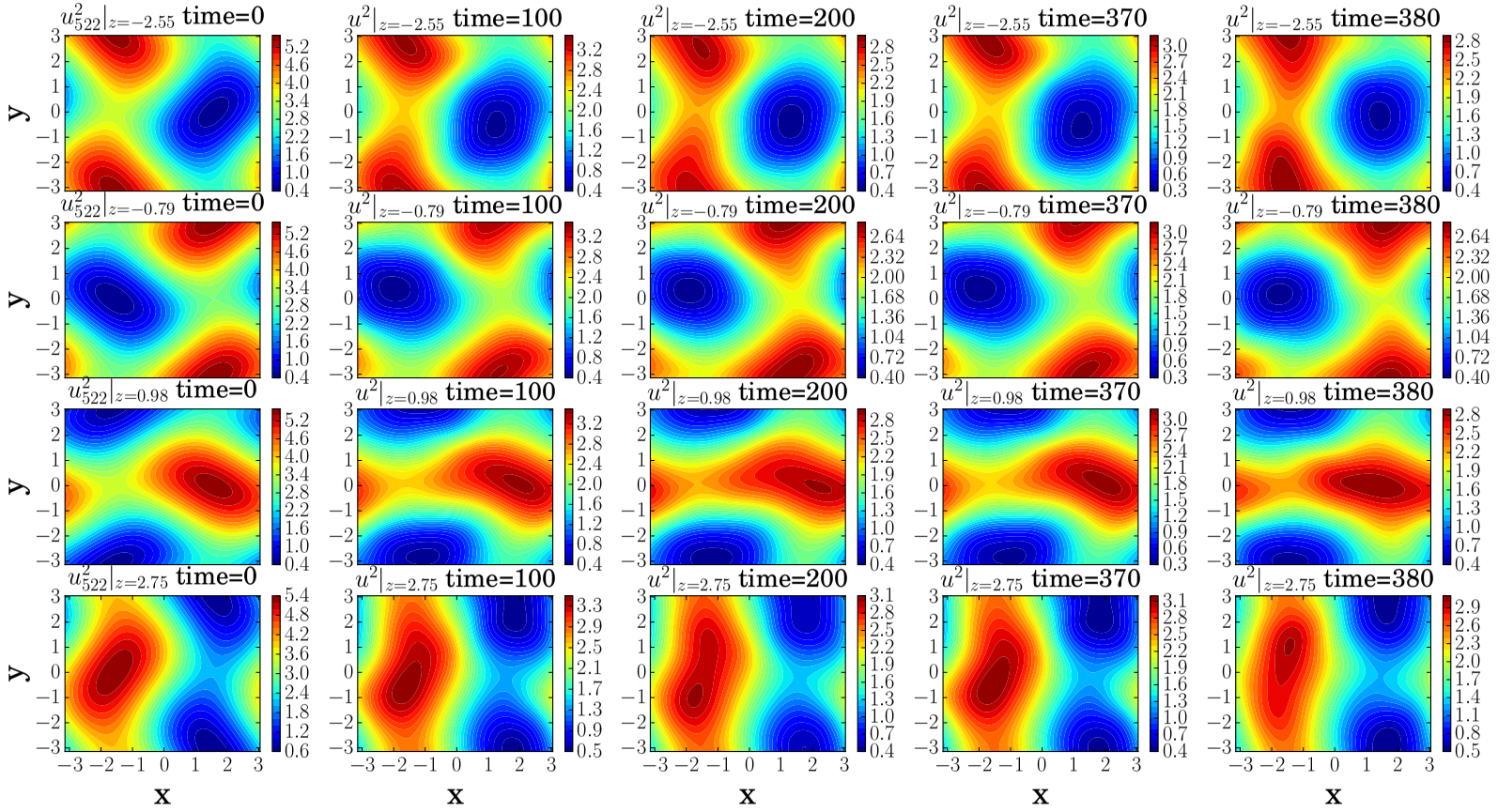

Figure 6.27: Contours of $\mathbf{u}^2$ for $\eta^{-1} = 14$.

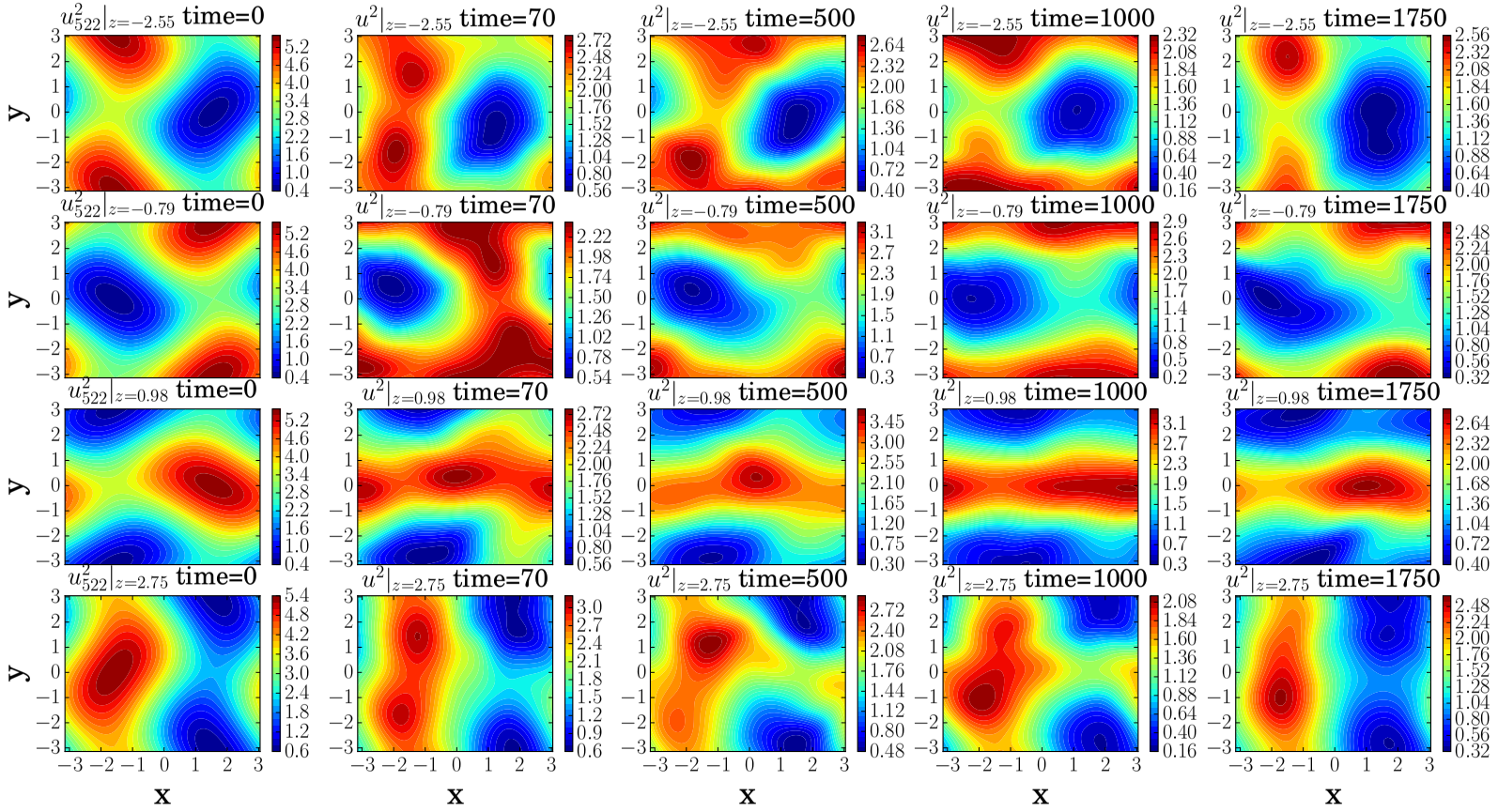

Figure 6.28: Contours of $\mathbf{u}^2$ for $\eta^{-1} = 56$.

In summary; isosurfaces of the magnetic field have shown that the magnetic field at a given field strength is confined to large structures throughout the domain. There appears to be very little change in the structures as the dynamo saturates however oscillations between a number of structures is seen for $\eta^{-1} = [7, 14, 28]$. Time dependent behaviour is seen for $\eta^{-1} = [56, 112]$ in the nonlinear regime however the broad features of the structure remain similar. The oscillation between field structures for $\eta^{-1} = [7, 14, 28]$ correspond to maxima and minima of the energy curves respectively.

Descriptions of the 111 nonlinear dynamo by Archontis [5] describe a transition from cigar like structures to structures that are more flat in appearance, and are thus similar in structure to those seen here. Furthermore, results within section 6.4.1 suggest that both the 111 and the 522 dynamo grow energy within the regions of weak magnetic field. These results together suggest that the 111 and 522 dynamo have much more in common in the nonlinear regime then their kinematic dynamo counterparts did.

6.4.3 Analysis of 3D Field Structure Using Minkowski Functions

In section 6.4.2 I examined the three dimensional structure of the magnetic field using isosurfaces. I now apply the Minkowski Functions outlined in section 6.2 to the magnetic field in order to quantify the changes to its structure.

The Minkowski Functions will be used for a number of purposes. They will be used to examine whether the magnetic structures for each η^{-1} are ribbons, pancakes or filaments. They will also be used to examine whether the field changes when the dynamo saturates although this will be hindered by the shortness of some of the kinematic regimes. Finally they will be used to compare some of the average properties of the structures for smaller ($[7, 14, 28]$) and larger ($[56, 112]$) η^{-1}.

I first examine whether the magnetic field structure changes upon saturation of the 522 nonlinear dynamo. At intervals of 5 whole time units I calculate the Minkowski Functions of $\mathbf{B}^2$ for $\eta^{-1} = [7, 14, 28, 56, 112]$. As previously shown the magnetic field exhibits an oscillatory behaviour for $\eta^{-1} = [7, 14, 28]$ and as such we expect oscillations in the Minkowski

Functions.

Time series of P and F are shown in figure 6.29 and L, W and T are shown in figure 6.30. For $\eta^{-1} = 7$ we see no change in the time dependence of any of these quantities upon saturation to the nonlinear state ($t \approx 400$). The Minkowski Functions oscillate between being marginally filamentary and being ribbon-like. For $\eta^{-1} = 14$ and $\eta^{-1} = 28$ (not shown) the magnetic field structure is ribbon-like both immediately before and for all time after saturation (which is at $t \approx 100$ for $\eta^{-1} = 14$). The Minkowski Functions (MF) show that the periodic oscillations in the magnetic field structure for $\eta^{-1} = 14$ and $\eta^{-1} = 28$ appear only once the dynamo saturates and thus appear to be a product of the saturation mechanism. For $\eta^{-1} = 56$ and $\eta^{-1} = 112$ (not shown) the magnetic field structure is again ribbon-like both before and after saturation however its structure is highly time dependent.

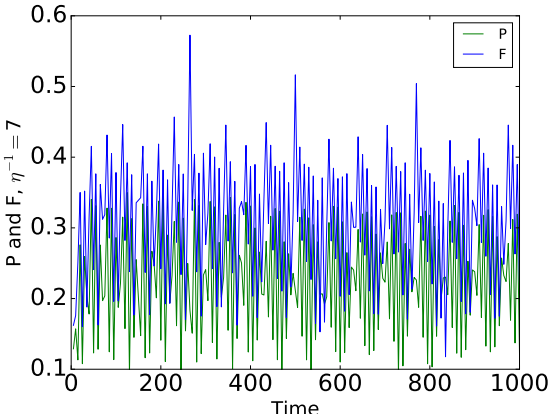

(a) $\eta^{-1} = 7$

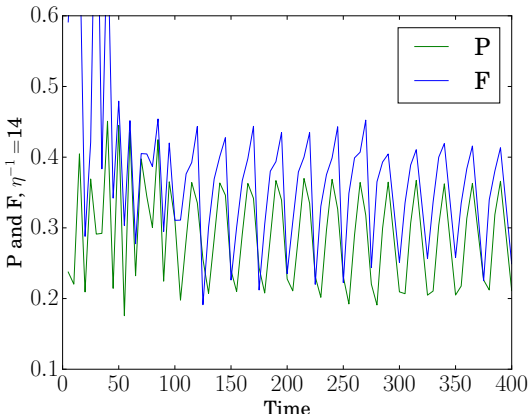

(b) $\eta^{-1} = 14$

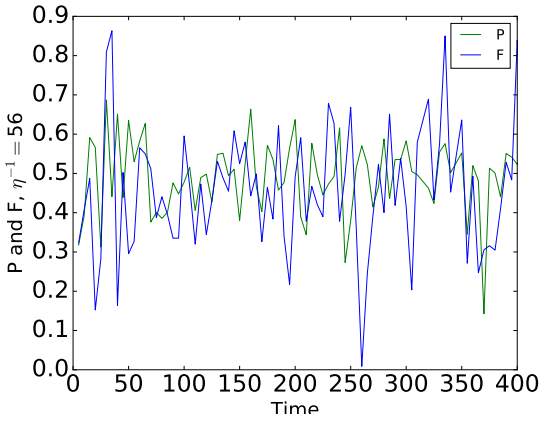

(c) $\eta^{-1} = 56$

Figure 6.29: P and F for 40% isosurfaces of $\mathbf{B}^2$ and $1/\eta = [7, 14, 56]$. $\eta^{-1} = 7$ does not appear to change magnetic field structure upon saturation. For $\eta^{-1} = 14$ we see onset of a periodic component to P and F upon saturation. For $\eta^{-1} = 56$ the field is ribbon-like.

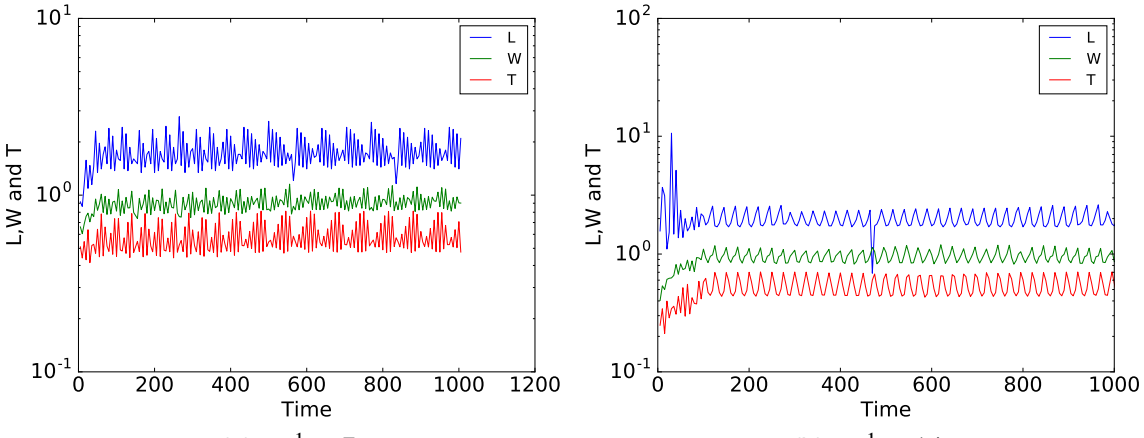

(a) $\eta^{-1} = 7$ (b) $\eta^{-1} = 14$

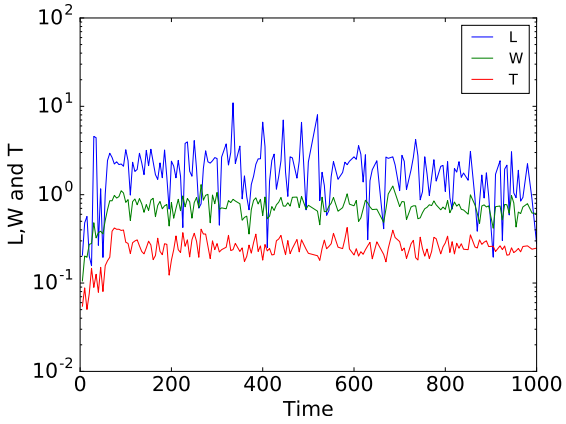

(c) $\eta^{-1} = 56$

Figure 6.30: L, W and T for 40% isosurfaces of $\mathbf{B}^2$ and $1/\eta = [7, 14, 56]$. $1/\eta = [7, 14, 56]$. Clear separation between the three dimensions is seen, as seen in prototypical examples of ribbon magnetic field structures.

Together the results for the 522 dynamo show a strong preference for ribbon structures. The preference for ribbon-like structures is interesting as the magnetic field produced by the 111 ABC flow has been shown [37] to flatten out and form sheet-like structures upon saturation with the structures being observed by Galanti to be close to those of the 522 kinematic dynamo. The combined results are thus suggestive that ABC forced nonlinear dynamos preferentially form ribbons in their nonlinear regime at low R_m and R_e.

A mixture of behaviours are observed as the dynamos saturate to the nonlinear regime. For $\eta^{-1} = 7$ there is no change in structure or in time dependence possibly due to the weakness of the magnetic field. For $\eta^{-1} = [14, 28]$ the structures are ribbons in both regimes however the field structure becomes periodically time dependent once saturation occurs as energy is exchanged via the Lorentz force and the inductive term in the induction

equation. For $\eta^{-1} = [56, 112]$ the structure is ribbon-like throughout but varies in a highly time dependent manner.

From the results so far the behaviours appear to be different for the "large scale" (LS) $[7, 14, 28]$ and the "small scale" (SS) $[56, 112]$ values of η. I will now compare these two groups. I calculate a time average of each of L, W, T and the ratio P/F for each η and then calculate an average of the LS and SS values respectively. Figure 6.31 shows the result for all isovalues. We see that the SS values are consistently smaller than the LS values. This is expected as a reduction in diffusion allows smaller scale structure to persist. Furthermore from figure 6.31d we see that the SS values are more planar than their LS counterparts.

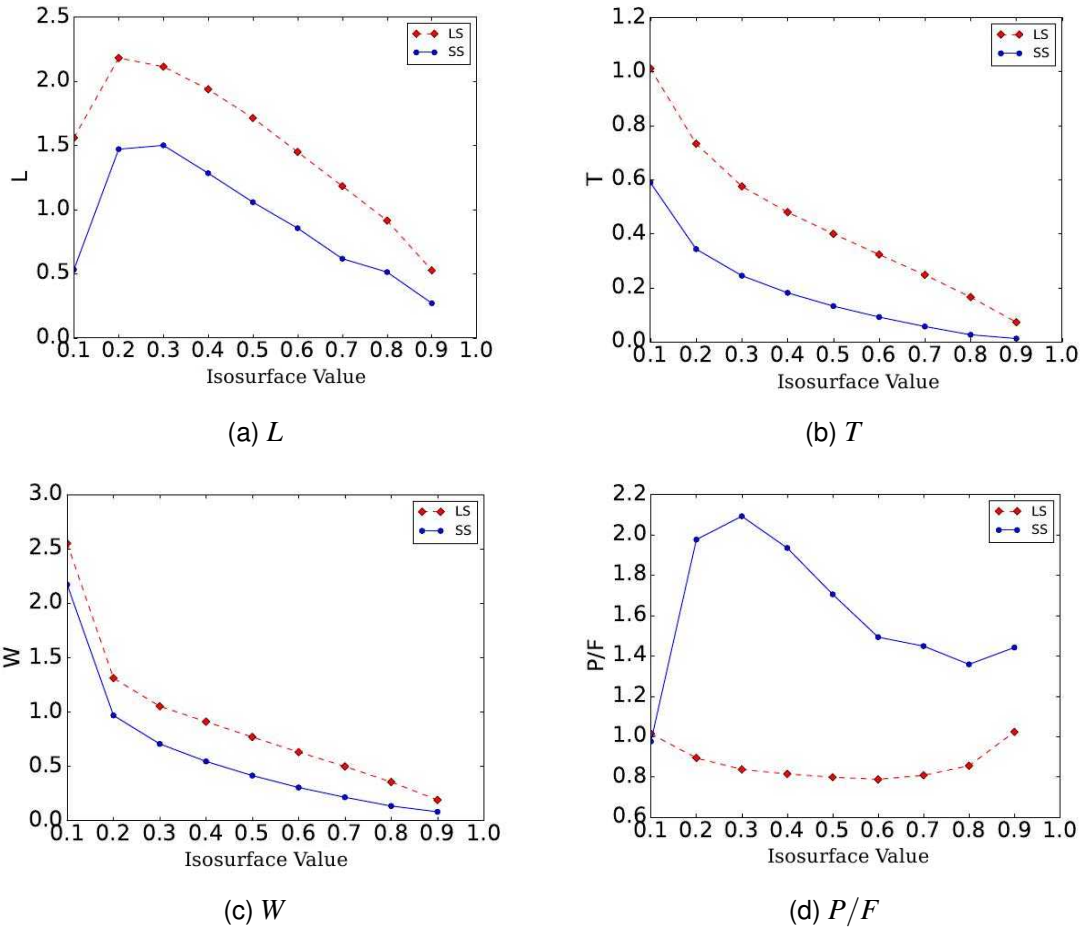

(a) L (b) T

(c) W (d) P/F

Figure 6.31: L, W and T against isosurface value for LS and SS η. We observe that the SS values have smaller values of the lengths across all isosurface values. The reduction with increasing isosurface value is down to the magnetic field becoming less space filling as we consider its stronger elements.

To summarise: time series of L, W and T as well as P and F have shown that the mag-

netic field is best described as being ribbon-like at all η, although it becomes marginally filamentary periodically for $\eta^{-1} = 7$. For $\eta^{-1} = 7$ we observe no change in magnetic field structure between the kinematic and nonlinear stages of the dynamo and very little change in the flows morphology upon entering the nonlinear regime. This appears to be a result of the weak saturation value of the magnetic energy. For $\eta^{-1} = [14, 28]$ the MF gain a periodic time dependence upon entering the nonlinear regime. For $\eta^{-1} = [56, 112]$ the field is highly time dependent with a short kinematic regime and so examining the saturation is difficult with the only conclusions being that the magnetic field remains ribbon-like throughout. Finally it was found that the SS values of η^{-1} have a flatter average structure than that of the LS values and smaller values for all three of the length measure Minkowski Functions.

6.5 Comparisons between the 522 and 111 Nonlinear dynamo

In this section I use Minkowski Functions (MF) to draw comparisons between the 522 and 111 dynamos. Frequently I will draw comparisons between the results I obtain and those obtained by Galanti et al. within [37].

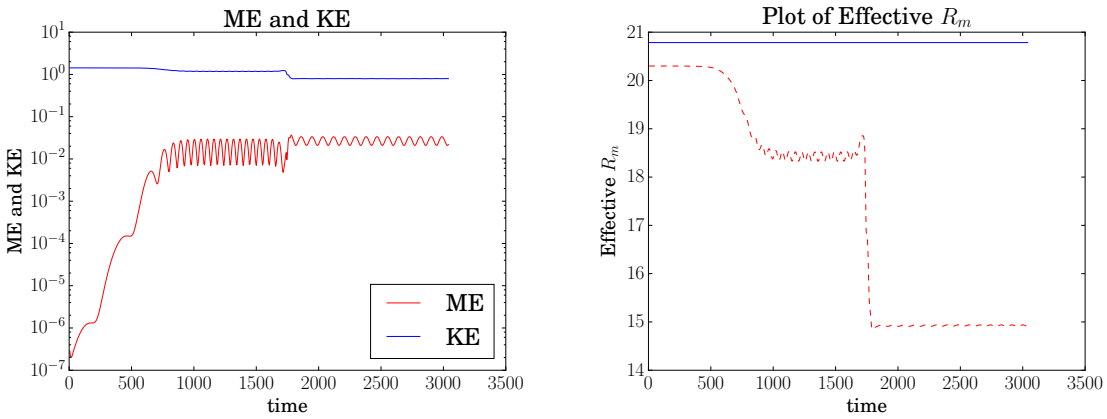

(a) Plot of KE and ME vs time. We see the ME can be divided into 3 stages; the kinematic phase, the primary saturation and the secondary saturation.

(b) Effective R_m of the 111 nonlinear dynamo began with $1/\eta = 1/\nu = 12$. The blue line is a theoretical result and indicates where the initial red line should be.

Figure 6.32

So as to draw comparisons between my results and those of Galanti I run a 111 simulation

with $1/\eta = 1/\nu = 12$. Figure 6.32a shows the KE and ME of the run. 3 distinct regions can be seen for the ME, the kinematic phase where the magnetic field experiences exponential growth, the primary saturation where as noted by Galanti et al the flow differs very little from the 111 flow and finally the secondary saturation where the flow differs more from the 111 flow. In particular the flow loses its stagnation points, this is shown in figure 6.33 with the small regions being close to, but not equal to, zero.

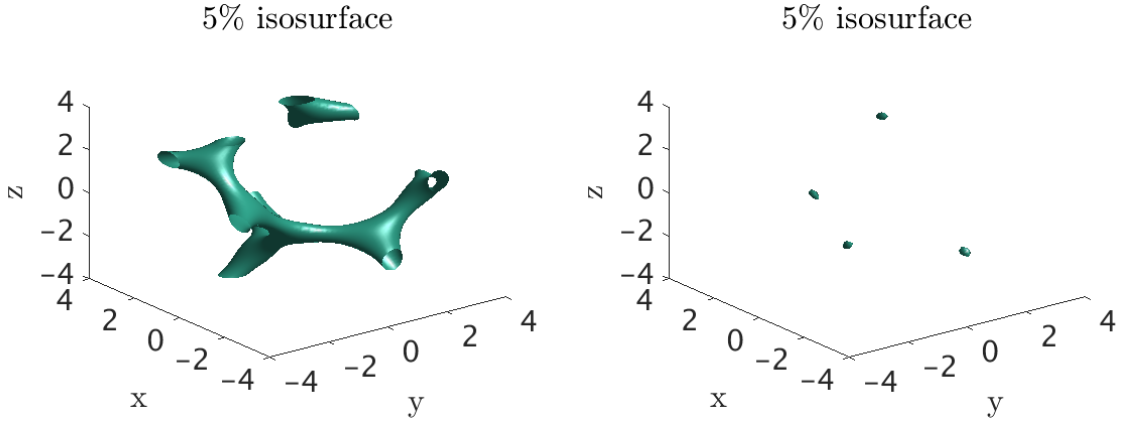

(a) 5% isosurface at $t = 1205$ (b) 5% isosurface at $t = 2505$

Figure 6.33: 5% isosurfaces of $\mathbf{u}^2$. We see that upon saturation the weak flow is almost completely eliminated.

In figure 6.32b I show the effective R_m during the simulation calculated using equations (6.20a)-(6.20d).

$$(u_{rms}^{111})^2 = \frac{1}{V}\int_V \left(\mathbf{u}^{111}\right)^2 dV \quad \text{(6.20a)} \qquad \left(l^{111}\right)^2 = \frac{\int_V \left(\mathbf{u}^{111}\right)^2 dV}{\int_V \left|\nabla \times \mathbf{u}^{111}\right|^2 dV} \quad \text{(6.20b)}$$

$$R_e^{111} = \frac{u_{rms}^{111} l^{111}}{\nu} \quad \text{(6.20c)} \qquad R_m^{111} = \frac{u_{rms}^{111} l^{111}}{\eta} \quad \text{(6.20d)}$$

We see that as the dynamo enters its primary and secondary saturation phases the effective R_e gets reduced. This is in agreement with Galanti et al who noted that the Lorentz force acts to reduce the effective R_m and R_e via a reduction in root mean squared velocity. This suggests the following picture of why we observe two saturated states within figure 6.32a. Initially the flow induces the magnetic field to grow exponentially until eventually the Lorentz force acts to reduce the root mean square flow (and so the effective R_e) and saturate the dynamo. This primary saturation process changes the flow structure to a flow close to a no stagnation point ABC flow which in turn induces the magnetic field to

grow and then resaturate with a structure similar to that seen within kinematic dynamo simulations with no stagnation point ABC forcings.

Podvigina and Pouquet [84] examined the hydrodynamic stability of the 111 flow and found that when it becomes unstable ($R_e > 13$ in the hydrodynamic case) the main attractors are close to the $1 : 0.38 : 0.38$ ABC flow (which has no stagnation points). This suggests that the changes made by the Lorentz force to the flow, for the MHD case, induce an instability which changes the flow structure in a similar manner to the hydrodynamic instability in the hydrodynamic case.

One consequence of the changing flow properties is that where we draw comparisons between results for the 522 and 111 dynamos we are comparing dynamos at different effective R_m and R_e. This makes directly contrasting the amount of energy difficult however a comparison of the morphology of the two is still beneficial because as we shall see the two are in fact remarkably similar during the nonlinear (secondary saturation in the 111 case) regime.

Figure 6.34 shows P, F and the ratio P/F for the 111 dynamo with a median filter (as described within section 6.2) applied to remove spurious points and values below $t = 500$ ignored due to the weakness of the magnetic field. Comparing this to the kinetic and magnetic energies within figure 6.32a yields a number of interesting things. First, there is no obvious change in structure of the field (on average) when the primary saturation occurs. There is however a flattening out of the magnetic field structures in the secondary saturation phase to ribbon-like structures.

Galanti et al. showed that there isn't a large change in the modes occupied by the energy of the flow upon the saturation to the principle state. The new result here is therefore that not only does the energy occupy the same modes but the actual morphology (shape) of the field as quantified by the Minkowski Functions remains the same in this primary saturation phase.

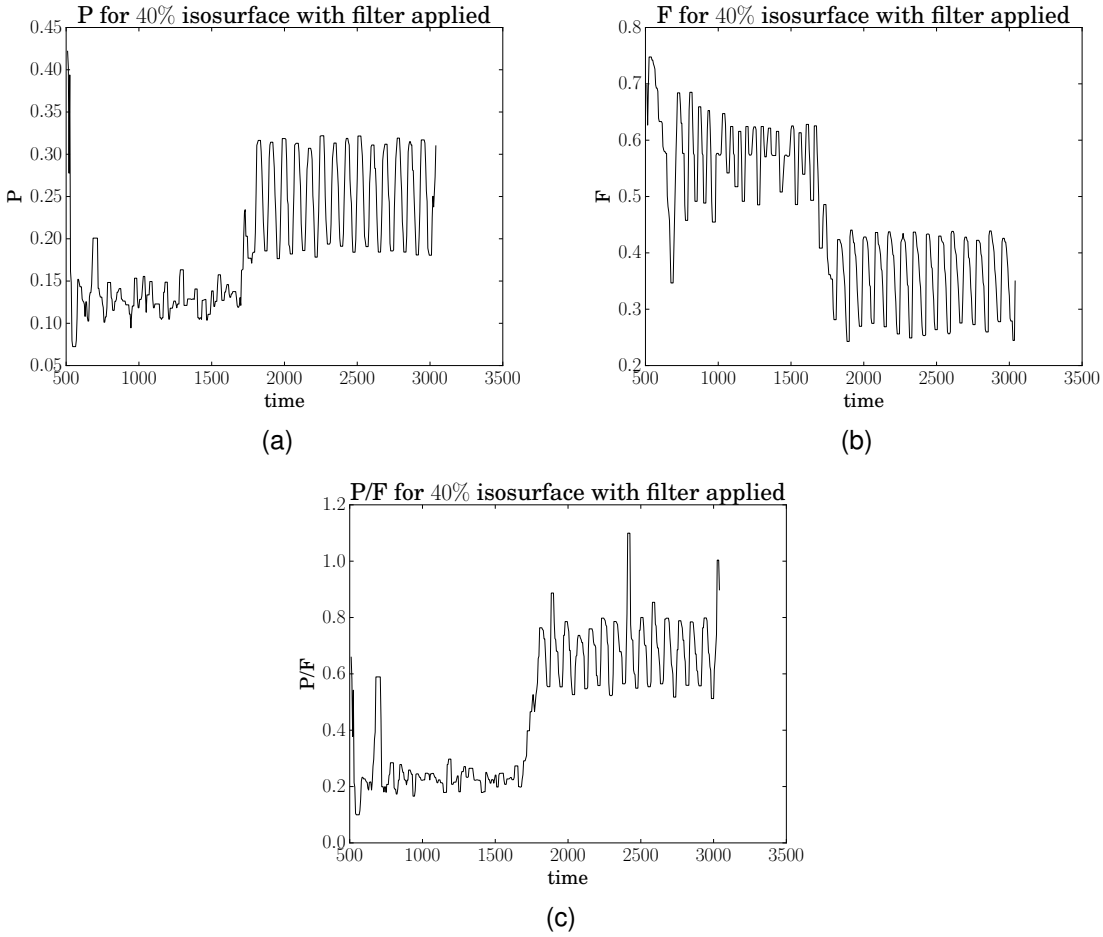

Figure 6.34: Planarity, Filamentarity and the ratio of the two vs time with a median filter applied. We see no change in structure of the magnetic field in going from the kinematic to the primary saturation phases however we see an increased planarity (and reduced filamentarity) when entering the secondary saturation, indicating that the magnetic field becomes more stretched out into sheet like structures. The ratio of P/F then tells us these sheet like structures are best described as ribbons.

Saturation of the 111 dynamo here therefore appears to result in a reduced effective R_m and R_e simultaneously with a flattening of the magnetic field structure. Although I have shown the 40% isosurface here the result was found for all isovalues from 10% to 90%.

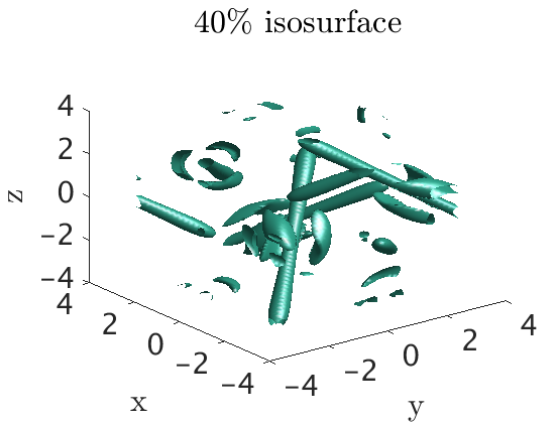

(a) 40% isosurface at $t = 715$

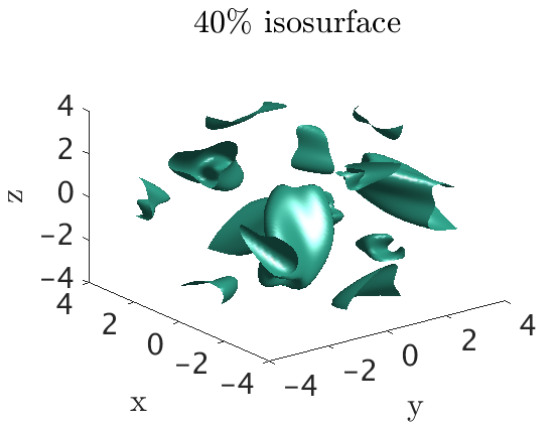

(b) 40% isosurface at $t = 970$

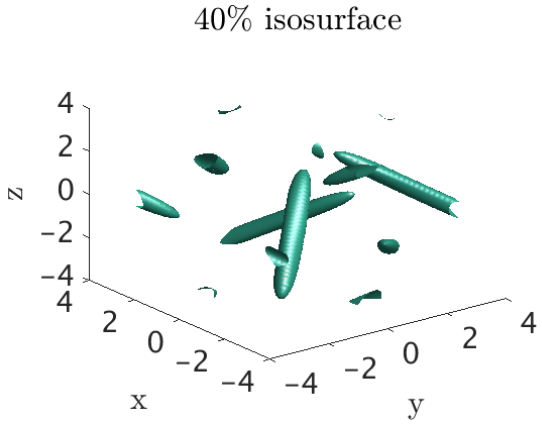

(c) 40% isosurface at $t = 1310$

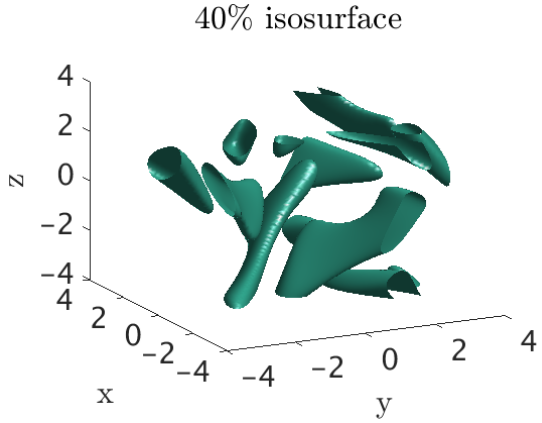

(d) 40% isosurface at $t = 1825$. The distinctive 'boomerang' structure we saw for the 522 dynamo is present.

Figure 6.35: 40% isosurfaces of $\mathbf{B}^2$. Before saturation the magnetic field is predominantly within filaments however it becomes ribbon-like in structure upon saturation.

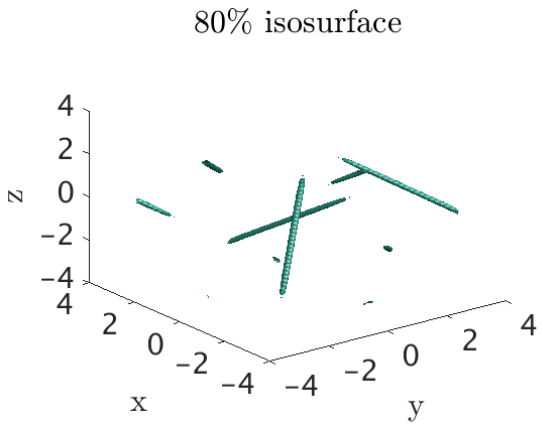

(a) 80% isosurface at $t = 715$

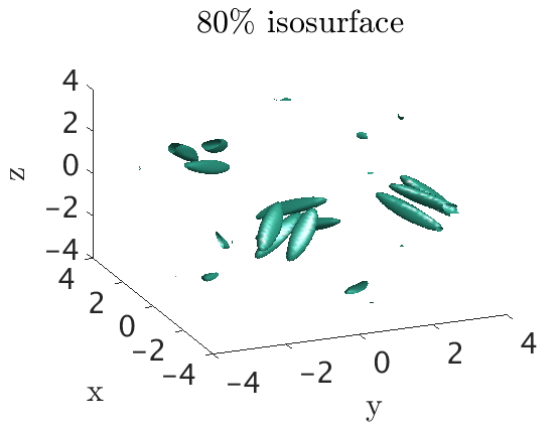

(b) 80% isosurface at $t = 970$

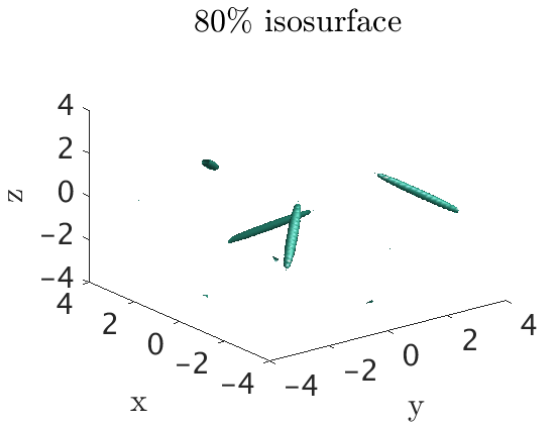

(c) 80% isosurface at $t = 1310$

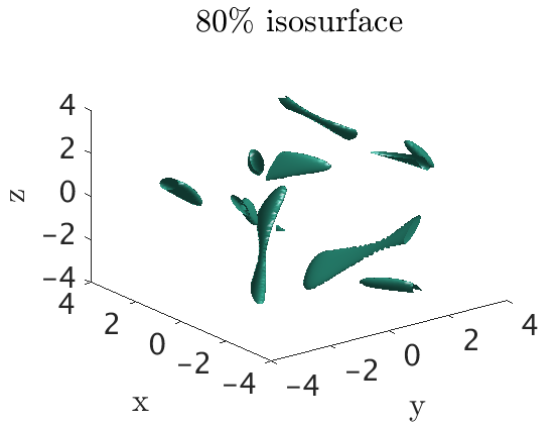

(d) 80% isosurface at $t = 1825$

Figure 6.36: 80% isosurfaces of $\mathbf{B}^2$. We see that the thick structures in figure 6.35b in fact hide double filaments of stronger field. Before saturation the magnetic field is predominantly within filaments however it becomes ribbon-like in structure upon saturation.

In figures 6.35 and 6.36 I show 40% and 80% isosurfaces of $\mathbf{B}^2$. Figures (a) and (b) within each correspond to the kinematic regime, figure (c) the primary saturation and figure (d) is the secondary saturation. In the kinematic phase and the first saturation the magnetic field appears to undergo a process of expulsion and periodic replenishment of the filamentary flux cigars in a manner similar to that seen for the Kolmogorov flow within kinematic dynamo theory that I have previously examined within section 4.4. Subplots (a) and (c) show single filaments whereas (b) shows a fatter structure that we see within the 80% isosurfaces to contain two cigars of strong field, again this is similar to the Kolmogorov flow results. Within both the kinematic and primary saturation phases we see a periodic transition between field resembling (a)/(c) and field resembling (b). This suggests a periodic process of flux being removed from double cigar structures, possibly by reconnection, and then gradually building up again into the two cigars. Figure subplots (d) show the sec-

ondary saturation stage of the process. The field structure exhibited here are much flatter and resemble the flat structures seen for large scale R_m in the 522 dynamo.

Results for the 111 dynamo at $R_m = R_e = 12$ and the 522 dynamo together suggest that the magnetic field naturally evolves to flat ribbon-like structures once the Lorentz force acts on the flow. Flattening out of filaments in the 111 case allows the dynamo to evade the result by Moffatt and Proctor [76] that the magnetic energy will go to zero as R_m increases if the magnetic field is confined to filaments. The results show that although the magnetic field within the 522 and 111 ABC flow driven dynamos at the low R_m examined here differ greatly in structure within the kinematic regime their morphology becomes remarkably similar once the magnetic field saturates. Both saturate into oscillatory states where periodic stretching of the magnetic field is seen alongside a periodic exchange of energy between the flow and magnetic fields via advection and the Lorentz force. That two extremely different examples within the family evolve to a nonlinear where the magnetic field is similar in morphology is suggestive that ribbon-like magnetic structures may be an attractor for the whole family of forcings. In an ideal scenario a large parameter scan would be performed on the ABC forcings to ascertain whether the final magnetic field structure obtained within the 111 and 522 cases is a broad property of the family of forcings. This however is beyond my computational resources and so a more restricted parameter search will be performed within the next section.

6.6 Magnetic Field Morphology of Nonlinear ABC Dynamos Whose Forcings Have Stagnation Points

6.6.1 Energy Saturation and Morphology Changes

In this section I examine whether the flattening from filamentary magnetic field structures to ribbon-like structures during the saturation process of nonlinear ABC dynamos with stagnation points is a general property of the family of dynamos.

Ideally the hypothesis would be tested via an extensive parameter scan of ν, η and the

coefficients A, B and C within the ABC flow. However this is computationally infeasible and as such certain restrictions have to be made. The first is that I will restrict my examination to $\nu = \eta = 1/12$, the value used by Galanti et al [37]. This is restrictive as it restricts us to drawing conclusions that are relevant only at small R_m and for a Magnetic Prandtl number of one. The second restriction that I make is also one inspired by [37] in that I will take $1 = A > B = C$. This means that I have a clear criterion on which values of A, B and C are stagnation point flows, $B = C > \sqrt{0.5}$, as well as reducing the parameter space to scan. Furthermore I am able to use the kinematic growth rates of the ABC flows obtained by Galanti and shown within figure 6.1 to see what affect kinematic growth rate has on obtaining a successful nonlinear dynamo. Unless otherwise stated simulations are run with an Adams-Bashforth numerical method with diffusion handled exactly and a resolution of 64^3 with a timestep of 0.01. For further information see section 2.3.

The choices of B/A examined are $[0.75, 0.8, 0.84, 0.88, 0.95]$. These were chosen by examining lower resolution runs for a larger number of values which identified 5 different windows of energy behaviour and a value is taken in each. The results can be broadly split into two groups $0.75, 0.95$ and $0.8, 0.84, 0.88$.

I first begin with $0.8, 0.84, 0.88$. The ME and KE are shown in figure 6.37. For 0.8 we see that a saturated dynamo phase is not reached and for 0.88 we see that the saturated ME is too small to act significantly on the flow. For 0.84 the ME is three orders of magnitude weaker than the flow. The result is that in all three cases the magnetic field morphology does not change significantly upon entering the nonlinear regime and is still filamentary. This filamentary structure for $\mathbf{B}^2$ is shown in figure 6.38. For these values we therefore conclude that ribbon-like structures are not obtained however this is due to not obtaining a nonlinear regime.

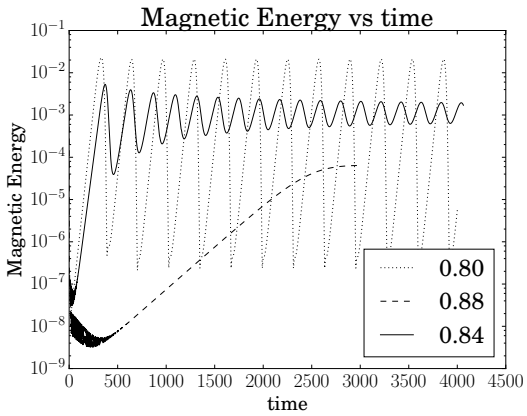

(a) Magnetic Energy for $B/A = 0.80, 0.84, 0.88$

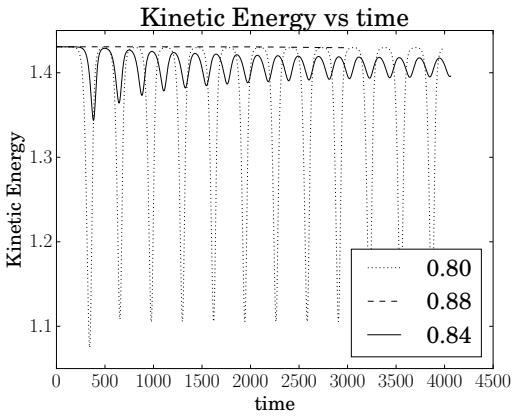

(b) Kinetic Energy for $B/A = 0.80, 0.84, 0.88$

Figure 6.37

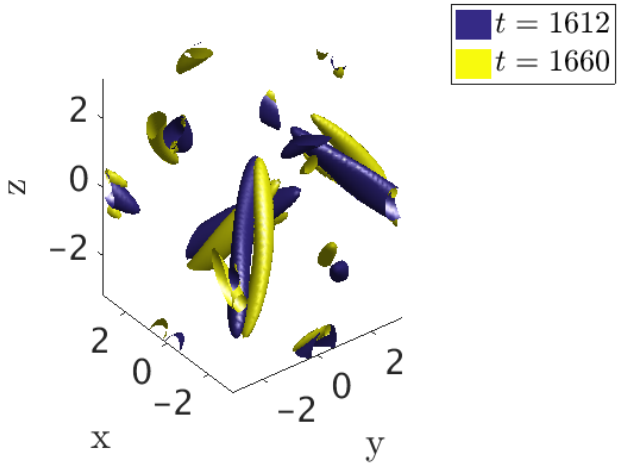

(a) $B/A = 0.8$ at $t = 1612$ (ME maxima) and $t = 1660$ (going to ME minima). Evolution of the cigar structures behaves similarly to the Kolmogorov kinematic dynamo in section 4.4 with a second cigar growing and shrinking periodically.

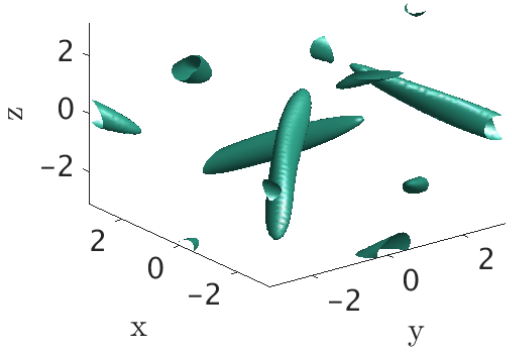

(b) $B/A = 0.84$ at $t = 3000$ (maxima and minima look identical)

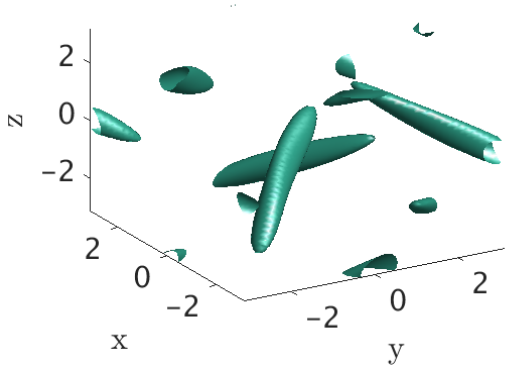

(c) $B/A = 0.88$ at $t = 2990$.

Figure 6.38: 40% isosurfaces of $\mathbf{B}^2$ for $0.8, 0.84, 0.88$. In all cases we see that the magnetic field has a filamentary appearance and thus has not changed upon entering the nonlinear regime.

I now consider 0.75 and 0.95. In figure 6.39 I show the magnetic and kinetic energies for 0.75 and 0.95. We see that both achieve a saturated state where the magnetic energy is within an approximate order of magnitude of the flow. As such we achieve a true nonlinear state where the magnetic and flow fields are able to influence each other significantly.

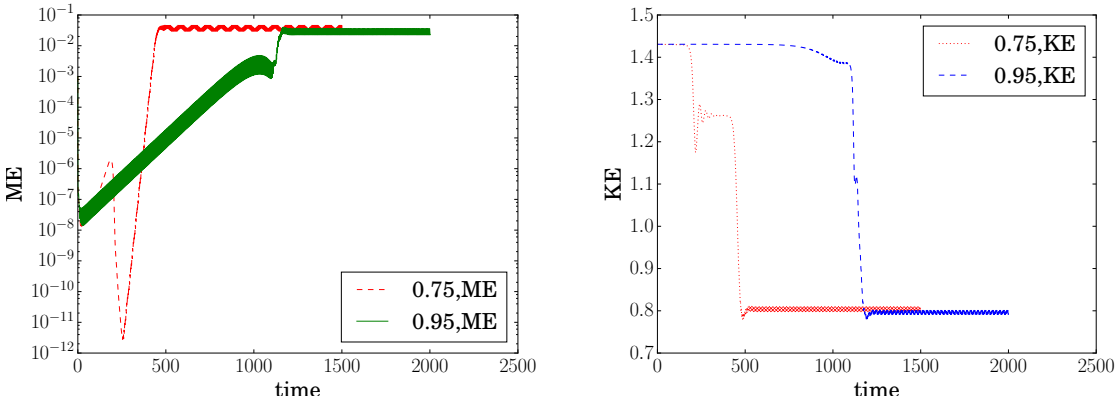

(a) Magnetic Energy for $B/A = 0.75, 0.95$

(b) Kinetic Energy for $B/A = 0.75, 0.95$

Figure 6.39

In figure 6.40 I show isosurfaces of $\mathbf{B}^2$ for 0.75 and 0.95 both before and after the kinematic regime. In both cases we see that the magnetic field begins filamentary in structure and then flattens out.

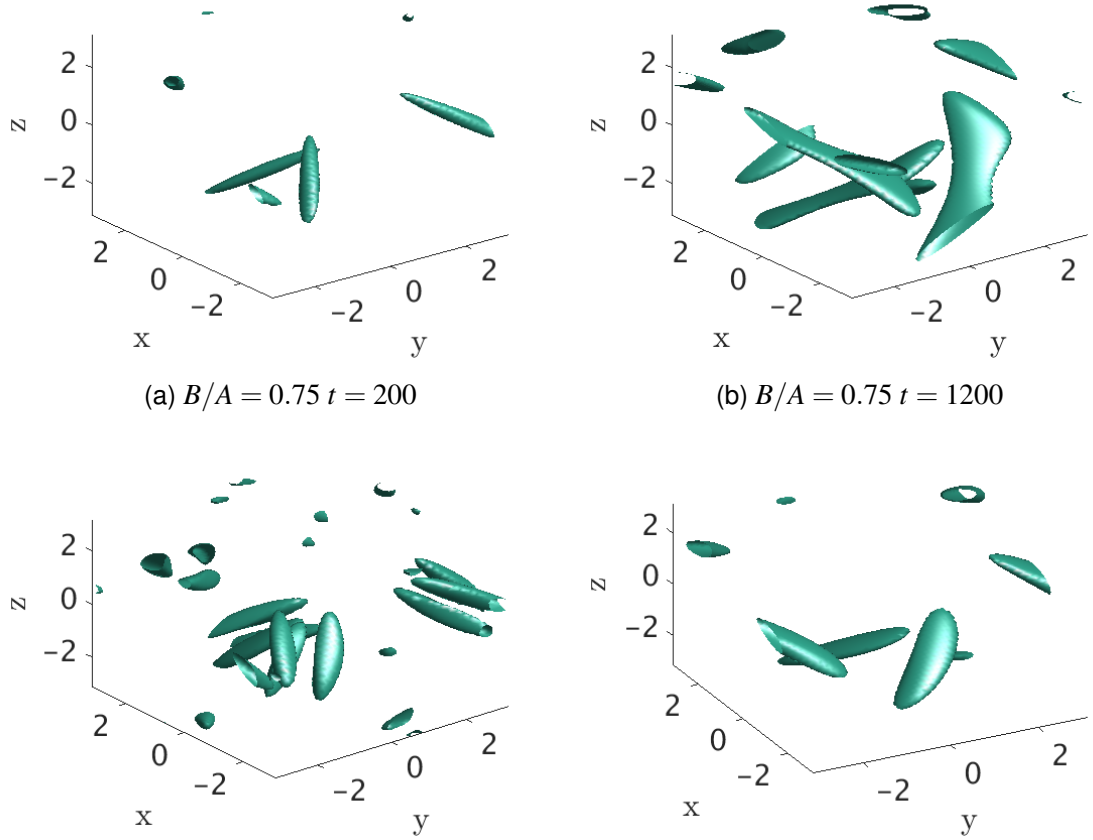

(a) $B/A = 0.75$ $t = 200$

(b) $B/A = 0.75$ $t = 1200$

(c) $B/A = 0.95$ $t = 805$

(d) $B/A = 0.95$ $t = 1800$

Figure 6.40: 40% isosurfaces of $\mathbf{B}^2$ for 0.75 and 0.95.

This flattening out is then seen within the Minkowski Functions within figures 6.41 and 6.42. In both cases we begin with $F >> P$ but then as we approach saturation the two become approximately the same magnitude as the ribbon structures are formed. I note that these structures form much earlier for 0.75. This can be seen for $t \in (200, 400)$ in figure 6.41b.

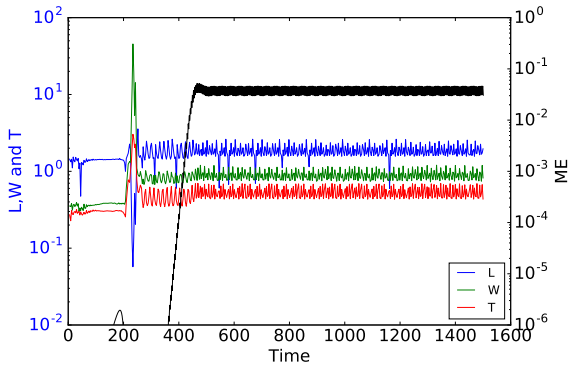

(a) L (blue), W (green) and T (red) for 40% isosurfaces of $\mathbf{B}^2$

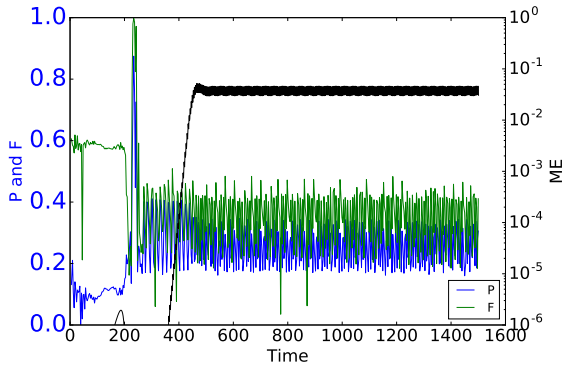

(b) P (blue) and F (green) for 40% isosurfaces of $\mathbf{B}^2$

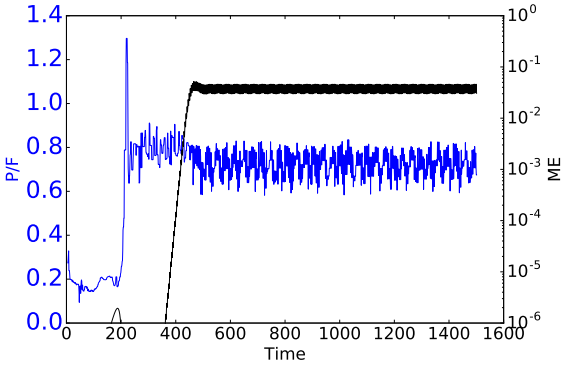

(c) P/F for 40% isosurfaces of $\mathbf{B}^2$

Figure 6.41: $B/A = 0.75$. A reduction in F as well as an increase in P (occurring before $t = 200$) is seen with the magnetic field structures changing from being filamentary and predominantly confined to cigar structures to ribbon like via a flattening out of the cigars.

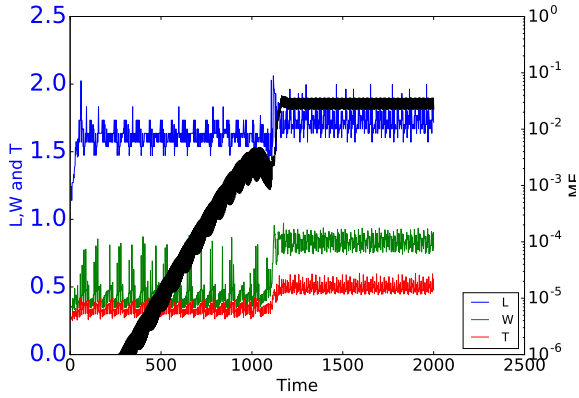

(a) L (blue), W (green) and T (red) for 40% isosurfaces of $\mathbf{B}^2$

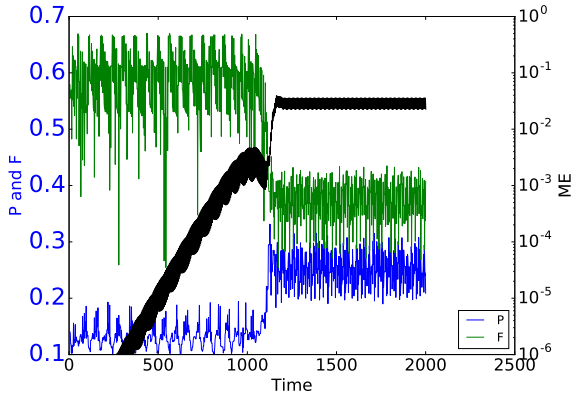

(b) P (blue) and F (green) for 40% isosurfaces of $\mathbf{B}^2$

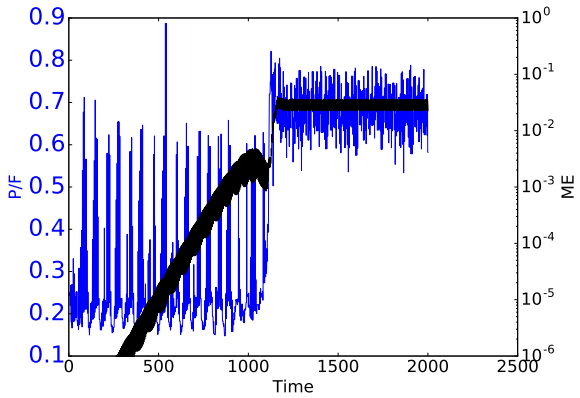

(c) P/F for 40% isosurfaces of $\mathbf{B}^2$

Figure 6.42: $B/A = 0.95$. As with $B/A = 0.75$ A reduction in F as well as an increase in P is seen upon saturation of the dynamo with the magnetic field structures changing from being filamentary and predominantly confined to cigar structures to ribbon like via a flattening out of the cigars. A rather abrupt jump in ME is also observed, similar to that seen for the 111.

Finally in figure 6.43 I show the $B = 0.75$, $B = 0.95$ and $B = 0.84$ counterparts to the effective Reynolds numbers calculated for $B = 1$ in section 6.5. As was the case for the 111 dynamo we see a large drop in R_m and R_e as the dynamo begins to saturate for 0.75 and 0.95. As such we can infer that a similar flattening process is occurring for these values of B as was seen for $B = 1$. This was described in section 6.5. For 0.84 we see only a small change in R_m and R_e. This supports the idea of the flow changing very little during the run.

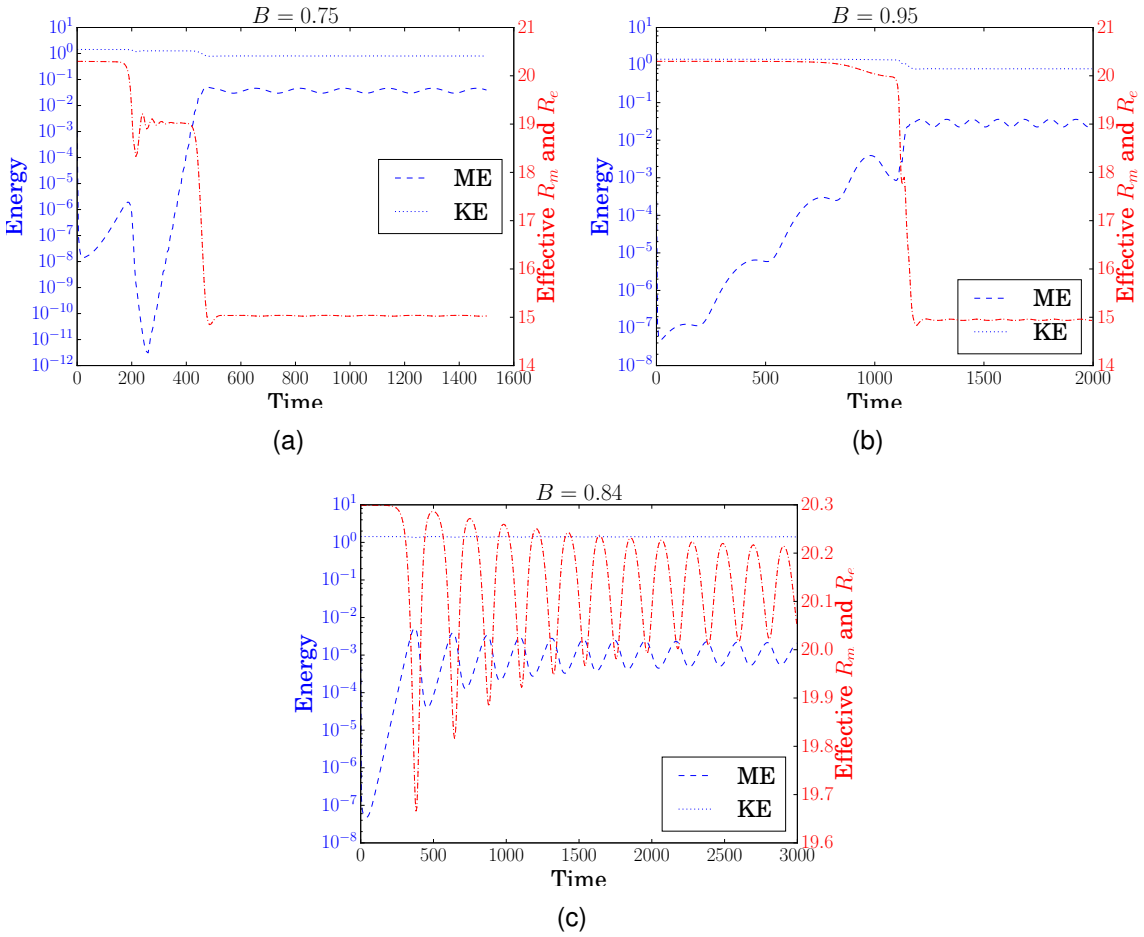

Figure 6.43: Energies (blue, left axis) and effective R_m and R_e (red, right axis) calculated in the same way as those for the 111 dynamo in section 6.5. We see that for the values where filamentary structures flatten a reduction in the Reynolds numbers occurs whereas a much smaller difference occurs for the others.

The simulations performed therefore provide evidence to suggest that where significant ME is produced during the kinematic phase of the ABC forced dynamo the result will be a ribbon-like magnetic field structure during the nonlinear regime. This coupled with the ribbon-like structures obtained within section 6.4 also suggest that ribbon structures seem to be the most natural structures formed by the magnetic field during the nonlinear regime in ABC forced dynamos at small R_m and R_e.

6.6.2 Ability of the Saturated State to Amplify a Seed Field

Within section 6.6.1 I examined the nonlinear dynamos driven by ABC forcings with stagnation points. These investigations were restricted to the parameter values $A = 1$ and $A > B = C$. I identified a number of different regimes as $B = C$ was varied, each with a

different magnetic energy behaviour. A number of the dynamos show oscillations within both of the energies upon saturation showing that once the magnetic energy has left its kinematic regime exchange of energy between the two fields via induction and the Lorentz force is playing a role in maintaining a statistically steady dynamo.

One question that we can ask is whether or not the flow is still capable of amplifying a seed magnetic field once the magnetic field has stopped growing. This then tells us whether the saturation mechanism works by stopping the flow from amplifying the magnetic field or whether the saturation is caused by something different for example a change in the magnetic field which alters its ability to be amplified by the flow. Furthermore as the flows have been altered, in varying amounts, from the original ABC flow there is no guarantee that the magnetic fields they generate will be filamentary.

I consider four of the five different cases from the previous section for $B = C$, which are $[0.75, 0.8, 0.84, 0.95]$. 0.88 is omitted due to the fact that the flow never changes significantly due to the weakness of the magnetic field. In each of these cases a number of different points are picked within the nonlinear regime (or at large time if this is not clearly present) of the dynamo. Where the flow oscillates the minima and maxima of the oscillations are examined to investigate whether their dynamo properties differ. The flow is then used as a prescribed flow within a kinematic calculation where the induction equation is timestepped. The flow is considered steady and is not evolved. The resolution of the simulation is fixed by the resolution used within the nonlinear calculations and so is 64^3 and an Adams-Bashforth:Adams-Moulton predictor-corrector scheme is employed for timestepping. To assess the structures of the magnetic fields produced I again use Minkowski Functions via Crofton's method, see section 6.2.1.

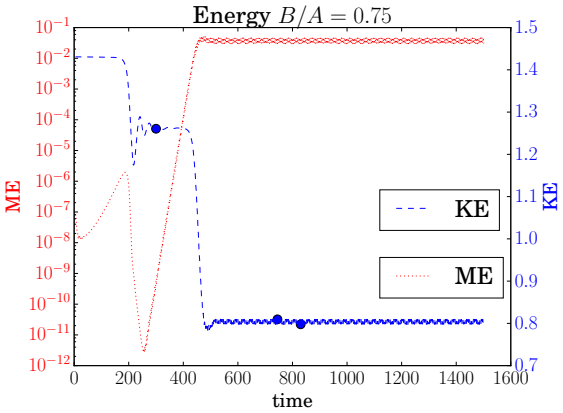

(a) $B/A = 0.75$

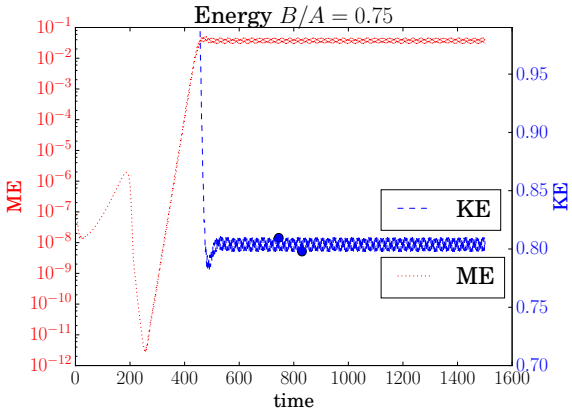

(b) $B/A = 0.75$ a zoom in to show the second and third points.

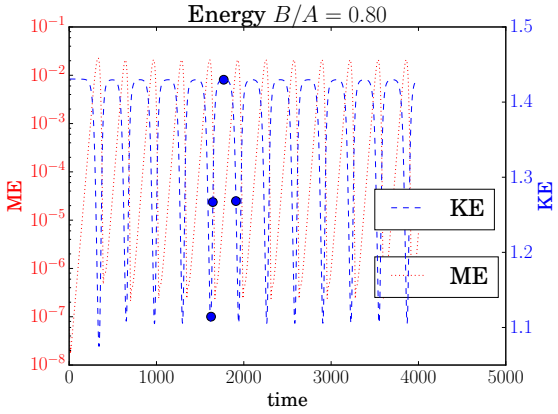

(c) $B/A = 0.80$

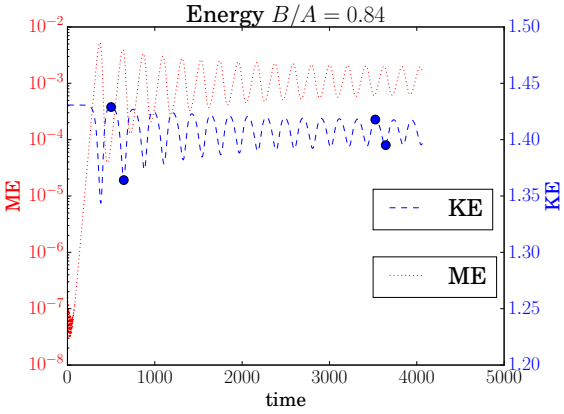

(d) $B/A = 0.84$

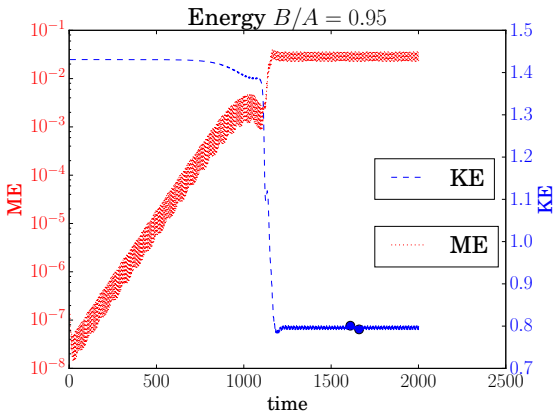

(e) $B/A = 0.95$

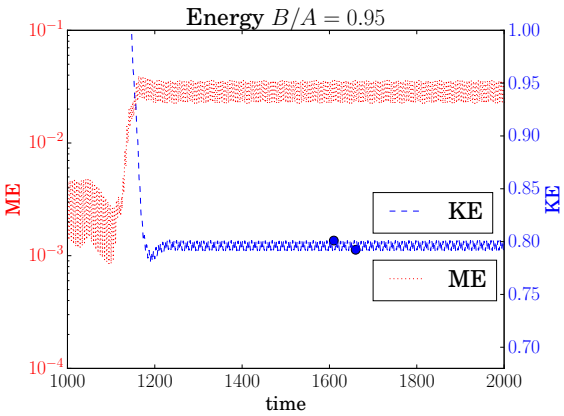

(f) $B/A = 0.95$. A zoom in to show the two points.

Figure 6.44: Kinetic and Magnetic energies for nonlinear dynamo simulations with various ratios of B/A. Large dots on the kinetic energy curves indicate snapshots in time where a flow is taken and used as the prescribed, steady, flow during a kinematic simulation.

In figure 6.44 I show the magnetic and kinetic energies within the nonlinear simulations for a variety of B/A. The dots shown on the kinetic energy curves indicate the times at which kinematic dynamo simulations were performed. For $B/A = 0.75$ kinematic simulations were run at 3 times; at $t = 300$ after the flow has first perturbed and then a maxima

($t = 745$) and minima ($t = 830$) of the oscillations during the final statistically steady state of the flow. For $B/A = 0.8$ kinematic simulations were performed at four points of the kinetic energy; a minima ($t = 1625$), a point where the kinetic energy is increasing ($t = 1645$) a maxima ($t = 1770$) and a point where the kinetic energy is decreasing ($t = 1910$). For $B/A = 0.84$ again four points are taken; a maxima and minima immediately proceeding saturation ($t = 500$ and $t = 645$) and a maxima and minima once the amplitude of the oscillations has reduced ($t = 3525$ and $t = 3645$). Finally for $B/A = 0.95$ kinematic simulations were performed at the maxima and minima of the oscillations ($t = 1610$ and $t = 1660$).

	Growth Rate	P	F	P/F
$B/A = 0.75\ t = 300$	0.065	0.35	0.53	0.67
$B/A = 0.75\ t = 745$	0.0039	0.19	0.38	0.5
$B/A = 0.75\ t = 830$	0.007	0.19	0.36	0.52
$B/A = 0.8\ t = 1625$	0.0018	0.5	0.15	3.3
$B/A = 0.8\ t = 1645$	0.0093	0.16	0.25	0.63
$B/A = 0.8\ t = 1770$	0.025	0.094	0.59	0.16
$B/A = 0.8\ t = 1910$	0.015	0.12	0.56	0.21
$B/A = 0.84\ t = 500$	0.014	0.11	0.58	0.19
$B/A = 0.84\ t = 645$	-0.00017	N/A	N/A	N/A
$B/A = 0.84\ t = 3525$	0.0047	0.11	0.58	0.19
$B/A = 0.84\ t = 3645$	-0.0015	N/A	N/A	N/A
$B/A = 0.95\ t = 1610$	0.0016	0.26	0.42	0.6
$B/A = 0.95\ t = 1660$	0.0056	0.14	0.39	0.37

Table 6.1: Table showing growth rate and Minkowski Functions of 40% isosurfaces of kinematic dynamo runs using flows from nonlinear dynamo runs.

Table 6.1 shows the results of the kinematic simulations. For $B/A = 0.75$ two things are evident. The first is that the growth rate at $t = 300$, where the flow has perturbed but not yet reached its final state, is much higher than it is in the saturated state. In looking at figure 6.44a we see that this is coinciding with rapid growth of the magnetic field and so a large kinematic growth rate is sensible. Furthermore the ratio of P/F is indicative of a ribbon-like structure of the magnetic field. The flow thus appears to have perturbed

to a form which drives a magnetic field which is ribbon-like, unlike the original flow which produces a filamentary magnetic field. Furthermore comparing this value to figure 6.41c which shows the ratio P/F for the nonlinear dynamo we see that the values are almost identical. As we have already seen that nonlinear dynamos forced by ABC flows without stagnation points change very little upon saturation the two being comparable again makes sense if we assume that, as was the case for $B/A = 1$, the perturbed flow (at $t = 300$) is close to a no stagnation point ABC flow. Once saturation of the dynamo has occurred we see that the new flow does not amplify a seed field very well at all and a reduced P/F is seen with the new value being somewhere between filamentary and ribbon-like.

For $B/A = 0.8$ the evolution of the magnetic and fluid fields within the nonlinear simulation plays an important role in dictating the properties of the flow which is then used within the kinematic simulations. The energies are shown in figure 6.44c where the four points used within the kinematic simulations are also shown as dots. Looking at this and table 6.1 the following picture emerges. As we increase from a minima of the kinetic energy to the maxima the growth rate of the corresponding kinematic simulation increases. The growth rate is therefore maximal at the peak of the kinetic energy, which also corresponds to a minima of the magnetic energy within the nonlinear simulations. The growth rates that we see within table 6.1 therefore show that the flow goes through a process of restructuring to better amplify magnetic field as a maxima of the kinetic energy approaches. Furthermore the corresponding Minkowski Functions show that as we approach a maxima of kinetic energy the corresponding magnetic field from the kinematic simulation becomes increasingly filamentary. Correspondingly a marginally pancake like structure is produced at the minima of the kinetic energy.

For $B/A = 0.84$ (energies shown in figure 6.44d) the same behaviour is seen initially after saturation and close to the end of the run. We see that at the minimas of kinetic energy the growth rate is negative and so the flow does not amplify a seed field and at the maximas the growth rate is positive, with it being more positive immediately proceeding saturation. We also see that the Minkowski Functions are filamentary at the maxima. Any analysis of the Minkowski Functions where the growth rate is negative is problematic due to the weak

magnetic field so they are not calculated. Comparing the results to the maxima and minima of the kinetic energies of the $B/A = 0.8$ runs we see that in both cases the largest growth rates arise at maxima of kinetic energies and that here the B/A correspond to filamentary magnetic fields thus they share common traits.

For $B/A = 0.95$ both a minima and maxima of oscillations in the kinetic energy were examined to look at their kinematic properties. As was seen in the investigation of their nonlinear dynamo properties $B/A = 0.95$ and $B/A = 0.75$ share many similarities. In particular we see that the growth rate at the minima of the kinetic energy is much larger than the maxima although both are weak. The growth rate being strongest at the minima of the kinetic energy is opposite to that seen for the 0.8 and 0.84 cases. Finally the Minkowski Functions show the magnetic field to be marginally filamentary.

Examination of kinematic simulations using flows from the nonlinear regime of ABC forced dynamos has yielded a number of results. The first is that, as was the case with the nonlinear results, the results should be divided in two, with 0.75 and 0.95 being considered together and 0.8 and 0.84 being broadly considered together. This split appears to be defined by which flows were altered by the magnetic field before the kinematic simulations were performed. Where the magnetic field is significant (0.75 and 0.95) we observe that the growth rate is extremely small within the nonlinear regime of the dynamo. The Minkowski Functions indicate the magnetic field to be filamentary however it is close to being ribbon-like. For the cases where the magnetic energy is small we see within 0.8 a smooth transition in behaviour as the kinetic energy increases to one of its periodic maxima. We observe the flow becoming a better amplifier of seed magnetic field and this field becoming increasingly filamentary as we approach the maxima. For $B/A = 0.84$ we observe negative as well as positive growth rates. The positive growth rates correspond to minima of ME and thus indicate that the flow has reformed so as to amplify the magnetic field and bring the energy back to a maxima. During this process within the nonlinear run the flow properties then change again, halting the flow's ability to amplify magnetic field and causing the magnetic energy to decrease again. The periodic nature of the oscillations in the energy curves indicate that this alteration to the properties of the flow occurs in

a periodic fashion but decreases in its intensity the longer the saturated regime continues.

6.7 Discussion of Nonlinear ABC Dynamo Results

In this section I refer back to the aims outlined at the beginning of the chapter and highlight what has been shown within the section. I then highlight possible avenues of future research.

- **To examine the suitability of the 522 flow as a nonlinear dynamo.**

  I have shown that the 522 forcing produces a nonlinear dynamo with a saturated magnetic energy regime. The ME becomes comparable in size to the KE for $P_m > 1$ and the magnetic field structure is ribbon-like. Furthermore I have shown that the energy growth occurs in the regions of weak magnetic field due to the reduced $\mathbf{B} \cdot \nabla^2 \mathbf{B}$ in these regions.

- **To examine whether the flattening of magnetic field structures is a broad feature of nonlinear stagnation point ABC dynamos.**

  I have performed a number of numerical simulations for nonlinear ABC dynamos with $B = C$ and which have stagnation points in their forcings. I have shown that when the ME is comparable in magnitude to the KE flattening of the magnetic field structures occurs. If the ME remains weak or never reaches a saturated regime the magnetic field remains filamentary.

- **To compare the magnetic field morphologies (in the saturated regime) of the 522 and 111 dynamos**.

  In examining the 111 dynamo I found a transition to ribbon-like structures upon entering the saturated regime. I find a reduction in the effective R_m in agreement with that found by Galanti et al. [37] and link the flattening of the magnetic field structures to the result by Podvigina and Pouquet [84].

  More broadly I find that all ABC forced nonlinear dynamos which produce significant

magnetic energy in a nonlinear regime produce ribbon-like magnetic field structures. This suggests that these may be the most common magnetic field structures during the nonlinear regime of ABC forced dynamos. The flattening of filaments observed for dynamos with stagnation point forcings hints at this being a possible saturation mechanism.

- **To examine how magnetic field structures change when a dynamo saturates**.

  I have shown that for ABC forced dynamos with ribbon-like magnetic field structures the morphology does not change dramatically upon saturation. I have however shown that for some values of η in the 522 dynamo a periodic stretching of these ribbons occurs, however they remain ribbon-like. For filamentary magnetic field structures saturation has been shown to correspond to flattening to ribbons.

- **To apply morphology tools (the Minkowski Functions) to nonlinear dynamos to quantify structure changes in the magnetic field.**

  I have used Minkowski Functions to examine the magnetic field structure for a variety of dynamos. The functions successfully highlight large changes to field structure (for example going from filaments to ribbons) and also highlight where periodic stretching of the magnetic field occurs (see the work on the 522 dynamo). The limitation on them I have found however is in using the numbers obtained to attach a label of "ribbon", "pancake" or "filament" to a particular structure. For example $P = 0.1$ and $F = 0.8$ is clearly a filament and $P = 0.75$, $F = 0.8$ is a ribbon but at what value of P do we say this change occurs? The Minkowski Functions work particularly well in examining changes to the field structure however the attaching of a label becomes somewhat subjective which is unfortunate as the original aim of their use was to remove the subjective element of examining structure. On the whole however I believe their use has been successful and that they are a viable alternative, and complement to, 3D visualisation techniques.

There are a number of natural extensions to the research within this chapter. The first is to examine the general properties of no stagnation point forced ABC dynamos in a similar

manner to how I have studied the stagnation point forced ABC dynamos with the aim of seeing if ribbons are the predominant magnetic field features during the nonlinear regime. Secondly, due to time and computational restraints I have had to examine a small number of the possible parameter values for ν, η, A, B and C. It would be interesting to see how the structures change with increasing and decreasing magnetic and fluid diffusivity. Finally, the Minkowski Functions could be used to examine structure changes in the magnetic field in more complex simulations with additional features such as rotation and for more complex geometries. The aim for these would then be to examine whether filamentary structures formed as the magnetic field grows flatten when the dynamo saturates.

Chapter 7

References

1. E.Abbena, S.Salamon and A.Gray(2006), *"Modern Differential Geometry of Curves and Surfaces with Mathematica, Third Edition"*, Boca Raton Florida: Chapman and Hall.

2. A.Alexakis(2011), *"Nonlinear dynamos at infinite magnetic Prandtl number"*, Physical Review E, 83.

3. A.Alexakis(2011), *"Searching for the fastest dynamo: Laminar ABC flows"*, Physical Review E, 84.

4. V.Archontis and B.Dorch(1999), *"Numerical simulations of Dynamos Associated with ABC Flows"*,
   Workshop on Stellar Dynamos
   Asp Conference Series, Vol.178
   Editors: M.Nunez and A.Ferriz-Mas.

5. V.Archontis, S.B.F.Dorch and A.Nordlund(2003), *"Dynamo action in turbulent flows "*, Astronomy and Astrophysics, 410, 759-766.

6. V.Archontis, S.B.F.Dorch and A.Nordlund(2003), *"Numerical simulations of kinematic dynamo action"*, Astronomy and Astrophysics, 397, 393-399.

7. V.Archontis, S.B.F.Dorch and A.Nordlund(2007), *"Nonlinear MHD dynamo operating at equipartition"*, Astronomy and Astrophysics, 472, 715-726.

8. V.Archontis(2000), *"Linear, non-linear and turbulent dynamos"*, PhD thesis, University of Copenhagen.

9. V.I. Arnold(1965), *"Sur la topologie des écoulements stationnaires des fluides parfaits"*, Comptes Rendus, 261, 17-20.

10. V.I.Arnold and I.E.Korkina(1983), *"The growth of a magnetic field in a three-dimensional steady incompressible flow"* (in Russian), Vest. Mosk. Un. Ta. Ser 1 Matematika Mecanika, 43-46, (1983,3).

11. B.Bavassano and R.Bruno(1989), *"Large scale solar wind fluctuations in the inner heliosphere at low solar activity"*, J. Geophys. Research, 94, A1, 168-176.

12. J.W.Belcher and L.Davis, JR(1971), *"Large-Amplitude Alfvén Waves in the Interplanetary Medium,2"*, J. Geophys. Research, 76, 16, 3534-3563.

13. A.Beresnyak and A.Lazarian(2008), *"Strong Imbalanced Turbulence"*, The Astrophysical Journal, 682.

14. A.Beresnyak and A.Lazarian(2010), *"Scaling Laws and Diffuse Locality of Balanced and Imbalanced Magnetohydrodynamic Turbulence"*, The Astrophysical Journal, 722.

15. A.Beresnyak(2012), *"Basic properties of magnetohydrodynamic turbulence in the inertial range"*, Mon. Not. R.Astron. Soc, 422, 3495-3502.

16. S.Boldyrev(2005), *"On the Spectrum of Magnetohydrodynamic Turbulence"*, The Astrophysical Journal, 626.

17. S.Boldyrev(2006), *"Spectrum of Magnetohydrodynamic Turbulence"*, Phys. Rev. Lett., 96.

18. S.Boldyrev, J.Mason and F.Cattaneo(2009), *"Dynamic Alignment and Exact Scaling Laws in Magnetohydrodynamic Turbulence"*, The Astrophysical Journal, 699.

19. I.Bouya and E.Dormy(2013), *"Revisiting the ABC flow dynamo"*, Physics of Fluids, 25.

20. I.Bouya and E.Dormy(2015), *"Towards an asymptotic behaviour of the ABC dynamo"*, EPL, 110.

21. N.H.Brummell, F.Cattaneo, S.M.Tobias(1998), *"Linear and nonlinear dynamo action"*, Physics Letters A, 249, 437-442.

22. R.Cameron and D.Galloway(2006), *"Saturation properties of the Archontis dynamo"*, Mon. Not. R. Astron. Soc., 365, 735-746.

23. R.Cameron and D.Galloway(2006), *"High field strength modified ABC and Rotor Dynamos"*, Mon. Not. R. Astron. Soc., 367, 1163-1169.

24. F.Cattaneo, D.W.Hughes and E.Kim(1996), *"Suppression of Chaos in a Simplified Nonlinear Dynamo Model"*, Phys. Rev. Lett., 76, 12.

25. F.Cattaneo and S.M.Tobias(2009), *"Dynamo properties of the turbulent velocity field of a saturated dynamo"*, J. Fluid Mech., 621, 205-214.

26. B.D.G.Chandran(2008), *"Strong Anisotropic MHD Turbulence with Cross-Helicity "*, The Astrophysical Journal, 685, 646-658.

27. P.Charbonneau(2013),*"Solar and Stellar Dynamos"*, Berlin Heidelberg: Springer Verlag.

28. S.Childress(1970), *"New solutions of the kinematic dynamo problem"*, J. Math. Phys., 11, 3063-3076.

29. S.Childress and A.D.Gilbert(1995), *"Stretch, Twist, Fold: The Fast Dynamo"*, Berlin Heidelberg:Springer-Verlag.

30. A.Courvoisier, A.D.Gilbert and Y.Ponty(2005), *"Dynamo action in flows with cat's eyes"*, Geophys. Astrophys. Fluid Dyn. , 99, 413-429.
http://www.tandfonline.com

31. A.Courvoisier(2006), *"Dynamo Action and the Generation of Large-Scale Magnetic Fields in Astrophysics"*, PhD thesis, University of Leeds.

32. V.Dallas and A.Alexakis(2015), *"Self-organisation and non-linear dynamics in driven magnetohydrodynamic turbulent flows"*, Physics of Fluids, 27, 4.

33. M.Dobrowolny, A.Mangeney and P.Veltri(1980),*" Fully Developed Anisotropic Hydromagnetic Turbulence in Interplanetary Space"*, Phys. Rev. Lett., 45, 2, 144-147.

34. T.Dombre, U.Frisch, J.M.Greene, M.Henon, A.MEHR and A.M.Soward(1986), *"Chaotic streamlines in ABC flows"*, J. Fluid Mech. , 167.

35. S.B.F.Dorch(2000), *"On the Structure of the Magnetic Field in a Kinematic ABC Flow Dynamo"*, Physica Scripta, 61, 717-722.

36. S.B.F.Dorch and V.Archontis(2004), *"On The Saturation Of Astrophysical Dynamos: Numerical Experiments With The No-Cosines Flow"*, Solar Physics, 224, 171-178.

37. B.Galanti, P.L.Sulem and A.Pouquet(1992), *"Linear and Non-Linear Dynamos Associated with ABC Flows"*, Geophys. Astrophys. Fluid Dyn., 66, 183-208.
http://www.tandfonline.com

38. D.J.Galloway(2003),*"Fast dynamos"*,
Advances in Nonlinear Dynamos.
The Fluid Mechanics of Astrophysics and Geophysics.
Editors: A.Ferriz-Mas and M.Nunez.

39. D.J.Galloway(2011), *"Nonlinear Dynamos"*,
Astrophysical Dynamics: From Stars to Galaxies.
Proceedings IAU Symposium No. 271, 2010.
Editors: N.H.Brummell, A.S. Brun, M.S.Miesch and Y.Ponty.

40. D.Galloway(2012), *"ABC flows then and now"*, Geophys. Astrophys. Fluid Dyn., 106, 450-467.

41. D.Galloway and U.Frisch(1984), *"A numerical investigation of magnetic field generation in a flow with chaotic streamlines"*, Geophys. Astrophys. Fluid Dyn., 29, 13-18.

42. D.Galloway and U.Frisch(1986), *"Dynamo action in a family of flows with chaotic streamlines"*, Geophys. Astrophys. Fluid Dyn., 36, 53-83.

43. D.Galloway and U.Frisch(1987), *"A note on the stability of a family of space-periodic Beltrami flows"*, J.Fluid Mech., 180.

44. D.J.Galloway and N.R.O'Brian(1994), *"Numerical Calculations of Dynamos for ABC and Related Flows"*,
Solar and Planetary Dynamos, pp. 105-111.
Cambridge: Cambridge University Press.
M.R.E.Proctor, P.C.Matthews and A.M.Rucklidge.

45. D.J.Galloway and M.R.E.Proctor(1992), *"Numerical calculations of fast dynamos in smooth velocity fields with realistic diffusion"*, Nature, 356, 691-693.

46. A.D.Gilbert(1988),*"Fast Dynamo Action In the Ponomarenko Dynamo"*, Geophys. Astrophys. Fluid Dyn., 44, 241-258.

47. A.D.Gilbert(1991), *"Fast dynamo action in a steady chaotic flow"*, Nature, 350.

48. A.D.Gilbert, Y.Ponty and V.Zheligovsky(2011), *"Dissipative structures in a nonlinear dynamo"*, Geophys. Astrophys. Fluid Dyn., 105, 629-653.

49. L.Gleser, A.Nusser, B.Ciardi and V.Desjacques(2006), *"The morphology of cosmological reionization by means of Minkowski functionals"*, Mon. Not. R. Astron. Soc., 370, 1329-1338.

50. P.Goldreich and S.Sridhar(1995), *"Towards a Theory of Interstellar Turbulence II. Strong Alfvénic Turbulence"*, The Astrophysical Journal, 438, 763-775.

51. B.E.Goldstein, E.J.Smith, A.Balogh, T.S.Horbury, M.L.Goldstein and D.A.Roberts(1995), *Properties of magnetohydrodynamic turbulence in the solar wind as observed by Ulysses at high heliographic latitudes*, Geophys Research Letters, 22, 23, 3393-3396.

52. R.Grappin, U.Frisch, J.Leorat and A.Pouquet(1982), *"Dependence of MHD turbulence spectra on the velocity field-magnetic field correlation"*, Astronomy and Astrophysics, 105, 6-14.

53. R.Grappin, A.Pouquet and J.Leorat(1983), *"Alfvénic Fluctuations as Asymptotic States of MHD Turbulence"*, Astronomy and Astrophysics, 105, 6-14.

54. D.H.Hathaway and L.Upton(2018), *"Discover the Solar Cycle!"*, Available at: `http://solarcyclescience.com/solarcycle.html`, Date Accessed: 30/08/2018.

55. D.W.Hughes, F.Cattaneo and E.Kim(1996), *"Kinetic helicity, magnetic energy and fast dynamo action"*, Physics Letters A, 223, 167-172.

56. P.S.Iroshnikov(1964), *"Turbulence of a Conducting Fluid in a Strong Magnetic Field"*, Soviet Astronomy, 7, 4.

57. S.E.Jones(2013), *"Symmetries in the Kinematic Dynamos and Hydrodynamic Instabilities of the ABC flows"*, PhD thesis, University of Exeter.

58. S.E.Jones and A.D.Gilbert(2014), *"Dynamo action in the ABC flows using symmetries"*, Geophys. Astrophys. Fluid Dyn., 108.

59. R.H.Kraichnan(1965), *"Inertial-Range Spectrum of Hydromagnetic Turbulence"*,Physics of Fluids, 8, 7.

60. Y.lithwick, P.Goldreich and S.Sridhar(2007), *" Imbalanced Strong MHD Turbulence"*, The Astrophysical Journal, 655, 269-274.

61. J.Maron and P.Goldreich(2001), *"Simulations of Incompressible Magnetohydrodynamic Turbulence"*, The Astrophysical Journal, 554, 1175-1196.

62. J.Mason, F.Cattaneo and S.Boldyrev(2006), *"Dynamic Alignment in Driven Magnetohydrodynamic Turbulence"*, Phys. Rev. Lett., 97, 255002.

63. J.Mason, F.Cattaneo and S.Boldyrev(2008), *"Numerical Measurements of the spectrum in magnetohydrodyamic turbulence"*, Phys. Rev. E, 77.

64. J.Mason, J,C.Perez,F.Cattaneo and S.Boldyrev(2011), *"Extended Scaling Laws in Numerical Simulations of Magnetohydrodynamic Turbulence"*, The Astrophysical Journal Letters, 735.

65. W.H.Matthaeus and D.Montgomery(1980), *"SELECTIVE DECAY HYPOTHESIS AT HIGH MECHANICAL AND MAGNETIC REYNOLDS NUMBERS"*, Annals of the New York Academy of Sciences, 357,1, 203-222.

66. W.H.Matthaeus and M.L.Goldstein(1982), *"Measurement of the Rugged Invariants of Magnetohydrodynamic Turbulence in the Solar Wind"*, J. Geophysical Research, 87, 6011-6028.

67. W.H.Matthaeus, M.L.Goldstein and D.C.Montgomery(1983), *"Turbulent Generation of Outward-Traveling Interplanetary Alfvénic Fluctuations"*, Phys. Rev. Lett., 51, 16.

68. W.H.Matthaeus, J.Minnie, B.Breech, S.Parhi, J.W.Bieber and S.Oughton(2004), *"Transport of cross helicity and radial evolution of Alfvénicity in the solar wind"*, Geophys Research Letters, 31, L12803.

69. W.H.Matthaeus, A.Pouquet, P.D.Mininni, P.Dmitruk and B.Breech(2008), *"Rapid Alignment of Velocity and Magnetic Field in Magnetohydrodynamic Turbulence"*, Phys. Rev. Lett., 100.

70. W.H.Matthaeus, D.C.Montgomery, M.Wan and S.Servidio(2012), *"A review of relaxation and structure in some turbulent plasmas: magnetohydrodynamics and related models"*, Journal of Turbulence, 13.

71. W.H.Matthaeus, M.Wan, S.Servidio, A.Greco, K.T.Osman, S.Oughton and P.Dmitruk(2015), *"Intermittency, nonlinear dynamics and dissipation in the solar wind and astrophysical plasmas"*, Philosophical Transactions Of The Royal Society A, 373.

72. M.E.McKay, M.Linkmann, D.Clark, A.A.Chalupa and A.Berera(2017), *"Comparison of forcing functions in magnetohydrodynamics"*,Physical Review Fluids, 2, 11.

73. D.Miller(2018),*"Alignment as an Indicator of Changes to Modal Structure within the Roberts Flow"*,
Space Weather of the Heliosphere: Processes and Forecasts.
Proceedings of the International Astronomical Union, IAU Symposium, Volume 335, pp.26-28.
Editors: C.Foullon and O.E.Malandraki.

74. H.K.Moffatt(1969), *"The degree of knottedness of tangled vortex lines"*, J. Fluid Mech., 35, 117-129.

75. H.K.Moffatt(1978), *"Magnetic Field Generation in Electrically Conducting Fluids"*, Cambridge: Cambridge University Press.

76. H.K.Moffatt and M.R.E.Proctor(1985), *"Topological constraints associated with fast dynamo action"*, J. Fluid Mech., 154, 493-507.

77. W.C.Muller, D.Biskamp and R.Grappin(2003), *"Statistical anisotropy of magnetohydrodynamic turbulence"*, Phys. Rev E, 67.

78. N.F.Otani(1993), *"A fast kinematic dynamo in two-dimensional time-dependent flows"*, J. Fluid Mech., 253, 327-340.

79. J.C.Perez and S.Boldyrev(2009), *"Role of Cross-Helicity in Magnetohydrodynamic Turbulence"*, Phys. Rev. Lett., 102.

80. J.C.Perez and S.Boldyrev(2010), *"Strong magnetohydrodynamic turbulence with cross helicity"*, Physics of Plasmas, 17, 5.

81. J,C.Perez,J.Mason,S.Boldyrev and F.Cattaneo(2012), *"On the Energy Spectrum of Strong Magnetohydrodynamic Turbulence"*, Physical Review X, 2.

82. J.J.Podesta and A.Bhattacharjee(2010), *"Theory of Incompressible MHD Turbulence with Scale-Dependent Alignment and Cross-Helicity"*, The Astrophysical Journal, 718, 2.

83. J.J.Podesta, A.Bhattacharjee, B.D.G.Chandran, M.L.Goldstein and D.A.Roberts(2008), *"Scale dependent alignment between velocity and magnetic field fluctuations in the solar wind and comparisons to Boldyrev's phenomenological theory"*,
Particle acceleration and Transport in the Heliosphere and Beyond.
7th Annual Astrophysics conference.
Editors: G.Li, Q.Hu, O.Verkhoglyadova, G.P.Zank, R.P.Lin and J.Luhmann.

84. O.Podvigina and A.Pouquet(1994), *"On the non-linear stability of the 1:1:1 ABC flow"*, Physica D, 471-508.

85. A.Pouquet, M.Meneguzzi and U.Frisch(1986), *"Growth of correlations on magneto-hydrodynamic turbulence"*, Phys. Rev A, 33, 6.

86. A.Pouquet(2012), *"A review of the possible role of constraints in MHD turbulence"*, Reviews of the Theory of Magnetized Plasmas: Volume 2 Rotation and Momentum Transport in Magnetized Plasmas.
Chapter 2, pp.45-79.
Editors: P.H.Diamond, X.Garbet, P.Ghendrih and Y.Sarazin.

87. E.Priest(2014), *"Magnetohydrodynamics of the Sun"*, New York: Cambridge University Press.

88. M.R.E.Proctor and A.D.Gilbert(1994), *"Lectures on Solar and Planetary Dynamos"*, Great Britain, Cambridge University Press.

89. G.O.Roberts(1972), *"Dynamo Action of Fluid Motions with Two-Dimensional Periodicity"*, Philosophical Transactions Of The Royal Society A, 271, 1216, 411-454.

90. D.A.Roberts, M.L.Goldstein, L.W.Klein and W.H.Matthaeus(1987), *"Origin and evolution of fluctuations in the solar wind: Helios observations and Helios-Voyager Comparisons"*, J. Geophys Research, 92, A11, 12, 023-12, 035.

91. D.A.Roberts, M.L.Goldstein, W.H.Matthaeus and S.Ghosh(1992), *"Velocity Shear Generation of Solar Wind Turbulence"*, J. Geophys Research, 97, A11, 17, 115-117.

92. A.Ruzmaikin, D.Sokoloff and A.Shukurov(1988),*"Hydromagnetic screw dynamo"*, J. Fluid Mech., 197, 39-56.

93. V.Sahni, B.S.Sathyaprakash and S.F.Shandarin(1998), *"Shapefinders: A new shape diagnostic for large-scale structure"*, The Astrophysical Journal, 495.

94. J.Schmalzing and T.Buchert(1997), *"Beyond Genus Statistics: A Unifying Approach to the Morphology of Cosmic Structure"*, The Astrophysical Journal, 482.

95. S.Servidio, W.H.Matthaeus and P.Dmitruk(2008), *"Depression of Nonlinearity in Decaying Isotropic MHD turbulence"*, Phys. Rev. Lett., 100.

96. S.Servidio, C.Gurgiolo, V.Carbone and M.L.Goldstein(2014), *"Relaxation processes in solar wind turbulence"*, The Astrophysical Journal Letters, 789, L44.

97. A.Seta, P.J.Bushby, A.Shukurov and T.S.Wood(2018),*"Nonlinear states of fluctuation dynamo"*, Manuscript in preparation.

98. V.Shumaylova, R.J.Teed and M.R.E.Proctor(2017), *"Large- to small-scale dynamo in domains of large aspect ratio: kinematic regime"*, MNRAS, 466.

99. A.M.Soward(1987), *"Fast dynamo action in a steady flow"*, J. Fluid Mech., 180, 267-295.

100. A.M.Soward(1990),*"A unified approach to a class of slow dynamos"*, Geophys. Astrophys. Fluid Dyn., 53, 81-107.

101. O.Steiner and A.Ferriz-Mas(2005),*"Connecting solar radiance variability to the solar dynamo with the virial theorem"*, Astron. Nachr, 326, 190-193.

102. T.Stribling and W.H.Matthaeus(1990), *"Statistical properties of ideal three-dimensional magnetohydrodynamics"*, Phys. Fluids B, 2, 9.

103. T.Stribling and W.H.Matthaeus(1991), *"Relaxation processes in a low order three-dimensional magnetohydrodynamics model"*, Phys. Fluids B, 3, 8.

104. A.Tilgner, A.Brandenburg(2008), *"A growing dynamo from a saturated Roberts flow dynamo"*, Mon. Not. R. Astron. Soc., 391, 1477-1481.

105. A.C.Ting, W.Matthaeus and D.Montgomery(1986), *"Turbulent relaxation processes in magnetohydrodynamics"*, Phys. Fluids, 10.

106. N.Weiss(2001), *"Turbulent magnetic fields in the Sun"*, Astronomy and Geophysics, 42, 3

107. J.M.Weygand, W.H.Matthaeus, S.Dasso, M.G.Kivelson and R.J.Walker(2007), *"Taylor scale and effective magnetic Reynolds number determination from plasma sheet and solar wind magnetic field fluctuations"*, Jorunal of Geophysical Research, 112.

108. S.L.Wilkin(2006),*"Magnetic Structures produced by the Fluctuation Dynamo"*, PhD thesis, Newcastle University.

109. S.L.Wilkin, C.Barenghi and A.Shukarov(2007), *"Magnetic structures produced by the small scale dynamo"*, Phys. Rev. Lett., 99.

110. O.Zheligovsky and A.Pouquet(1994), *"Hydrodynamic Stability of the ABC Flow"* Solar and Planetary Dynamos, pp. 347-354.
Cambridge:Cambridge University Press.
M.R.E.Proctor, P.C.Matthews and A.M.Rucklidge.

Appendix A

Proofs of Anti-Dynamo Theorems and Bounds on R_m

In this appendix I prove the anti-dynamo theorems and bounds on dynamo action that are stated in chapter 1.

A.1 Impossibility of Maintaining $\mathbf{B}(x,y,t)$ by Dynamo Action

A magnetic field that vanishes at infinity, is of the form $(B_x(x,y,t),B_y(x,y,t),B_z(x,y,t))$ in a cartesian geometry and is driven by an incompressible flow cannot be maintained by dynamo action.

The first thing to note is that if the driving flow $\mathbf{u}$ had a dependence on z then due to the induction equation being a function of $\mathbf{u}$ the magnetic field would also depend upon z. It must therefore be true that the flow field driving the evolution of the magnetic field is of the form $(u_x(x,y,t),u_y(x,y,t),u_z(x,y,t))$. Of course it is not generally true that having a flow field independent of z yields a magnetic field independent of z. It can in fact be shown that magnetic fields generated by dynamo action involving a driving flow of the form $\mathbf{u}=\mathbf{u}(x,y,t)$ are of the form $\mathbf{B}=\mathbf{b}(x,y,t)e^{ik_z z}$.

As neither the flow or the magnetic field are functions of z and $\nabla\cdot\mathbf{u}=\nabla\cdot\mathbf{B}=0$ a poloidal-

toroidal decomposition may be introduced.

$$\mathbf{B} = \mathbf{B}_T + \mathbf{B}_P \tag{A.1}$$

$$= \nabla \times (A(x,y,t)\hat{\mathbf{z}}) + B(x,y,t)\hat{\mathbf{z}} \tag{A.2}$$

$$\mathbf{u} = \mathbf{u}_T + \mathbf{u}_P \tag{A.3}$$

$$= \nabla \times (\psi(x,y,t)\hat{\mathbf{z}}) + w(x,y,t)\hat{\mathbf{z}} \tag{A.4}$$

where we also impose the Coulomb gauge $\nabla \cdot \mathbf{A} = 0$ as else we could simply add the gradient of any scalar onto $\mathbf{A}$. Thus the advection term of the induction equation may be decomposed

$$\nabla \times (\mathbf{u} \times \mathbf{B}) = \nabla \times \Big((\mathbf{u}_T + \mathbf{u}_P) \times (\mathbf{B}_T + \mathbf{B}_P) \Big) \tag{A.5}$$

$$\mathbf{u}_T \times \mathbf{B}_T = \big[(-\partial_x A)(\partial_y \psi) + (\partial_y A)(\partial_x \psi) \big] \hat{\mathbf{z}} \tag{A.6}$$

$$\nabla \times (\mathbf{u}_T \times \mathbf{B}_T) = F_{11}(x,y,t)\hat{\mathbf{x}} + F_{12}(x,y,t)\hat{\mathbf{y}} \tag{A.7}$$

$$\mathbf{u}_P \times \mathbf{B}_P = \mathbf{0} \tag{A.8}$$

$$\mathbf{u}_P \times \mathbf{B}_T = w(\partial_x A)\hat{\mathbf{x}} + w(\partial_y A)\hat{\mathbf{y}} \tag{A.9}$$

$$\nabla \times \big(\mathbf{u}_P \times \mathbf{B}_T \big) = F_2(x,y,t)\hat{\mathbf{z}} \tag{A.10}$$

$$\mathbf{u}_T \times \mathbf{B}_P = -(\partial_x \psi) B \hat{\mathbf{x}} - (\partial_y \psi) B \hat{\mathbf{y}} \tag{A.11}$$

$$\nabla \times \big(\mathbf{u}_T \times \mathbf{B}_P \big) = F_3(x,y,t)\hat{\mathbf{z}} \tag{A.12}$$

where F_{11}, F_{12}, F_2 and F_3 are introduced to show, in a way that is easy to read, which terms are toroidal and which terms are poloidal once the curl is taken. Thus the induction equation may be decomposed into

$$\frac{\partial}{\partial t}(B\hat{\mathbf{z}}) = \nabla \times (\mathbf{u}_P \times \mathbf{B}_T + \mathbf{u}_T \times \mathbf{B}_P) + \eta \nabla^2 (B\hat{\mathbf{z}}) \tag{A.13}$$

$$\frac{\partial}{\partial t}(\mathbf{B}_T) = \nabla \times (\mathbf{u}_T \times \mathbf{B}_T) + \eta \nabla^2 (\mathbf{B}_T) \tag{A.14}$$

The induction equation can therefore be decomposed into two equations, one describing how the toroidal component of the magnetic field evolves

$$\nabla \times \frac{\partial (A\hat{\mathbf{z}})}{\partial t} = \nabla \times (\mathbf{u}_T \times \mathbf{B}_T + \eta \nabla^2 (A\hat{\mathbf{z}})) \tag{A.15}$$

and one describing how the poloidal component of the magnetic field evolves

$$\frac{\partial}{\partial t}(B\hat{\mathbf{z}}) = \nabla \times (\mathbf{u}_P \times \mathbf{B}_T + \mathbf{u}_T \times \mathbf{B}_P) + \eta \nabla^2 (B\hat{\mathbf{z}}) \tag{A.16}$$

uncurling equation (A.15) yields

$$\frac{\partial (A\hat{\mathbf{z}})}{\partial t} = \mathbf{u}_T \times \mathbf{B}_T + \eta \nabla^2 (A\hat{\mathbf{z}}) + \nabla \phi \tag{A.17}$$

a simple expansion and rearrangement of $\mathbf{u}_T \times \mathbf{B}_T$ yields $\mathbf{u}_T \times \mathbf{B}_T = -(\mathbf{u}_T \cdot \nabla)(A\hat{\mathbf{z}})$ thus allowing equation (A.15) to be written as the scalar equation

$$\frac{\partial A}{\partial t}\hat{\mathbf{z}} + (\mathbf{u}_T \cdot \nabla) A\hat{\mathbf{z}} = \eta \nabla^2 A\hat{\mathbf{z}} + \nabla \phi \tag{A.18}$$

Now I take the dot product of (A.18) with $A\hat{\mathbf{z}}$ and use vector calculus to rearrange it to a suitable form

$$\frac{\partial}{\partial t}\frac{A^2}{2} + \nabla \cdot \left(\frac{A^2 \mathbf{u}_T}{2} \right) = A\eta \nabla^2 A + \nabla \cdot (\mathbf{A}\phi) \tag{A.19}$$

Equation (A.19) can be rearranged using the identity $\nabla \cdot (A\nabla A) = A\nabla^2 A + (\nabla A)^2$ to give

$$\frac{\partial}{\partial t}\frac{A^2}{2} + \nabla \cdot \left(\frac{A^2 \mathbf{u}_T}{2} \right) = \eta (\nabla \cdot (A\nabla A) - (\nabla A)^2) + \nabla \cdot (\mathbf{A}\phi) \tag{A.20}$$

thus, rearranging and integrating over a fixed volume and interchanging the time derivative with the volume integral yields

$$\frac{d}{dt}\int_V \frac{A^2}{2} dV = \int_V \nabla \cdot \left(\eta A \nabla A - \frac{A^2 \mathbf{u}_T}{2} \right) dV - \eta \int_V (\nabla A)^2 dV + \int_V \nabla \cdot (\mathbf{A}\phi) dV \tag{A.21}$$

$$= \int_S \mathbf{n} \cdot \left(\eta A \nabla A - \frac{A^2 \mathbf{u}_T}{2} \right) dS - \eta \int_V (\nabla A)^2 dV + \int_S \mathbf{n} \cdot (\mathbf{A}\phi) dS \tag{A.22}$$

and for boundary conditions for which the first and last terms on the right hand side vanish we obtain the equation

$$\frac{d}{dt}\int_V \frac{A^2}{2} dV = -\eta \int_V (\nabla A)^2 dV \tag{A.23}$$

as the right hand side of this is negative definite it must be true that A^2 and thus A decays with time. The exception to this is if we have $\nabla A = constant$ however when taking the curl of this to obtain $\mathbf{B}_T$ we would again yield zero. This therefore means that $\mathbf{B}_T$ decays with time. For a suitably large time where the toroidal magnetic field has decayed equation (A.16) can therefore be rewritten as

$$\frac{\partial}{\partial t}(B\hat{\mathbf{z}}) = \nabla \times (\mathbf{u}_T \times \mathbf{B}_P) + \eta \nabla^2 (B\hat{\mathbf{z}}) \tag{A.24}$$

Equation (A.24) may be rewritten as

$$\frac{\partial}{\partial t}(B\hat{\mathbf{z}}) = -(\mathbf{u}_T \cdot \nabla)\mathbf{B}_P + \eta \nabla^2 (B\hat{\mathbf{z}}) \tag{A.25}$$

$$\frac{\partial B}{\partial t} = -(\mathbf{u}_T \cdot \nabla)B + \eta \nabla^2 (B) \tag{A.26}$$

$$\frac{\partial B}{\partial t} + (\mathbf{u}_T \cdot \nabla)B = \eta \nabla^2 (B) \tag{A.27}$$

which is of the same form as (A.18) (minus the gradient term arising from the uncurling) and therefore B, and consequently $\mathbf{B}_P$ decays in time for all cases other than $\nabla B = 0$. For this case the only allowed form of the magnetic field would be $\mathbf{B} = B(t)\hat{\mathbf{z}}$. Substituting this into the induction equation yields $\frac{\partial B}{\partial t} = 0$ and thus B cannot be a function of time either, the only allowable value would be for it to be a uniform magnetic field, B_0, in the $\hat{\mathbf{z}}$ direction. Now imposing our criterion that the magnetic field vanishes at infinity yields

$$\lim_{\mathbf{x}\to\infty} \mathbf{B} = \lim_{\mathbf{x}\to\infty} B_0 \hat{\mathbf{z}} \tag{A.28}$$

$$= 0 \tag{A.29}$$

thus the magnetic field in this case must be zero for all time and we therefore have that

magnetic fields of the form $(B_x(x,y,t), B_y(x,y,t), B_z(x,y,t))$ cannot sustain dynamo action.

A.2 Zeldovich's Anti-Dynamo Theorem

Zeldovich's theorem states that: A planar incompressible flow $\mathbf{u} = \big(u_x(x,y,z,t), u_y(x,y,z,t), 0\big)$ in a bounded volume V at whose boundaries the magnetic field vanishes cannot maintain a magnetic field. This theorem is proved in a similar manner to theorem 1. First we state the induction equation in incompressible form

$$\frac{\partial \mathbf{B}}{\partial t} = (\mathbf{B}\cdot\nabla)\mathbf{u} - (\mathbf{u}\cdot\nabla)\mathbf{B} + \eta\nabla^2\mathbf{B} \tag{A.30}$$

next we consider only the $\hat{\mathbf{z}}$ component of this. As $u_z = 0$ we obtain

$$\frac{\partial B_z}{\partial t} + (\mathbf{u}\cdot\nabla)B_z = \eta\nabla^2 B_z \tag{A.31}$$

multiplying by B_z and using vector calculus identities gives

$$\frac{\partial}{\partial t}\frac{B_z^2}{2} + \nabla\cdot\left(\frac{\mathbf{u}B_z^2}{2}\right) = \eta(\nabla\cdot(B_z\nabla B_z) - (\nabla B_z)^2) \tag{A.32}$$

thus integrating equation (A.32) over the volume and using the divergence theorem yields

$$\int_V \frac{\partial}{\partial t}\frac{B_z^2}{2}dV = \int_V -\nabla\cdot\left(\frac{\mathbf{u}B_z^2}{2}\right) + \eta(\nabla\cdot(B_z\nabla B_z) - (\nabla B_z)^2)dV \tag{A.33}$$

$$= \int_S \mathbf{n}\cdot\left(\eta B_z\nabla B_z - \frac{\mathbf{u}B_z^2}{2}\right)dS - \eta\int_V |\nabla B_z|^2 dV \tag{A.34}$$

and therefore for suitable boundary conditions the first term is 0 and after exchanging the time derivative with the integral on the left we obtain

$$\frac{d}{dt}\int_V \frac{B_z^2}{2}dV = -\eta\int_V |\nabla B_z|^2 dV \tag{A.35}$$

as the right is negative definite B_z must decay with time in all cases except $\nabla B_z = 0$ which I will return to later. Now in all cases but $\nabla B_z = 0$ B_z decays to 0. Thus at some point the

field will become two dimensional. This allows us to express the magnetic field using a stream function

$$\mathbf{B} = \nabla \times (A\hat{\mathbf{z}}) \tag{A.36}$$

substituting this into the induction equation gives

$$\nabla \times \left(\frac{\partial A}{\partial t} \hat{\mathbf{z}} \right) = \nabla \times (\mathbf{u} \times \mathbf{B}) + \nabla \times (\eta \nabla^2 A \hat{\mathbf{z}}) \tag{A.37}$$

now $\mathbf{u} \times \mathbf{B} = -(\mathbf{u} \cdot \nabla) A\hat{\mathbf{z}}$ and therefore uncurling and taking the dot product of equation (A.37) with $A\hat{\mathbf{z}}$ yields

$$A \frac{\partial A}{\partial t} = -A(\mathbf{u} \cdot \nabla) A + \eta A \nabla^2 A + A\hat{\mathbf{z}} \cdot \nabla \phi \tag{A.38}$$

Thus by looking at equation (A.19) and the subsequent analysis we see that A decays to 0 and thus the magnetic field cannot be maintained by dynamo action if B_z decays to 0. Now if B_z is a constant other than 0 we would define $\mathbf{B}$ to be

$$\mathbf{B} = \nabla \times (A\hat{\mathbf{z}}) + B_z \hat{\mathbf{z}} \tag{A.39}$$

substituting this into the induction equation would yield an equation identical to (A.37) with the only difference that $\mathbf{u} \times \mathbf{B} = -(\mathbf{u} \cdot \nabla) A\hat{\mathbf{z}} - u_x B_z \hat{\mathbf{y}}$. Thus the dot product with $\mathbf{A}$ would be equivalent to (A.38) meaning that the horizontal components of the magnetic field would still decay away. This means that the only allowable magnetic field configuration would be a constant vertical magnetic field everywhere, $\mathbf{B} = B_0 \hat{\mathbf{z}}$ ($\nabla B_z = 0$ appears to allow time dependence however substituting this into the induction equation we see that no time dependence is possible). However the magnetic field vanishing at the boundaries means that it must be 0 everywhere (else it would contain a spatial dependence which we have shown is not allowed).

Thus the magnetic field in this case must be zero for all time and therefore a planar incompressible flow $\mathbf{u} = \big(u_x(x,y,z,t), u_y(x,y,z,t), 0\big)$ and that vanishes at infinity cannot maintain a magnetic field. Note that many statements of this theorem instead of imposing a "van-

ishes at infinity" condition impose that the magnetic field vanish at the boundary of the fixed volume V

A.3 Cowling's Anti-Dynamo Theorem

This theorem, attributed to Cowling, states that an axisymmetric magnetic field which vanishes at infinity cannot be maintained by dynamo action. In spherical polar coordinates this is of the form $\mathbf{B} = \mathbf{B}(r, \theta, t)$, with its axisymmetric nature resulting in no dependence on the azimuthal coordinate ϕ. The first thing to note is that due to the fact that the induction equation contains $\mathbf{u}$ a flow field that depended on ϕ would result in a magnetic field that has a ϕ dependence, thus we must also have that $\mathbf{u}$ is axisymmetric. Note also that our proof depends on $\mathbf{u}$ being incompressible.

The first step is to write the magnetic field and flow field in terms of an axisymmetric poloidal-toroidal decomposition.

$$\mathbf{B} = \mathbf{B}_T + \mathbf{B}_p \tag{A.40}$$

$$= B\hat{\phi} + \nabla \times (A\hat{\phi}) \tag{A.41}$$

$$\mathbf{u} = \mathbf{u}_T + \mathbf{u}_p \tag{A.42}$$

$$= s\Omega\hat{\phi} + \nabla \times \left(\frac{\Psi}{s}\hat{\phi}\right) \tag{A.43}$$

where $s = r\sin(\theta)$. The proof revolves around decomposing the induction equation into a toroidal part and a poloidal part and showing that each decays. First consider the laplacian of $B\hat{\phi}$

$$\nabla^2(B\hat{\phi}) = \left(\nabla^2(B) - \frac{B}{s^2}\right)\hat{\phi} \tag{A.44}$$

similarly by using the fact that we may exchange partial derivatives

$$\nabla^2\big(\nabla\times(A\hat{\phi})\big)=\nabla\times\left[\left(\nabla^2(A)-\frac{A}{s^2}\right)\hat{\phi}\right] \tag{A.45}$$

$$=A_1\hat{\mathbf{r}}+A_2\hat{\theta} \tag{A.46}$$

thus the laplacian of $\mathbf{B}$ may be decomposed into a toroidal component involving B and a poloidal component involving A. Thus the induction equation may be written

$$\frac{\partial B}{\partial t}\hat{\phi}+\nabla\times\left(\frac{\partial A}{\partial t}\hat{\phi}\right)=\nabla\times(\mathbf{u}\times\mathbf{B})+\eta\left(\nabla^2(B)-\frac{B}{s^2}\right)\hat{\phi}+\eta\nabla\times\left[\left(\nabla^2(A)-\frac{A}{s^2}\right)\hat{\phi}\right] \tag{A.47}$$

$$=(\mathbf{B}\cdot\nabla)\mathbf{u}-(\mathbf{u}\cdot\nabla)\mathbf{B}+\eta\left(\nabla^2(B)-\frac{B}{s^2}\right)\hat{\phi}+\eta\nabla\times\left[\left(\nabla^2(A)-\frac{A}{s^2}\right)\hat{\phi}\right] \tag{A.48}$$

the toroidal component of equation (A.48) is given by

$$\frac{\partial B}{\partial t}=\big[(\mathbf{B}\cdot\nabla)\mathbf{u}-(\mathbf{u}\cdot\nabla)\mathbf{B}\big]_\phi+\eta\left(\nabla^2B-\frac{B}{s^2}\right) \tag{A.49}$$

now

$$[(\mathbf{B}\cdot\nabla)\mathbf{u}]_\phi=s(\mathbf{B}_P\cdot\nabla)\Omega+\Omega(B_r\sin(\theta)+B_\theta\cos(\theta))+\frac{B}{r\sin(\theta)}\big(u_r\sin(\theta)+u_\theta\cos(\theta)\big) \tag{A.50}$$

$$[(\mathbf{u}\cdot\nabla)\mathbf{B}]_\phi=(\mathbf{u}_P\cdot\nabla)B+\Omega\big(B_r\sin(\theta)+B_\theta\cos(\theta)\big) \tag{A.51}$$

$$[(\mathbf{B}\cdot\nabla)\mathbf{u}]_\phi-[(\mathbf{u}\cdot\nabla)\mathbf{B}]_\phi=s(\mathbf{B}_P\cdot\nabla)\Omega-(\mathbf{u}_P\cdot\nabla)B+\frac{B}{s}\big(u_r\sin(\theta)+u_\theta\cos(\theta)\big) \tag{A.52}$$

therefore the contribution of the $\hat{\phi}$ direction can be reduced to the scalar equation (A.53)

$$\frac{\partial B}{\partial t} = s(\mathbf{B}_P \cdot \nabla)\Omega - (\mathbf{u}_P \cdot \nabla)B + \frac{B}{s}\big(u_r \sin(\theta) + u_\theta \cos(\theta)\big) + \eta\left(\nabla^2 B - \frac{B}{s^2}\right) \tag{A.53}$$

this may be further simplified to give

$$\frac{\partial B}{\partial t} = s(\mathbf{B}_P \cdot \nabla)\Omega - s(\mathbf{u}_P \cdot \nabla)\frac{B}{s} + \eta\left(\nabla^2 B - \frac{B}{s^2}\right) \tag{A.54}$$

the poloidal component of (A.47) may be written

$$\nabla \times \left(\frac{\partial A}{\partial t}\hat{\phi}\right) = \Big[\nabla \times (\mathbf{u} \times \mathbf{B})\Big]_P + \eta \nabla \times \left[\left(\nabla^2(A) - \frac{A}{s^2}\right)\hat{\phi}\right] \tag{A.55}$$

and it was shown in the first anti-dynamo theorem that

$$\Big[\nabla \times (\mathbf{u} \times \mathbf{B})\Big]_P = \nabla \times (\mathbf{u}_P \times \mathbf{B}_P) \tag{A.56}$$

thus

$$\nabla \times \left(\frac{\partial A}{\partial t}\hat{\phi}\right) = \nabla \times (\mathbf{u}_P \times \mathbf{B}_P) + \eta \nabla \times \left[\left(\nabla^2(A) - \frac{A}{s^2}\right)\hat{\phi}\right] \tag{A.57}$$

uncurling gives

$$\frac{\partial A}{\partial t}\hat{\phi} = \mathbf{u}_P \times \mathbf{B}_P + \eta\left(\nabla^2(A) - \frac{A}{s^2}\right)\hat{\phi} \tag{A.58}$$

as $\mathbf{u}_P \times \mathbf{B}_p$ only has a azimuthal component

$$\mathbf{u}_P \times \mathbf{B}_p = [\mathbf{u}_P \times \mathbf{B}_p]_\phi \hat{\phi} \tag{A.59}$$

$$[\mathbf{u}_P \times \mathbf{B}_p]_\phi = \frac{-u_r}{r}\frac{\partial}{\partial r}(rA) - \frac{u_\theta}{r\sin(\theta)}\frac{\partial}{\partial \theta}\big(A\sin(\theta)\big) \tag{A.60}$$

subtle manipulation allows for simplification

$$\frac{1}{s}(\mathbf{u}_P\cdot\nabla)(sA) = (\mathbf{u}_P\cdot\nabla)A + \frac{A}{s}(u_r\sin(\theta)+u_\theta\cos(\theta)) \tag{A.61}$$

$$= \frac{u_r}{r}\left(r\frac{\partial A}{\partial r}+A\right) + \frac{u_\theta}{r\sin(\theta)}\left(\sin(\theta)\frac{\partial A}{\partial\theta}+A\cos(\theta)\right) \tag{A.62}$$

$$= \frac{u_r}{r}\frac{\partial}{\partial r}(rA) + \frac{u_\theta}{r\sin(\theta)}\frac{\partial}{\partial\theta}\big(A\sin(\theta)\big) \tag{A.63}$$

$$= -[\mathbf{u}_P\times\mathbf{B}_p]_\phi \tag{A.64}$$

thus the poloidal component may be expressed as a scalar equation for A

$$\frac{\partial A}{\partial t}+\frac{1}{s}(\mathbf{u}_P\cdot\nabla)(sA) = \eta\left(\nabla^2(A)-\frac{A}{s^2}\right) \tag{A.65}$$

To proceed I first show that A decays. Multiplying (A.65) by s^2A, defining $X = sA$ and manipulating yields

$$\frac{\partial}{\partial t}\frac{X^2}{2}+\nabla\cdot\left(\mathbf{u}_P\frac{X^2}{2}\right) = \eta X\left(s\nabla^2\left(\frac{X}{s}\right)-\frac{X}{s^2}\right) \tag{A.66}$$

further manipulation then yields

$$\frac{\partial}{\partial t}\frac{X^2}{2}+\nabla\cdot\left(\mathbf{u}_P\frac{X^2}{2}\right)-\eta X\nabla^2X = -\eta\nabla\cdot\left(\frac{X^2}{s}\nabla s\right) \tag{A.67}$$

I can now use the standard manipulations within the previous two anti-dynamo theorems to show that X decays

$$\frac{\partial}{\partial t}\frac{X^2}{2}+\nabla\cdot\left(\mathbf{u}_P\frac{X^2}{2}\right)-\eta X\nabla^2X = -\eta\nabla\cdot\left(\frac{X^2}{s}\nabla s\right) \tag{A.68}$$

$$\frac{\partial}{\partial t}\frac{X^2}{2} = -\nabla\cdot\left(\eta\frac{X^2}{s}\nabla s+\mathbf{u}_P\frac{X^2}{2}-\eta X\nabla X\right)-\eta|\nabla X|^2 \tag{A.69}$$

$$\frac{d}{dt}\int_V\frac{X^2}{2}dV = \int_S-\mathbf{n}\cdot\left(\eta\frac{X^2}{s}\nabla s+\mathbf{u}_P\frac{X^2}{2}-\eta X\nabla X\right)dS-\eta\int_V|\nabla X|^2dV \tag{A.70}$$

thus with appropriate boundary conditions the first term on the right disappears and we are left with

$$\frac{d}{dt}\int_V \frac{X^2}{2}dV = -\eta\int_V |\nabla X|^2 dV \tag{A.71}$$

thus X and subsequently A decays to 0. The exception is $A = s^{-1}$ however the curl of this is 0. Thus for all cases after a sufficient time A and thus $\mathbf{B}_P$ will have decayed to 0. This means that (A.54) becomes

$$\frac{\partial B}{\partial t} = -s(\mathbf{u}_P\cdot\nabla)\frac{B}{s} + \eta\left(\nabla^2 B - \frac{B}{s^2}\right) \tag{A.72}$$

multiplying by Bs^{-2} and defining $Y = Bs^{-1}$ yields

$$\frac{\partial}{\partial t}\frac{Y^2}{2} = -\nabla\cdot\left(\mathbf{u}_P\frac{Y^2}{2}\right) + \eta Y\left(\frac{1}{s}\nabla^2(sY) - \frac{Y}{s^2}\right) \tag{A.73}$$

by use of a number of vector calculus identities we can manipulate this to the following form

$$\frac{\partial}{\partial t}\frac{Y^2}{2} = -\nabla\cdot\left(\mathbf{u}_P\frac{Y^2}{2}\right) + \eta Y\left(\nabla^2 Y - 2s\nabla\left(\frac{1}{s}\right)\cdot\nabla Y\right) \tag{A.74}$$

using the standard manipulations (A.74) becomes

$$\frac{\partial}{\partial t}\frac{Y^2}{2} = -\nabla\cdot\left(\mathbf{u}_P\frac{Y^2}{2}\right) + \eta Y\nabla^2 Y - 2\eta Y s\nabla\left(\frac{1}{s}\right)\cdot\nabla Y \tag{A.75}$$

$$= \nabla\cdot\left(-\mathbf{u}_P\frac{Y^2}{2} + \eta Y\nabla Y - \eta s Y^2\nabla\left(\frac{1}{s}\right)\right) - \eta|\nabla Y|^2 \tag{A.76}$$

$$\frac{d}{dt}\int_V \frac{Y^2}{2}dV = \int_S \mathbf{n}\cdot\left(-\mathbf{u}_P\frac{Y^2}{2} + \eta Y\nabla Y - \eta s Y^2\nabla\left(\frac{1}{s}\right)\right)dS - \eta\int_V |\nabla Y|^2 dV \tag{A.77}$$

therefore with the correct boundary conditions we obtain

$$\frac{d}{dt}\int_V \frac{Y^2}{2}dV = -\eta\int_V |\nabla Y|^2 dV \tag{A.78}$$

and Y and subsequently B decays. The only exception being if $B \propto s$. In this case the advective component of (A.72) is

$$-s(\mathbf{u}_P \cdot \nabla)\frac{\alpha s}{s} = 0 \tag{A.79}$$

where α is the constant of proportionality. This means that equation (A.72) becomes

$$\frac{\partial B}{\partial t} = \eta\left(\nabla^2 B - \frac{B}{s^2}\right) \tag{A.80}$$

multiplying by B and manipulating we obtain

$$\frac{\partial}{\partial t}\frac{B^2}{2} = \eta B\nabla^2 B - \eta\frac{B^2}{s^2} \tag{A.81}$$

$$= \eta\nabla\cdot(B\nabla B) - \eta|\nabla B|^2 - \eta\frac{B^2}{s^2} \tag{A.82}$$

$$\frac{d}{dt}\int_V \frac{B^2}{2}dV = \eta\int_S \mathbf{n}\cdot(B\nabla B)dS - \eta\int_V |\nabla B|^2 dV - \eta\int_V \left|\frac{B}{s}\right|^2 dV \tag{A.83}$$

with appropriate boundary conditions this becomes

$$\frac{d}{dt}\int_V \frac{B^2}{2}dV = -\eta\int_V |\nabla B|^2 dV - \eta\int_V \left|\frac{B}{s}\right|^2 dV \tag{A.84}$$

thus B decays and an axisymmetric magnetic field which vanishes at infinity cannot be maintained by dynamo action.

A.4 Impossibility of a Dynamo Driven by a Purely Toroidal Flow

An incompressible, purely toroidal, flow of the form $\mathbf{u} = \mathbf{u}_T = \nabla\times(\mathbf{x}\psi_T) = -\mathbf{x}\times\nabla\psi_T$, where $\mathbf{x}$ is the position vector, cannot maintain a dynamo. Note that due to the form of this flow, within spherical polar coordinates, the radial component of the flow is zero, $u_r = 0$.

A magnetic field may be decomposed into its toroidal and poloidal components

$$\mathbf{B} = \mathbf{B}_T + \mathbf{B}_P \tag{A.85}$$

where we have that

$$\mathbf{B}_T = \nabla \times \big(\mathbf{x}T(\mathbf{x})\big) \tag{A.86}$$

$$= -\mathbf{x} \times \nabla T \tag{A.87}$$

$$\mathbf{B}_P = \nabla \times \nabla \times \big(\mathbf{x}P(\mathbf{x})\big) \tag{A.88}$$

$$= -\nabla \times \big(\mathbf{x} \times \nabla P\big) \tag{A.89}$$

now consider the induction equation

$$\frac{\partial \mathbf{B}}{\partial t} = \nabla \times (\mathbf{u} \times \mathbf{B}) + \eta \nabla^2 \mathbf{B} \tag{A.90}$$

taking its scalar product with the position vector $\mathbf{x}$ yields

$$\mathbf{x} \cdot \frac{\partial \mathbf{B}}{\partial t} = \mathbf{x} \cdot \nabla \times (\mathbf{u} \times \mathbf{B}) + \eta \mathbf{x} \cdot \nabla^2 \mathbf{B} \tag{A.91}$$

we have that

$$\mathbf{x} \cdot \frac{\partial \mathbf{B}}{\partial t} = -\nabla \cdot \Big(\mathbf{u}(\mathbf{x} \cdot \mathbf{B}) - \mathbf{B}(\mathbf{x} \cdot \mathbf{u})\Big) + \eta \mathbf{x} \cdot \nabla^2 \mathbf{B} \tag{A.92}$$

and due to the form of $\mathbf{u}$ we have $\mathbf{x} \cdot \mathbf{u} = 0$ thus

$$\mathbf{x} \cdot \nabla \times (\mathbf{u} \times \mathbf{B}) = -(\mathbf{u} \cdot \nabla)(\mathbf{x} \cdot \mathbf{B}) \tag{A.93}$$

the diffusive term can also be put into a similar form

$$\nabla^2 (\mathbf{x} \cdot \mathbf{B}) = \mathbf{x} \cdot \nabla^2 \mathbf{B} \tag{A.94}$$

thus the induction equation may be rewritten as

$$\frac{\partial}{\partial t}(\mathbf{x} \cdot \mathbf{B}) + (\mathbf{u} \cdot \nabla)(\mathbf{x} \cdot \mathbf{B}) = \eta \nabla^2 (\mathbf{x} \cdot \mathbf{B}) \tag{A.95}$$

defining $\xi = \mathbf{x} \cdot \mathbf{B}$ and multiplying equation (A.95) by ξ yields

$$\xi\frac{\partial}{\partial t}\xi+\xi(\mathbf{u}\cdot\nabla)\xi=\eta\xi\nabla^2\xi \tag{A.96}$$

I now perform the standard manipulations to show that this decays

$$\frac{\partial}{\partial t}\frac{\xi^2}{2}=-\nabla\cdot\left(\mathbf{u}\frac{\xi^2}{2}\right)+\eta\nabla\cdot(\xi\nabla\xi)-\eta|\nabla\xi|^2 \tag{A.97}$$

$$\frac{d}{dt}\int_V\frac{\xi^2}{2}dV=-\int_S\mathbf{n}\cdot\left(\mathbf{u}\frac{\xi^2}{2}\right)dS+\eta\int_S\mathbf{n}\cdot(\xi\nabla\xi)dS-\eta\int_V|\nabla\xi|^2dV \tag{A.98}$$

with appropriate boundary conditions equation (A.98) becomes

$$\frac{d}{dt}\int_V\frac{\xi^2}{2}dV=-\eta\int_V|\nabla\xi|^2dV \tag{A.99}$$

and $\xi=\mathbf{x}\cdot\mathbf{B}$ decays with time. Thus, as it can be seen by considering the toroidal and poloidal components of the magnetic field that $\mathbf{x}\cdot\mathbf{B}=\mathbf{x}\cdot\mathbf{B}_P$, $\mathbf{B}_P$ and $P(\mathbf{x})$ decay with time. For further details see page 119 of [75].

The decay of the poloidal magnetic field means that after a long enough time period we will be left with just the toroidal magnetic field. Thus the induction equation becomes

$$\frac{\partial\mathbf{B}_T}{\partial t}=\nabla\times(\mathbf{u}_T\times\mathbf{B}_T)+\eta\nabla^2\mathbf{B}_T \tag{A.100}$$

now as defined above $\mathbf{B}_T=\nabla\times(\mathbf{x}T(\mathbf{x}))$ therefore equation (A.100) may be expressed in this form and then uncurled to give

$$\frac{\partial}{\partial t}(\mathbf{x}T(\mathbf{x}))=\mathbf{u}_T\times\mathbf{B}_T+\eta\nabla^2(\mathbf{x}T(\mathbf{x}))+\nabla\xi \tag{A.101}$$

in spherical polar coordinates $\mathbf{x}=r\hat{\mathbf{r}}=\mathbf{r}$ therefore equation (A.101) becomes

$$\frac{\partial}{\partial t}(\mathbf{r}T(\mathbf{r}))=\mathbf{u}_T\times\mathbf{B}_T+\eta\nabla^2(\mathbf{r}T(\mathbf{r}))+\nabla\xi \tag{A.102}$$

due to the form of $\mathbf{u}_T$ and $\mathbf{B}_T$ each has only a $\hat{\theta}$ and a $\hat{\phi}$ component. $\mathbf{B}_T$ can be expressed in terms of the scalar function T as

$$\mathbf{B}_T = \frac{1}{\sin(\theta)}\frac{\partial T}{\partial \phi}\hat{\theta} - \frac{\partial T}{\partial \theta}\hat{\phi} \tag{A.103}$$

and the flow field is of the form

$$\mathbf{u}_T = u_{T\theta}\hat{\theta} + u_{T\phi}\hat{\phi} \tag{A.104}$$

the element of (A.102) arising from the advective contribution to the induction equation becomes

$$\mathbf{u}_T \times \mathbf{B}_T = \left(u_{T\theta}\frac{\partial T}{\partial \theta} + \frac{u_{T\phi}}{\sin(\theta)}\frac{\partial T}{\partial \phi}\right)\hat{\mathbf{r}} \tag{A.105}$$

$$= -\mathbf{r}(\mathbf{u}_T \cdot \nabla)T \tag{A.106}$$

therefore the induction equation is given by

$$\frac{\partial}{\partial t}(\mathbf{r}T(\mathbf{r})) = -\mathbf{r}(\mathbf{u}_T \cdot \nabla)T + \eta\nabla^2(\mathbf{r}T(\mathbf{r})) + \nabla\xi \tag{A.107}$$

now we have that

$$\frac{\partial}{\partial t}(\mathbf{r}T(\mathbf{r})) = \mathbf{r}\frac{\partial}{\partial t}(T(\mathbf{r})) \tag{A.108}$$

$$\nabla^2(\mathbf{r}T(\mathbf{r})) = \mathbf{r}\nabla^2 T + 2\nabla T \tag{A.109}$$

thus

$$\mathbf{r}\frac{\partial}{\partial t}(T(\mathbf{r}))) == -\mathbf{r}(\mathbf{u}_T \cdot \nabla)T + \eta\mathbf{r}\nabla^2 T + \nabla F \tag{A.110}$$

by looking at the $\hat{\theta}$ and $\hat{\phi}$ components of (A.110) we see immediately that $F = F(r,t)$ and therefore we can simply write $\nabla F = \mathbf{r}f(r,t)$. This then allows for a scalar function of T to be formed

$$\frac{\partial T}{\partial t} = -(\mathbf{u}_T \cdot \nabla)T + \eta\nabla^2 T + f(r,t) \tag{A.111}$$

I now multiply by T and use the standard manipulations

$$T\frac{\partial T}{\partial t} = -T(\mathbf{u}_T \cdot \nabla)T + \eta T\nabla^2 T + Tf(r,t) \tag{A.112}$$

$$\frac{\partial}{\partial t}\frac{T^2}{2} = -\nabla \cdot \left(\mathbf{u}_T \frac{T^2}{2}\right) + \eta\nabla \cdot (T\nabla T) - \eta|\nabla T|^2 + Tf \tag{A.113}$$

$$\frac{d}{dt}\int_V \frac{T^2}{2}dV = -\int_S \mathbf{n} \cdot \left(\mathbf{u}_T \frac{T^2}{2}\right)dS + \eta\int_S \mathbf{n} \cdot (T\nabla T)dS - \eta\int_V |\nabla T|^2 dV + \int_V Tf dV \tag{A.114}$$

with appropriate boundary conditions

$$\frac{d}{dt}\int_V \frac{T^2}{2}dV = -\eta\int_V |\nabla T|^2 dV + \int_V Tf dV \tag{A.115}$$

the last thing to note is that the addition of any function of r and t only to T would have no effect on the form of the toroidal field

$$\mathbf{B}_T = -\mathbf{r} \times \nabla T' \tag{A.116}$$

$$= -\mathbf{r} \times \nabla(T + f(r,t)) \tag{A.117}$$

$$= -\mathbf{r} \times \nabla T - \mathbf{r} \times \nabla f(r,t) \tag{A.118}$$

$$= -\mathbf{r} \times \nabla T \tag{A.119}$$

without loss of generality we can assume T has 0 average on spherical surfaces, i.e. that

$$< T > = \frac{1}{4\pi^2}\int_0^{2\pi}\int_0^{\pi} T\sin(\theta)d\phi d\theta \tag{A.120}$$

$$= 0 \tag{A.121}$$

therefore

$$\int_V T f dV = \int_r 4\pi^2 < T > f(r,t) r dr \tag{A.122}$$

$$= 0 \tag{A.123}$$

equation (A.115) then becomes

$$\frac{d}{dt}\int_V \frac{T^2}{2} dV = -\eta \int_V |\nabla T|^2 dV \tag{A.124}$$

and T decays to 0. An incompressible, purely toroidal, flow therefore cannot maintain a dynamo.

A.5 The Childress Bound on R_m

As well as anti-dynamo theorems which tell us whether a particular flow can generate dynamo action (or whether a flow can sustain a magnetic field with a particular structure) there are also a number of proofs giving lower bounds on what R_m is needed for dynamo action. One such bound is the Childress bound named after Stephen Childress which states that for dynamo action to occur we requre that

$$R_m > \pi. \tag{A.125}$$

To prove this, consider taking the dot product of the induction equation with $\mathbf{B}/\mu$ and manipulating to give

$$\frac{\partial}{\partial t}\frac{\mathbf{B}^2}{2\mu} = \nabla \cdot \left(\frac{\mathbf{B}}{\mu} \times (\mathbf{u} \times \mathbf{B})\right) + \mathbf{j} \cdot (\mathbf{u} \times \mathbf{B}) + \eta \frac{\mathbf{B}}{\mu} \cdot \nabla^2 \mathbf{B} \tag{A.126}$$

various vector calculus identities then allow (A.126) to become

$$\frac{\partial}{\partial t}\frac{\mathbf{B}^2}{2\mu} = \nabla \cdot \left(\frac{\mathbf{B}}{\mu} \times (\mathbf{u} \times \mathbf{B})\right) + \mathbf{j} \cdot (\mathbf{u} \times \mathbf{B}) + \eta \frac{\mathbf{B}}{\mu} \cdot \nabla^2 \mathbf{B} \tag{A.127}$$

$$= \nabla \cdot \left(\frac{\mathbf{B}}{\mu} \times (\mathbf{u} \times \mathbf{B})\right) + \mathbf{j} \cdot (\mathbf{u} \times \mathbf{B}) + \eta\mu \left(\nabla \cdot \left(\frac{\mathbf{B}}{\mu} \times \mathbf{j}\right) - \mathbf{j}^2\right) \tag{A.128}$$

where $\mu\mathbf{j} = \nabla \times \mathbf{B}$. Integration over a fixed volume allows the divergence terms to be converted to surface integrals via the divergence theorem

$$\frac{d}{dt}\int_V \frac{\mathbf{B}^2}{2\mu}dV = \int_V \nabla\cdot\left(\frac{\mathbf{B}}{\mu}\times(\mathbf{u}\times\mathbf{B})\right)dV + \int_V \mathbf{j}\cdot(\mathbf{u}\times\mathbf{B})dV + \eta\mu\int_V \nabla\cdot\left(\frac{\mathbf{B}}{\mu}\times\mathbf{j}\right)dV - \eta\mu\int_V \mathbf{j}^2 dV \tag{A.129}$$

$$= \int_S \mathbf{n}\cdot\left(\frac{\mathbf{B}}{\mu}\times(\mathbf{u}\times\mathbf{B})\right)dS + \int_V \mathbf{j}\cdot(\mathbf{u}\times\mathbf{B})dV + \eta\mu\int_S \mathbf{n}\cdot\left(\frac{\mathbf{B}}{\mu}\times\mathbf{j}\right)dS - \eta\mu\int_V \mathbf{j}^2 dV \tag{A.130}$$

$$= \int_V \mathbf{j}\cdot(\mathbf{u}\times\mathbf{B})dV - \eta\mu\int_V \mathbf{j}^2 dV \tag{A.131}$$

where in the last line I have assumed boundary conditions to enable the surface integrals to vanish. Now if we define the magnetic energy, E_M, such that

$$E_M = \int_V \frac{\mathbf{B}^2}{2\mu}dV \tag{A.132}$$

then multiplication of equation (A.131) by μ yields

$$\mu\frac{dE_M}{dt} = \int_V (\nabla\times\mathbf{B})\cdot(\mathbf{u}\times\mathbf{B})dV - \eta\int_V |\nabla\times\mathbf{B}|^2 dV \tag{A.133}$$

the first integrand is a triple product, therefore we have the inequality $\mathbf{a}\cdot(\mathbf{b}\times\mathbf{c}) \leq |\mathbf{a}||\mathbf{b}||\mathbf{c}|$. This leads to the inequality

$$\int_V \mathbf{j}\cdot(\mathbf{u}\times\mathbf{B})dV \leq \left(\int_V |\mathbf{u}|^2 dV\right)^{\frac{1}{2}}\left(\int_V |\mathbf{B}|^2 dV\right)^{\frac{1}{2}}\left(\int_V |\nabla\times\mathbf{B}|^2 dV\right)^{\frac{1}{2}} \tag{A.134}$$

$$\leq u_{max}\left(\int_V |\mathbf{B}|^2 dV\right)^{\frac{1}{2}}\left(\int_V |\nabla\times\mathbf{B}|^2 dV\right)^{\frac{1}{2}} \tag{A.135}$$

a general result for divergence free fields confined to a sphere of radius a and matching to an exterior decaying potential is that

$$\int_V |\nabla\times\mathbf{B}|^2 dV \geq \frac{\pi^2}{a^2}\int_V |\mathbf{B}|^2 dV \tag{A.136}$$

and this therefore allows for the inequality (A.135) to become

$$\int_V \mathbf{j} \cdot (\mathbf{u} \times \mathbf{B}) dV \leq \frac{a u_{max}}{\pi} \int_V |\nabla \times \mathbf{B}|^2 dV \tag{A.137}$$

substituting this into equation (A.133) yields

$$\mu \frac{dE_M}{dt} \leq \frac{a u_{max}}{\pi} \int_V |\nabla \times \mathbf{B}|^2 dV - \eta \int_V |\nabla \times \mathbf{B}|^2 dV \tag{A.138}$$

$$= \left(\frac{a u_{max}}{\pi} - \eta \right) \int_V |\nabla \times \mathbf{B}|^2 dV \tag{A.139}$$

a growing dynamo requres the magnetic energy to grow with time thus we require

$$\frac{a u_{max}}{\pi} - \eta > 0 \tag{A.140}$$

$$\frac{a u_{max}}{\eta} > \pi \tag{A.141}$$

and as the definition of the magnetic Reynolds number is

$$R_m = \frac{\textit{Typical Velocity} \times \textit{Typical Length}}{\eta} \tag{A.142}$$

$$= \frac{u_{max} a}{\eta} \tag{A.143}$$

for dynamo action we must have

$$R_m > \pi \tag{A.144}$$

and this is the so called Childress bound.

A.6 The Backus Bound on R_m

We can in fact find a second bound by going in a different direction at equation (A.133). This bound is named after G.Backus.

First by using the identity $(\nabla \times \mathbf{B}) \times \mathbf{B} = (\mathbf{B} \cdot \nabla)\mathbf{B} - 0.5\nabla|\mathbf{B}|^2$ we may decompose the first integral on the right hand side of (A.133) into

$$\mathbf{u} \cdot \Big((\nabla \times \mathbf{B}) \times \mathbf{B} \Big) = \mathbf{u} \cdot \Big((\mathbf{B} \cdot \nabla)\mathbf{B} - 0.5\nabla|\mathbf{B}|^2 \Big) \tag{A.145}$$

to proceed I switch to tensor notation and perform some manipulations to give

$$u_i B_j \partial_j B_i = -B_i B_j \partial_j u_i + \partial_j (u_i B_i B_j) \tag{A.146}$$

$$-\frac{1}{2} u_j \partial_j (B_i B_i) = -\frac{1}{2} \partial_i (B_j B_j u_i) \tag{A.147}$$

substituting these two identities into (A.145) and integrating yields

$$u_i \varepsilon_{ijk} \varepsilon_{jmn} \partial_m B_n B_k = -B_i B_j \partial_j u_i + \partial_j (u_i B_i B_j) - \frac{1}{2} \partial_i (B_j B_j u_i) \tag{A.148}$$

$$\int_V (\nabla \times \mathbf{B}) \cdot (\mathbf{u} \times \mathbf{B}) = -\int_S \mathbf{n} \cdot \left((\mathbf{u} \cdot \mathbf{B})\mathbf{B} - \frac{\mathbf{B}^2}{2}\mathbf{u} \right) dS + \int_V \mathbf{B} \cdot (\mathbf{B} \cdot \nabla)\mathbf{u} dV \tag{A.149}$$

and thus if we have the boundary conditions $\mathbf{n} \cdot \mathbf{B} = \mathbf{n} \cdot \mathbf{u} = 0$ the surface integrals vanish, leaving

$$\int_V (\nabla \times \mathbf{B}) \cdot (\mathbf{u} \times \mathbf{B}) = \int_V \mathbf{B} \cdot (\mathbf{B} \cdot \nabla)\mathbf{u} dV \tag{A.150}$$

Now defining the rate of strain tensor, e_{ij}, such that

$$2e_{ij} = \partial_i u_j + \partial_j u_i \tag{A.151}$$

we have that

$$B_i B_j e_{ij} = B_j B_i \partial_i u_j \tag{A.152}$$

therefore

$$\int_V (\nabla \times \mathbf{B}) \cdot (\mathbf{u} \times \mathbf{B}) dV = \int_V B_i B_j e_{ij} dV \tag{A.153}$$

$$\leq \left(\int_V |e_{ij}|^2 dv \right)^{\frac{1}{2}} \int_V |\mathbf{B}|^2 dV \tag{A.154}$$

$$= e_{max} \int_V |\mathbf{B}|^2 dV \tag{A.155}$$

substituting this into (A.133) yields

$$\mu \frac{dE_M}{dt} = \int_V (\nabla \times \mathbf{B}) \cdot (\mathbf{u} \times \mathbf{B}) dV - \eta \int_V |\nabla \times \mathbf{B}|^2 dV \tag{A.156}$$

$$\leq e_{max} \int_V |\mathbf{B}|^2 dV - \eta \int_V |\nabla \times \mathbf{B}|^2 dV \tag{A.157}$$

using the condition in equation (A.136) we have that

$$\mu \frac{dE_M}{dt} \leq e_{max} \int_V |\mathbf{B}|^2 dV - \frac{\pi^2 \eta}{a^2} \int_V |\mathbf{B}|^2 dV \tag{A.158}$$

$$= \left(e_{max} - \frac{\pi^2 \eta}{a^2} \right) \int_V |\mathbf{B}|^2 dV \tag{A.159}$$

and for dynamo action we thus require

$$\frac{e_{max} a^2}{\eta} > \pi^2 \tag{A.160}$$

finally a look at our units tells us that this is in fact a condition upon the magnetic Reynold's number

$$R_m = \frac{e_{max} a^2}{\eta} > \pi^2 \tag{A.161}$$

Appendix B

Conserved Quantities

There are three conserved quantities within unforced, incompressible, three dimensional MHD with zero diffusion. To prove their conservation, I begin by writing down the equation of motion for the fluid and the induction equation without forcing and diffusion.

$$\frac{\partial \mathbf{u}}{\partial t} = -(\mathbf{u}\cdot\nabla)\mathbf{u} - \nabla P + \mathbf{J}\times\mathbf{b} \tag{B.1}$$

$$\frac{\partial \mathbf{b}}{\partial t} = \nabla\times(\mathbf{u}\times\mathbf{b}) \tag{B.2}$$

Note, that here I have divided by the density ρ in (B.1) and rescaled the magnetic field such that

$$\mathbf{b} = \frac{\mathbf{B}}{\sqrt{\rho}} \tag{B.3a}$$

$$\mathbf{J} = \nabla\times\mathbf{b} \tag{B.3b}$$

$$P = \frac{p}{\rho} \tag{B.3c}$$

An incompressible flow and solenoidal magnetic field also mean that

$$\nabla\cdot\mathbf{u} = 0 \tag{B.4a}$$

$$\nabla\cdot\mathbf{b} = 0 \tag{B.4b}$$

I will now show that the following three quantities

$$E = \int_v \frac{\mathbf{u}^2}{2} + \frac{\mathbf{b}^2}{2} dV$$

$$H_m = \int_V \mathbf{A}\cdot\mathbf{b} dV \qquad H_c = \int_V \mathbf{u}\cdot\mathbf{b} dV$$

(where $\mathbf{b} = \nabla\times\mathbf{A}$) are conserved.

My thanks go to the authors of [66] for providing surface integrals to aim for when deriving the conserved quantities and the paper also provides an excellent description of the suitable boundary conditions.

B.0.1 Conservation of Energy

The energy is given by the sum of the kinetic and magnetic energies and is defined to be

$$E = \int_v \frac{\mathbf{u}^2}{2} + \frac{\mathbf{b}^2}{2} dV \tag{B.6}$$

Taking the dot product of (B.2) with $\mathbf{b}$ and the dot product of (B.1) with $\mathbf{u}$, summing, and making use of a number of different vector identities yields

$$\frac{\partial}{\partial t}\left(\frac{\mathbf{u}^2+\mathbf{b}^2}{2}\right) = \nabla\cdot\big((\mathbf{u}\times\mathbf{b})\times\mathbf{b}\big) - \nabla\cdot\left(\frac{\mathbf{u}^2}{2}+P\right)\mathbf{u} \tag{B.7}$$

and now we see that after integrating over the volume, exchanging the time derivative and the integral and using the divergence theorem that we have

$$\frac{d}{dt}\int_V \left(\frac{\mathbf{u}^2+\mathbf{b}^2}{2}\right) dV = \int_V \nabla\cdot\big((\mathbf{u}\times\mathbf{b})\times\mathbf{b}\big) - \nabla\cdot\left(\frac{\mathbf{u}^2}{2}+P\right)\mathbf{u} dV \tag{B.8}$$

$$\frac{d}{dt}E = \int_S \mathbf{n}\cdot\big((\mathbf{u}\times\mathbf{b})\times\mathbf{b}\big) dS - \int_S \mathbf{n}\cdot\left(\frac{\mathbf{u}^2}{2}+P\right)\mathbf{u} dS \tag{B.9}$$

Thus a number of different boundary conditions will provide $\frac{dE}{dt} = 0$ and a conservation of energy. The first of these is both $\mathbf{n}\cdot\mathbf{u}$ and $\mathbf{n}\cdot\mathbf{b}$ being zero (referred to, in [66] for example, as perfectly conducting and free slip boundary conditions). The second is $\mathbf{u} = 0$ on the surface S and the third and final condition would be $\mathbf{u}$,$\mathbf{b}$ and P being periodic on the boundary, thus yielding cancelling surface terms.

B.0.2 Conservation of Cross-Helicity

The cross-helicity is defined to be

$$H_c = \int_V \mathbf{u}\cdot\mathbf{b}dV \tag{B.10}$$

To prove that this is conserved I take the dot product of (B.1) with $\mathbf{b}$, noting that $\mathbf{b}\cdot(\mathbf{J}\times\mathbf{b}) = 0$ and the dot product of (B.2) with $\mathbf{u}$. I then sum these two quantities and make use of a number of different standard vector identities to yield

$$\frac{\partial}{\partial t}(\mathbf{u}\cdot\mathbf{b}) = \nabla\cdot\left(\mathbf{b}\left(\frac{\mathbf{u}^2}{2}-P\right)\right) - \nabla\cdot\big(\mathbf{u}(\mathbf{u}\cdot\mathbf{b})\big) \tag{B.11}$$

as with the energy we see that after integrating over the volume, exchanging the time derivative and the integral and using the divergence theorem that we have

$$\frac{d}{dt}\int_V \mathbf{u}\cdot\mathbf{b}dV = \int_V \nabla\cdot\left(\mathbf{b}\left(\frac{\mathbf{u}^2}{2}-P\right)\right) - \nabla\cdot\big(\mathbf{u}(\mathbf{u}\cdot\mathbf{b})\big)dV \tag{B.12}$$

$$= \int_S \mathbf{n}\cdot\left(\mathbf{b}\left(\frac{\mathbf{u}^2}{2}-P\right)\right)dS - \int_S \mathbf{n}\cdot\big(\mathbf{u}(\mathbf{u}\cdot\mathbf{b})\big)dS \tag{B.13}$$

Thus with the appropriate boundary conditions the time derivative of the cross-helicity is zero and thus cross-helicity is conserved. Boundary conditions for which the cross-helicity is conserved are 1) $\mathbf{n}\cdot\mathbf{b} = 0$ and $\mathbf{n}\cdot\mathbf{u} = 0$, 2) $\mathbf{b} = 0$ on the surface S and 3) periodic $\mathbf{u}$,$\mathbf{b}$,P on the boundary.

B.0.3 Conservation of Magnetic-Helicity

The magnetic-helicity is defined to be

$$H_m = \int_V \mathbf{A}\cdot\mathbf{b}dV \tag{B.14}$$

Where $\mathbf{b} = \nabla\times\mathbf{A}$. To prove the conservation of this quantity I first use equation (B.2) to find an equation for $\mathbf{A}$.

$$\frac{\partial(\nabla\times\mathbf{A})}{\partial t}=\nabla\times(\mathbf{u}\times\mathbf{b}) \tag{B.15}$$

$$\nabla\times\frac{\partial\mathbf{A}}{\partial t}=\nabla\times(\mathbf{u}\times\mathbf{b}) \tag{B.16}$$

$$\nabla\times\left(\frac{\partial\mathbf{A}}{\partial t}-(\mathbf{u}\times\mathbf{b})\right)=0 \tag{B.17}$$

Now noting that the curl of any gradient $\nabla\psi$ is 0 we can write down an evolution equation for $\mathbf{A}$.

$$\frac{\partial\mathbf{A}}{\partial t}=(\mathbf{u}\times\mathbf{b})-\nabla\psi \tag{B.18}$$

Here the minus sign of the gradient is simply a convention. Now in a similar manner to the proofs of cross-helicity and energy I take the dot product of (B.18) with $\mathbf{b}$ and the dot product of (B.2) with $\mathbf{A}$ and sum the two, again making use of vector calculus identities. This gives

$$\frac{\partial}{\partial t}(\mathbf{A}\cdot\mathbf{B})=-\nabla\cdot(\mathbf{b}\psi)+\nabla\cdot\big(\mathbf{b}(\mathbf{u}\cdot\mathbf{A})-\mathbf{u}(\mathbf{A}\cdot\mathbf{b})\big) \tag{B.19}$$

$$\frac{d}{dt}\int_V(\mathbf{A}\cdot\mathbf{B})dV=\int_V-\nabla\cdot(\mathbf{b}\psi)+\nabla\cdot\big(\mathbf{b}(\mathbf{u}\cdot\mathbf{A})-\mathbf{u}(\mathbf{A}\cdot\mathbf{b})\big)dV \tag{B.20}$$

$$=\int_S\mathbf{n}\cdot\mathbf{b}(\mathbf{u}\cdot\mathbf{A}-\psi)dS-\int_S\mathbf{n}\cdot\mathbf{u}(\mathbf{A}\cdot\mathbf{b})dS \tag{B.21}$$

Thus we see that magnetic-helicity will be conserved provided that $\mathbf{n}\cdot\mathbf{b}=0$ and $\mathbf{n}\cdot\mathbf{u}=0$. As shown in [66] alternate boundary conditions which yield conservation of magnetic-helicity can be found by making further use of vector calculus identities. We may express equation (B.19) in the form

$$\frac{d}{dt}\int_V(\mathbf{A}\cdot\mathbf{B})dV=\int_S-\mathbf{n}\cdot(\mathbf{A}\times\nabla\psi)+\mathbf{n}\cdot\mathbf{b}(\mathbf{u}\cdot\mathbf{A})-\mathbf{n}\cdot\mathbf{u}(\mathbf{A}\cdot\mathbf{b})dS \tag{B.22}$$

equation (B.22) shows that provided $\mathbf{n}\cdot(\mathbf{A}\times\nabla\psi)=0$, $\mathbf{u}=\mathbf{b}=0$ yields conservation of magnetic-helicity. Finally using equation (B.18) we have that

$$\nabla \cdot \left(\mathbf{A} \times \frac{\partial \mathbf{A}}{\partial t} \right) = \nabla \cdot \big(\mathbf{A} \times (\mathbf{u} \times \mathbf{B}) - \mathbf{A} \times \nabla \psi \big) \tag{B.23}$$

$$= \nabla \cdot \big(-\mathbf{b}(\mathbf{A} \cdot \mathbf{u}) + \mathbf{u}(\mathbf{A} \cdot \mathbf{b}) - \mathbf{A} \times \nabla \psi \big) \tag{B.24}$$

and therefore

$$\nabla \cdot \big(\mathbf{b}(\mathbf{A} \cdot \mathbf{u}) - \mathbf{u}(\mathbf{A} \cdot \mathbf{b}) - \mathbf{A} \times \nabla \psi \big) = -\nabla \cdot \left(\mathbf{A} \times \frac{\partial \mathbf{A}}{\partial t} \right) - 2\nabla \cdot (\psi \mathbf{b}) \tag{B.25}$$

now as the volume integral of the left hand side of this equation after the use of the divergence theorem is identical to the right hand side of (B.22) the evolution of magnetic-helicity may be expressed in the following manner

$$\frac{d}{dt} \int_V (\mathbf{A} \cdot \mathbf{B}) dV = -\int_S \mathbf{n} \cdot \left(\mathbf{A} \times \frac{\partial \mathbf{A}}{\partial t} \right) dS - 2 \int_S \mathbf{n} \cdot \mathbf{b} \psi dS \tag{B.26}$$

and thus a magnetic field with $\mathbf{n} \cdot \left(\mathbf{A} \times \frac{\partial \mathbf{A}}{\partial t} \right) = 0$ and $\mathbf{n} \cdot \mathbf{b} = 0$ has magnetic-helicity as a conserved quantity.